

DNA-inspired chromophore assembly – on the way to 2D supramolecular polymers

Inauguraldissertation

der Philosophisch-naturwissenschaftlichen Fakultät

der Universität Bern

vorgelegt von

Mykhailo Vybornyi

von Ukraine

Leiter der Arbeit

Prof. Dr. R. Häner

Departement Chemie und Biochemie der Universität Bern

DNA-inspired chromophore assembly – on the way to 2D supramolecular polymers

Inauguraldissertation
der Philosophisch-naturwissenschaftlichen Fakultät
der Universität Bern

vorgelegt von
Mykhailo Vybornyi
von Ukraine

Leiter der Arbeit
Prof. Dr. R. Häner

Departement Chemie und Biochemie der Universität Bern

von der Philosophisch-naturwissenschaftlichen Fakultät angenommen

Bern, December 3, 2015

Der Dekan

ACKNOWLEDGMENT

Firstly, I would like to express my sincere gratitude to my advisor Prof. Robert Häner for the continuous support during my PhD studies. His guidance and advices have helped me during all these years. I very appreciate his willingness to conduct fruitful discussions on different topics.

Besides my advisor, I would like to thank the rest of my thesis committee: Prof. Jean-François Lutz and Prof. Philippe Renaud for taking the time to read and evaluate my work.

I would like to thank Prof. Dr. G. Calzaferri for his wonderful work and help with the interpretation of the spectroscopic data and calculations. Collaboration with T. Wandlowski and A. Rudnev was extremely important in many projects. My sincere thanks also goes to Dr. Villari, Dr. Micali, and Dr. Mineo, who provided me an opportunity to solve the puzzling behavior of 2D supramolecular polymers. Without their precious support it would not be possible to conduct this research.

I also want to thank all current and former members of the Häner group. The supporting services in-house (Ausgabe, facility management, MS-team, NMR-team and crystallography-team) and financial support of the Swiss National Science Foundation (SNF) and the University of Bern are gratefully acknowledged.

Last but not the least, I would like to thank my family: my parents, brother and wife for supporting me spiritually during these years.

ABSTRACT

The precise arrangement of functional entities in morphologically well-defined shapes remains one of the key challenges in the processing of organic molecules. Targeting the preparation of functional systems with a high degree of complexity, the self-assembly of small molecules or oligomers can be used as an efficient method. In this work, the bottom-up approach was applied to prepare one-dimensional (1D) and two-dimensional (2D) arrays of different chromophores. Substituted pyrenes and porphyrins were used as chromophores. A set of unique properties made these molecules attractive for the utilization in the systems studied.

This thesis is separated in seven chapters. Some of the general methods for the arraying of chromophores, including pyrenes and porphyrins, are described in the introduction part (Chapter I). Chapters II-VI are fully devoted to the properties of self-assembled structures prepared in a bottom-up approach. The amphiphilic oligomers described in Chapters II-V consist of phosphodiester-linked pyrenes. Depending on the geometry of a pyrene core substitution (1,6 or 2,7 type), self-assembly allows the preparation of supramolecular architectures of different morphologies: 2D nanosheets are formed in case of 1,6- and 2,7-substitution whereas 1D tubular structures could be built from 2,7-substituted isomers. The morphologies of the assemblies are established by AFM and TEM, and the results are further correlated with spectroscopic and scattering data.

Chapter II introduces the spectroscopic effects of the internal alignment of 1,6-substituted pyrenes in 2D assemblies, which leads to strong exciton coupling with an unprecedented observation – simultaneous development of the J- and H-bands from two different electronic transitions.

Chapter III describes the morphological properties of 2D structures. The assemblies consist of an inner layer of highly hydrophobic pyrenes, sandwiched

between a net of phosphates. Due to the repulsion of the negative charges, the 2D assemblies exist mostly as free-standing sheets. Despite the similarity in spectroscopic properties, the structural parameters of the 2D aggregates drastically depend on the preparation procedure. Under optimized conditions, extra-large sheets (thickness of 2 nm, aspect ratio area/thickness $\sim 10^7$) in aqueous solution are formed.

Chapter IV shows that the chiroptical properties of 2D supramolecular assemblies of achiral, charged pyrene trimers are efficiently rendered chiral by asymmetric physical perturbations (vortex, thermophoretic force). The chiroptical activity strongly depends on the degree of supramolecular order of the nanosheets, which is easily controlled by the method of preparation (Chapter III). The high degree of structural order ensures strong cooperative effects within the aggregates, rendering them more susceptible to external stimuli.

Chapter V describes the divergent assembly pathways of 2,7-substituted pyrene oligomers. The self-assembly process leads to the simultaneous formation of tubular and sheetlike objects. TEM data confirmed a hollow structure of the tubes, whereas AFM studies revealed the difference in a thickness between individual sheets and collapsed tubes.

In Chapter VI, double-stranded DNA hybrids containing up to four consecutive, face-to-face stacked porphyrins are described. The formation of double strands containing up to four free base porphyrins is enabled without compromising duplex stability.

Finally, general conclusions and outlook are presented in Chapter VII.

Contents

ACKNOWLEDGMENT	v
ABSTRACT	vii
CHAPTER I. GENERAL INTRODUCTION	2
1. π -Conjugated molecules in materials science	2
2. Supramolecular chemistry in materials science	4
2.1 Supramolecular polymerization	7
2.2 DNA-guided assembly of π -conjugated molecules.....	11
2.3 Non-natural phosphodiester in materials science	14
3. Aim of the study	19
4. References	20
CHAPTER II. SPECTROSCOPIC PROPERTIES AND MORPHOLOGY OF THE ASSEMBLES FROM 1.6-SUBSTITUTED PYRENE-BASED TRIMERS	26
1. Abstract	26
2. Introduction	26
3. Results	28
3.1 Synthesis of pyrene oligomers	28
3.2 Atomic Force Microscopy (AFM)	29
3.3 Spectroscopic experiments.....	32
4. Discussion.....	40
5. Conclusions	42
6. Experimental part	42
7. References	46
CHAPTER III. FORMATION OF EXTRA-LARGE NANOSHEETS	54
1. Abstract	54
2. Introduction	54
3. Methods of poly16Py ₃ preparation	56
4. Results and discussion	57

4.1	Spectroscopic studies	57
4.2	Atomic Force Microscopy (AFM) and Transmission Electron Microscopy studies (TEM)	62
4.3	Investigation of the self-assembly mechanism	66
5.	Conclusions	68
6.	Experimental part	69
7.	References	71
CHAPTER IV. HYDRODYNAMIC AND THERMOPHORETIC EFFECTS ON THE SUPRAMOLECULAR CHIRALITY OF PYRENE-DERIVED NANOSHEETS		76
1.	Abstract	76
2.	Introduction	77
3.	Results and Discussion.....	79
3.1	Morphological properties.....	79
3.2	Supramolecular optical activity and alignment effects.....	87
4.	Conclusions	95
5.	Experimental Section.....	96
6.	References	101
CHAPTER V. TUBES OR SHEETS: DIVERGENT AGGREGATION PATHWAYS OF AN AMPHIPHILIC 2,7-SUBSTITUTED PYRENE TRIMER		106
1.	Abstract	106
2.	Introduction	106
3.	Results	108
3.1	Synthesis of pyrene oligomers	108
4.	Conclusions	112
5.	Experimental part	113
6.	References	116
CHAPTER VI. ASSEMBLING MULTIPORPHYRIN STACKS INSIDE THE DNA DOUBLE HELIX		120
1.	Abstract	120
2.	Introduction	120

3. Results	122
3.1 Synthesis of the porphyrin phosphoramidite and preparation of oligonucleotides	122
3.2 Hybrid stability	124
3.3 UV/vis spectroscopy	127
3.4 Fluorescence spectroscopy	131
3.5 Excitation spectra	132
3.6 CD spectroscopy	134
4. Conclusions	137
5. Experimental part	137
6. References	142
CHAPTER VII. GENERAL CONCLUSIONS AND OUTLOOK	148
APPENDIX A. FRONTISPIECE IN <i>ANGEW. CHEM. INT. ED.</i> 2013, 52, 11488	150
APPENDIX B. COVER IMAGE IN <i>BIOCONJUG. CHEM.</i> 2014, 25, 1785	151
APPENDIX C. NMR SPECTRA OF 1.6-SUBSTITUTED DERIVATIVES OF PYRENE	152
APPENDIX D. HPLC PURIFICATION AND CHARACTERIZATION OF 16PY ₃	156
APPENDIX E. ADDITIONAL AFM IMAGES OF POLY16PY ₃ PREPARED BY SLOW COOLING	157
APPENDIX F. ADDITIONAL TEM IMAGES OF POLY16PY ₃ PREPARED BY SLOW COOLING	158
APPENDIX G. X-RAY DATA OF 16PY	159
APPENDIX K. NMR SPECTRA OF 2.7-SUBSTITUTED DERIVATIVES OF PYRENE	161
APPENDIX L. HPLC PURIFICATION AND CHARACTERIZATION OF 27PY ₃	165
APPENDIX M. ADDITIONAL AFM IMAGES OF POLY27PY ₃	166
APPENDIX N. NMR SPECTRA OF COMPOUNDS FROM CHAPTER VI	167
APPENDIX N. MS SPECTRA AND HPLC TRACES OF OLIGONUCLEOTIDES FROM CHAPTER VI	171

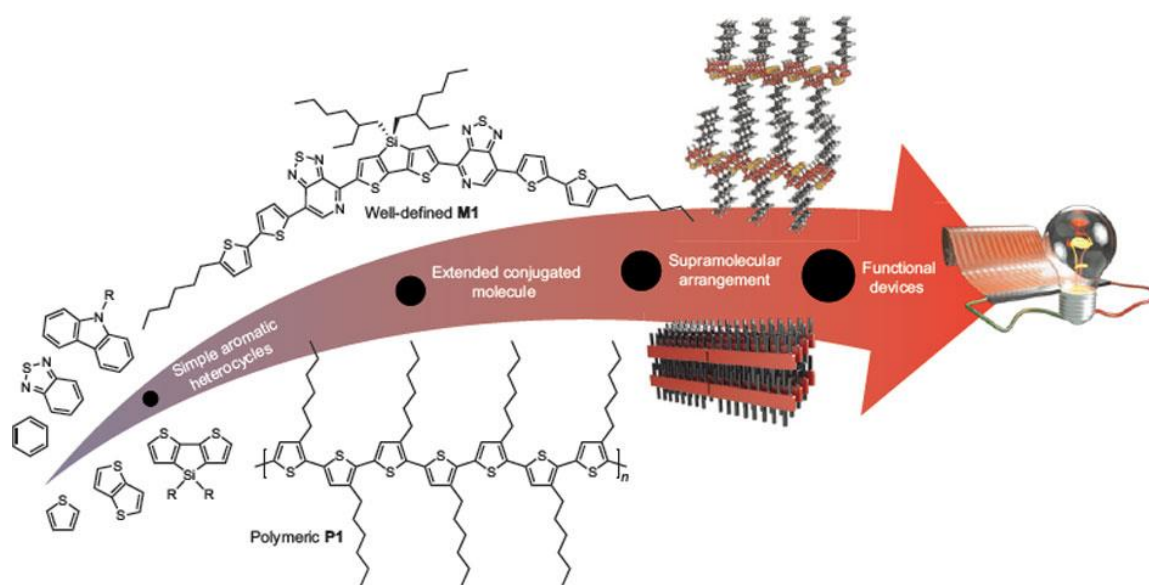
CHAPTER I. GENERAL INTRODUCTION

1. π -Conjugated molecules in materials science

Functional organic materials represent an extremely diverse family of compounds. They share only basic structural and constitutional similarities: a network of carbon atoms, which is decorated with various chemical elements. The chemical and physical properties of such carbon-rich molecules on a molecular level are defined by a combination of atomistic properties of the individual constituents. However, the creation of materials at higher levels of the structural organization requires a spatial confinement of many molecules in three dimensions.^[1] The interactions between molecular units express the overall properties of materials, which can differ tremendously and are mostly unpredictable across various length scales. The challenge is to achieve a control over properties upon the transition from individual (molecular) to the ensemble behavior characteristics (for example see Scheme 1).^[2] Not surprisingly, ordering at the nanoscale – the following level of structural hierarchy – is one of the greatest challenges for modern materials science. Many efforts are directed to understanding and predicting the consequences of intermolecular interactions between organic molecules.

A special place in the family of functional organic materials is occupied by π -conjugated molecular systems (precisely defined structure) and polymers (consisting of many repeating units). A huge amount of diverse polyaromatic entities was designed and prepared over the last decades. These compounds were used as active components in functional materials. The results obtained clearly demonstrate that the major challenges arise from considerations that lie beyond the chemical structure. Recent technological advances not only enabled throughout investigations of these substances but also created a growing demand in novel high-performance

organic systems. The widespread interest largely originates from their versatile properties. Some of the most important characteristics of the systems containing an electronically delocalized structure include: high and tunable photoluminescence quantum efficiency, high absorption in UV or visible spectrum ranges, structural processability, efficient electron and charge transfer, and a relatively low cost production. These properties are the basis of many already existing and emerging applications of organic materials: fabrication of organic electronic devices (OFETs, OLEDs, photovoltaic cells)^[3], ferroelectric organics^[4], photonics, optoelectronic biomaterials and biosensing, light-harvesting systems^[5], catalysts^[6], storage and separation systems^[7].



Scheme 1. Beyond the molecular level: a complex transition from small molecules to materials. The image is taken from ref.^[2]

The preparation of materials is a delicate and tedious process, involving cooperation of several disciplines (for example chemistry, physics and engineering). The process requires reliable designing of and constant controlling over each fabrication step.^[8] The highest performance is achieved only when the net effect of intermolecular interactions is optimized for an aimed application, and the

contribution of the undesired processes is reduced. The properties of organic materials are dependent on the intermolecular interactions between individual molecules. The importance of structural control becomes one of the most vital aspects in this field. The structural control across multiple length becomes essential towards practical implementations. Precise placing of every functional unit at the nanoscale could be regarded as a reliable approach to control the overall interactions. This assumption reflects the possibility to transfer nanoscale order to microscopic and macroscopic levels. Importantly, a well-defined macroscopic state of matter determines the properties of materials.^[1]

Unfortunately, it remains challenging to reach the high level of the hierarchical organization in complex systems in a routine fashion. Our modern capabilities in the field pale compared with the nature's sophistication. The manner nature has ordered a large number of molecules into functional systems evidently remains unmatched. The light-harvesting photosynthetic system is one of the examples in which individual chromophores are arranged into a highly efficient way for the energy transfer. All biosystems demonstrate that the functions are directly linked to noncovalent interactions between molecules, and the utilization of the bioinspired assembling strategy has given rise to a field of supramolecular chemistry.

2. Supramolecular chemistry in materials science

Supramolecular chemistry, defined by Lehn as the chemistry beyond the molecule, has offered a platform to design and prepare highly complex functional systems.^[9,10] Although 1987 Nobel Prize in Chemistry was awarded to Donald Cram, Charles Pedersen and Jean-Marie Lehn for syntheses of molecules that mimic important biological processes, their findings has significantly impacted other scientific domains. The IUPAC definition states:

Supramolecular chemistry is a field of chemistry related to species of greater complexity than molecules that are held together and organized by means of intermolecular interactions. The objects of supramolecular chemistry are supermolecules and other polymolecular entities that result from the spontaneous association of a large number of components into a specific phase (membranes, vesicles, micelles, solid state structures etc).

The utilization of the term has been developed and become slightly broader over the years. A large class of polymolecular assemblies, as defined by Lehn, emerged and formed a separate domain in the realm of supramolecular chemistry. However, the central paradigm of molecular recognition has remained unchanged.

Table 1. Strength of some noncovalent forces^[11]

Type of interaction or bonding	Strength (kJ·mol ⁻¹)
covalent	100-400
Coulomb	250
hydrogen bond	10-65
ion-dipole	50-200
dipole-dipole	5-50
cation-π	5-80
π-π stacking	0-50
van der Waals forces	≤5
hydrophobic effects	difficult to evaluate
metal-ligand	0-400

Self-assembly is regarded as an efficient bottom-up strategy for the controllable organization of functional molecules in a desired manner. In the 1990s, George Whitesides' laboratory pioneered the concept of self-assembly of nanoscale structures^[12] and the Stupp's laboratory developed the concept of self-assembly for functional bulk materials using designed molecules.^[13] It was shown that the self-assembly is guided by the action of subtle noncovalent (supramolecular) force.^[14] The forces, which hold up supramolecular bonds, are weaker comparing to covalent analogues. However, they can be sufficient to link molecular blocks in a stable construction. A modern toolbox of supramolecular forces includes: Coulomb interactions, hydrogen bonds, hydrophobic effect, donor-acceptor pairs, aromatic,

and dipole interactions. Table 1 illustrates typical values of different noncovalent forces.

While the construction of molecules is realized *via* covalent synthesis, supramolecular chemistry enables noncovalent synthesis of materials. The noncovalent nature of the bonds ensures dynamic properties of a system.^[15] Noteworthy, most of supramolecular constructs are reversible. The dynamic nature brings following valuable characteristics for supramolecular materials: correction of errors during noncovalent synthesis, adaptability and self-healing behavior, mastering over kinetically and thermodynamically stable states, the phenomenon of amplification of chirality, etc. An additional benefit of supramolecular interactions is their tunability and strong dependence both on chemical structure and environmental factors (concentration, temperature, solvent, pressure, irradiation, etc.). Moreover, reliable rules for orthogonal self-assembly, which is one of the essential features for the formation of tertiary structures in biological systems, and self-sorting^[16] become possible in a field of systems chemistry.

Owing to the vast amount of both practical and theoretical knowledge, it is possible to encode properties of materials in the molecular structure. The possibility allows the rational approach toward noncovalent synthesis. The understanding how to design molecules that can form morphologically and dimensionally defined architectures through noncovalent interactions is a landmark of synthetic organic materials. Although the field of noncovalent synthesis is still in its infancy, the strategy is conceptually powerful. Currently, the major obstacle is a limited number of molecules (and often with a small number of functional groups) which behave in a predictable manner. The self-assembly properties of supramolecular synthons are determined rather empirically, and most of the learning is done in retrospect, after analysis of structure-functions correlations.^[17] The amount of knowledge acquired

over the last years ensures the future advances in the field of noncovalent synthesis of artificial functional systems.^[18]

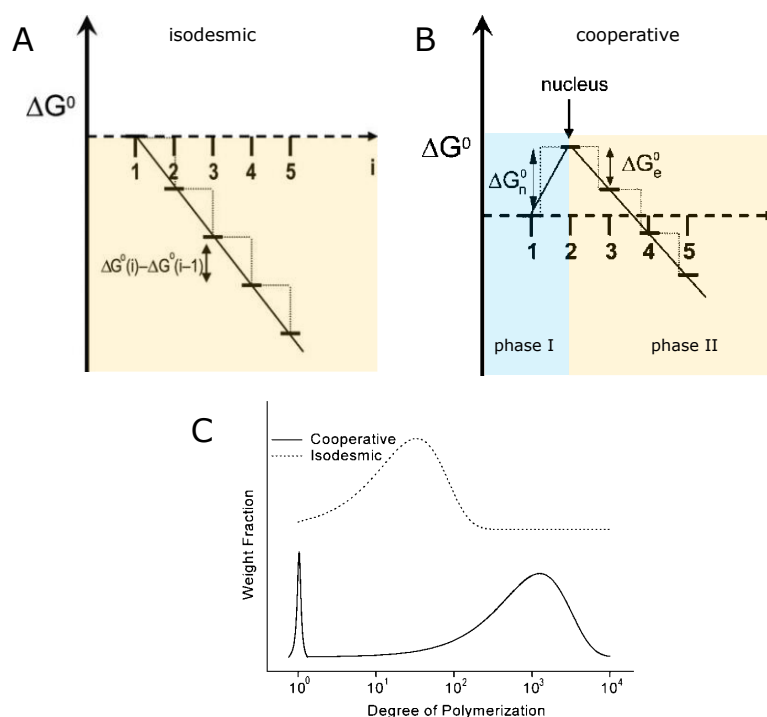
Finally, self-assembly provides an attractive route to functional organic materials. The properties and performance depend sensitively on the organization of the molecular building blocks. Research in the area has to include learning not only to design structures for spontaneous self-assembly but also to control the details of their architecture and internal constitution. In the following sections, two types of assembly approaches are presented: supramolecular polymerization or scaffold-directed arraying of functional blocks.

2.1 Supramolecular polymerization

Supramolecular polymers, as proposed by E.W. Meijer and co-workers^[11], “are defined as polymeric arrays of monomeric units that are brought together by reversible and highly directional secondary interactions, resulting in polymeric properties in dilute and concentrated solution as well as in the bulk.” Supramolecular polymers offer the opportunity to create structures that integrate unprecedented order in assemblies with interesting dynamics through bond reversibility.

The formation of supramolecular polymers occurs via supramolecular polymerization of individual molecular blocks (“unimers” according to Ciferri^[19]). Depending on various parameters (molecular structure of the unimers, concentration and environmental conditions), the supramolecular polymerization could be described by different mechanisms: isodesmic, cooperative (nucleation-elongation) and ring chain.^[11] For the isodesmic model, a step-by-step addition of unimers to a growing chain occurs with the same energy independent on its length (Scheme 2A). This mechanism is reminiscent of Flory’s “principle of equal reactivity”. The energetic profile of the isodesmic supramolecular polymerization leads to a

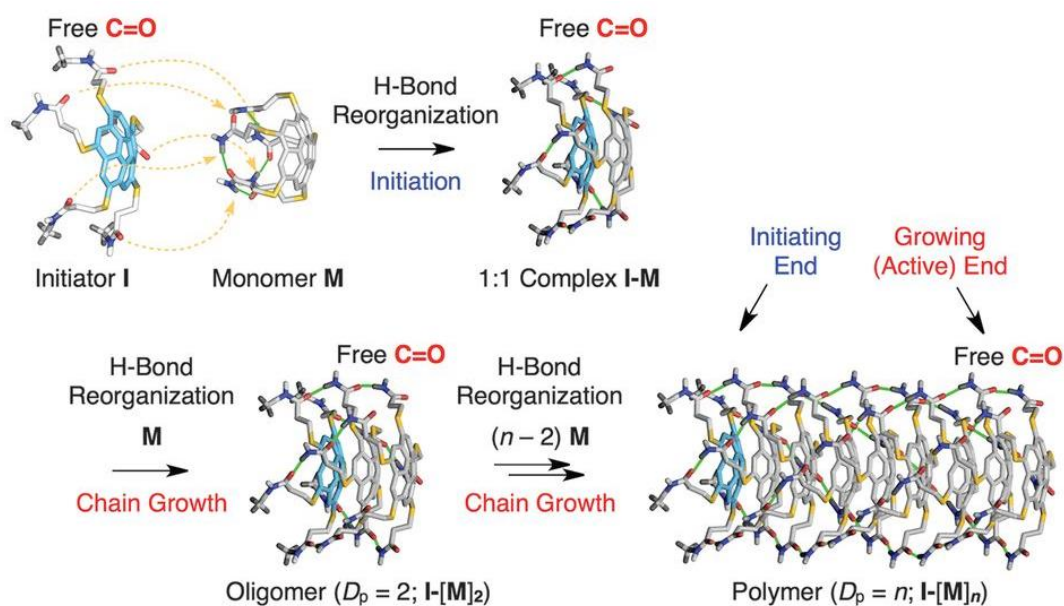
continuous equilibration between polymeric species and unimers. The exchange results in a broad mass distribution (Scheme 2C). The ring–chain equilibrium mechanism depicts an equilibrium between a linear chain and a cyclic counterpart during the supramolecular polymerization process. The cooperative model is reliably described by two consecutive assembly phases: nucleation and elongation (Scheme 2B). The former phase is energetically unfavorable, and it operates until the assemblies reach a certain number of unimers (such aggregates are called nucleus). In the elongation phase, a stepwise addition of unimers is energetically favorable ($\Delta G < 0$). Such a two-phase mechanism leads to a bimodal mass distribution in supramolecular polymers (Scheme 2C).



Scheme 2. A) Energy profile for the isodesmic model B) energy profile for the cooperative model C) Weight fraction vs. degree of polymerization plot for isodesmic (dotted) and cooperative (solid) models. Adapted from ref.^[11]

The supramolecular polymerization occurs either under isothermal or temperature-variable conditions. For isothermal conditions, the self-assembly is

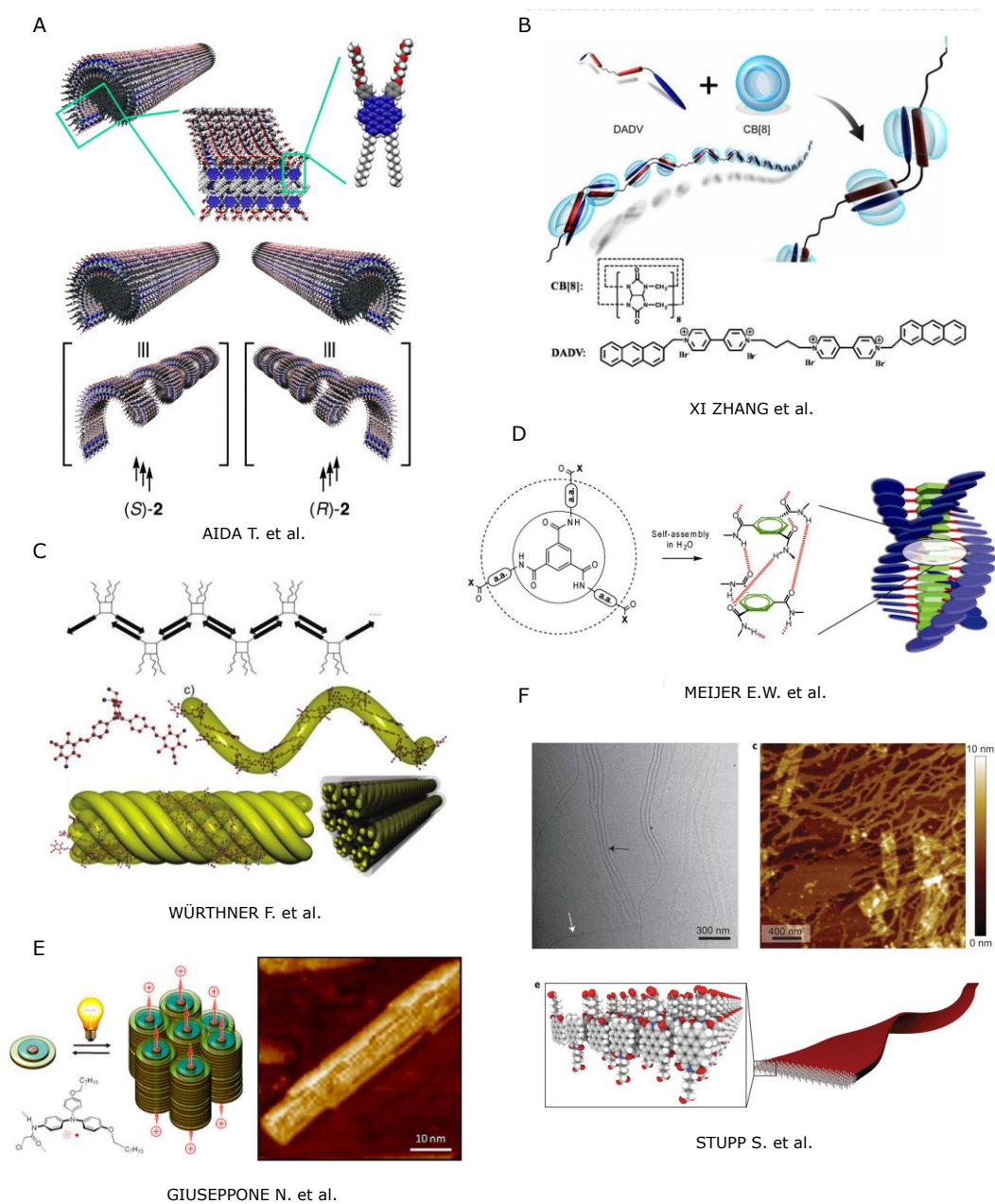
triggered by increase of a unimer's concentration, by change of a solvent or, as recently demonstrated by Aida^[20], by addition of a supramolecular initiator (Scheme 3). Cooperative isothermal supramolecular polymerization is often characterized by a lag phase, which is a direct consequence of pathway complexity and presence of kinetically-trapped or pre-nucleus states.^[21]



Scheme 3. A rational strategy for the realization of chain-growth supramolecular polymerization. The image is taken from ref.^[20]

The preparation and functions of complex supramolecular systems have been deeply studied over the recent years.^[22] The influence of the aggregation pathways on the molecular organization of functional n -conjugated materials emphasizes the importance of mechanistic insights into molecular self-assembly. A throughout understanding of the mechanisms has become vital for the creation of smart and stimuli-responsive materials.^[23] Scheme 4 highlights some of the recent examples in the field of supramolecular polymers. It should be stated that the selection of examples is not meant to provide a full overview of the field, but rather to illustrate some of the well-known types of supramolecular polymers. The most used unimers

are based on polyaromatic species such as anthracenes, pyrenes, coronenes, OPVs, PDIs, oligothiophenes, porphyrins, phthalocyanines.

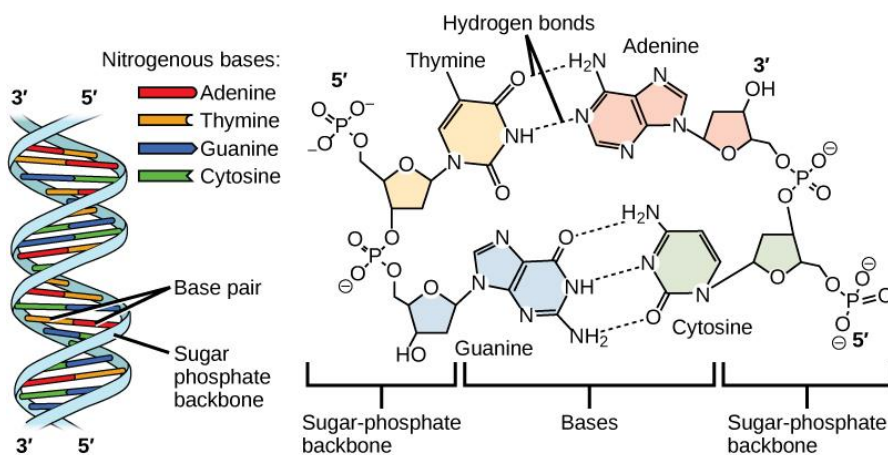


Scheme 4. Selected examples in the field of supramolecular polymers: A) nanotubes from Aida et al.^[24] B) host-guest systems from Zhang et al.^[22] C) merocyanine assemblies from Würthner et al.^[25] D) BTAs from Meijer et al.^[26] E) triarylamines from Giuseppone et al.^[27] F) perylene nanosheets from Stupp et al.^[6]

Most of the examples of supramolecular polymers share the common strategy in processing of π -conjugated materials. The approach starts with conditions where the molecules, oligomers or polymers are molecularly dissolved. The supramolecular polymerization is a multistep process occurring through several steps (folding, stepwise association, fragmentation). The revealing of self-assembly pathways which yield optimal molecular organization is still a challenge that largely relies on a trial-and-error approach.

2.2 DNA-guided assembly of π -conjugated molecules

Scaffold-guided assembly is an alternative strategy for the controlled arrangement of π -conjugated molecules. It enables positioning of molecular blocks with a nanometer precision in dimensionally variable architectures. The strategy benefits primarily from a predictable behavior of a scaffold. Importantly, biology often achieves synthesis of materials with structural features and functions across scales using templates.



Scheme 5. Illustrative structure of DNA double helix (left) and nucleotide base pairing.

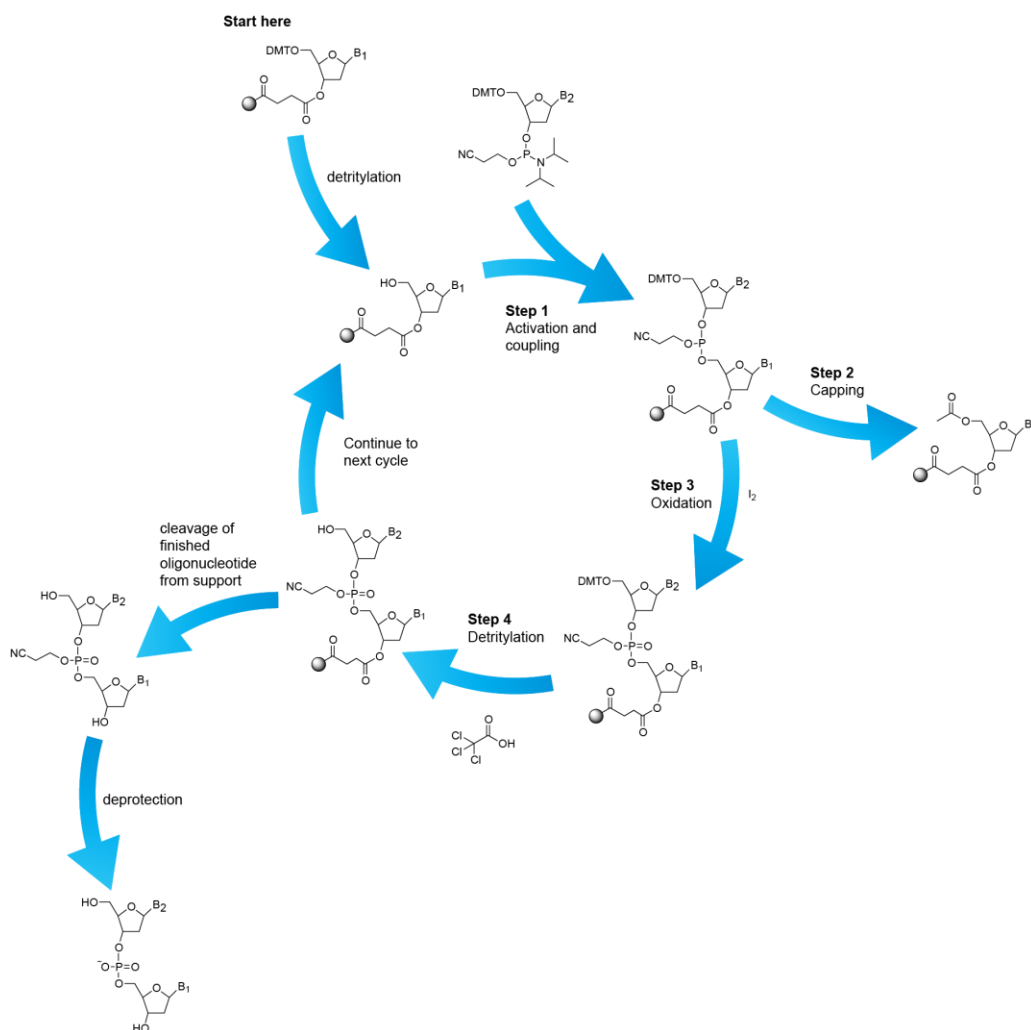
DNA is one of the most efficient scaffolds in modern nanotechnology (Scheme 5). DNA is a polymer with a precise sequence, consisting of only four nucleotides

(adenine-A, guanine-G, cytosine C, thymine-T). Combined in a linear chain, these blocks form single strands of oligonucleotides. Each of the four units has its preferred binding partner. For example, A base binds selectively to T base via two hydrogen bonds, and C binds correspondingly to G through three hydrogen bonds. The most prominent property of DNA is the formation of a double-stranded helix. The assembly process occurs upon binding of complementary strands. Depending on conditions, double helix exists in A, B or Z forms. The B-type DNA double helix – the most abundant form under biological conditions – exhibits a regular turn of 10.5 nm. This parameter allows the prediction of spatial orientation of all nucleobases. Importantly, oligonucleotides in DNA materials are held together by strong non-covalent forces: stacking interactions and selective hydrogen bonding. Both forces could be controlled by a rational sequence design.^[28]

Oligonucleotides of various lengths and sequences are currently available and are relatively cheap, due to the established solid-phase synthesis through phosphoramidite chemistry.^[29,30] It allows stepwise addition of functional units in a controlled and efficient manner. The addition of dA, dG, dC, dT blocks to a growing oligonucleotide chain occurs through several steps for each incorporation (activation and coupling, capping, oxidation, detritylation, for more detail see Scheme 6). The following step in the synthesis is cleavage of the oligonucleotides from a solid support. The crude oligonucleotide is consequently subjected to an appropriate purification method (HPLC, PAGE, affinity chromatography, precipitation).

Apart from the field of controlled DNA folding, DNA hybrids are powerful systems for the assembly of n-conjugated molecules.^[31] The potential of DNA for the scaffolding applications is well-recognized. The approach relies on the synthesis of chimeric oligonucleotide chains. The chain is a sequence with a precise position of every unit. The units of choice can be either standard nucleotides or any molecule

applicable for the solid-phase synthesis. The oligonucleotides prepared possess recognition sites (nucleobases), which are able to form a DNA double strand scaffold upon binding with a complementary sequence. Therefore, the formation of the double strand guides the assembly of chromophores. Lots of examples are found in recent review papers.^[32-36]



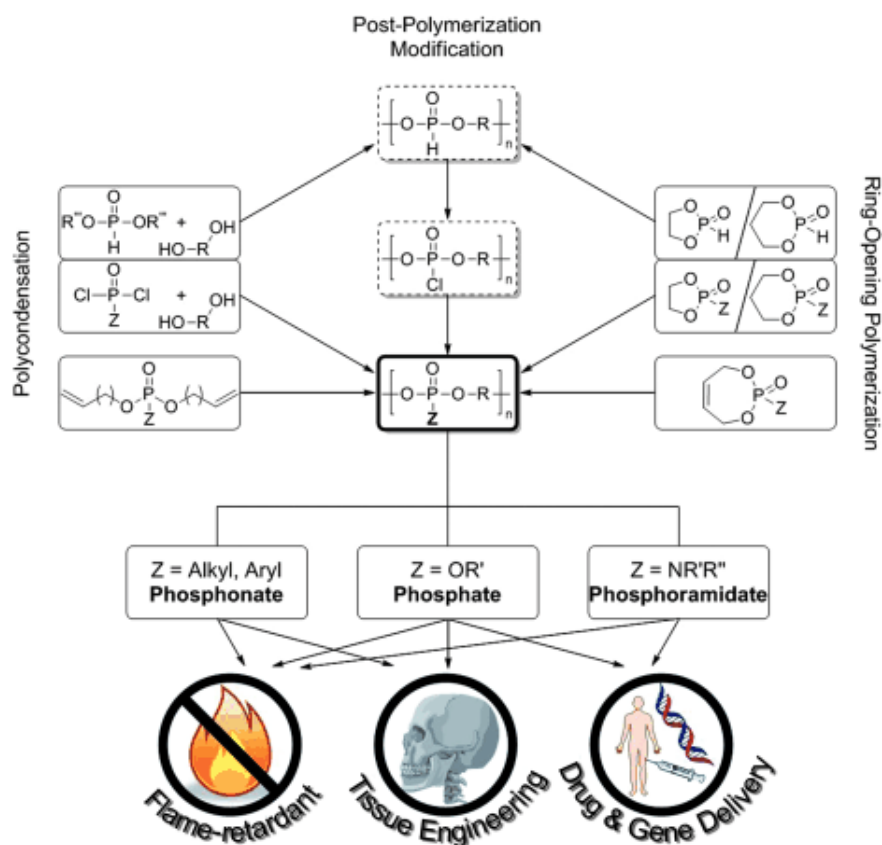
Scheme 6. A cycle of the solid-phase DNA synthesis.

DNA is a polymer chain with a precise sequence of functional units.^[37] The marvelous properties of DNA are reliably encoded in its constitution. The potential of the solid-phase synthesis approach, with the emphases on the partial modification of

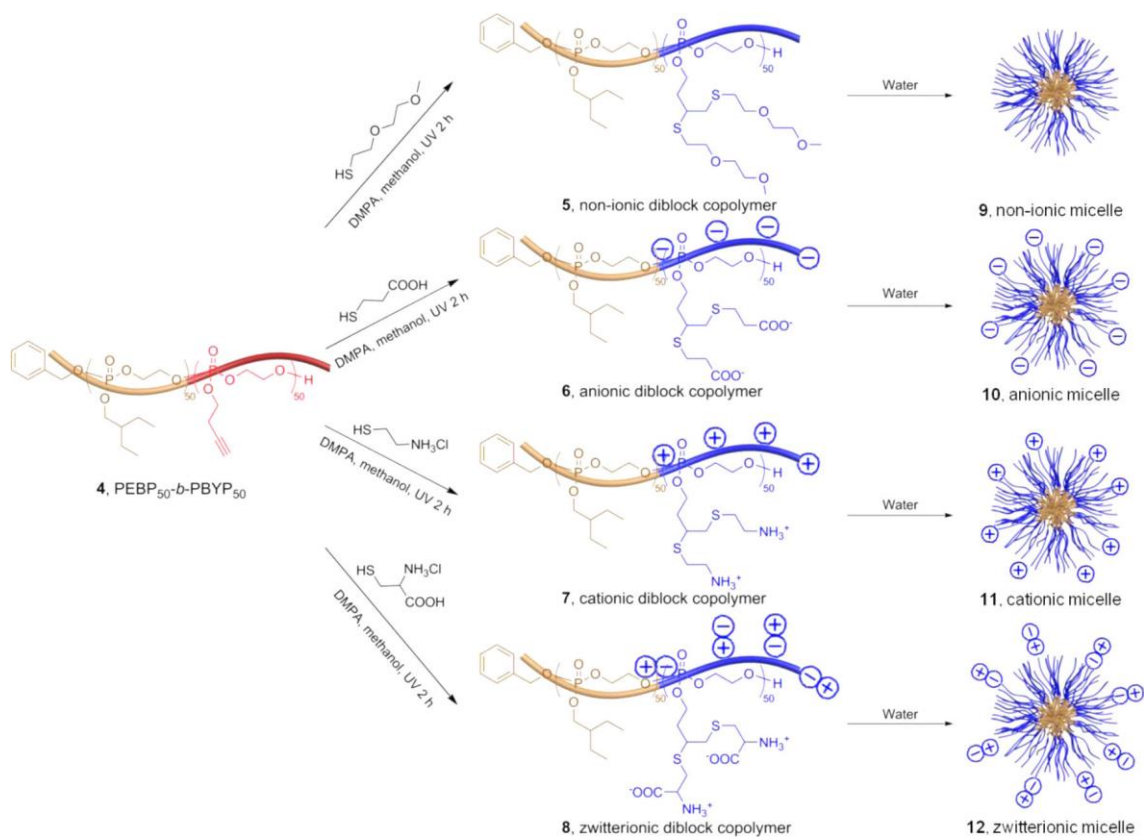
the DNA chain, was highlighted in this section. The next section introduces selected examples of other polyphosphodiesters.

2.3 Non-natural phosphodiesters in materials science

The major synthetic approach toward functional polyphosphodiesters is polymerization in melt or solution, which often leads to a variety of products and lacks control over macromolecular sequences (Scheme 7).^[38] Such polymer materials gained considerable attention as drug delivery systems^[39] and flame retardants.^[38] Thus, Wooley and co-workers described the preparation and analyzed properties of various polyphosphodiesters. One of the recent examples is a block-copolymer **4**, which could be post-modified to derive different micelles (Scheme 8).^[40]



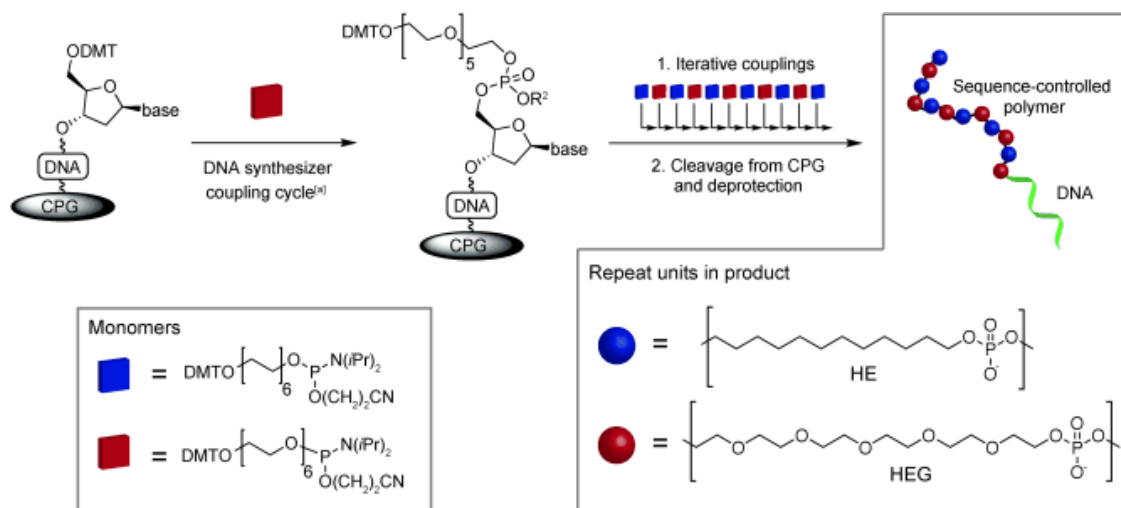
Scheme 7. Some of the synthetic approaches toward polyphosphodiesters. The image is taken from ref.^[38]



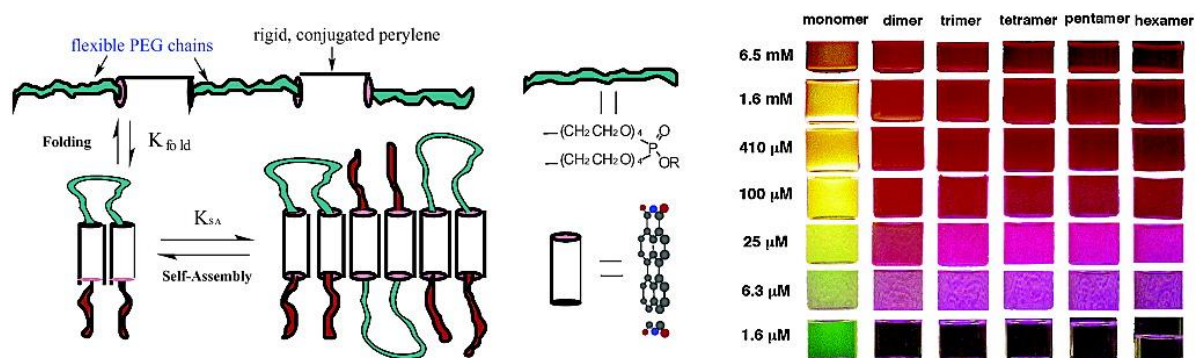
Scheme 8. Schematic representation of the functionalization of block copolymer **4** with four different charged or non-charged thiols and the self-assembly of four resulting amphiphilic block copolymers **5-8**. The scheme is taken from ref.^[40]

Solid-phase synthesis using phosphoramidite chemistry has been rarely exploited for the preparation of non-natural blocks with potential applications in materials science.^[41,42] For a long time, phosphoramidite chemistry in materials science has belonged solely to DNA chemists. One of the undesirable characteristics of the solid-phase method is a small amount of materials derived from one synthesis. This drawback is compensated by high complexity and sequence specificity of the oligomers prepared. Using iterative couplings, it is possible to introduce up to several dozen functional units (even different) in a desired order, which is a challenge for organic chemists. Recently, Lutz and co-workers developed an efficient procedure for the synthesis and post-modifications of various aliphatic phosphodiester-linked

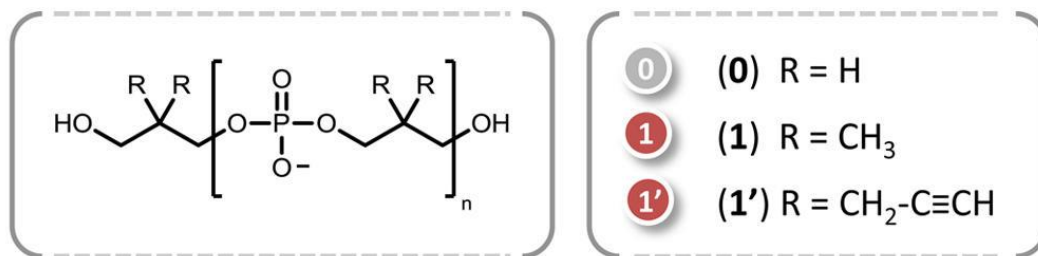
oligomers (Scheme 11).^[43] The strategy used is not limited to oligomers and can further derive high-molecular weight polymers. Sleiman and co-workers demonstrated an approach toward monodisperse and sequence-defined DNA-polymer conjugates (Scheme 9).^[44] The conjugates were used as supramolecular synthons for the hierarchical organization in functional structures.^[45] Li and co-workers studied phenomena of folding and assembly in phosphodiester-linked PDI oligomers (Scheme 10).^[46,47]



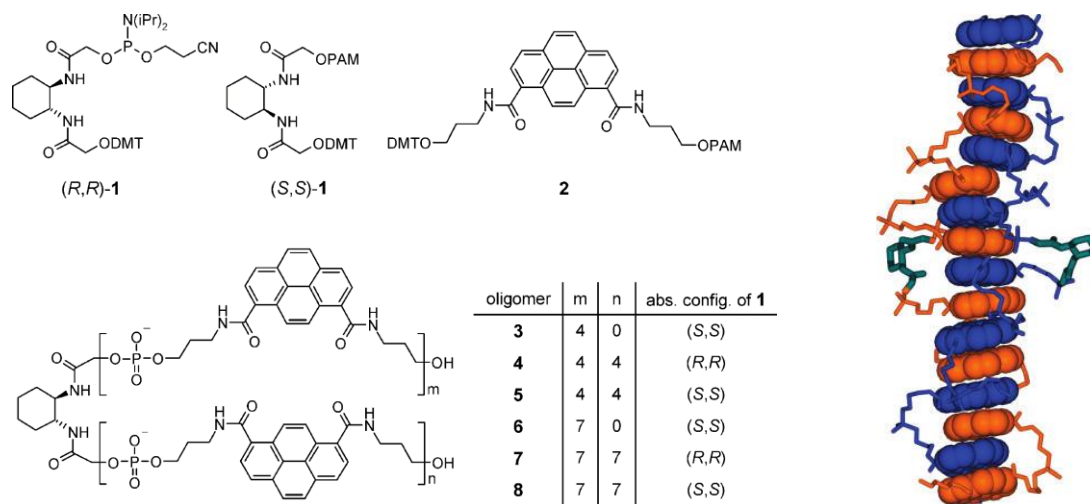
Scheme 9. Solid-phase synthesis of sequence-controlled DNA copolymers. The image is taken from ref.^[44]



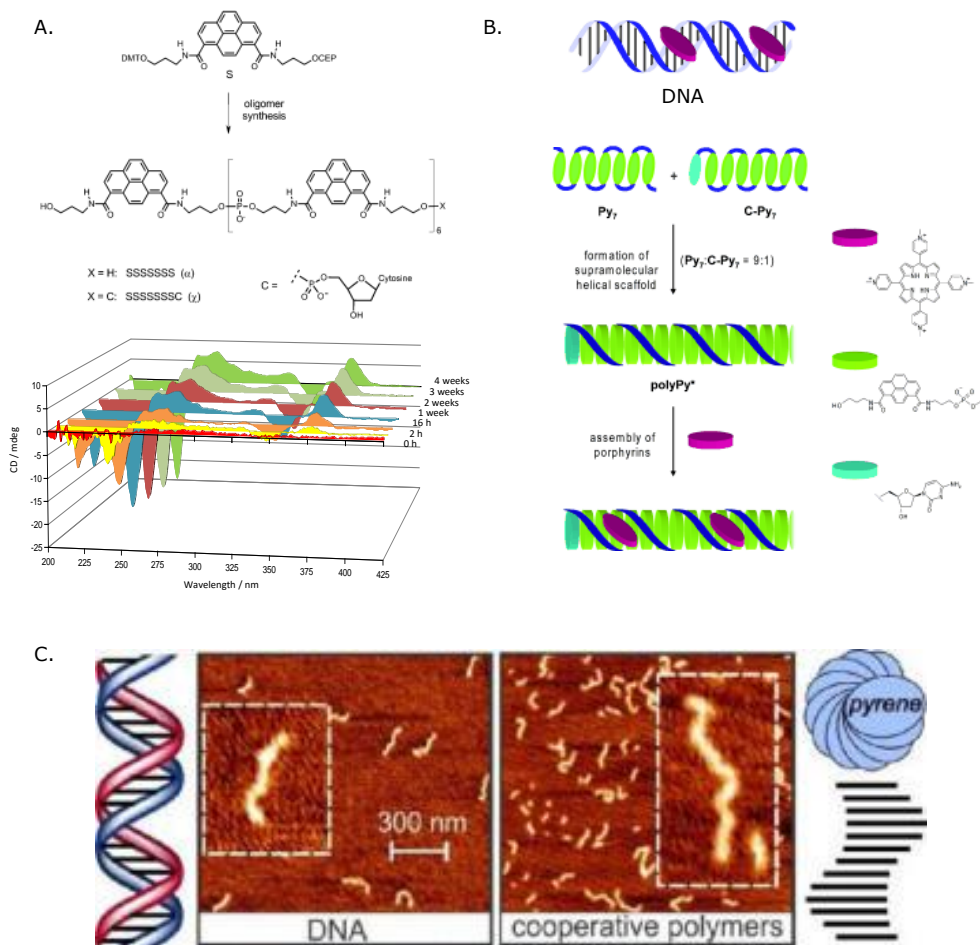
Scheme 10. Folding and assembly of various PDI oligomers. The image is taken from ref.^[45]



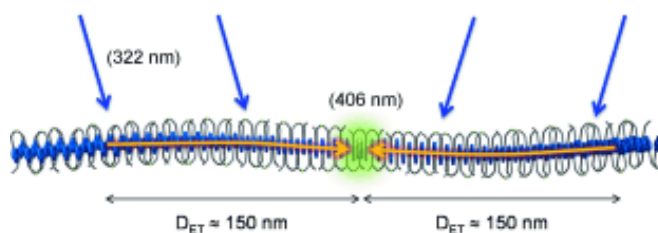
Scheme 11. Illustrative image of sequence-specific polymers prepared by Lutz and co-workers. The image is taken from ref. [43]



Scheme 12. Folding of oligopyrenotides. The image is taken from ref. [48]



Scheme 13. Properties of oligopyrenotides: A) amplification of chirality^[49] B) nanoscale scaffold^[50] C) structural DNA mimic.^[51]



Scheme 14. Illustrative structure of the light-harvesting supramolecular polymer. The image is taken from ref.^[54]

Häner and co-workers described controlled folding of pyrene-based oligomers, which were called oligopyrenotides.^[48] However, the term was further developed to oligopyrenotide, since it covers a broader set of compounds. Oligopyrenotide is a

covalent chain of aromatic molecules, which are linked by phosphodiester groups in a regular manner. The concept of co-existing folding and assembly stages plays an important role in the supramolecular chemistry of oligoarenotides. Folding is characterized as an intramolecular event, whereas assembly is intermolecular. It was shown that oligopyrenotides, constructed from 1.8-carboxamide pyrenes, are able to form one-dimensional (1D) fibrillar structures reminiscent of the DNA double helix.^[51] The structures of fibers were resolved by microscopic techniques and correlated with spectroscopic data. The AFM data demonstrate that the fibers appear on the surface with a thickness of 0.8 nm.^[52] This value is decreased compared to a theoretical one due to a collapse on the surface. Supramolecular nature of the fibers allowed to study the phenomenon of amplification of chirality.^[49] Chiral information was embedded in the oligomer chain as a nucleotide.^[53] The chirality from the nucleotides was transmitted to the supramolecular level. It was further shown that the 1D assemblies serve as a nanoscale scaffold for the controlled arrangement of porphyrins.^[50] Later, it was demonstrated that phenanthrene-based self-assembled structures also form one-dimensional architectures. Doping the polymer chains with a pyrene-containing oligomer during the assembly process was sufficient to achieve an efficient energy transfer over long distances.^[54]

3. Aim of the study

Ordering of the matter is key to advance the field of materials science. Understanding self-assembly codes leading to dimensionally and morphologically defined architectures is of great importance in many areas of research. Therefore, creation of general guidelines for self-assembly of functional organic systems remains necessary in processing and fabrication of materials with improved

properties. In this work, an attempt to find general patterns in self-assembly of short chromophore-based oligomers is performed.

Supramolecular chemistry is utilized to arrange various chromophores (pyrenes and porphyrins) in morphologically-defined arrays in a predictable and controllable manner. The individual chromophores are placed in short oligomers, which are prepared via solid-phase synthesis using phosphoramidite chemistry. This approach enables successful linking of many functional units in a desirable and controllable manner. The self-assembly behavior of all oligomers is defined by the sequence and nature of chromophores. The behavior is additionally controlled by noncovalent forces and environmental factors. It is shown that, alternatively to small molecules or polymer-based materials, sequence-defined oligomers can find their applications in materials science as reliable supramolecular synthons.

Self-assembly is highly dependent on environmental factors. An important direction is to explore how methods of preparation of the assemblies affect their final structure and properties. It is noteworthy that changes in the nature of solvents, and other processing issues such as heating and cooling rates or even stirring, can have profound effects on the nature of the final structures.

4. References

- [1] K. Müllen, *Angew. Chem. Int. Ed.* **2015**, *54*, 10040–10042.
- [2] Z. B. Henson, K. Müllen, G. C. Bazan, *Nat. Chem.* **2012**, *4*, 699–704.
- [3] J. Mei, Y. Diao, A. L. Appleton, L. Fang, Z. Bao, A. L. Appleton, *J. Am. Chem. Soc.* **2013**, *135*, 6724–6746.
- [4] A. S. Tayi, A. Kaeser, M. Matsumoto, T. Aida, S. I. Stupp, *Nat. Chem.* **2015**, *7*, 281–294.

- [5] M. Graetzel, R. A. J. Janssen, D. B. Mitzi, E. H. Sargent, *Nature* **2012**, *488*, 304–312.
- [6] A. S. Weingarten, R. V. Kazantsev, L. C. Palmer, M. McClendon, A. R. Koltonow, A. P. S. Samuel, D. J. Kiebala, M. R. Wasielewski, S. I. Stupp, *Nat. Chem.* **2014**, *6*, 964–970.
- [7] S.-Y. Ding, W. Wang, *Chem. Soc. Rev.* **2013**, *42*, 548–568.
- [8] G. Giri, E. Verploegen, S. C. B. Mannsfeld, S. Atahan-Evrenk, D. H. Kim, S. Y. Lee, H. A. Becerril, A. Aspuru-Guzik, M. F. Toney, Z. Bao, *Nature* **2011**, *480*, 504–508.
- [9] J.-M. Lehn, *J. Incl. Phenom.* **1988**, *6*, 351–396.
- [10] J.-M. Lehn, *Science* **2002**, *295*, 2400–2403.
- [11] T. F. A. De Greef, M. M. J. Smulders, M. Wolffs, A. P. H. J. Schenning, R. P. Sijbesma, E. W. Meijer, *Chem. Rev.* **2009**, *109*, 5687–5754.
- [12] G. M. Whitesides, J. P. Mathias, C. T. Seto, *Science* **1991**, *254*, 1312–1319.
- [13] S. I. Stupp, V. LeBonheur, K. Walker, L. S. Li, K. E. Huggins, M. Keser, A. Amstutz, *Science* **1997**, *276*, 384–389.
- [14] S. Stupp, L. Palmer, *Chem. Mater.* **2014**, *26*, 507–518.
- [15] J.-M. Lehn, *Angew. Chem. Int. Ed.* **2015**, *54*, 3276–3289.
- [16] M. M. Safont-Sempere, G. Fernández, F. Würthner, *Chem. Rev.* **2011**, *111*, 5784–5814.
- [17] Y. Yao, H. Dong, W. Hu, *Polym. Chem.* **2013**, *4*, 5197–5205.
- [18] M. T. Dang, L. Hirsch, G. Wantz, J. D. Wuest, *Chem. Rev.* **2013**, *113*, 3734–3765
- [19] A. Ciferri, *Supramolecular Polymers*, **2005**.
- [20] J. Kang, D. Miyajima, T. Mori, Y. Inoue, Y. Itoh, T. Aida, *Science* **2015**, *479*, 1173–1176.

- [21] P. A. Korevaar, T. F. A. De Greef, E. W. Meijer, *Chem. Mater.* **2014**, *26*, 576–586.
- [22] L. Yang, X. Tan, Z. Wang, X. Zhang, *Chem. Rev.* **2015**, *115*, 7196–7239.
- [23] T. Aida, E. W. Meijer, S. I. Stupp, *Science* **2012**, *335*, 813–817.
- [24] T. Yamamoto, T. Fukushima, T. Aida, *Adv. Polym. Sci.* **2008**, *220*, 1–27.
- [25] A. Lohr, F. Würthner, *Angew. Chem. Int. Ed.* **2008**, *47*, 1232–1236.
- [26] L. Albertazzi, D. Van Der Zwaag, C. M. A. Leenders, R. Fitzner, R. W. Van Der Hofstad, E. W. Meijer, *Science* **2014**, *344*, 491–495.
- [27] E. Busseron, Y. Ruff, E. Moulin, N. Giuseppone, *Nanoscale* **2013**, *5*, 7098–140.
- [28] S. Woo, P. W. K. Rothmund, *Nat. Chem.* **2011**, *3*, 620–627.
- [29] S. L. Beaucage, R. P. Iyer, *Tetrahedron* **1993**, *49*, 1925–1963.
- [30] E. M. LeProust, B. J. Peck, K. Spirin, H. B. McCuen, B. Moore, E. Namsaraev, M. H. Caruthers, *Nucleic Acids Res.* **2010**, *38*, 2522–2540.
- [31] Y. N. Teo, E. T. Kool, *Chem. Rev.* **2012**, *112*, 4221–4245.
- [32] C. K. McLaughlin, G. D. Hamblin, H. F. Sleiman, *Chem. Soc. Rev.* **2011**, *40*, 5647–5656.
- [33] E. Stulz, *Chem.-Eur. J.* **2012**, *18*, 4456–4469.
- [34] S.-S. Jester, M. Famulok, *Acc. Chem. Res.* **2014**, *47*, 1700–1709
- [35] K. Pan, E. Boulais, L. Yang, M. Bathe, *Nucleic Acids Res.* **2014**, *42*, 2159–2170.
- [36] V. L. Malinovskii, D. Wenger, R. Häner, *Chem. Soc. Rev.* **2010**, *39*, 410–422.
- [37] J. F. Lutz, M. Ouchi, D. R. Liu, M. Sawamoto, *Science* **2013**, *125*, 13924–13925.
- [38] B. Clément, D. G. Molin, C. Jérôme, P. Lecomte, *J. Polym. Sci. Part A Polym. Chem.* **2015**, 10.1002/pola.27732.

- [39] Y. C. Wang, Y. Y. Yuan, J. Z. Du, X. Z. Yang, J. Wang, *Macromol. Biosci.* **2009**, *9*, 1154–1164.
- [40] S. Zhang, J. Zou, F. Zhang, M. Elsbahy, S. E. Felder, J. Zhu, D. J. Pochan, K. L. Wooley, *J. Am. Chem. Soc.* **2012**, *134*, 18467–18474.
- [41] M. Dubber, J. M. J. Fréchet, *Bioconjug. Chem.* **2003**, *14*, 239–246.
- [42] H. Lönnberg, *Bioconjug. Chem.* **2009**, *20*, 1065–1094.
- [43] A. Al Ouahabi, L. Charles, J.-F. Lutz, *J. Am. Chem. Soc.* **2015**, *137*, 5629–5635.
- [44] T. G. W. Edwardson, K. M. M. Carneiro, C. J. Serpell, H. F. Sleiman, *Angew. Chem. Int. Ed. Engl.* **2014**, 1–6.
- [45] C. J. Serpell, T. G. W. Edwardson, P. Chidchob, K. M. M. Carneiro, H. F. Sleiman, *J. Am. Chem. Soc.* **2014**, *136*, 15767–15774.
- [46] W. Wang, L. S. Li, G. Helms, H. H. Zhou, A. D. Q. Li, *J. Am. Chem. Soc.* **2003**, *125*, 1120–1121.
- [47] A. D. Q. Li, W. Wang, L. Q. Wang, *Chem.-A Eur. J.* **2003**, *9*, 4594–4601.
- [48] R. Häner, F. Garo, D. Wenger, V. L. Malinovskii, *J. Am. Chem. Soc.* **2010**, *132*, 7466–7471.
- [49] A. L. Nussbaumer, F. Samain, V. L. Malinovskii, R. Häner, *Org. Biomol. Chem.* **2012**, *10*, 4891–8.
- [50] V. L. Malinovskii, A. L. Nussbaumer, R. Häner, *Angew. Chem. Int. Ed.* **2012**, *51*, 4905–4908.
- [51] A. L. Nussbaumer, D. Studer, V. L. Malinovskii, R. Häner, *Angew. Chem. Int. Ed.* **2011**, *50*, 5490–5494.
- [52] A. V. Rudnev, V. L. Malinovskii, A. L. Nussbaumer, A. Mishchenko, R. Häner, T. Wandlowski, *Macromolecules* **2012**, *45*, 5986–5992.

- [53] F. Simona, A. L. Nussbaumer, R. Häner, M. Cascella, *J. Phys. Chem. B* **2013**, *117*, 2576–85.
- [54] C. B. Winiger, S. Li, G. R. Kumar, S. M. Langenegger, R. Häner, *Angew. Chem. Int. Ed.* **2014**, *53*, 13609–13613.

CHAPTER II. SPECTROSCOPIC PROPERTIES AND MORPHOLOGY OF THE ASSEMBLES FROM 1.6-SUBSTITUTED PYRENE-BASED TRIMERS

Published: Vybornyi, M.; Rudnev, A. V; Langenegger, S. M.; Wandlowski, T.; Calzaferri, G.; Häner, R. *Angew. Chem., Int. Ed.* **2013**, 52, 11488 (Frontispiece).

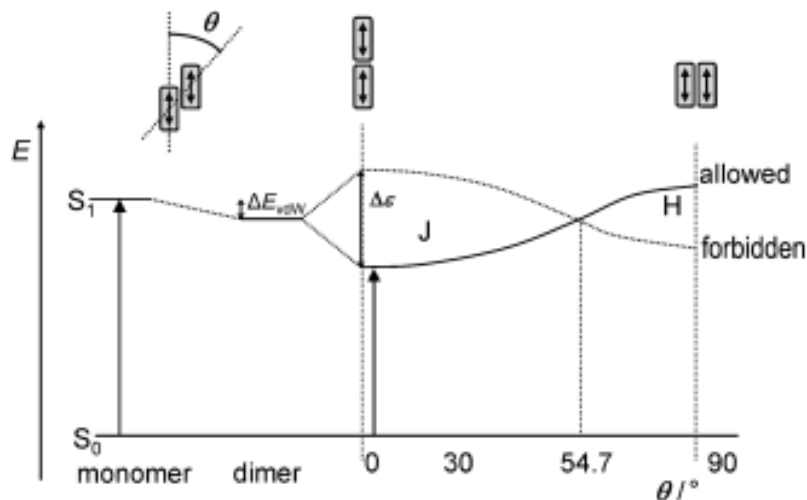
1. Abstract

Amphiphilic pyrene trimers self-assemble into two-dimensional, supramolecular polymers in aqueous medium. Folding and aggregation processes are accompanied by unprecedented simultaneous development of J- and H-bands and significant changes in the fluorescence properties. The spectroscopic properties are correlated with the formation of sheetlike supramolecular assemblies, which is unambiguously confirmed by atomic force microscopy (AFM).

2. Introduction

Organic π -conjugated molecules are attractive objects in the materials sciences.^[1-8] The properties of dye aggregates critically depend on the degree of structural order. Control of the precise arrangement of chromophores into dimensionally and morphologically defined shapes is a key aspect in the development of optoelectronic devices.^[9-17] Close spatial proximity and in-plane alignment of chromophores in 2D structural motifs^[18-27] often results in distinct electronic interactions between the partners^[28-36] leading to charge separation and transport, directional energy transfer, new optical and photophysical properties not observed in the separate molecules.^[37-46] Moreover, spectroscopic changes often provide valuable information about the relative orientation of adjacent chromophores in a given environment.^[39,47-50] Among the most prominent examples of electronic interactions

with pronounced effects is the formation of J- and H-aggregates.^[51-55] The type of aggregation strongly depends on the geometry and orientation of the interacting molecules as described by the theory of exciton coupling.^[56,57]



Scheme 1. A schematic energy diagram for aggregated dimers with coplanar inclined transition dipoles. The geometry and the slip angle θ are illustrated above. For parallel aligned dimers the optical excitation is only allowed from the ground state to one of the two excitonic states depending on the angle θ . For $\theta < 54.7^\circ$ the lower energy state is allowed (leading to a bathochromically shifted J-band), while for $\theta > 54.7^\circ$ the allowed state is at higher energy (leading to a hypsochromically shifted H-band). The image is taken from ref.^[54]

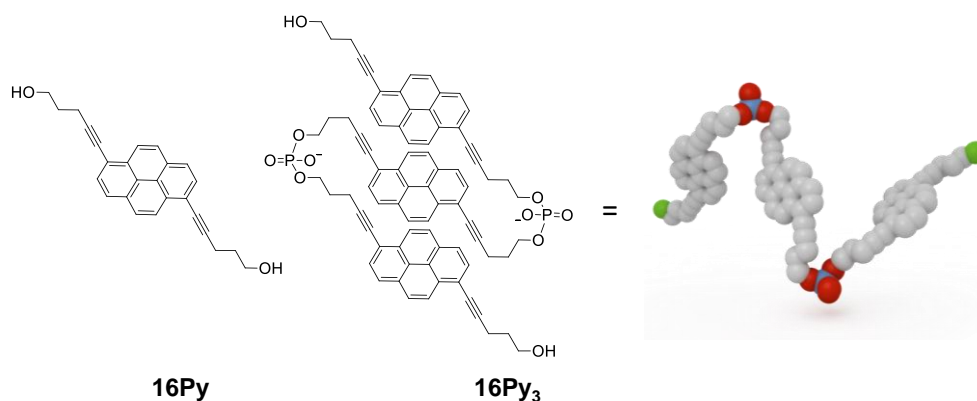
Due to their exceptional optical and electronic properties, pyrene derivatives find applications as chemical and biological sensors and labels, as components of dye-sensitized solar cells, in light-emitting diodes or for photovoltaic applications.^[58] Despite abundant information about its behaviour in the aggregated state, data on J- and/or H-type interactions between pyrenes is very limited.^[59,60] In the Häner group pyrene-modified nucleic acids are used as biosensors,^[61] DNA-based light-harvesting^[62,63] and energy transfer systems^[64] or as nanoscale templates for chromophore assembly.^[65] Recently, a phosphodiester-linked pyrene heptamer (or heptapyrenotide^[66]) was found to form rod-like structures via supramolecular polymerization.^[67-69] In this chapter, the synthesis and the self-assembly behavior, morphological studies and the spectroscopic properties of a phosphodiester linked,

1,6-dialkynyl substituted pyrene trimer (**16Py₃**, Scheme 2) are presented. This tripyrenotide exhibits solvent-dependent aggregation behaviour that results in the formation of two-dimensional supramolecular polymers which is revealed by the unprecedented simultaneous occurrence of J- and H-type couplings for different electronic transitions. The results are in a sharp contrast with previously reported studies on similar 1.8-substituted pyrene oligomers.

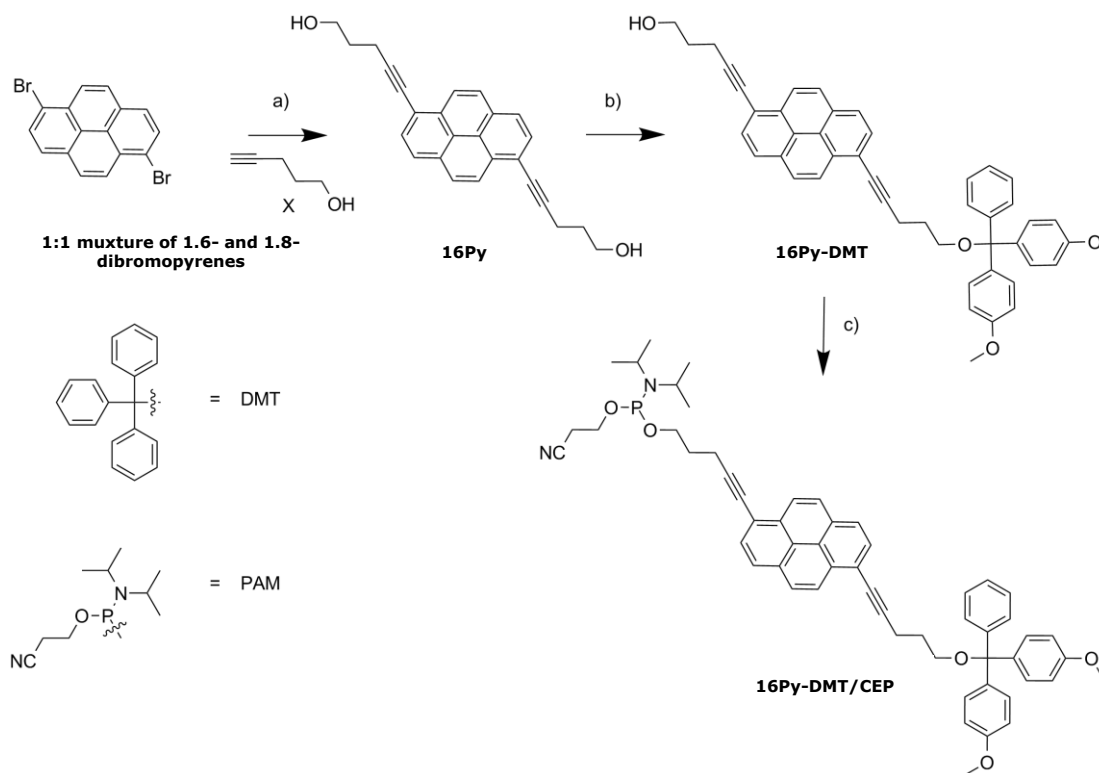
3. Results

3.1 Synthesis of pyrene oligomers

Synthesis of the 1,6-dipentynyl pyrene (**16Py**, Scheme 3) followed a previously reported, one-step procedure.^[70] This derivative was further transformed into a suitably protected phosphoramidite building block **16Py-DMT/CEP** and oligomerized by automated solid phase synthesis. The obtained trimer **16Py₃** was purified by RP-HPLC. The final purity of the oligomer was confirmed by mass spectrometry and an HPLC trace.



Scheme 2. Structure of the phosphodiester-linked, 1,6-dipentynyl substituted pyrene **16Py** and the trimer **16Py₃**.



Scheme 3. Synthesis of the building block **16Py-DMT/CEP**

3.2 Atomic Force Microscopy (AFM)

The formation of supramolecular polymers was unambiguously confirmed by AFM experiments. Since oligopyrenotide are structurally similar to DNA,^[69] we followed the protocol developed for AFM investigations of DNA molecules.^[78] Supramolecular assemblies were deposited on a mica surface modified with 3-aminopropyltriethoxy silane (APTES-mica) from a chosen sample solution. A representative AFM image is depicted in Figure 1. It displays clearly distinguishable, free-standing 2D objects, like nanosheets. The AFM results with APTES-mica as a substrate were highly reproducible. We detected nanosheets of 50-250 nm lateral size as deposited from the sample solutions in current solvent mixture (more details on preparation procedures see Chapters IV and V). The nanosheets possess a rigid

structure, as multiple AFM imaging of the same area did not lead to any morphological changes of the assemblies.

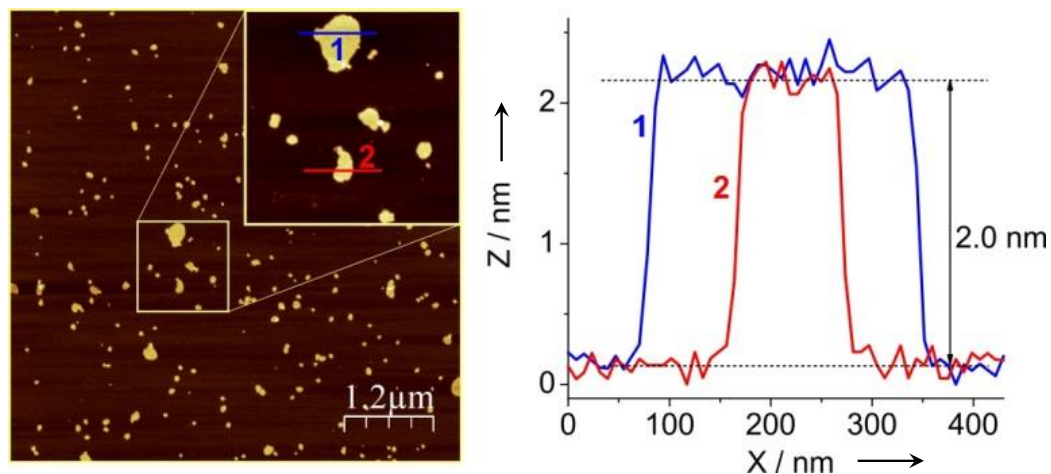


Figure 1. Representative AFM images in a tapping mode of 2D supramolecular polymers **poly16Py₃** deposited on APTES-mica from aqueous solution of **16Py₃** containing 10% methanol. The right panel represents typical cross sections of two nanosheets.

Importantly, the deposition of 2D nanosheets on unmodified mica was unsuccessful, while 2D nanosheets were observed on APTES-mica in every experiment. Dropping pure buffer solution (without **16Py₃**) on APTES-mica led to featureless AFM images. The latter confirmed that the 2D objects observed in AFM are supramolecular polymers **poly16Py₃**. We estimate the effective diameter d_{eff} and the height of **poly16Py₃** nanosheets from analysis of AFM images (Figure 2). The lateral size of the nanosheets reaches 250 nm and $d_{\text{eff}} = 65 \pm 10$ nm as estimated from AFM images obtained at different places as well as different experiments. The height distribution shows two very pronounced peaks (panels E and F in Figure 2). The left one corresponds to the mica substrate and the right one to the top of **poly16Py₃** nanosheets. The difference between peak positions represents the height of the polymers and amounts to 2.0 nm.

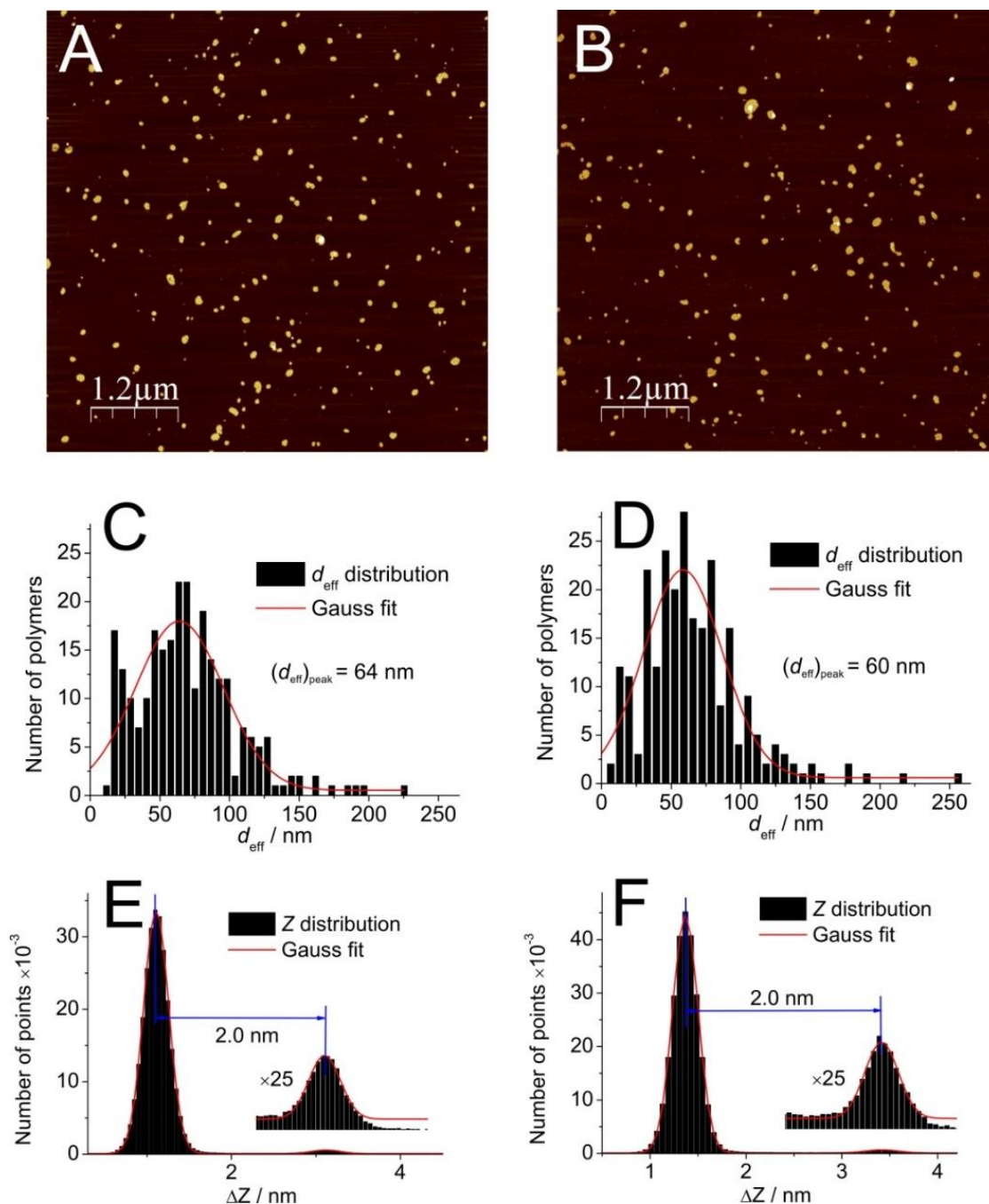


Figure 2. (A, B) Representative AFM images of supramolecular polymers **poly16Py₃** deposited on APTES-mica from water solution with 10% MeOH (frame size $6 \times 6 \mu\text{m}^2$). (C, D) Distribution of diameters of **poly16Py₃** nanosheets and (E, F) height distribution of corresponding AFM images.

3.3 Spectroscopic experiments

The absorption spectrum of **16Py₃** in ethanol (Figures 2 and 3) shows the first electronic transition in the range 330-400 nm. A ratio of the intensities of the vibronic bands 1.2 is observed. The ratio is lower comparing to a monomer compound **16Py** ($S_1^{0\rightarrow0}/S_1^{0\rightarrow1} = 1.5$).

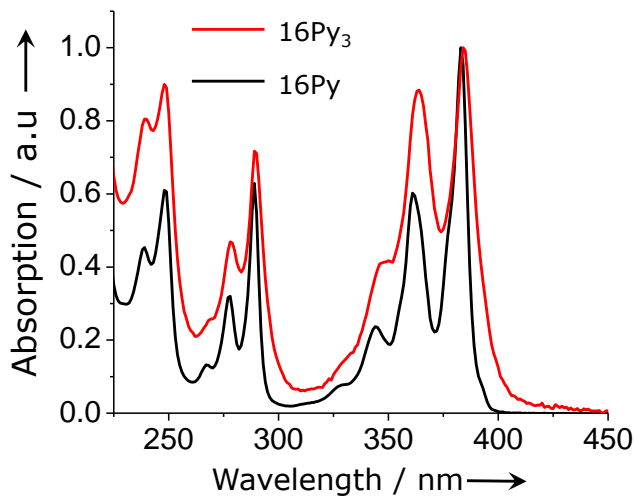


Figure 2. Normalized UV/vis of **16Py₃** and **16Py** in ethanol (concentration $\approx 1 \mu\text{M}$).

In aqueous medium (10 mM sodium phosphate, pH 7.2, 10 mM sodium chloride and 10 % v/v of ethanol), several significant changes occur (Figure 3). Firstly, the ratio of the intensities $S_1^{0\rightarrow0}/S_1^{0\rightarrow1}$ decreases to 0.8, which shows a high degree of pyrene aggregation.^[70,71] Secondly, the intensity of the $S_1^{0\rightarrow0}/S_1^{0\rightarrow1}$ transition decreases dramatically and a new blue-shifted band with a $\lambda_{\text{max}} = 335 \text{ nm}$ appears (specified as H-band). Thirdly, the $S_0 \rightarrow S_2$ signals that were observed in ethanol mostly disappear. Instead, an intense, narrow and red-shifted band at $\lambda_{\text{max}} = 305 \text{ nm}$ (J-band) arises. These changes suggest that **16Py₃** units are involved in a self-assembly process in aqueous medium leading to supramolecular polymers (SPs).^[4,72-77] Additional evidences for the formation of aggregates of **16Py₃** was provided by dynamic light scattering (DLS) experiments (Figure 4) indicating a

medium particle size of 150-200 nm at 20°C. The presence of a small amount of alcohol (10% ethanol was used routinely) is required to ensure the reversibility of the assembly/disassembly process.

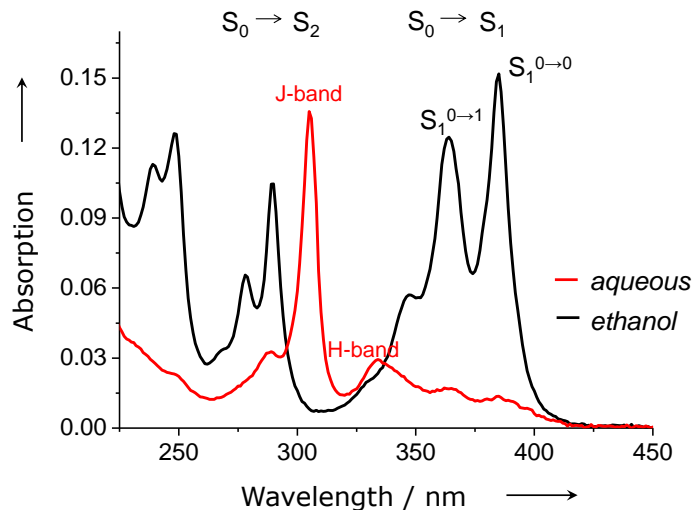


Figure 3. UV/vis spectra of **16Py₃** (1 μ M) in ethanol (black line) and in aqueous medium (10 mM sodium phosphate buffer, pH = 7.2, 10 mM sodium chloride, ethanol 10 vol%, 20°C).

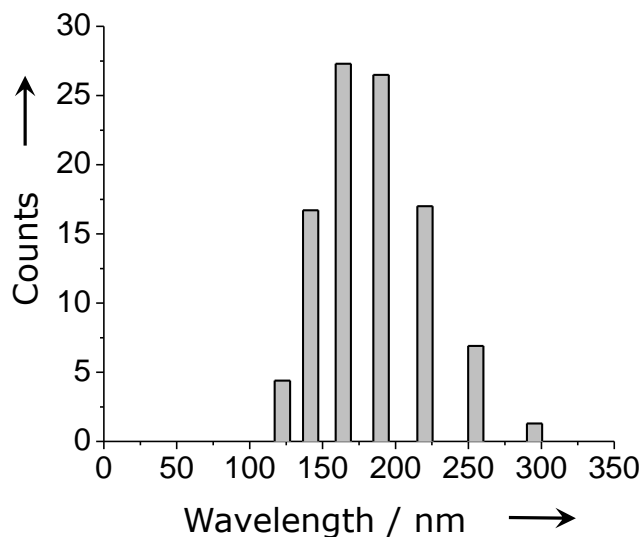


Figure 4. Dynamic light scattering (DLS) measurements showing the particle size distribution (hydrodynamic diameter, D_h) of aggregates formed by **16Py₃** in aqueous solution (10 mM sodium chloride, 10mM sodium phosphate buffer, pH=7.2, ethanol 10 vol.%) 20°C.

The self-assembly process was further studied by temperature-dependent experiments (Figure 5). Heating to 80°C disrupts the structure of the SPs and J- and H-bands disappear concurrently. Intramolecular folding of pyrenes in **16Py₃** is supported by the ratio $S_1^{0\rightarrow0}/S_1^{0\rightarrow1} = 0.8$. Cooling of the solution leads to reappearance of the J- and H-bands. The positions of both, J- and H-band, remain the same over the whole temperature range.

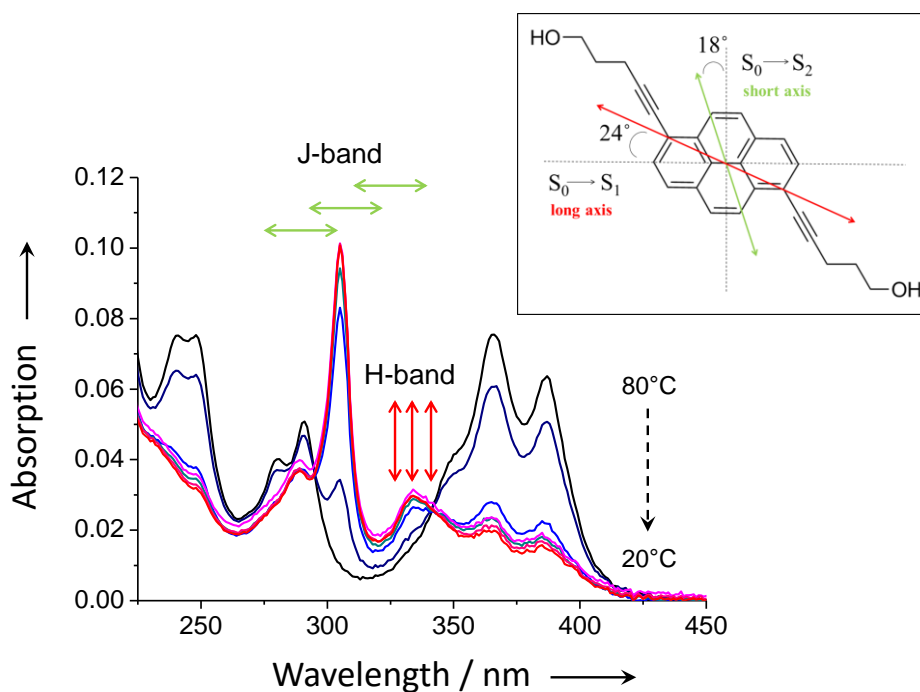


Figure 5. Temperature dependent UV/vis absorption spectra of **16Py₃** in aqueous medium (conditions see Fig. 1; equilibration was allowed for 20 min at each temperature). Double-headed arrows illustrate the relative orientations of the electronic transition dipole moments. Box: Orientation of the electronic transition dipole moments (red) in 1,6-dialkylpyrene (rotated by approx. 24° relative to the long and 18° to the short axis of unsubstituted pyrene, shown dashed).

UV/vis-monitored cooling curves (Figure 6) reveal a highly cooperative supramolecular polymerization process according to the nucleation-elongation model.^[79,80] Absorption changes were recorded at three different wavelengths (305 nm, appearance of J-band; 365 and 385 nm, vibronic bands of the first electronic transition). Evaluation of the curves according to the method by van der Schoot and

co-workers ^[81] gives an approximated elongation temperature (T_e) of 73 °C for the given conditions.

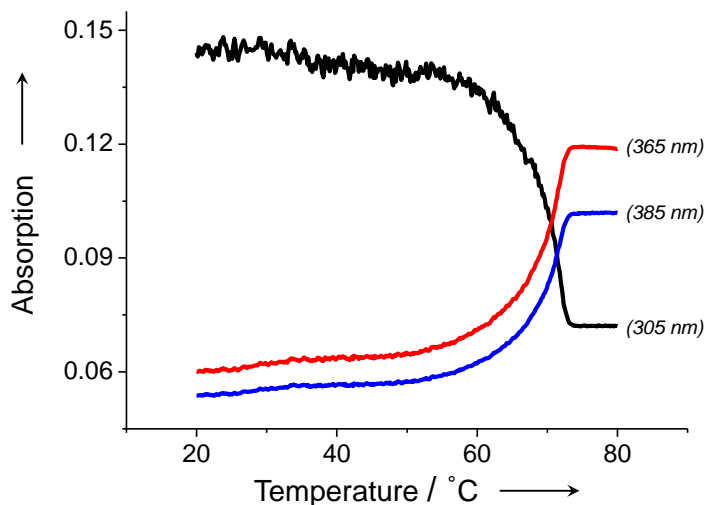


Figure 6. Supramolecular polymer formation curves (cooling rate 0.1 °C/min) recorded in aqueous medium (conditions as in Fig. 1).

Cooperative supramolecular polymerization could be characterized by the T-dependent model proposed by van der Schoot and co-workers. ^[81] The mole fraction of the aggregates at a certain temperature ($a_{agg}(T)$) for the **16Py₃**-derived supramolecular polymers could be estimated based on the following approximations: the predominant quantity of the **16Py₃** units exists in a self-assembled state ($a_{agg}=1$) at 20 °C, and in a disassembled state at the 80 °C (for an aqueous solution containing 10% ethanol).

$$\alpha_{agg}(T) = \frac{A(T) - A_{mon}}{A_{pol} - A_{mon}} \quad \text{equation 1}$$

In this equation A_{pol} describes an absorption of the supramolecular polymers, $A(T)$ corresponds to an absorption of a solution at a certain temperature and A_{mon} to a solution containing individual Py₃ units (all values were taken at 365 nm). In the elongation regime the fraction of the aggregated species could be estimated by the following equation ($a_{sat} = 1.0$):

$$\alpha_{agg}(T) = \alpha_{sat} \left(1 - \exp \left[\frac{-\Delta H_e (T - T_e)}{RT_e^2} \right] \right) \quad \text{equation 2}$$

It is assumed that an elongation occurs via addition of individual **16Py₃** units to a growing polymer chain. Applying the equation 2 for the **16Py₃** supramolecular polymers, following values were found: $T_e=346.2$ K, $\Delta H_e= -143000$ J/mol.

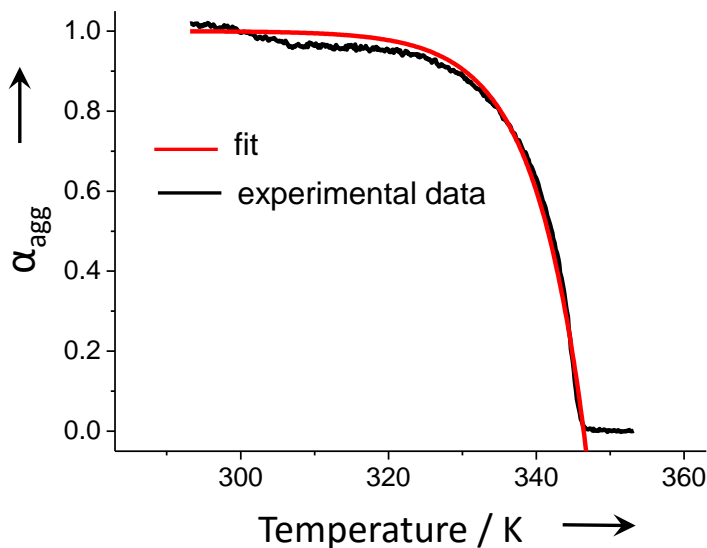


Figure 7. Fitting of the experimental data for the cooling curves (cooling rate 0.1 K/min) of $1\mu\text{M}$ **16Py₃** in aqueous solution (system 10mM sodium chloride, 10 mM sodium phosphate buffer, pH=7.2, ethanol 10 vol.%)

The spectroscopic observations described can be rationalized by the formation of a two-dimensional supramolecular polymer (2DSP), which is confirmed by AFM. In ethanol, **16Py₃** exists as random coils. The addition of water promotes intramolecular folding and formation of sheetlike supramolecular polymers (Scheme 4). Within the supramolecular polymer, **16Py₃** units are individually folded in a staircase-like manner which results in the proper alignment of the corresponding transition moments, as derived from the appearance of J- and H-bands in the UV/vis spectra. Compared to unsubstituted pyrene, the introduction of the alkynyl linkers in the 1- and 6-position leads to a slight twisting of the orientation of the electronic

transition dipole moments by approximately 24° relative to the long and 18° to the short axis of pyrene (Figure 5, inset) caused by the interaction of the alkyne substituents with the π -system; configuration interaction plays a less important role because of the lower symmetry (see box in Scheme 4, and Figure 8).^[82-84] The first intense electronic transition of **16Py**, $S_0 \rightarrow S_1$, is of HOMO to LUMO type while some admixture HOMO-2, HOMO-1 and LUMO+1, LUMO+2 occurs in the intense $S_0 \rightarrow S_2$ transition. The oscillator strength of both transitions are in the order of one, which is important because exciton splitting is directly proportional to the oscillator strength (see e.g. eq. (1) in ref.^[49]). Folding of the amphiphilic **16Py₃** in a staircase-like mode causes the $S_0 \rightarrow S_1$ and $S_0 \rightarrow S_2$ electronic transition dipole moments to adopt an H- and a J-type orientation. To the best of our knowledge, this is the first example of a multichromophore in which the first two electronic transitions are both very sensitive to excitonic coupling and leads to the simultaneous appearance of J- and H-type coupling. This is a different situation with respect to the simultaneous occurrence of H- and J-coupling of degenerate states, known from porphyrins.^[39,47,48]

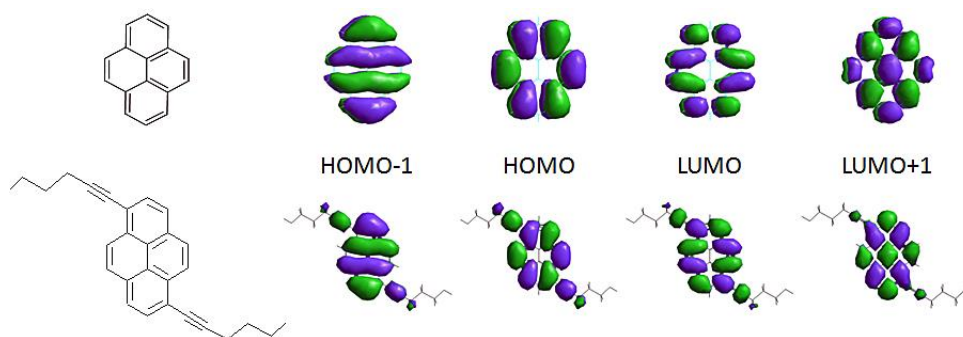


Figure 8. Comparison of the frontier orbitals for native pyrene and 1,6-dipropynylpyrene

Molecular orbitals calculations were performed using the molecular modeling program HyperChem 8 (release 8.0.4, Hypercube, Inc.). Geometry optimization was performed by means of MM+ and molecular orbital calculations by using AM1

procedure, including configuration interaction; 18 configurations, nine occupied and nine unoccupied levels. Configuration interaction was observed to be less important for **16Py** than for the unsubstituted pyrene, which was to be expected because of the symmetry lowering. The influence of the alkyne can be readily understood by comparing the frontier molecular orbitals of the pyrene and the substituted 1,6-dipropynylpyrene in Figure 8 which also explains why the electronic transition dipole moments adapt according to the new situation. The numbers calculated for **16Py** differ slightly from those of 1,6-dipropynylpyrene we therefore give the numbers obtained for the former; the differences are, however, of no significance within the present context. The $S_0 \rightarrow S_1$ transition of the is a pure HOMO to LUMO transition calculated at 423 nm with an oscillator strength of 0.91 while some admixture HOMO-2, HOMO-1 and LUMO+1, LUMO+2 occurs in the $S_0 \rightarrow S_2$ transition, calculated at 260 nm with an oscillator strength of 1.1.

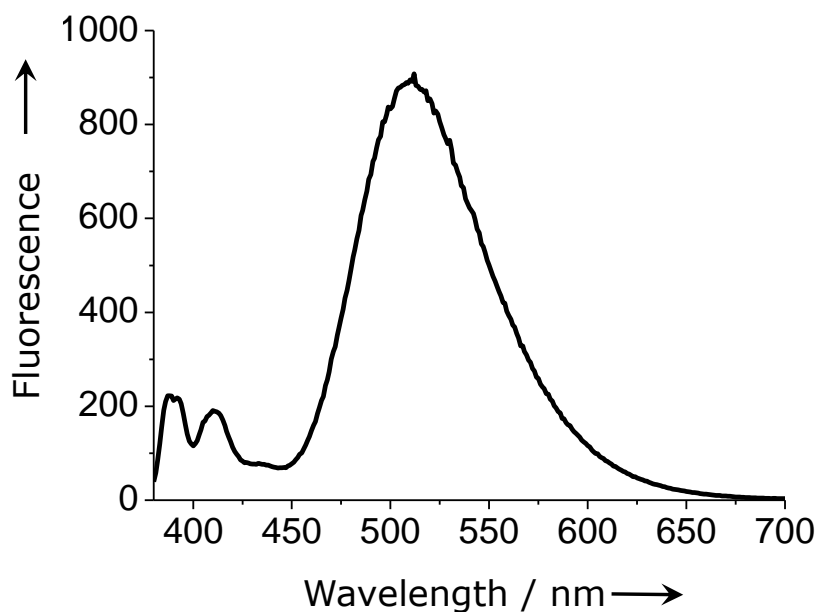


Figure 9. Fluorescence spectrum of 1 μ M **16Py₃** in ethanol (excitation wavelength 365 nm) at 20°C

Further spectroscopic studies included fluorescence properties of **16Py₃** under different conditions. Pyrenes are well-known to form excimers given that association of two monomers is geometrically possible.^[85-87] The most favorable geometry consists in a slightly slipped, sandwich-like orientation.^[88] The fluorescence spectrum of **16Py₃** in ethanol (Figure 9) shows a strong excimer signal ($\lambda_{\text{max}} = 509 \text{ nm}$).

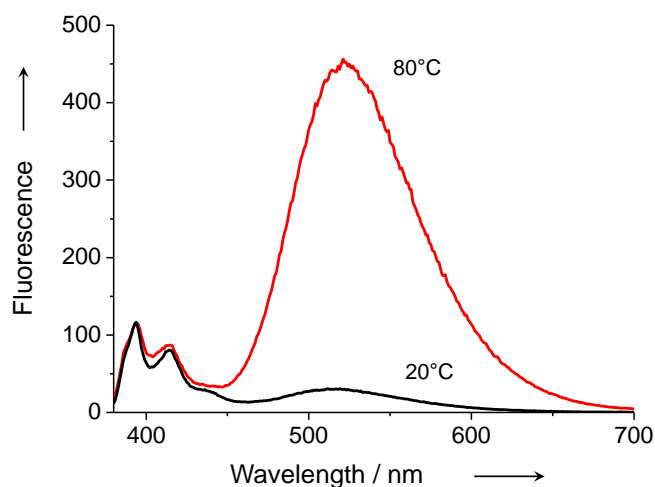


Figure 10. Fluorescence spectra of $1 \mu\text{M}$ **16Py₃** at 20 and 80°C; exc. 365 nm; conditions as in Fig. 1; monomer: 380-450 nm; excimer: 450-700nm.

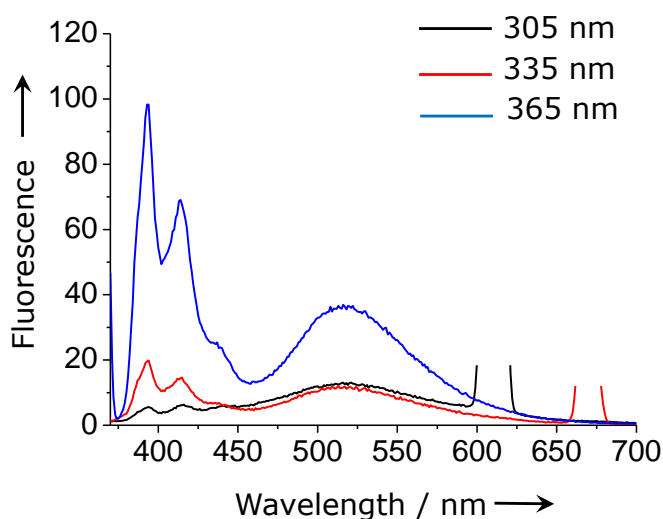


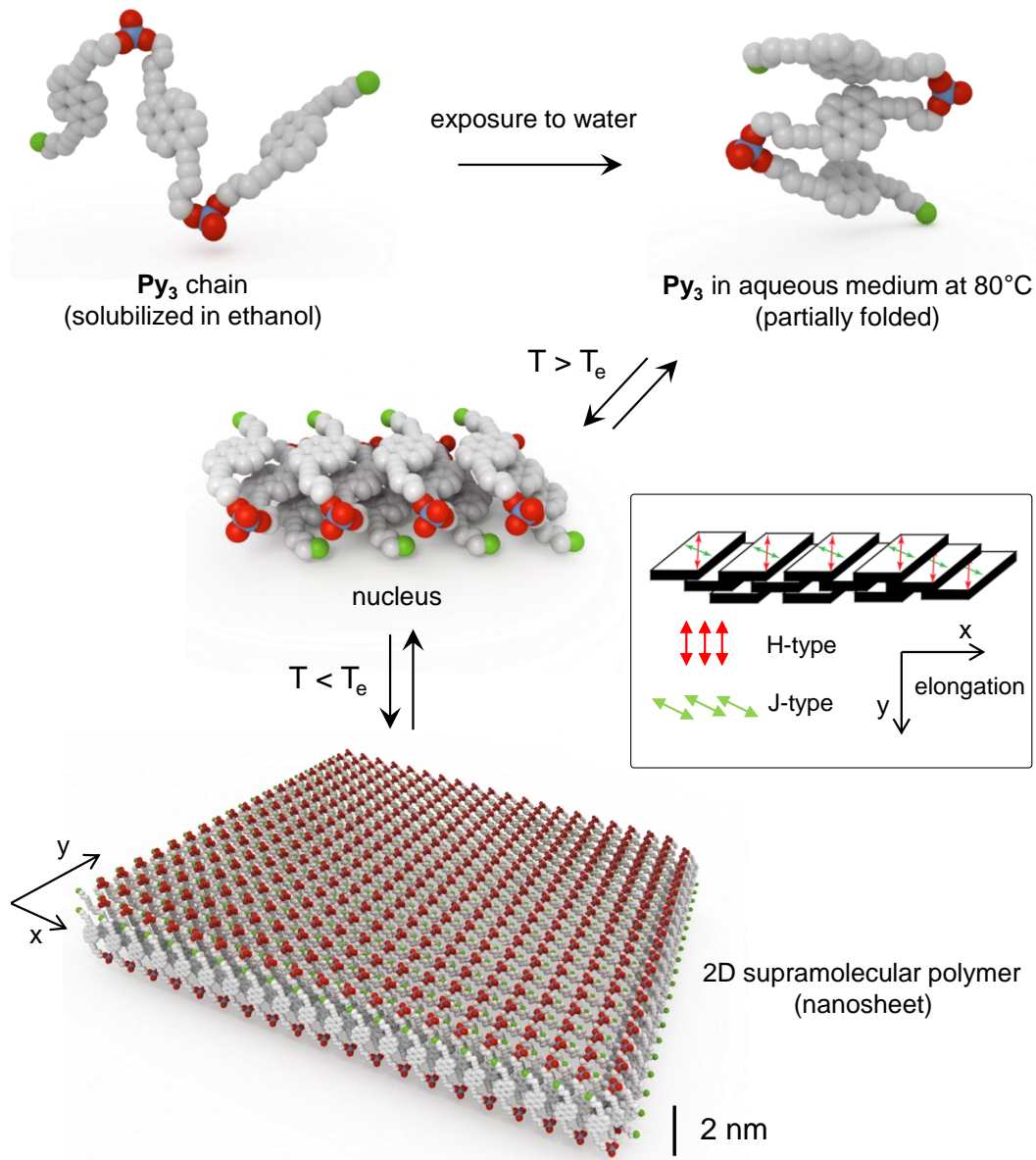
Figure 11. Fluorescence spectrum of $1 \mu\text{M}$ **16Py₃** in aqueous solution (10mM sodium chloride, 10mM sodium phosphate buffer, pH=7.2, ethanol 10 vol.%) at different excitation wavelengths at 20°C (The intense bands at 620 and 670 nm, respectively, are artifacts caused by the second order transmission of the monochromator ($610 \text{ nm} = 2 \times 305 \text{ nm}$ and $670 \text{ nm} = 2 \times 335 \text{ nm}$)).

In aqueous medium, **16Py₃** exhibits predominantly monomer fluorescence (380-450 nm) and only very weak excimer emission upon excitation at 365 nm (Figure 10). However, the shape of a fluorescence spectrum is wavelength-dependent (Figure 11). Upon heating, the excimer signal increases and at 80°C it is the dominant band of the spectrum. This observation is consistent with a rigid two-dimensional structure at 20°C, in which pyrene units are arranged at fixed positions and, hence, cannot adopt the sandwich-like arrangement of two pyrene units required for excimer formation. Residual excimer emission may originate from pyrenes located at the edges of the nanosheets, where the structure would be expected to be less rigid due to the dynamic nature of the supramolecular polymers. Increasing temperatures lead to dissociation of the aggregates and the higher flexibility of the pyrenes in separate trimeric units allows the formation of excimers. In addition, aggregation results in a general reduction of pyrene fluorescence. This is consistent with the well-known quenching effect of H-aggregates.^[89]

4. Discussion

The supramolecular polymerization process follows a nucleation-elongation pathway. The high degree of cooperativity may arise from the adoption of a defined staircase-like intramolecular fold of **16Py₃** within the assemblies. This well-defined fold is absent at temperatures above. Once formed ($T = T_e$), the nucleus serves as a template that facilitates proper folding and assembly of additional **16Py₃** units (elongation). The 2D polymeric structure further implies that the negatively charged phosphodiester groups are arranged on the outsides of the nanosheet, while the pyrene units form a hydrophobic inner layer in an aqueous environment. AFM visualization demonstrates that the nanosheets have a highly-uniform height of 2.0 ± 0.1 nm

(right panel), which represents the thickness of the monolayer assembly (Scheme 4). The value is equal to the length of the long molecular axis of a phosphate-linked pyrene unit and, thus, in a good agreement with the proposed model.



Scheme 4. Illustration of 2D supramolecular polymerization. Amphiphilic **16Py₃** units self-assemble in a temperature and solvent controlled process to form nano-sized sheets. The polymerization follows a nucleation-elongation pathway. Individual **16Py₃** units are folded in a staircase-like fashion forming a hydrophobic pyrene layer (grey). Negatively charged phosphodiester (red) are arranged on the outsides of the sheet.

5. Conclusions

In conclusion, we have demonstrated that phosphodiester-linked trimers of a 1,6-dialkynyl substituted pyrene behave as staircase-like foldamers, which cooperatively self-assemble into two-dimensional supramolecular polymers in aqueous medium. Folding and aggregation processes are accompanied by simultaneous development of J- and H-bands caused by the second and the first allowed electronic transitions, respectively, and significant changes in the fluorescence properties. In the amphiphilic sheetlike polymers, the negatively charged phosphodiester groups are arranged on the outsides of the layer formed by the hydrophobic pyrene units. The data presented here differ significantly from previous findings with 1,8-disubstituted pyrene carboxamides, which give rise to quasi-one dimensional supramolecular polymers.^[69,90] Effects of different linker types and substitution patterns are the topic of on-going investigations.

6. Experimental part

General information. All chemical reagents and solvents required for the synthesis have been purchased from commercial suppliers (Aldrich, Alfa Aesar or TCI) and used without further purification. All required reagents and products for solid-phase synthesis were purchased from Glen Research (solid support, columns) or Proligo[®] Reagents (Cap A, Cap B, 0.02 M I₂/THF/py, TCA deblock, DCI activator). Water was used from a MilliQ system. Analytical thin layer chromatography (TLC) was carried out using aluminium sheets, precoated with silica gel 60 and fluorescent indicator. The silica gel for the column chromatography had 60Å pore size, 230-400 mesh. Air-sensitive reactions and manipulations have been carried out under Ar atmosphere using standard Schlenk technique. Glassware was dried in an oven at 110 °C. All synthesized compounds were stored at 0°C under Ar. NMR spectra were

obtained on a Bruker AV 300 (300 MHz) spectrometer at 298 K. Mass-spectrometric data were obtained on Thermo Fisher LTQ Orbitrap XL using Nano Electrospray Ionization. DLS measurements have been carried out on a Zetasizer Nano instrument (Malvern Instruments). We followed standard operation procedure for the oligonucleotide particles size determination. Pre-washed plastic cuvettes were used for the measurements.

Spectroscopic measurements. UV/VIS spectra were collected with an optical path of 1 cm over the range of 200-500 nm on a Varian Cary-100 Bio-UV/VIS spectrophotometer equipped with a Varian Cary-block temperature controller. Fluorescence data were collected on the Varian Cary Eclipse fluorescence spectrofluorimeter equipped with the Varian Cary-block temperature controller using. Unless otherwise noted the following settings of the instrument were used: the excitation wavelength 365 nm, the slit width 5 nm for emission and excitation, medium sensitivity of the detector. The concentration of **16Py₃** was determined using a value of $\epsilon^{365} = 35000 \text{ dm}^3 \text{ mole}^{-1} \text{ cm}^{-1}$ in EtOH for single pyrene unit.

AFM experiments. AFM imaging was performed under ambient conditions in air with a Nanosurf FlexAFM (Nanosurf AG, Switzerland). All measurements were carried out in tapping mode employing PPP-NCHR-W cantilevers from Nanosensors (resonance frequency $\sim 280 \text{ kHz}$, tip radius $\sim 10 \text{ nm}$). The mica substrates ($20 \times 20 \text{ mm}^2$) were attached to a steel baseplate with Scotch tape and freshly cleaved prior to each new experiment. The protocol of deposition of supramolecular assemblies on a mica substrate followed a strategy originally developed for DNA. A mica surface was modified with 3-aminopropyltriethoxy silane (APTES-mica). The APTES changes the mica surface charge to positive due to amino-groups. Thus, the attachment of **poly16Py₃** is realized by electrostatic interactions between negatively charged phosphate-groups of pyrenyl assemblies and positively charged amines of APTES-

mica. 20 μL of 1.0 μM oligomer solutions was drop-casted onto the mica substrate. After an incubation time of 7 min, the modified mica sample was rinsed with 15 ml of Milli-Q water ($>18 \text{ M}\Omega \text{ cm}^{-1}$, 3 ppb TOC) and dried in a gentle stream of Ar (CarbaGas). This experimental protocol enabled uniform distributions of supramolecular polymers (SPs) over more than 1 cm^2 of the mica surface.

Synthesis and characterization of compounds

5,5'-(Pyrene-1,6-diyl)dipent-4-yn-1-ol (16Py): The mixture of dibromopyrenes (2.20 g, 6.1 mmol), bis-(triphenylphosphine) palladium (II) chloride (100 mg, 0.142 mmol) and copper (I) iodide (15.0 mg, 0.079 mmol) were suspended in THF (50 mL) under argon and heated to 70 $^{\circ}\text{C}$. After addition of triethylamine (30 mL), 3-pentyn-1-ol (2.21 mL, 24.4 mmol) was added to the mixture which was stirred at this temperature overnight. After cooling to room temperature, the solvents were removed under reduced pressure. The residue was dissolved in THF (50 mL), filtered through celite, evaporated to dryness, re-dissolved in ethyl acetate (100 mL), washed with aqueous citric acid (10%) and saturated sodium carbonate solution. After drying with sodium sulphate and filtration, the solution was evaporated to dryness. The column chromatography ($\text{CH}_2\text{Cl}_2/\text{PhMe}/\text{MeOH}$ 87:10:3) furnished yellow solid **16Py** (450 mg). Analytical data for **16Py**: R_f 0.29 ($\text{CH}_2\text{Cl}_2/\text{methanol}$ 97:3); ^1H NMR (300 MHz, DMSO) δ 8.49 (d, $J = 9.1 \text{ Hz}$, 2H), 8.28 (d, $J = 8.5 \text{ Hz}$, 4H), 8.12 (d, $J = 8.0 \text{ Hz}$, 2H), 3.65 (t, $J = 6.2 \text{ Hz}$, 4H), 2.72 (t, $J = 7.1 \text{ Hz}$, 4H), 1.89 (d, $J = 5.5 \text{ Hz}$, 4H). ^{13}C NMR (75 MHz, DMSO) δ 131.1, 130.0, 128.2, 125.3, 123.4, 118.6, 97.3, 78.9, 59.5, 31.7, 15.8. HRMS for $\text{C}_{26}\text{H}_{22}\text{O}_2$: found 366.1607 (calculated 366.1614). m.p. 147 $^{\circ}\text{C}$

5-(6-(5-(Bis(4-methoxyphenyl)(phenyl)methoxy)pent-1-ynyl)pyren-1-yl)pent-4-yn-1-ol (16Py-DMT): To a solution of **16Py** (450 mg, 1.23 mmol) in pyridine (10 mL), a solid 4,4'-dimethoxytrityl chloride (419 mg, 1.23 mmol, 1 eq)

was added dropwise. The mixture was stirred overnight and evaporated afterwards. The residue was dissolved in a small volume of CH₂Cl₂ and subjected to column chromatography (CH₂Cl₂/ MeOH/ NEt₃ 97/2/1). The fractions containing **16Py-DMT** were collected. This furnished 340 mg (41%) of yellow solid **16Py-DMT**. Analytical data for **16Py-DMT**: R_f=0.5 (CH₂Cl₂/MeOH/NEt₃ 97/2/1); ¹H NMR (300 MHz, CDCl₃) δ 8.48 (dd, *J* = 28.4, 9.1 Hz, 2H), 8.15 – 7.91 (m, 6H), 7.53 – 7.31 (m, 7H), 7.18 (s, 2H), 6.78 (d, *J* = 8.9 Hz, 4H), 3.96 (d, *J* = 5.4 Hz, 2H), 3.67 (s, 6H), 3.35 (d, *J* = 6.0 Hz, 2H), 2.80 (t, *J* = 7.2 Hz, 4H), 2.15 – 1.94 (m, 4H), 1.21 (d, *J* = 6.1 Hz, 2H). ¹³C NMR (75 MHz, DMSO) δ 157.9, 145.2, 135.9, 131.1, 129.9, 128.2, 127.7, 126.5, 125.2, 123.3, 118.6, 113.1, 97.2, 96.7, 85.3, 79.4, 79.0, 61.6, 59.5, 54.2, 31.7, 28.7, 16.3, 15.8. HRMS for C₄₇H₄₀O₄: found 668.2915 (calculated 668.2921)

5-(6-(5-(Bis(4-methoxyphenyl)(phenyl)methoxy)pent-1-ynyl)pyren-1-yl)pent-4-ynyl 2-cyanoethyl diisopropylphosphoramidite (16Py-DMT/CEP): **16Py-DMT** (340 mg, 0.509 mmol) was dissolved in CH₂Cl₂ (15 mL). After addition of DIPEA (263 μL, 1.53 mmol, 3 eq), a solution of 2-cyanoethyl-N,N-diisopropylchlorophosphoramidite (154 mg, 0.662 mmol, 1.3 eq). The mixture was stirred for 3 h. The solution was evaporated and the residue was dissolved in hexane/EtOAc/NEt₃ 50/49/1 and purified by a flash chromatography (hexane/EtOAc/NEt₃ 50/49/1), furnished 290 mg (66%) **16Py-DMT/CEP** as a yellowish solid. Analytical data for **16Py-DMT/CEP**: R_f= 0.68 (hexane/ EtOAc/NEt₃ 50/49/1); ¹H NMR (300 MHz, DMSO) δ 8.47 (d, *J* = 9.1 Hz, 1H), 8.31 (d, *J* = 9.1 Hz, 1H), 8.25 – 8.17 (m, 3H), 8.10 (t, *J* = 8.4 Hz, 2H), 7.97 (d, *J* = 8.0 Hz, 1H), 7.43 (d, *J* = 7.4 Hz, 2H), 7.28 (dd, *J* = 4.8, 4.0 Hz, 6H), 7.19 (d, *J* = 7.2 Hz, 1H), 6.81 (d, *J* = 8.9 Hz, 4H), 3.89 – 3.70 (m, 4H), 3.60 (s and m, 8H), 3.24 (t, *J* = 6.0 Hz, 2H), 2.86 – 2.68 (m, 6H), 1.97 (dd, *J* = 8.3, 4.1 Hz, 4H), 1.12 (dd, *J* = 6.7, 2.9 Hz, 12H) ¹³C NMR (75 MHz, DMSO) δ 157.9, 145.2, 135.9, 131.1, 129.9, 128.1, 127.7, 126.5, 125.3,

123.3, 118.9, 118.5, 113.1, 96.67, 96.4, 85.3, 79.4, 61.7, 58.2, 54.8, 42.4, 29.9, 28.7, 24.3, 19.9, 16.3, 15.8. ^{31}P NMR (122 MHz, DMSO) δ 146.90. HRMS for $\text{C}_{56}\text{H}_{57}\text{N}_2\text{O}_5\text{P}$: found 869.4069 (calculated 869.4078)

Solid-phase synthesis of 16Py₃. The **16Py₃** was synthesized on the Applied Biosystems 394 DNA synthesizer using preloaded USIII support. We followed a standard cyanoethyl phosphoramidite coupling protocol for the 1 μmol synthesis ("trityl-off" mode). The coupling time of the building block **16Py-DMT/CEP** was increased to 120 sec. The coupling yields per single step were between 90 % and 95 % (monitoring by "trityl assay"). The cleavage of the **16Py₃** from the support was achieved by treatment with 0.8 ml of 2M NH_3 / MeOH (Aldrich) for 12 hours at 50°C in a closed vial with vigorous shaking. The supernatant was separated from the support by centrifugation. The remained beads were treated with 0.8 ml of 2M NH_3 /MeOH two times. All supernatants were collected, and 1 ml of aqueous NH_3 was added. After automated oligomer synthesis, the crude product was purified by reverse-phase HPLC (LiChrospher 100 RP-C8, 5 μm , Merck, Bio-Tek Instruments); eluent A=(Et_3NH)OAc (50 mM, pH 7.0)/ CH_3CN in 50/50 v/v; eluent B= CH_3CN ; gradient 0–100% B over 14 min, then 100% B over 9 min. Gradient flow 1 ml/min. The pure compound was characterized by mass spectrometry: HRMS for $\text{C}_{78}\text{H}_{62}\text{O}_{10}\text{P}_2^{2-}$: found 1220.3852 (calculated 1220.3830).

7. References

- [1] F. J. M. Hoeben, P. Jonkheijm, E. W. Meijer, A. P. H. J. Schenning, *Chem.Rev.* **2005**, *105*, 1491-1546.
- [2] L. Zang, Y. Che, J. S. Moore, *Acc. Chem. Res.* **2008**, *41*, 1596-1608.

- [3] Z. J. Chen, A. Lohr, C. R. Saha-Moller, F. Würthner, *Chem. Soc. Rev.* **2009**, 38, 564-584.
- [4] T. Aida, E. Meijer, S. I. Stupp, *Science* **2012**, 335, 813-817.
- [5] C. Li, M. Y. Liu, N. G. Pschirer, M. Baumgarten, K. Müllen, *Chem. Rev.* **2010**, 110, 6817-6855.
- [6] A. Geim, K. Novoselov, *Nat. Mater.* **2007**, 6, 183-191.
- [7] E. Orentas, M. Lista, N. T. Lin, N. Sakai, S. Matile, *Nat. Chem.* **2012**, 4, 746-750.
- [8] T. Fenske, H. G. Korth, A. Mohr, C. Schmuck, *Chem.-Eur. J.* **2012**, 18, 738-755.
- [9] A. P. H. J. Schenning, E. W. Meijer, *Chem. Commun.* **2005**, 3245-3258.
- [10] M. Muccini, *Nat. Mater.* **2006**, 5, 605-613.
- [11] E. R. Kay, D. A. Leigh, F. Zerbetto, *Angew. Chem. Int. Ed.* **2007**, 46, 72-191.
- [12] S. Liu, W. M. Wang, A. L. Briseno, S. C. Mannsfeld, Z. Bao, *Adv. Mater.* **2009**, 21, 1217-1232.
- [13] T. F. A. De Greef, M. M. J. Smulders, M. Wolfs, A. P. H. J. Schenning, R. P. Sijbesma, E. W. Meijer, *Chem. Rev.* **2009**, 109, 5687-5754.
- [14] K. Liu, C. Wang, Z. Li, X. Zhang, *Angew. Chem. Int. Ed.* **2011**, 50, 4952-4956.
- [15] Y. Chen, B. Zhu, Y. Han, Z. Bo, *J. Mater. Chem.* **2012**, 22, 4927-4931.
- [16] R. Nomura, R. Moriai, M. Kudo, T. Hoshino, J. Watanabe, S. Funyu, K. Ishitsuka, S. Okamoto, *J. Polym. Sci. Part A: Polym. Chem.* **2013**, 51, 3412-3419.
- [17] S. S. Babu, S. Prasanthkumar, A. Ajayaghosh, *Angew. Chem. Int. Ed.* **2012**, 51, 1766-1776.
- [18] S. I. Stupp, S. Son, H. C. Lin, L. S. Li, *Science* **1993**, 259, 59-63.

- [19] S. I. Stupp, V. LeBonheur, K. Walker, L. S. Li, K. E. Huggins, M. Keser, A. Amstutz, *Science* **1997**, 276, 384-389.
- [20] J. Sakamoto, J. van Heijst, O. Lukin, A. D. Schlüter, *Angew. Chem. Int. Ed.* **2009**, 48, 1030-1069.
- [21] J. W. Colson, W. R. Dichtel, *Nat. Chem.* **2013**, 5, 453-465.
- [22] K. Baek, G. Yun, Y. Kim, D. Kim, R. Hota, I. Hwang, D. Xu, Y. H. Ko, G. H. Gu, J. H. Suh, C. G. Park, B. J. Sung, K. Kim, *J. Am. Chem. Soc.* **2013**, 135, 6523-6528.
- [23] Y. Anraku, A. Kishimura, Y. Yamasaki, K. Kataoka, *J. Am. Chem. Soc.* **2013**, 135, 1423-1429.
- [24] B. Narayan, S. P. Senanayak, A. Jain, K. Narayan, S. J. George, *Adv. Funct. Mater.* **2013**, 23, 3053-3060.
- [25] F. Li, Q. Song, L. Yang, G. Wu, X. Zhang, *Chem. Commun.* **2013**, 49, 1808-1810.
- [26] Y. Zheng, H. Zhou, D. Liu, G. Floudas, M. Wagner, K. Koynov, M. Mezger, H. J. Butt, T. Ikeda, *Angew. Chem. Int. Ed.* **2013**, 52, 4845-4848.
- [27] T. Govindaraju, M. B. Avinash, *Nanoscale* **2012**, 4, 6102-6117.
- [28] G. D. Scholes, G. Rumbles, *Nat. Mater.* **2006**, 5, 683-696.
- [29] G. D. Scholes, *ACS Nano* **2008**, 2, 523-537.
- [30] M. R. Wasielewski, *Acc. Chem. Res.* **2009**, 42, 1910-1921.
- [31] L. D. A. Siebbeles, F. C. Grozema, *Charge and Exciton Transport through Molecular Wires*, Wiley-VCH, Weinheim **2011**.
- [32] M. Porel, S. Jockusch, A. Parthasarathy, V. Rao, N. J. Turro, V. Ramamurthy, *Chem. Commun.* **2012**, 48, 2710-2712.
- [33] M. Han, Y. Okui, T. Hirade, *J. Mater. Chem. C* **2013**, 1, 3448-3453.

- [34] O. N. Sancho, W. R. Browne, G. Roelfes, *Chem.- Eur. J.* **2013**, *19*, 2457-2461.
- [35] V. Garg, G. Kodis, P. A. Liddell, Y. Terazono, T. A. Moore, A. L. Moore, D. Gust, *J. Phys. Chem. B* **2013**, *117*, 11299-11308
- [36] N. Yan, Z. Xu, K. K. Diehn, S. R. Raghavan, Y. Fang, R. G. Weiss, *Langmuir* **2013**, *29*, 793-805.
- [37] F. C. De Schryver, T. Vosch, M. Cotlet, M. Van der Auweraer, K. Müllen, J. Hofkens, *Acc. Chem. Res.* **2005**, *38*, 514-522.
- [38] G. Calzaferri, A. Devaux, in *Supramolecular Photochemistry - Controlling Photochemical Processes*, Eds.: V. Ramamurthy, Y. Inoue, John Wiley & Sons, Hoboken, NJ, **2011**, pp. 285-387.
- [39] *J-Aggregates*, (Ed.: T. Kobayashi) World Scientific Publishing Co. Pte. Ltd., Singapore **2012**.
- [40] Z. Zhao, J. W. Lam, B. Z. Tang, *J. Mater. Chem.* **2012**, *22*, 23726-23740.
- [41] D. Goerl, X. Zhang, F. Würthner, *Angew. Chem. Int. Ed.* **2012**, *51*, 6328-6348.
- [42] P. D. Frischmann, K. Mahata, F. Würthner, *Chem. Soc. Rev.* **2013**, *42*, 1847-1870.
- [43] D. Haldar, C. Schmuck, *Chem. Soc. Rev.* **2009**, *38*, 363-371.
- [44] S. Prasanthkumar, A. Saeki, S. Seki, A. Ajayaghosh, *J. Am. Chem. Soc.* **2010**, *132*, 8866-8867.
- [45] K. K. Kartha, S. S. Babu, S. Srinivasan, A. Ajayaghosh, *J. Am. Chem. Soc.* **2012**, *134*, 4834-4841.
- [46] A. Ajayaghosh, V. K. Praveen, *Acc. Chem. Res.* **2007**, *40*, 644-656.
- [47] B. A. Friesen, K. R. Nishida, J. L. McHale, U. Mazur, *J. Phys. Chem. C* **2009**, *113*, 1709-1718.

- [48] C. C. Rich, J. L. McHale, *J. Phys. Chem. C* **2013**, *117*, 10856-10865.
- [49] G. Calzaferri, D. Brühwiler, T. Meng, L. Q. Dieu, V. L. Malinovskii, R. Häner, *Chem.-Eur. J.* **2010**, *16*, 11289-11299.
- [50] G. Sargsyan, A. A. Schatz, J. Kubelka, M. Balaz, *Chem. Commun.* **2013**, *49*, 1020-1022.
- [51] E. E. Jelley, *Nature* **1936**, *138*, 1009-1010.
- [52] G. Scheibe, *Angew. Chem.* **1936**, *49*, 563.
- [53] M. Kasha, *Radiat. Res.* **1963**, *20*, 55-70.
- [54] F. Würthner, T. E. Kaiser, C. R. Saha-Möller, *Angew. Chem. Int. Ed.* **2011**, *50*, 3376-3410.
- [55] D. Möbius, *Adv. Mater.* **1995**, *7*, 437-444.
- [56] M. Kasha, H. R. Rawls, M. Ashraf El-Bayoumi, *Pure Appl. Chem.* **1965**, *11*, 371-392.
- [57] S. E. Boiadjev, D. A. Lightner, *Monatsh. Chem.* **2005**, *136*, 489-508.
- [58] T. M. Figueira-Duarte, K. Müllen, *Chem. Rev.* **2011**, *111*, 7260-7314.
- [59] D. Bhattacharjee, K. Mukherjee, T. N. Misra, *J. Phys. Chem. Solids* **2000**, *61*, 751-756.
- [60] A. T. Haedler, H. Misslitz, C. Buehlmeier, R. Q. Albuquerque, A. Köhler, H. W. Schmidt, *ChemPhysChem* **2013**, *14*, 1818-1829.
- [61] S. M. Biner, D. Kummer, V. L. Malinovskii, R. Häner, *Org. Biomol. Chem.* **2011**, *9*, 2628-2633.
- [62] O. O. Adeyemi, V. L. Malinovskii, S. M. Biner, G. Calzaferri, R. Häner, *Chem. Commun.* **2012**, *48*, 9589-9591.
- [63] F. Garo, R. Häner, *Angew. Chem. Int. Ed.* **2012**, *51*, 916-919.
- [64] F. Garo, R. Häner, *Bioconjug. Chem.* **2012**, *23*, 2105-2113.

- [65] V. L. Malinovskii, A. L. Nussbaumer, R. Häner, *Angew. Chem. Int. Ed.* **2012**, *51*, 4905-4908.
- [66] R. Häner, F. Garo, D. Wenger, V. L. Malinovskii, *J. Am. Chem. Soc.* **2010**, *132*, 7466-7471.
- [67] A. L. Nussbaumer, D. Studer, V. L. Malinovskii, R. Häner, *Angew. Chem. Int. Ed.* **2011**, *50*, 5490-5494.
- [68] A. L. Nussbaumer, F. Samain, V. L. Malinovskii, R. Häner, *Org. Biomol. Chem.* **2012**, *10*, 4891-4898.
- [69] A. V. Rudnev, V. L. Malinovskii, A. L. Nussbaumer, A. Mishchenko, R. Häner, T. Wandlowski, *Macromolecules* **2012**, *45*, 5986-5992.
- [70] H. Bittermann, D. Siegemund, V. L. Malinovskii, R. Häner, *J. Am. Chem. Soc.* **2008**, *130*, 15285-15287.
- [71] W. Wang, L. S. Li, G. Helms, H. H. Zhou, A. D. Q. Li, *J. Am. Chem. Soc.* **2003**, *125*, 1120-1121.
- [72] T. F. A. Greef, E. W. Meijer, *Nature* **2008**, *453*, 171-173.
- [73] J. M. Lehn, *Prog. Polym. Sci.* **2005**, *30*, 814-831.
- [74] A. W. Bosman, R. P. Sijbesma, E. W. Meijer, *Mat. Today* **2004**, *7*, 34-39.
- [75] L. Brunsveld, B. J. B. Folmer, E. W. Meijer, R. P. Sijbesma, *Chem. Rev.* **2001**, *101*, 4071-4097.
- [76] J. S. Moore, *Curr. Opin. Colloid Interface Sci.* **1999**, *4*, 108-116.
- [77] J. M. Lehn, *Angew. Chem. Int. Ed.* **1990**, *29*, 1304-1319.
- [78] Y. L. Lyubchenko, B. L. Jacobs, S. M. Lindsay, *Nucl. Acids Res.* **1992**, *20*, 3983-3986.
- [79] P. A. Korevaar, S. J. George, A. J. Markvoort, M. M. Smulders, P. A. Hilbers, A. P. Schenning, T. F. De Greef, E. Meijer, *Nature* **2012**, *481*, 492-496.

- [80] M. M. J. Smulders, M. M. L. Nieuwenhuizen, T. F. A. de Greef, P. van der Schoot, A. P. H. J. Schenning, E. W. Meijer, *Chem. - Eur. J.* **2010**, *16*, 362-367.
- [81] P. Jonkheijm, P. van der Schoot, A. P. H. J. Schenning, E. W. Meijer, *Science* **2006**, *313*, 80-83.
- [82] A. G. Crawford, A. D. Dwyer, Z. Liu, A. Steffen, A. Beeby, L. O. Palsson, D. J. Tozer, T. B. Marder, *J. Am. Chem. Soc.* **2011**, *133*, 13349-13362.
- [83] T. Shyamala, S. Sankararaman, A. K. Mishra, *Chem. Phys.* **2006**, *330*, 469-477.
- [84] C. Lambert, J. Ehbets, D. Rausch, M. Steeger, *J. Org. Chem.* **2012**, *77*, 6147-6154.
- [85] F. M. Winnik, *Chem. Rev.* **1993**, *93*, 587-614.
- [86] F. C. De Schryver, P. Collart, J. Vandendriessche, R. Goedeweck, A. M. Swinnen, M. Van der Auweraer, *Acc. Chem. Res.* **1987**, *20*, 159-166.
- [87] K. Zachariasse, W. Kuhnle, *Z. Phys. Chem.* **1976**, *101*, 267-276.
- [88] A. Warshel, E. Huler, *Chem. Phys.* **1974**, *6*, 463-468.
- [89] U. Roesch, S. Yao, R. Wortmann, F. Würthner, *Angew. Chem. Int. Ed.* **2006**, *45*, 7026-7030.
- [90] F. Simona, A. L. Nussbaumer, R. Häner, M. Cascella, *J. Phys. Chem. B* **2013**, *117*, 2576-2585

CHAPTER III. FORMATION OF EXTRA-LARGE NANOSHEETS

Published: Vybornyi, M.; Rudnev, A.; Häner, R. *Chem. Mater.* **2015**, *27*, 1426.

1. Abstract

The importance of kinetic effects in the 2D self-assembly of a negatively charged pyrene trimer (**16Py₃**) in aqueous media is described. Under optimized experimental conditions, the chain-folded oligomers assemble into exceptionally thin planar assemblies (~ 2 nm thick) with a very high aspect ratio (area/thickness ratio $\sim 10^7$ nm). The morphology of the nanosheets was characterized by different microscopic techniques (AFM, TEM and optical microscopy), whereas UV/vis and fluorescence spectroscopy revealed details on the intramolecular folding of the oligomer stands. Temperature control was shown to be crucial for preventing the formation of kinetically trapped states thus allowing the development of extra-large 2D assemblies.

2. Introduction

The properties of materials often critically depend on the degree of order by which the elementary units are arranged on the nanoscale.^[1,2] The molecular and supramolecular organization strongly influences the interactions between individual components and, thus, directs the physical, optical, magnetic and further properties of polymers, crystals and other types of aggregates.^[3,4] Due to their special optical, electronic and mechanical properties, two-dimensional (2D) organic materials polymers have attracted considerable attention lately.^[5-15] By arranging functional groups in 2D arrays, structurally well-defined objects with dimensions in the nano- (thickness) and micrometer-scale (width) become accessible.^[16-23] Furthermore, due to their sheet- or layer-like shape, 2D polymers may serve as structural or functional platforms for higher-level architectures and assemblies. Yet, the controlled formation

of 2D molecular objects represents a formidable challenge.^[6] Extended 2D molecules, such as graphene, are often only accessible from three-dimensional aggregates through exfoliation procedures (top-down approach). A common strategy for the preparation of synthetic 2D polymers consists in the covalent linking of reactive entities that are preorganized in layers.^[24-28] For this purpose, the reactive supramolecular synthons need to be arranged in a 3D aggregate to ensure the required stability for the controlled crosslinking within the individual layers. Nanosheets are obtained by subsequent exfoliation. Exfoliation procedures, however, generally result in damage and size reduction of the original 2D objects. Reports on the bottom-up preparation of 2D organic materials through polymerization of suitable monomeric building blocks are, however, still rather limited.^[29] Alternatively, formation of 2D objects can be achieved by supramolecular polymerization.^[30] In supramolecular polymers, the molecular components are associated and organized through non-covalent interactions.^[31] The pathways of supramolecular polymerization into two-dimensional (2D) objects in solution have been studied recently. Thus, Zuckermann *et al.* studied mechanistic details of peptoid assembly and elaborated a preparative approach of 2D sheets production.^[32] Rybtchinski *et al.* analyzed a growth of 2D crystalline PDI-based assemblies arising from relatively slow assembly kinetics.^[33] Furthermore, Eisenberg *et al.* followed the formation of large sheets in water from the block-copolymers by TEM in detail.^[34] Recently, Ikeda demonstrated that the self-assembly of oligothiophenes into 2D objects significantly depends on the oligomer length.^[35]

In addition to the internal regularity with which the components are arranged, also the area/thickness aspect ratio will have an impact on the electronic and/or mechanical properties of nanosheets. The noncovalent nature of the forces joining the units in supramolecular polymers offers the possibility of controlling the

aforementioned parameters. Recently, we reported the assembly of 2D supramolecular polymers from anionic pyrene trimers (**16Py₃**, Scheme 1) in aqueous solution via a nucleation-elongation process.^[36] Here, we demonstrate the formation of 2D objects with an extreme area/thickness ratio ($\sim 10^7$ nm) under controlled conditions. As evidenced by microscopic techniques, even at low concentration (μM) the oligomer tends to form nanometer-thick two-dimensional structures with a surface area up to hundreds of μm^2 in aqueous solution. The aqueous environment promotes interactions between hydrophobic 1,6-bisalkynylpyrene residues. The membrane-like structure is composed of a pyrene layer which is covered by phosphate groups on the water-exposed surfaces. We show that size and homogeneity of the 2D supramolecular structures are highly sensitive to temperature and temperature gradient applied during the assembly process.

3. Methods of poly**16Py₃** preparation

The term 'aqueous medium' refers to a solvent mixture composed of 85% (v/v) aqueous buffer (10 mM sodium phosphate, pH = 7.2, and 10 mM sodium chloride) and 15% ethanol. **Method 1:** a 10 μL aliquot of **16Py₃** stock solution (~ 200 μM in ethanol) was added to 990 μL of aqueous medium. The mixture was briefly shaken and placed into a conventional heating block thermostated at 80°C (to ensure complete disassembly of any polymers present) and subsequently cooled to 20°C using a gradient of 0.1 °C/min (*slow cooling*). **Method 2:** a 10 μL aliquot from the **16Py₃** stock solution in ethanol was added to 990 μL of aqueous medium at 20°C, briefly shaken and placed in thermostat. The sample was equilibrated at 80°C (to ensure complete disassembly of any polymers present) and subsequently cooled to 20°C using a gradient of 20 °C/min (*fast cooling*). **Method 3:** a 10 μL aliquot of

16Py₃ stock solution was added to 990 μL of aqueous medium at 20°C and briefly shaken.

4. Results and discussion

The properties of 2D supramolecular assemblies obtained by methods 1-3 (see Section 3) were tested by different spectroscopic and microscopic techniques. UV/vis, fluorescence and CD spectroscopy allowed establishing the relative orientation of pyrenes within the polymers and delivered information on the mechanism of the polymerization process, while atomic force and transmission electron microscopy (AFM and TEM) provided insights on the morphological parameters of the formed assemblies.

4.1 Spectroscopic studies

UV/vis spectra obtained from **16Py₃** polymers prepared by any of the methods 1-3 possess high similarity (Figure 2). Changes in the UV/vis absorption spectra between dissolved and aggregated chromophores originate from changes in the interactions of the chromophore transition dipole moments. The staircase-like folding and aggregation process of **16Py₃** results in a two-fold exciton coupling. Thus, the interaction between the $S_0 \rightarrow S_1$ electronic transition dipole moments gives rise to a blue-shifted, low-intense H-band with a maximum at 335 nm, while the coupling of the $S_0 \rightarrow S_2$ electronic transition dipole moments results in the formation of an intense and narrow, red-shifted J-band (305 nm, Figure 1). The growth of these two bands can be observed (Figure 1A) upon cooling of an aqueous oligomer solution from 80°C to 20°C (as in methods 1 or 2). If an ethanol solution of **16Py₃** is added to aqueous buffer (method 3), solvent-induced aggregation also leads to the immediate appearance of the same J- and H-bands.

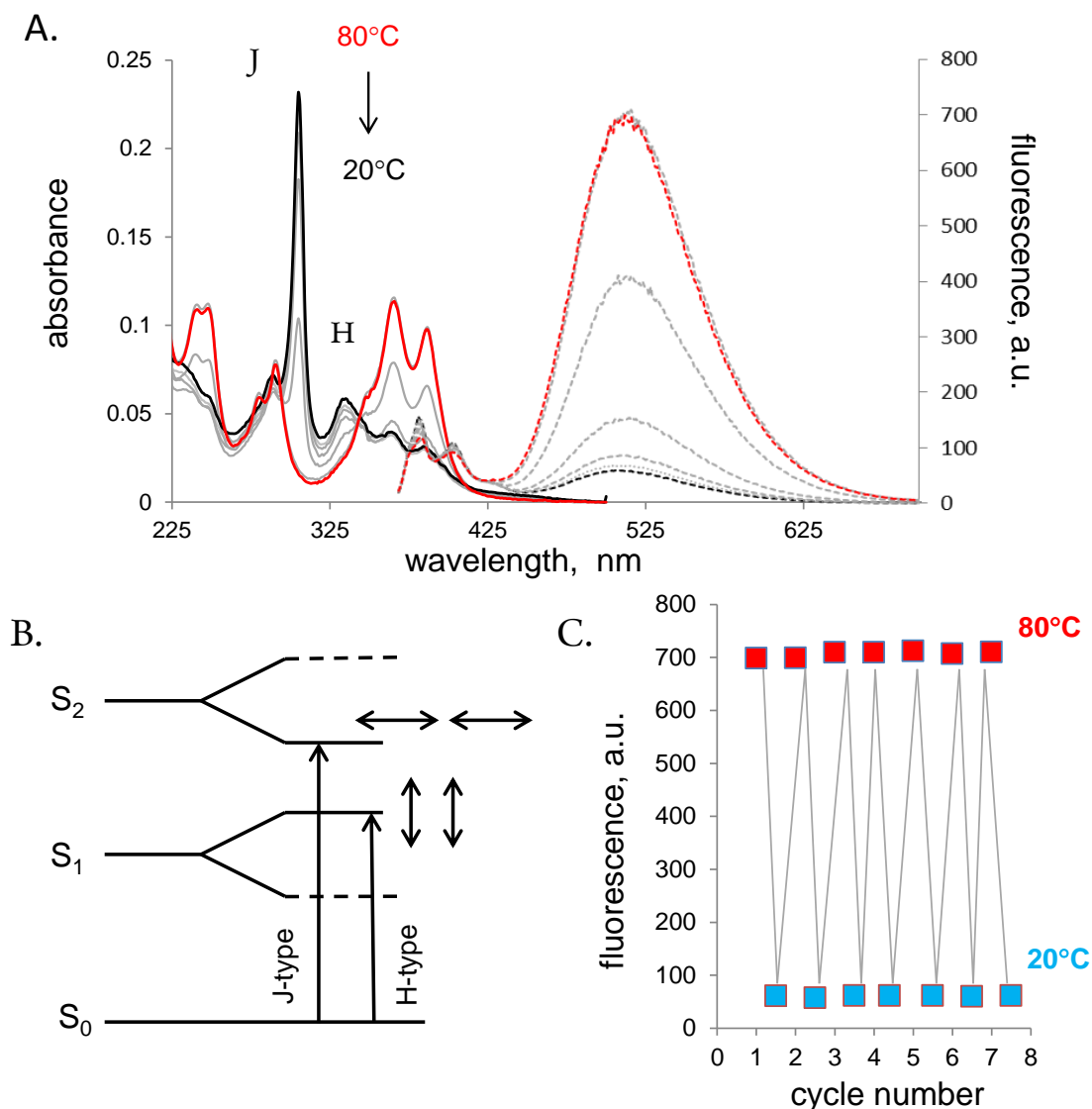


Figure 1. A) Temperature-dependent UV/vis (solid lines, left scale bar) and fluorescence (dashed lines, right scale bar, excitation at 365 nm) of a 2 μM aqueous solution of **16Py₃**. The data were recorded upon cooling the sample in 10°C steps. Red lines correspond to 80°C, black ones to 20°C; the grey lines represent subsequent 10°C temperature intervals. B) Illustration of J- and H-type exciton interaction. C) Reversibility of the polymerization monitored by the value of the maxima and minima of the excimer emission (excitation wavelength 365 nm, emission 521 nm) at 80°C (red squares) and 20°C (blue squares) for repeated cooling-heating cycles. After heating to 80°C, the sample was kept for 10 min before the emission intensity was measured; after each cooling to 20°C, the sample was equilibrated for 1 h before measurement.

The formation of the 2D supramolecular assemblies was further studied by fluorescence spectroscopy. At 80°C the flexibility of the **16Py₃** oligomers is high,

which is reflected by an intense excimer emission (maximum at 520 nm, Figure 1A) upon pyrene excitation. Excimer fluorescence, however, is significantly reduced when the temperature, and thus the flexibility of the oligomers, is lowered. Obviously, the 2D-array represents a rigid structure in which the pyrene units are tightly arranged, so that adoption of the sandwich-type arrangement required for excimer formation [37] is not possible. Scheme 1 shows an illustration of the 2D-pyrene array. Movement of pyrenes within the nanosheets is strongly handicapped. Suitable excimer geometry is less attainable in self-assembled structures at 20°C than in molecularly dissolved chains at 80°C. At room temperature, pyrene monomer fluorescence (signals around 400 nm) is the predominant feature in the emission spectrum. The process of thermally induced assembly and disassembly of the polymers is entirely reversible. This is confirmed by repeated cooling-heating cycles showing full recovery and disappearance of excimer fluorescence between individual cycles (Figure 1C).

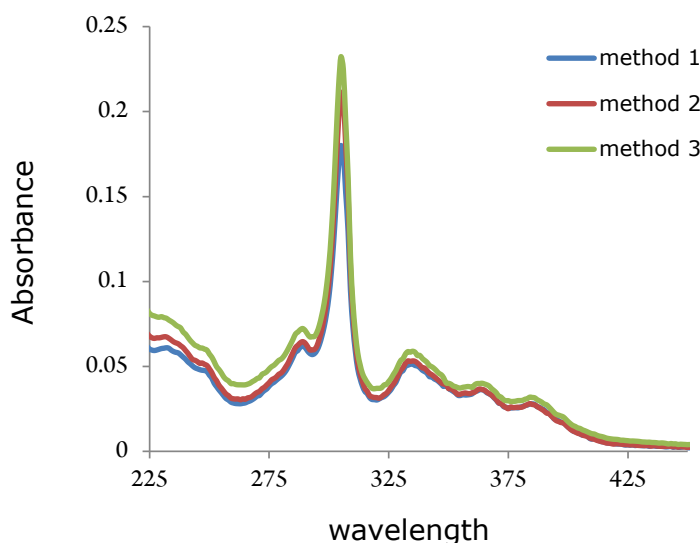


Figure 2. UV/vis spectra of 2D supramolecular assemblies after 1 day of aging. Blue line – method 1, red line – method 2, green line –method 3. Conditions: 2 μM **16Py₃**, 10 mM phosphate buffer pH = 7.2, 10 mM sodium chloride, 15 % ethanol (v/v).

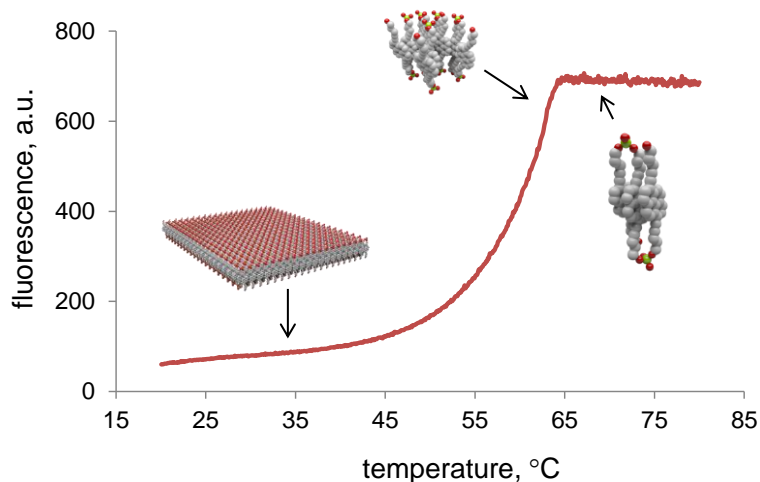


Figure 3. Temperature-dependent excimer fluorescence ($\lambda_{em} = 520 \text{ nm}$, $\lambda_{ex} = 365 \text{ nm}$) of **16Py3** in aqueous solution. Cooling ramp $0.1 \text{ }^\circ\text{C}/\text{min}$. Conditions: see Experimental Section.

The temperature dependence of excimer emission ($\lambda_{em}=520 \text{ nm}$) is displayed in Figure 3. The fluorescence intensity remains high above T_e ($\sim 63^\circ\text{C}$) and declines abruptly when the temperature decreases below T_e . The profile of the annealing curve reveals that the supramolecular self-assembly process follows a cooperative nucleation-elongation pathway.^[38]

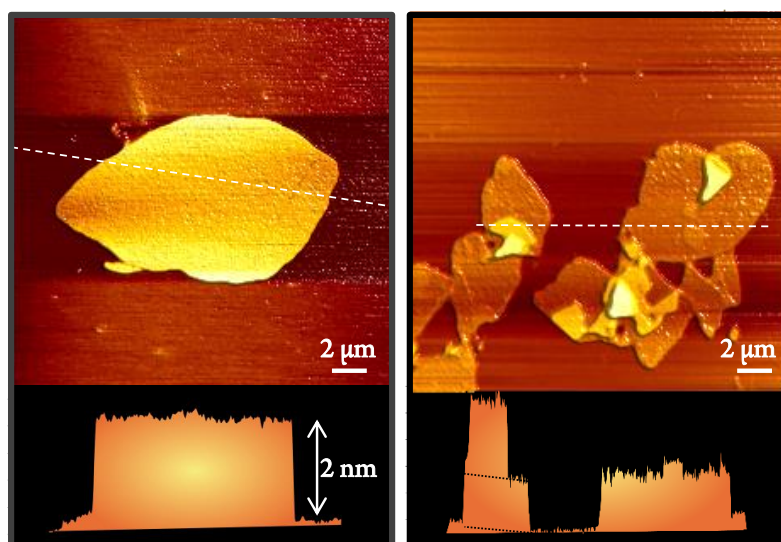


Figure 4. AFM images and the cross-sections along indicated lines of the 2D supramolecular polymers obtained by using method 1. Conditions: see Experimental Section.

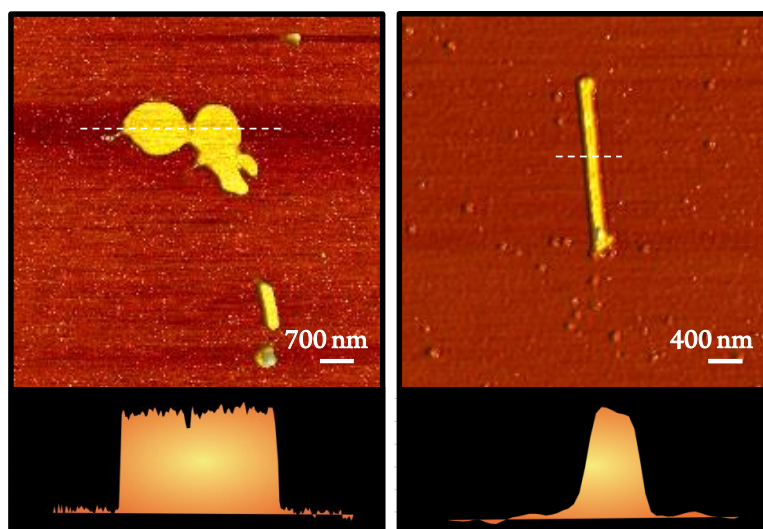


Figure 5. AFM images and the cross-sections along indicated lines of the 2D supramolecular polymers obtained by using method 2. Conditions: see Experimental Section.

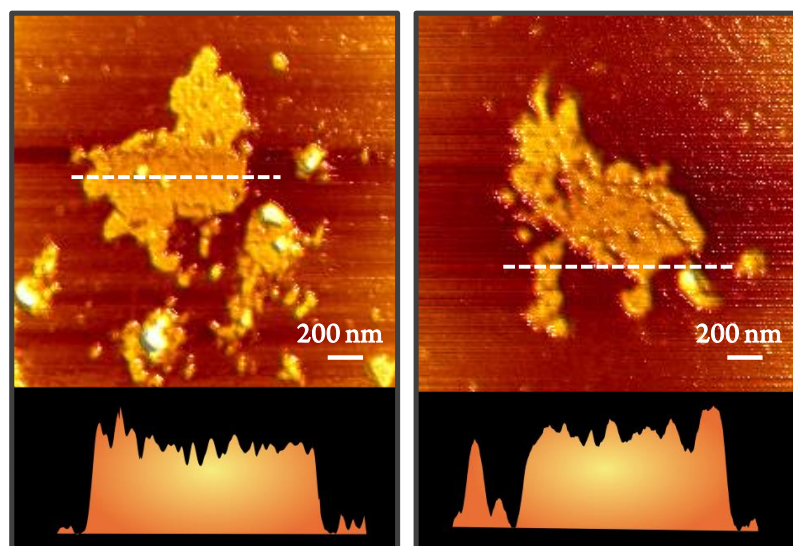


Figure 6. AFM images and the cross-sections along indicated lines of the 2D supramolecular polymers obtained by using method 3. Conditions: see Experimental Section.

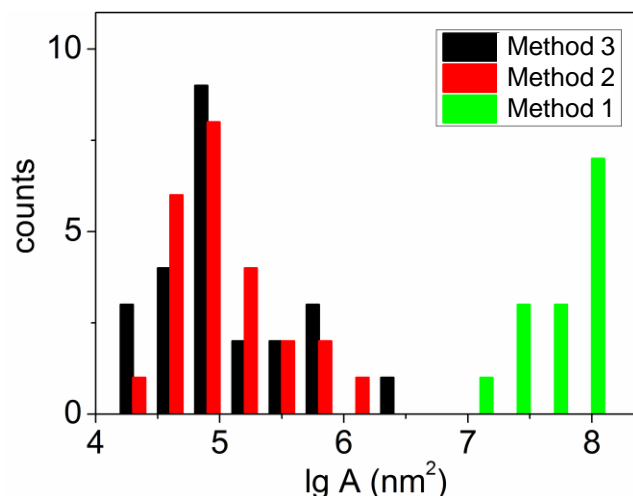


Figure 7. AFM images and the cross-sections along indicated lines of the 2D supramolecular polymers obtained by using method 3. Conditions: see Experimental Section.

4.2 Atomic Force Microscopy (AFM) and Transmission Electron Microscopy studies (TEM)

Detailed information on the morphology of the 2D assemblies was obtained by AFM and TEM techniques (Figures 4-7). The nanosheets formed in aqueous solution were deposited onto APTES modified mica (AFM) or on carbon surface (TEM, see Experimental Section). AFM measurements revealed the formation of 2D assemblies with a constant thickness of 1.9 ± 0.2 nm, irrespective of the method by which polymers were formed. The value correlates with the thickness of a monolayer formed by compact packing of **16Py₃** chain-folded oligomers (Scheme 1B). Most importantly, however, the size of individual nanosheets strongly depends on the preparation procedure. Samples prepared by method 1 consist of sharp-edged sheets with micrometer-scale contour lengths (Figure 4) and the area of single sheets can exceed $100 \mu\text{m}^2$ (Figure 7). Considering that the polymers are only 2 nm thick, an aspect ratio is of $\sim 10^7$ nm. Reports on the formation of noncovalent 2D

formations in solution of similar dimensions and a comparable aspect ratio are rare.^[6,16] In general, nanosheets prepared by method 1 exhibit a highly regular shape and a perfectly uniform thickness. On the other hand, imperfections, such as ruptures, folds and flexures (Figure 4) are also apparent. It is difficult, however, to establish whether these features arise during the deposition of the solution-formed polymers onto the surface, or if they already exist in solution.

Nanosheet prepared by methods 2 or 3 rarely exhibit a surface area exceeding a few μm^2 (Figure 5 and 6), even after several days of aging. Assemblies obtained by method 2 mostly appear as disk-shaped or stick-like (Figure 5) deposits with area dimensions below the square micrometer (see Figure 7). Some of the discs merge and form twin structures but in general individual nanosheets predominate. As seen from the cross-section analysis, the twins are individual aggregates, because overlapping or stapling results in a doubling of the assembly thickness.

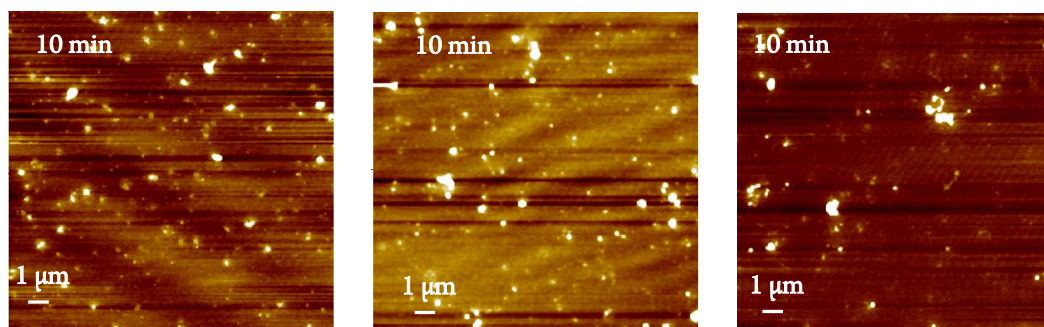


Figure 8. AFM images after 10 min of equilibration.

Nanosheets prepared by method 3 mostly exist as merged clusters of considerably smaller components (Figure 6). AFM analysis of these samples suggests a stepwise formation of 2D polymers formation under isothermal conditions at room temperature (i.e. significantly below T_e). First, a large number of small, ill-defined aggregates are formed quickly after mixing (Figure 8). Over the course of time, rearrangement and merging of small aggregates result in larger formations. This

morphology is a result of the kinetically restricted growth in solution. Similar multistep processes have been reported for the self-assembly of 2D organic crystals under isothermal conditions (see e.g. ref. ^{[[55]]})

Large supramolecular sheets prepared by method 1 and immobilized on APTES mica are easily visible in confocal microscope (CCD camera). The sheets are marked by arrows.

The surface area occupied by one folded **16Py₃** oligomer in the 2D polymer, implying the previously established ladder-type arrangement of pyrenes (Scheme 1B), is calculated to be approximately 1 nm². This value allows a rough estimation of the number of individual trimers in the 2D supramolecular assemblies. While the largest sheets obtained by methods 2 or 3 contain maximally 10⁶ oligomer units, an average sheet prepared by method 1 with a diameter of several micrometers, consists of ~10⁸ pyrenes regularly arranged in the 2D array. Thus, maintaining a slow cooling rate increases the number of molecules in assemblies by 2-3 orders of magnitude. The size distribution of the nanosheets obtained by three different methods is presented in Figure 3D.

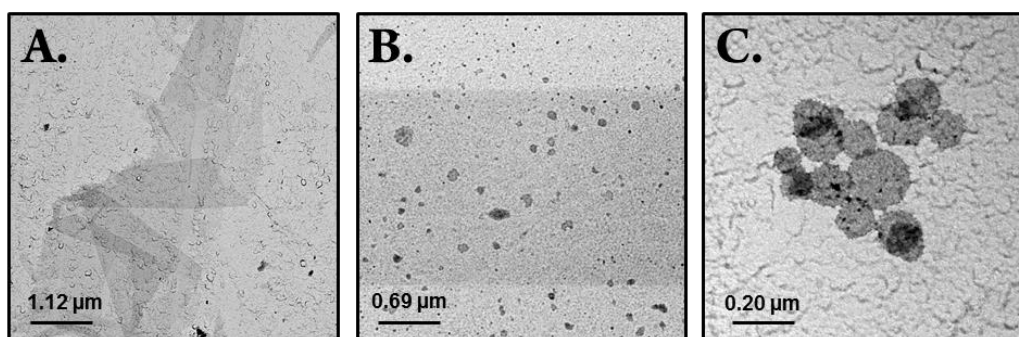


Figure 9. TEM images of nanosheets prepared by method 1 (A), method 2 (B) or method 3 (C). All samples were equilibrated for one day in solution before deposition on carbon surface.

AFM data confirmed the observation made by solution spectroscopy that formation of the nanosheets occurs within minutes. Thus, 2D polymers were

observed in samples taken less than five minutes after their preparation by mixing at room temperature (method 3) or after completing the fast cooling ramp (method 2). 2D assemblies prepared by method 1 could be visualized only after considerably longer times due to the much slower cooling process. Overall, sample preparation by method 1 requires approximately 10 hours rendering conclusions about the time scale of polymer formation under these conditions impossible.

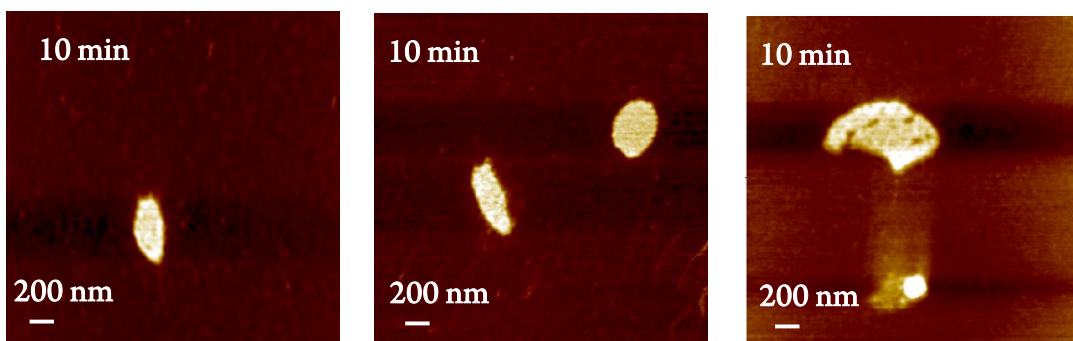


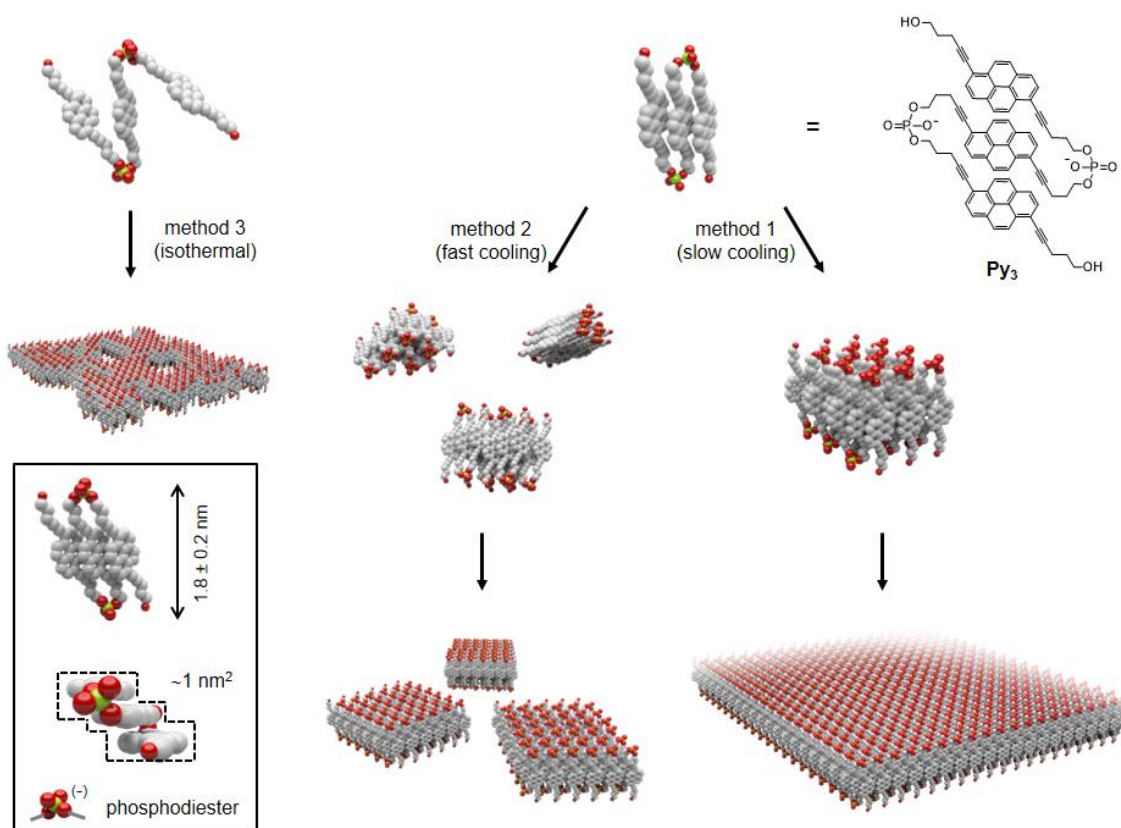
Figure 10. AFM images after 10 min of equilibration.

TEM experiments (Figure 9) complement the results obtained by AFM and they confirm the strong dependence of the size of the sheets on the polymerization conditions. The two-dimensional supramolecular polymers obtained by either method were efficiently adsorbed from aqueous solutions on carbon-coated copper grids. After one day of aging in solution, sheets from method 3 appear as circular objects with a comparably rough surface and a diameter of a few hundreds of nanometers (Figure 9C). The discs tend to associate and form clusters on the carbon surface, which is in line with the clustering observed also by AFM. Assemblies prepared by applying method 2 exist as individual sub-micron sized entities (Figure 4B). In contrast, sheets obtained according to method 1 exhibited considerably larger dimensions (Figure 4A). The values obtained for the surface areas are in agreement with those observed by AFM. Due to their large size, these sheets are often locally plied leading to areas of multiple layers that are visible as darker regions in TEM

pictures (Figure 9A). Due to their large size, polymers formed under conditions of method 1 are even detectable by confocal microscopy.

4.3 Investigation of the self-assembly mechanism

We further analyzed the self-assembly of the **16Py₃** oligomers in the context of cooperative supramolecular polymerization^[38,39] with the goal to correlate the size and appearance of the 2D crystallites with kinetic effects of the nucleation-elongation mechanism.



Scheme 1. Structure of 1,6-bisalkynylsubstituted oligomer **16Py₃** and pathways of supramolecular polymerization of **16Py₃** leading to 2D-arrays with inset showing enlarged aspect of arranged trimers. Box on lower right: calculated dimensions (extension and occupied surface area) of the folded trimer.

The formation of **16Py₃** supramolecular polymers is a multistep process involving intramolecular folding of the oligomer chain and intermolecular assembly of the folded trimer. In the relatively apolar solvent ethanol, the **16Py₃** oligomer exists as a molecularly dissolved chain (Scheme 1) with a high degree of flexibility, generally also described as 'random coil'. When ethanol-dissolved **16Py₃** is added to an aqueous environment at room temperature, as in method 3, the solvent change leads to a rapid aggregation of the hydrophobic pyrenes. The solvent-induced folding of the **16Py₃** leads to the rapid development of the characteristic J- and H-bands in the UV/vis spectrum and the simultaneous drop of the excimer emission intensity. While intramolecular folding of **16Py₃** occurs with a high degree of order, intermolecular assembly of individual trimers occurs very fast at room temperature. This leads to the formation of a large number of nuclei and, consequently, numerous small 2D assemblies. Subsequent clustering of individual small assemblies due to hydrophobic interactions results in the formation of irregular polymers with many defects in the crystallinity of the final nanosheets. AFM and TEM images demonstrate that 2D assemblies prepared by method 3 consist of many small, separate domains.

Two-dimensional sheets prepared by methods 1 or 2 (Scheme 1) appear differently. In these methods, an aqueous solution of **16Py₃** is heated to a temperature above T_e . At 80°C in aqueous environment, the trimers exist – similar as in ethanol at room temperature – as molecularly dissolved strands. Upon cooling, the flexibility of the strands is reduced, the degree of intra-strand folding increases and intermolecular aggregation leads to the formation of nuclei. Once a nucleus is formed, it serves as a hydrophobic template for the addition of further **16Py₃** units. The incorporation of additional units into the growing polymer is thermodynamically favorable and the propagation rate exceeds the dissociation rate. Thus, below T_e , a highly cooperative aggregation process leads to the formation of extended

supramolecular polymers. If the cooling rate is slow (0.1 °C/min, as in method 1), growth of the polymers can be regarded as occurring under thermodynamic control. The number of initially formed nuclei is small. Since the aggregation process is primarily driven by hydrophobic interactions and π -stacking, 2D growth of larger nanosheets (corresponding to the number of pyrenes on the edges of the sheet) is preferential as compared to the growth of small ones. Thus, a few initially formed nuclei will develop into a relatively small number of sheets that are of large size. On the other hand, fast cooling (20 °C/min, method 2) will induce the formation of a larger number of nuclei. Additionally, the growth of the supramolecular polymers does not occur under equilibrium conditions. Added **16Py₃** oligomers bind “irreversibly” to the first encountered nucleus or any growing sheet. As a result, discrimination is much less pronounced than under slow cooling conditions and 2D polymers are formed in larger numbers and smaller sizes. It should be noted that methods 1 and 2 both result in the formation of highly regular 2D polymers with the difference residing only in the size distribution: nanosheets obtained by slow cooling are 2-3 orders of magnitude larger than those obtained by applying a fast cooling rate.

5. Conclusions

We have demonstrated the formation of water soluble 2D supramolecular polymers with an aspect ratio up to 10^7 nm. Using a combination of spectroscopic and microscopic methods, the assembly process of amphiphilic pyrene trimers (**16Py₃**) in water was investigated. The polymerization process follows a highly cooperative nucleation-elongation mechanism. Size and homogeneity of the formed polymers critically depend on the temperature gradient applied during the supramolecular assembly process. A slow temperature gradient (0.1 °C/min) allows

growth of the 2D polymers under conditions that are near thermodynamic equilibrium. The growth of smaller aggregates and the formation of additional nuclei are disfavored, which results in the development of large and highly regular 2D polymers. In contrast, when much larger temperature gradients are applied, **16Py₃** oligomers are assembled onto the growing polymer templates under non-equilibrium conditions. This results in a comparatively larger number of nuclei and, consequently, also a larger number of nanosheets that are considerably smaller in size. Furthermore, polymers formed under isothermal conditions much below T_e appear as small and defect-rich nanosheets.

The findings are especially relevant for the preparation of supramolecular architectures in aqueous environment, which are characterized by complex folding patterns of the individual building blocks. Due to the negatively charged phosphodiester groups, the **16Py₃**-derived sheets are not only water soluble but they appear mostly as free-standing objects because of electrostatic repulsion between individual sheets.

6. Experimental part

TEM measurements. Experiments were performed on a FEI Morgagni 268 using an operating voltage of 80 kV. Sample preparation: a 5 μ L aliquot of the 2 μ M **16Py₃** solution obtained by any of the methods described above was placed on a carbon-coated grid (S160-3, 300 mesh Cu, AgarScientific). After 5 min, the remaining solution was blotted with a filter paper and of Milli-Q water (5 μ L) was added. After 1 min, the water was blotted and 0.8 % aqueous uranyl acetate (2 μ L) was added, which was blotted again after waiting for 30 sec. After repeating the uranyl staining procedure once again, the sample was used for the measurements.

AFM measurements. AFM imaging was performed under ambient conditions in air with a Nanosurf FlexAFM (Nanosurf AG, Switzerland) instrument using a $100 \times 100 \mu\text{m}^2$ (optimal for the nano-sheets obtained with Method 1) or a $10 \times 10 \mu\text{m}^2$ scanning head depending on the size of the 2D assemblies. The measurements were carried out in tapping mode employing either PPP-NCHR-W cantilevers from Nanosensors (resonance frequency ~ 280 kHz, tip radius ~ 10 nm) or Tap190Al-G from BudgetSensors (resonance frequency ~ 190 kHz, force constant 48 N/m). Both types of cantilevers gave reproducible results. Sample preparation: a $15 \mu\text{L}$ aliquot of the $2 \mu\text{M}$ **16Py₃** obtained by any of the methods described above was placed on an APTES-modified mica plate ($20 \times 20 \text{mm}^2$). The mica plates were fixed on a holder and used for AFM studies. After 5 min, the plate was rinsed with Milli-Q water (2 ml total volume) and dried under a stream of Ar for 30 sec.

Confocal microscopy. Confocal images were obtained using a LabRam HR800 confocal microprobe Raman system (HORIBA Jobin Yvon).

Spectroscopic studies

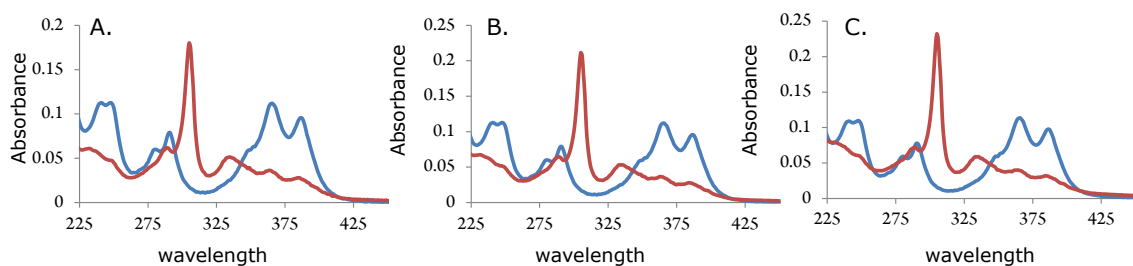


Figure 11. Temperature-dependent UV/vis spectra of disassembly of **16Py₃**-derived aggregates after 1 day of aging. This period of time is enough to ensure reaching of constant sizes of 2D assemblies (the range of values depends on preparation procedure). The equilibrated at 20°C (red) samples were heated to 80°C (blue). The spectroscopic data at 80°C were acquired after 15 min after reaching the temperature in thermostat. The typical for the stacked pyrenes spectra, characterized by a vibronic structure, are restored. The data suggest that the temperature-dependent dissociation process is fast, and occurs in several minutes. Figure A – method 1, Figure B – method 2, Figure C- method 3.

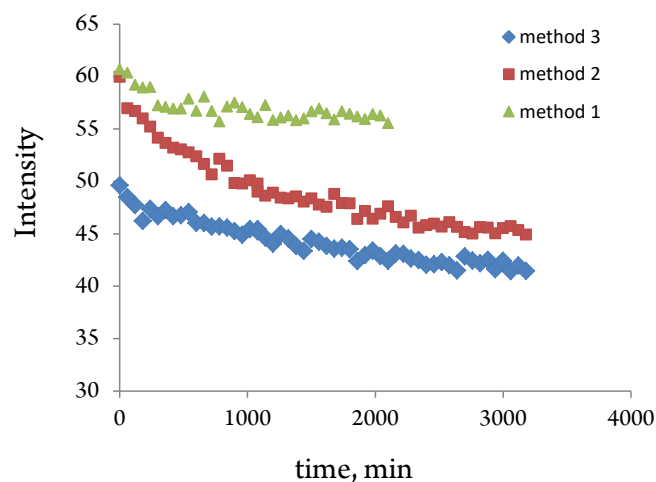


Figure 12. Time-dependent fluorescence at 20°C (monitored at 520 nm, excitation 365 nm). The starting point ($t = 0$ min) for method 3 corresponds to the addition of an aliquot from the stock solution, for method 2 and method 1 $t = 0$ min is defined as the end of the annealing step.

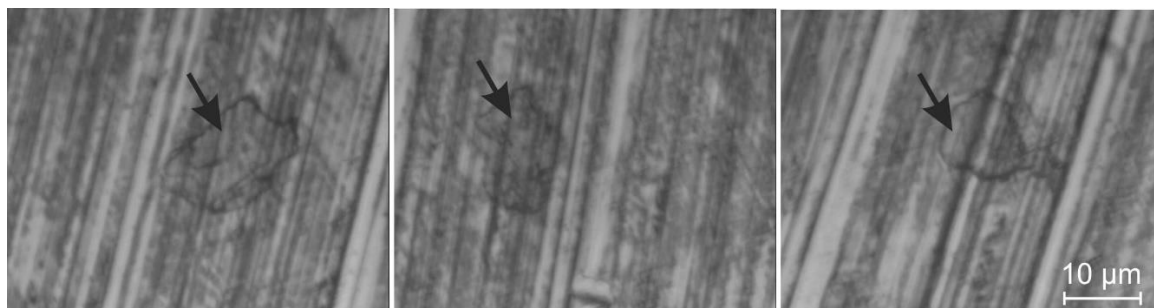


Figure 13. Confocal microscopy images of nanosheets (Method 1).

7. References

- [1] S. I. Stupp, L. C. Palmer, *Chem. Mater.* **2014**, *26*, 507.
- [2] K. Liu, Y. Kang, Z. Wang, X. Zhang, *Adv. Mater.* **2013**, *25*, 5530.
- [3] P. A. Korevaar, T. F. De Greef, E. W. Meijer, *Chem. Mater.* **2014**, *26*, 576.
- [4] M. R. Molla, S. Ghosh, *PhysChemChemPhys* **2014**, *16*, 26672.
- [5] T. Govindaraju, M. B. Avinash, *Nanoscale* **2012**, *4*, 6102.
- [6] J. Sakamoto, J. van Heijst, O. Lukin, A. D. Schlüter, *Angew. Chem. Int. Ed.* **2009**, *48*, 1030.

- [7] A. R. Aiyar, J. I. Hong, E. Reichmanis, *Chem. Mater.* **2012**, *24*, 2845.
- [8] C. Shahar, J. Baram, Y. Tidhar, H. Weissman, S. R. Cohen, I. Pinkas, B. Rybtchinski, *ACS Nano* **2013**, *7*, 3547.
- [9] T. Kudernac, S. Lei, J. A. Elemans, S. De Feyter, *Chem. Soc. Rev.* **2009**, *38*, 402.
- [10] H. Lim, S. I. Yoon, G. Kim, A. R. Jang, H. S. Shin, *Chem. Mater.* **2014**, *26*, 4891.
- [11] A. S. Weingarten, R. V. Kazantsev, L. C. Palmer, M. McClendon, A. R. Koltonow, A. P. Samuel, D. J. Kiebal, M. R. Wasielewski, S. I. Stupp, *Nat. Chem.* **2014**, *6*, 964.
- [12] X. Zhang, Y. Xie, *Chem. Soc. Rev.* **2013**, *42*, 8187.
- [13] F. Bonaccorso, L. Colombo, G. Yu, M. Stoller, V. Tozzini, A. C. Ferrari, R. S. Ruoff, V. Pellegrini, *Science* **2015**, *347*, 1246501.
- [14] M. E. Canas-Ventura, K. Ait-Mansour, P. Ruffieux, R. Rieger, K. Müllen, H. Brune, R. Fasel, *ACS Nano* **2011**, *5*, 457.
- [15] J. W. Colson, W. R. Dichtel, *Nat. Chem.* **2013**, *5*, 453.
- [16] K. T. Nam, S. A. Shelby, P. H. Choi, A. B. Marciel, R. Chen, L. Tan, T. K. Chu, R. A. Mesch, B. C. Lee, M. D. Connolly, C. Kisielowski, R. N. Zuckermann, *Nat. Mater.* **2010**, *9*, 454.
- [17] Y. Zheng, H. Zhou, D. Liu, G. Floudas, M. Wagner, K. Koynov, M. Mezger, H. J. Butt, T. Ikeda, *Angew. Chem. Int. Ed.* **2013**, *52*, 4845.
- [18] B. Yu, X. Jiang, J. Yin, *Macromolecules* **2014**, *47*, 4761.
- [19] L. Zhang, T. Y. Zhou, J. Tian, H. Wang, D. W. Zhang, X. Zhao, Y. Liu, Z. T. Li, *Polym. Chem.* **2014**, *5*, 4715.
- [20] T. Jiang, C. Xu, Y. Liu, Z. Liu, J. S. Wall, X. Zuo, T. Lian, K. Salaita, C. Ni, D. Pochan, V. P. Conticello, *J. Am. Chem. Soc.* **2014**, *136*, 4300.

- [21] H. Liu, C. H. Hsu, Z. Lin, W. Shan, J. Wang, J. Jiang, M. Huang, B. Lotz, X. Yu, W. B. Zhang, K. Yue, S. Z. Cheng, *J. Am. Chem. Soc.* **2014**, *136*, 10691.
- [22] Z. Wang, N. Su, F. Liu, *Nano Lett.* **2013**, *13*, 2842.
- [23] T. Y. Zhou, F. Lin, Z. T. Li, X. Zhao, *Macromolecules* **2013**, *46*, 7745.
- [24] M. J. Kory, M. Wörle, T. Weber, P. Payamyar, S. W. van de Poll, J. Dshemuchadse, N. Trapp, D. A. Schlüter, *Nat. Chem.* **2014**, *6*, 779.
- [25] P. Kissel, D. J. Murray, W. J. Wulftange, V. J. Catalano, B. T. King, *Nat. Chem.* **2014**, *6*, 774.
- [26] K. Baek, G. Yun, Y. Kim, D. Kim, R. Hota, I. Hwang, D. Xu, Y. H. Ko, G. H. Gu, J. H. Suh, C. G. Park, B. J. Sung, K. Kim, *J. Am. Chem. Soc.* **2013**, *135*, 6523.
- [27] S. Schrettl, C. Stefaniu, C. Schwieger, G. Pasche, E. Oveisi, Y. Fontana, A. Morral, J. Reguera, R. Petraglia, C. Corminboeuf, G. Brezesinski, H. Frauenrath, *Nat. Chem.* **2014**, *6*, 468.
- [28] L. Liu, Y. Xia, J. Zhang, *RSC Adv.* **2014**, *4*, 59102.
- [29] X. H. Liu, C. Z. Guan, D. Wang, L. J. Wan, *Adv. Mater.* **2014**, *26*, 6912.
- [30] R. K. Roy, E. B. Gowd, S. Ramakrishnan, *Macromolecules* **2012**, *45*, 3063.
- [31] T. Aida, E. Meijer, S. I. Stupp, *Science* **2012**, *335*, 813.
- [32] B. Sanii, R. Kudirka, A. Cho, N. Venkateswaran, G. K. Olivier, A. M. Olson, H. Tran, R. Harada, L. Tan, R. N. Zuckermann, *J. Am. Chem. Soc.* **2011**, *133*, 20808.
- [33] Y. Tidhar, H. Weissman, D. Tworowski, B. Rybtchinski, *Chem.-Eur. J.* **2014**, *20*, 10332.
- [34] G. Rizis, T. G. van de Ven, A. Eisenberg, *Angew. Chem. Int. Ed.* **2014**, *53*, 9000.
- [35] T. Ikeda, *Langmuir* **2014**, *31*, 667–673.
- [36] M. Vybornyi,; A. V. Rudnev, S. M. Langenegger, T. Wandlowski, G. Calzaferri, R. Häner, *Angew. Chem. Int. Ed.* **2013**, *52*, 11488.

- [37] F. M. Winnik, *Chem. Rev.* **1993**, *93*, 587.
- [38] P. Jonkheijm, P. van der Schoot, A. P. H. J. Schenning, E. W. Meijer, *Science* **2006**, *313*, 80.
- [39] C. Kulkarni, S. Balasubramanian, S. J. George, *ChemPhysChem* **2013**, *14*, 661.

CHAPTER IV. HYDRODYNAMIC AND THERMOPHORETIC EFFECTS ON THE SUPRAMOLECULAR CHIRALITY OF PYRENE-DERIVED NANOSHEETS

Published: Micali, N.; Vybornyi, M.; Mineo, P.; Khorev, O.; Häner, R.; Villari, V.
Chem.-A Eur. J. **2015**, *21*, 9505.

1. Abstract

Chiroptical properties of two-dimensional (2D) supramolecular assemblies (nanosheets) of achiral, charged pyrene trimers (**16Py₃**) are efficiently rendered chiral by asymmetric physical perturbations. Chiral stimuli in a cuvette can originate either from controlled temperature gradients or by very gentle stirring. The chiroptical activity strongly depends on the degree of supramolecular order of the nanosheets, which is easily controlled by the method of preparation. The high degree of structural order ensures strong cooperative effects within the aggregates, rendering them more susceptible to external stimuli. The samples prepared using slow thermal annealing protocols are both CD and LD active (in stagnant and stirred solutions), whereas for isothermally aged samples chiroptical activity was in all cases undetectable. In the case of temperature gradients, the optical activity of 2D assemblies could be recorded for a stagnant solution due to migration of the aggregates from the hottest to the coldest regions of the system. However, a considerably stronger exciton coupling, coinciding with the J-band of the interacting pyrenes, is developed upon subtle vortexing (0.5 Hz - 30 rpm) of the aqueous solution of the nanosheets. The sign of the exciton coupling is inverted upon switching between clockwise and counter-clockwise rotation. The supramolecular chirality is evidenced by the appearance of CD activity. To exclude artefacts from proper CD spectra, the contribution from LD to the observed CD was determined.

The data suggest that the aggregates experience asymmetrical deformation and alignment effects due to the presence of chiral flows.

2. Introduction

The origin of homochirality on our planet remains a mystery. In order to explain this fascinating phenomenon, it is vital to understand the consequences of mutual interactions between asymmetric physical perturbations and soft matter.^[1] The fascinating capability to imprint the chiral information by external physical fields on the supramolecular level^[2,3] holds great promise for the advancement of asymmetric synthesis^[4] and chiral sensing.^[5] Therefore, among various truly chiral physical fields, special attention is devoted to the hydrodynamic vortices^[6,7] and convective flows.^[8] Indeed, in seminal studies,^[9,10] the supramolecular chirality of assemblies of achiral porphyrins was triggered via exerting chiral flows. Further intriguing findings on induced supramolecular chirality have received different explanations^[11,12] and stimulated elaboration of novel techniques for a reliable probing of chiral effects.^[13] Despite certain discrepancy of interpretations, the generally accepted fact is that chiral flows are responsible for the observed CD/LD activity.^[14,15]

One of the most challenging aspects in the field of supramolecular chirality is a rational interpretation of how the size and dimensions of the self-assembled entities experiencing a chiral perturbation influence the phenomenon of optical activity.^[16-18] Both detection and induction of such chiroptical properties in the intentional absence of a chemical bias have been studied intensely over the past years.^[15,19] However, very few researchers paid sufficient attention to the preparation methodology and correlation of the chiroptical response with final morphology of self-assemblies.^[20] Recently, it has been shown that the pathway

complexity of aggregation of the classic TPPS porphyrin influences the final chiroptical response.^[21]

We previously described the induction of supramolecular chirality in one-dimensional assemblies by attachment of a chiral auxiliary.^[22-24] Here, we report on the triggering and control of supramolecular chirality either by applying hydrodynamic or thermophoretic forces in two-dimensional (2D) pyrene-based self-assembled materials.^[25,26] Although 2D organic polymers have been extensively studied,^[27-30] the data on chiroptical properties of 2D architectures remain extremely rare.^[31,32] It has been demonstrated that a supramolecular sheet could be intrinsically chiral^[33] due to deformations which could lead to tubular assemblies.^[34] In the absence of external perturbations such deformations would lead to a racemic mixture. The **16Py₃**-derived 2D supramolecular assemblies reported here reveal the first example of chiral induction, appearing as an exciton coupled signal, by hydrodynamic or thermophoretic effects on the pyrene-bearing supramolecular constructs.

The kinetics of self-assembly determine the final structure of the aggregates.^[35] Independent of the preparation procedure, the trimer **16Py₃** self-assembles into 2D supramolecular structures in an aqueous environment. However, distinct differences of the molecular organization are observed for the **16Py₃** units within 2D formations. We therefore postulate that supramolecular organization and size of aggregates influence supramolecular chirality. It is assumed that the torque effect on 2D supramolecular particles, caused by the asymmetric physical perturbation, dominates over Brownian motion effects. Very few experimental and theoretical studies,^[36-38] aimed at showing this correlation more quantitatively, exist. So far, all have dealt with hydrodynamic vortices, i.e., macroscopic flows in the solution. Herein we attempt to compare the effects of the hydrodynamic perturbation

with that of the thermophoretic chiral force^[39] (which acts only on the aggregates when the solvent is not stirred), and to determine experimentally the role of the aggregate constitution in supramolecular chirality response to these external fields. The chiroptical response of the different types of aggregates to the asymmetric field generated by hydrodynamic and thermophoretic forces is evaluated with circular (CD) and linear dichroism (LD) measurements. Along with the quantification of the linear birefringence of the system, this allows us to determine artifact-based CD activity. To correlate the spectroscopic readout with the structural properties of the 2D self-assemblies, the size and morphology of the aggregates are analyzed by UV/vis spectroscopy, as well as dynamic and static light scattering, and AFM. Finally, we propose a model in which soft supramolecular structures could behave as flexible modules, which are deformed by subtle mechanical stimuli.^[40]

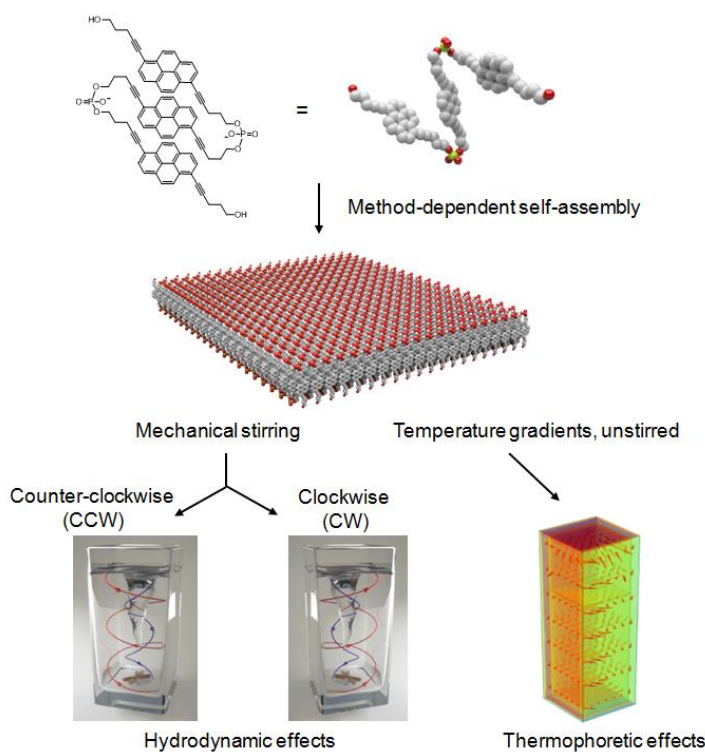
3. Results and Discussion

3.1 Morphological properties

It has been previously shown that the trimer **16Py₃** self-assembles in aqueous environment^[26] to form 2D supramolecular aggregates (Scheme 1). The supramolecular organization—and thus the morphology—of the nanosheets is considerably influenced by the specific procedure used for preparation. AFM visualization reveals that the deposited and dried 2D supramolecular constructs, prepared using **method 3** (for more information on methods see Chapter III), are sheetlike and exist as agglomerates of smaller individual aggregates (Figure 1A); therefore, the degree of internal order is low. The 2D structures prepared using **method 2** form an elongated planar shape (Figure 1B), whereas **method 1** of

preparation results in larger aggregates with micron-size scale length and ~ 2 nm thickness (Figure 1C).

However, for the latter method immaculate planar nanosheets are rarely observed. After deposition on the surface, these 2D aggregates appear with evident deformities such as folds, ruptures and flexures. When several sheets are overlaid, the thickness of 2 nm determined for each separate level remains constant. These data imply that the nanosheets are very sensitive to mechanical stress and that the observed structural properties are due to mechanical forces. The results below suggest that the observed structural features can originate from a relatively flexible structure of the sheets, which is an inherent property of supramolecular systems. As a consequence, applying a mechanical force, such as stirring, could lead to reversible configurational changes in the **16Py₃**-derived supramolecular polymers, as well as to interactions between aggregates in aligned flows.



Scheme 1. Structure of the **16Py₃** trimer, its assembly into 2D supramolecular polymers, and illustration of hydrodynamic and thermophoretic effects.

To correlate the supramolecular organization with the chiroptical properties of the aggregates in solution, different scattering techniques were used to investigate the morphology directly in the aqueous medium. Irrespective of the method of preparation, aggregates of **16Py₃** formed in aqueous buffer are able to significantly depolarize the incident light. The depolarization ratio is about 0.08, which is consistent with the existence of J-aggregates in which strong exciton coupling between monomers causes anisotropy in the polarizability tensor, and is analogous to what is observed for J-aggregates of porphyrins.^[41]

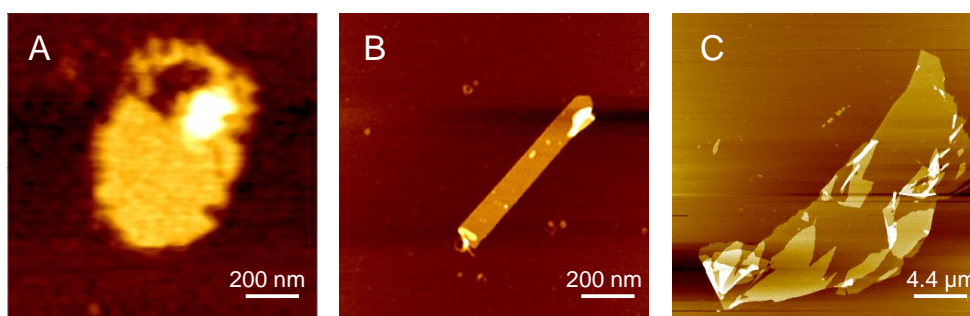


Figure 1. AFM images of the nanosheets prepared by **method 1** (A), **method 2** (B), **method 3** (C). For details see Experimental Section.

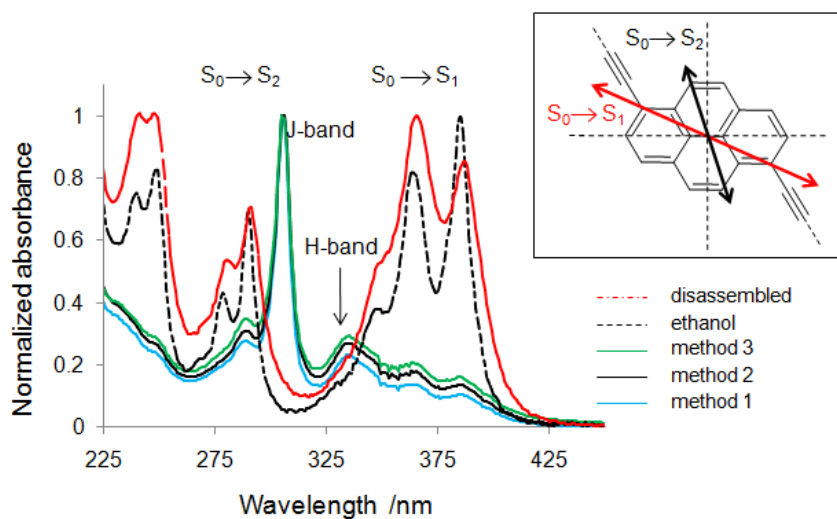


Figure 2. Normalized UV/vis spectra for the 3 μM non-aggregated **16Py₃** in pure ethanol (black, dashed) at 20 $^{\circ}\text{C}$, and disaggregated in aqueous solution (red, dot-dashed) at 80 $^{\circ}\text{C}$, and for the aggregated **Py₃** in aqueous solution at 20 $^{\circ}\text{C}$ prepared by different procedures (**method 3** - blue, **method 2** - black, **method 1** - green). Inset: calculated transition dipole moments for the 1,6-bisalkynylsubstituted pyrene.^[26] Conditions for aqueous mixtures: see Experimental Section.

Figure 2 shows that the absorption spectra for all samples display an intense, narrow band at 305 nm, significantly red-shifted with respect to the monomer band of the $S_0 \rightarrow S_2$ transition located at 290 nm when measured in pure ethanol.^[26] A low-intensity, blue-shifted band, assigned to H-type coupling of the $S_0 \rightarrow S_1$ transition, appears at 335 nm (Figure 2). While samples prepared by any of the three methods show very similar UV/vis absorption spectra, all other investigated properties vary greatly depending on the preparation method.

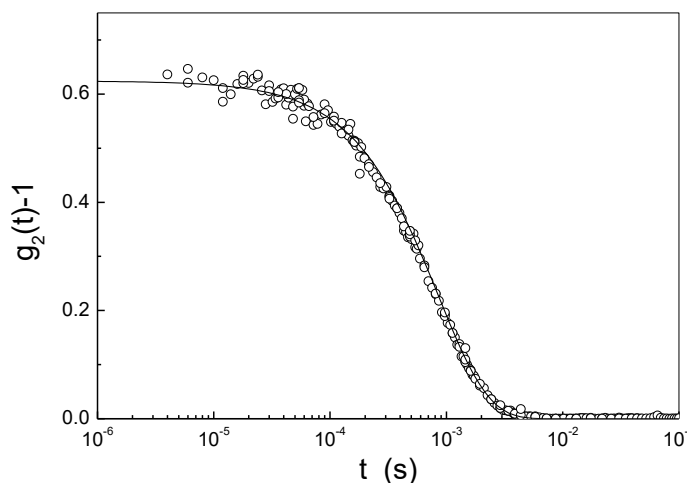


Figure 3. Intensity autocorrelation function collected for the buffered solvent. The decay rate is due to nano-domains of ethanol having different index of refraction with respect to water. As reported in the literature, these domains are characterized as almost spherical discrete regions in the aqueous buffer. A fit of the intensity autocorrelation function with an exponential law (continuous line) furnish a hydrodynamic radius of about 150 nm with a very low size polydispersity ($\sim 5\%$). The size of the nano-domains keeps constant, at least within one month.

Before discussing the scattering data obtained with **16Py₃** polymer solutions, it is important to note that ethanol does not dissolve and mix with water at a molecular level in aqueous buffered solvent, but rather occurs as nano-domains with a hydrodynamic radius of about 150 nm (Figure 3). This observation has been reported in the literature for ethanol and other organic solvents.^[42]

For a **16Py₃** polymer solution obtained by **method 3**, the slope of the decay rate (Γ_w) of the polarized correlation function gives a hydrodynamic radius of about

130 nm (with a size polydispersity of $\pm 5\%$), which is very close to the value of the nano-domains of pure ethanol in buffer. Since the amount of ethanol is not negligible, the polarized part of the scattered light could be due to the diffusion of both ethanol nano-domains and **16Py₃** aggregates. Therefore, in order to measure only the aggregate dynamics, the depolarized intensity autocorrelation function was also collected. The slope of the polarized (Γ_W) and depolarized (Γ_{VH}) decay rates, and thus the diffusion coefficient, is the same (Figure 4).

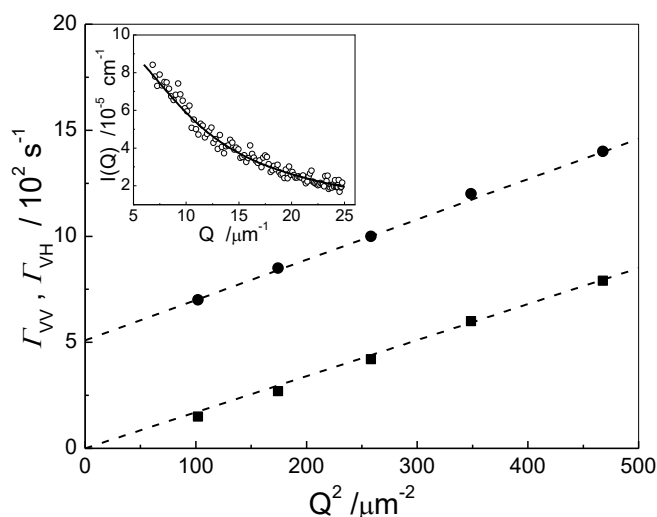


Figure 4. Polarized (squares) and depolarized (circles) relaxation rates measured at 20 °C for the solution of **16Py₃** aggregates prepared using **method 3**. The dashed lines are the linear fit whose slope gives the translational diffusion coefficient; the y-axis intercepts give the rotational diffusion coefficient (see the Experimental Section). The inset shows the total scattered intensity at 20 °C along with the fit (continuous line) obtained by using the homogeneous sphere form factor. Conditions: see Experimental Section.

This suggests that the **16Py₃** aggregate grows inside the ethanol nano-domain due to local confinement. It is reasonable to consider that ethanol plays a significant role in the aggregates formation by protecting them from contact with water.

The translational and rotational diffusion coefficients obtained from the fit of data in Figure 4 are consistent with a slightly anisotropic shape of the aggregates,

likely a prolate ellipsoid. These data are analysed in terms of Perrin's model (Experimental section) which gives the minor semiaxis of the prolate ellipsoid a value of 50-100 nm and the major semiaxis a value of about 150 nm. To assert the consistency of this model, we compare the hydrodynamic radius calculated by using the value of the ellipsoid semiaxes (110-130 nm) with the measured one (130 nm). Alternatively, the total scattered intensity profile can be fitted according to the simpler homogeneous sphere model after subtraction of the profile measured for the buffer alone (Figure 4, inset), giving an aggregate radius of about 110 nm. The small discrepancy with the conformation deduced from the dynamic properties could be due to the moderate shape anisotropy of the aggregates.

Conditions used in **method 3** imply that the preparation of the supramolecular constructs occurs under kinetic control. Therefore, kinetically-trapped states arise from ill-defined seeds formed at early stages of the aggregation. On the other hand, during cooling from 80 °C to 20 °C (**methods 1** and **2**), the self-assembly of **16Py₃** follows a nucleation-elongation mechanism. The internal ordering of nuclei is important, since it imposes the supramolecular organization of the final aggregates.^[18] As confirmed by UV/vis, heating the sample to 80 °C enables disassociation of the kinetically-trapped seeds (Figure 2).

For the aggregates formed via fast cooling to 20 °C (**method 2**), the polarized and depolarized decay rates (Figure 5) indicate a significantly larger hydrodynamic radius of 230 nm ($\pm 5\%$ size polydispersity). The prolate ellipsoid model shows that the aggregates take a much more elongated shape, with a length of about 1 μm , while the thickness remains almost the same as observed in **method 3** (50-100 nm). Such morphology is retained after deposition, as indicated by AFM data on mica (Figure 1). Also the total scattered intensity profile (Figure 5, inset) seems to agree with this picture, because the homogeneous sphere model does not

fit with the data, whereas the form factor of a homogeneous prolate ellipsoid reproduces better, even if not so well, the profile and gives a minor semiaxis of about 80 nm and length of about 1.4 μm .

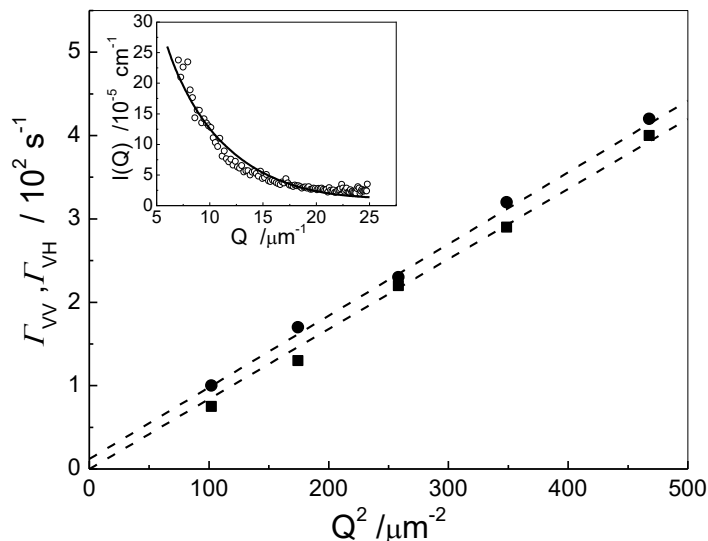


Figure 5. Polarized (squares) and depolarized (circles) relaxation rates measured at 20 °C for the solution of **16Py₃** aggregates prepared using **method 2**. The dashed lines are the linear fit result. The inset shows the total scattered intensity at 20 °C along with the fit (continuous line) obtained by using the homogeneous prolate ellipsoid form factor. Conditions: see Experimental Section.

In **method 1** the cooling ramp is controlled, and annealing of molecularly dissolved **16Py₃** chains occurs from 80 to 20 °C slowly (0.1 °C/min). As demonstrated by scattering results, aggregation kinetics give rise to two families of aggregates whose dynamics occur at two separate time-scales: the smaller aggregates display a diffusion dynamics from which a hydrodynamic radius of about 120 nm is extracted (data not shown); the larger aggregates follow the Q^3 - rather than Q^2 -dependence expected for a rigid diffusing entity, indicating that their hydrodynamic radius is so large (micrometric) that, in the Q range investigated, dynamics are governed by internal motions (Figure 6). Micron-sized aggregates of **16Py₃** are also observed by AFM.

It has to be stressed that large intensity fluctuations are caused by the presence of these large aggregates, so that data are very noisy, and therefore only the polarized geometry was adopted. This limitation does not allow us to conclude about the origin of the smaller species, namely if they are empty ethanol nano-domains or more stable **16Py₃** aggregates. Due to the micrometric size of the larger aggregates the approach by light scattering at small angle (SALS) is more appropriate. The size distribution obtained from the scattered intensity at a small angle is reported in the inset of Figure 6, and shows that the average aggregate size is about 3 μm .

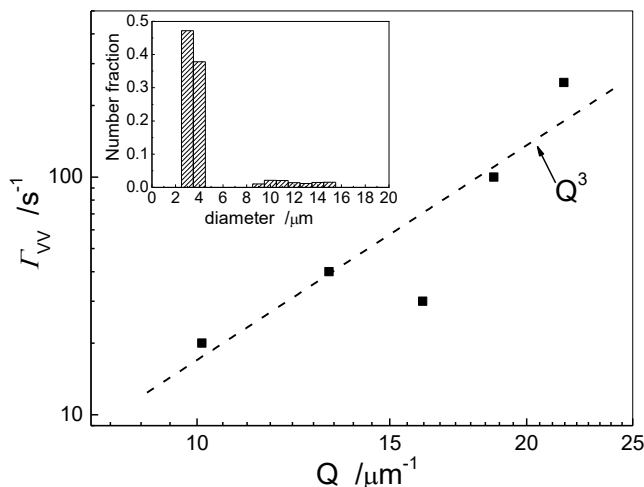


Figure 6. Log-log plot of the polarized relaxation rate measured at 20 °C for the solution of **16Py₃** aggregates (larger family) prepared using **method 1**. The dashed line represents the Q^3 dependence. The inset shows the number-weighted size distribution obtained by the SALS profile. Conditions: see Experimental Section.

Regardless of the method used, both static and dynamic properties are independent from temperature in the range of 20-35 °C. In particular, dynamic properties simply correlate with water viscosity (Figure 7).

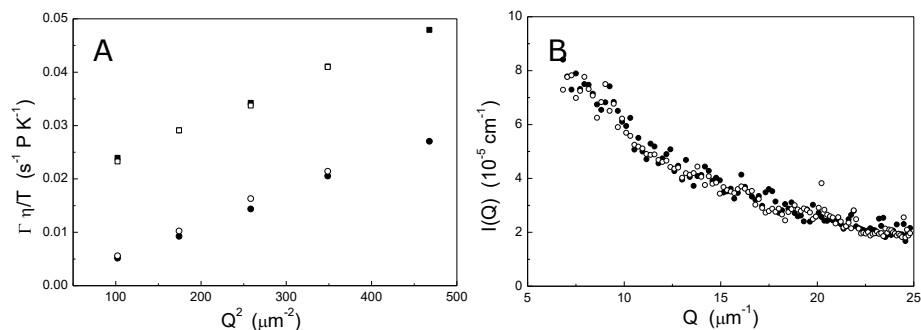


Figure 7. A) Decay rate of the polarized (circles) and depolarized (squares) intensity autocorrelation function corrected for temperature and solvent viscosity (at 20°C, full symbols and 35°C, open symbols). B) Total scattered intensity profile at 20°C and 35°C (same symbols as in A). The data refer to the **16Py₃** solution obtained with method 1.

3.2 Supramolecular optical activity and alignment effects

The microscopic and scattering studies clearly demonstrate that the supramolecular^[43] organization of **16Py₃**-derived 2D aggregates depends on the preparation procedures. To probe the supramolecular chirality response of different **16Py₃** aggregates to external asymmetrical fields, the chiral perturbations were generated through temperature gradients or hydrodynamic vortexes. The correlative CD and LD measurements allow us to evaluate the chiral properties of the 2D aggregates.

Temperature gradients are produced by the different temperature along the cuvette's walls from top to bottom. Such gradients generate the vortical motion of the aggregates alone (without stirring) through the resulting chiral thermophoretic force.^[39] The strength of the gradient, and its disappearance, is efficiently controlled by a home-made thermostat system, and it has been checked that all samples (methods 1-3) are completely CD and LD silent in the absence of the temperature gradient, irrespective of the thermostat setting (Figure 8). These data reveal the dramatic impact of minute temperature gradients (and soft chiral flows) on originally racemic supramolecular objects.

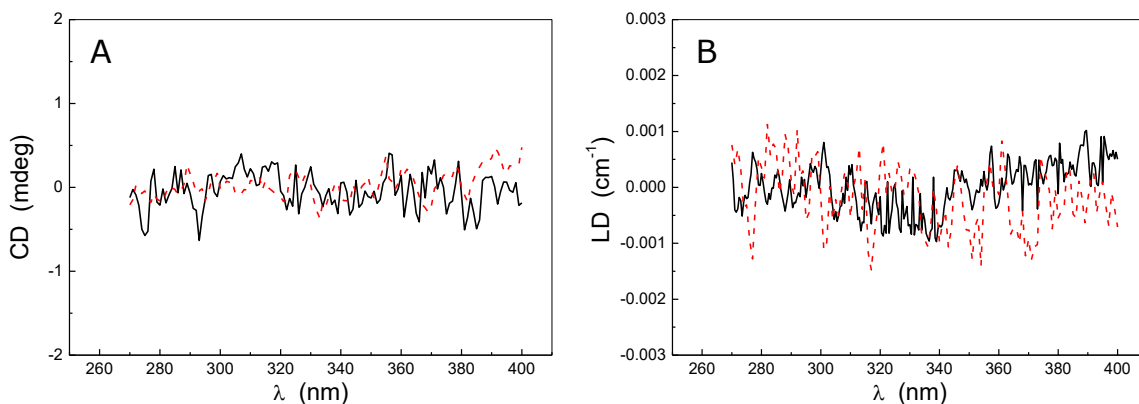


Figure 8. CD (plot A) and LD (plot B) spectra for the **16Py₃** solution obtained by method 3, in the absence of a temperature gradient, at different temperature value set by the thermostat (20°C continuous line, 35°C dashed line). These results prove that CD and LD signals do not depend on the temperature value but on the strength of the temperature gradient.

The **16Py₃**-based supramolecular assemblies prepared by methods 1-3 display distinct responses to the same asymmetric perturbations. Thus, aggregates obtained by **method 3** do not produce CD or LD signals in any of the conditions investigated (Figure 9). Again, this sample exhibits the lowest degree of supramolecular order compared to other preparation procedures. The relative orientations of the individual **16Py₃**-containing domains within the larger planar agglomerates are irregular and with well-distinguishable merging edges. The defect-rich supramolecular organization of the nanosheets leads to lack of chiroptical sensitivity towards asymmetric perturbations. The relative orientation of the transition dipole moments becomes irregular, and produces a zero net effect both for CD and LD signals even upon stirring.

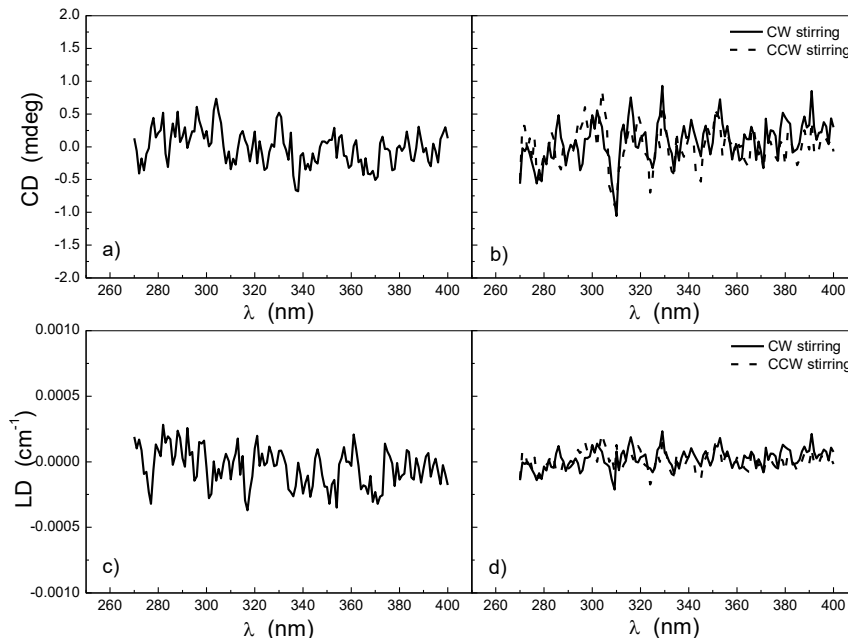


Figure 9. CD (a, b) and LD (c, d) spectra for the solution of **16Py₃** aggregates prepared by method 1 under temperature gradient (plots a and c) and under clockwise (CW) and counter-clockwise (CCW) stirring at 0.5 Hz (plots b and d). The sample is CD and LD silent either upon applying of different temperature gradient strengths or upon stirring at 0.5 Hz.

The AFM morphological studies on the surface and the scattering data in solution for **16Py₃** assemblies prepared by **method 2** are in good agreement with the chiroptical properties described below. A small bisignate CD signal (~ 1 mdeg), centered at 305 nm (coincides with the maximum absorption of the aggregated **16Py₃**), rises under temperature gradients (Figure 10A). It is noteworthy that these aggregates are unchanged by variable strengths of the temperature gradients, probably because the average size of aggregates is still small and the corresponding CD signal is too weak for measuring its dependence on weak asymmetrical fields like those generated by the thermophoretic effect under the temperature gradient.

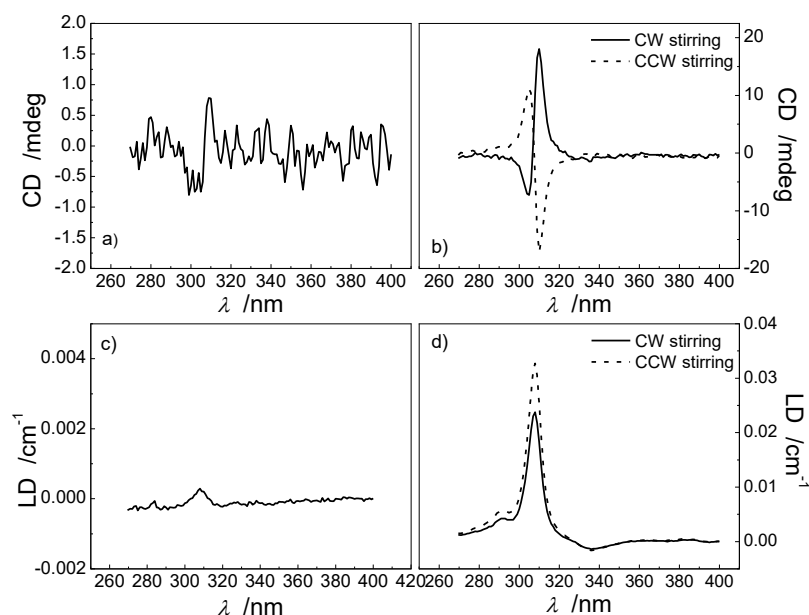


Figure 10. CD (a, b) and LD (c, d) spectra for the solution of **16Py₃** aggregates prepared using **method 2** under temperature gradient (plots a and c) and under CW and CCW stirring at 0.5 Hz (plots b and d). No significant differences appear under different temperature gradient strengths. Conditions: see Experimental Section.

However, very gentle stirring (0.5 Hz) of the solution gives rise to the exciton-coupled CD signals, whose sign depends on the stirring sense (Figure 10B). The clockwise (CW) rotation of the solution leads to a positive sign of the couplet, and counter-clockwise (CCW) gives rise to a negative signal. After turning off the stirring, the signal disappears gradually. Such behavior is an indication that vortex-induced chirality in our case does not belong to a family of symmetry-breaking events, but to enantiomeric enrichment. Also, under temperature gradients, an LD signal for the aggregated species appears with a maximum at 305 nm, but its intensity is relatively small ($\sim 2.5 \times 10^{-4} \text{ cm}^{-1}$) (Figure 6C) and remains constant upon change of the gradient strength. This observation resembles some previous data on LD of the supramolecular constructs in the absence of mechanical perturbations.^[3] The LD signal becomes more intense ($\sim 0.025 \text{ cm}^{-1}$) as a result of the hydrodynamic vortex, which is generated by the stirring at 0.5 Hz (Figure 10D). The LD signal at

305 nm is always positive, but the intensity is slightly dependent on the stirring sense (CW or CCW). The CCW rotation leads to a more intense signal.

It is worth noting that another band appears upon stirring at 335 nm in the LD spectrum with the opposite sign with respect to that at 305 nm, and it is considerably less intense. Probably, this signal is also present in an unstirred solution, but, due to the sensitivity of the method, it is undetectable. The shape of LD spectra under stirring is an indication that the dipole moments associated with these electronic transitions are mutually orthogonal, so that the band at 335 nm appears due to H-aggregates of **16Py₃** (Figure 2, inset). Because this band occurs at a longer wavelength than for that of the J-aggregates of **16Py₃**, this observation confirms previous conclusions that such J- and H-types of bands originate from the dual exciton coupling of consecutive first and second electronic transitions. Due to the lower molar extinction coefficient or close to parallel orientation of the transition dipole moments within the H-aggregates, no CD bands are detectable at this wavelength.

Since the CD spectra could be contaminated by the alignment effects of the aggregates, the reliable evaluation of artefacts becomes extremely important.^[44] The LD contribution to the CD signal is negligible (less than 5%) under the temperature gradient and less than 30% under stirring, as calculated through the measurement of the linear birefringence of the optical system (see Experimental section). The bisignate profile of the CD band under stirring is almost symmetric (more for CCW than for CW stirring), hence indicating that distortions caused by LD are not relevant.

An additional correlation of morphology and supramolecular order of 2D aggregates prepared by **method 1** with a chiroptical response to asymmetric perturbations unveils the strong impact of mechanical forces. The self-assembled structures prepared by **method 1** are the largest (by AFM, aspect ratio of

area/thickness is $\sim 10^7$) with respect to other methods. Therefore, the amount of the individual **16Py₃** trimers within aggregates, or in a pre-aligned conformation, is considerably higher (by 2-3 orders of magnitude). The chiroptical properties of these aggregates are more strongly influenced by the asymmetric perturbations. Thus, the shape of CD spectra of the sample reflects a high sensitivity to temperature gradient strength.

Figure 11A shows that, as long as the temperature gradient strength is small, a CD response is also small and bisignate, but upon increasing the gradient strength, the CD signal increases significantly and becomes relatively distorted. The distortions resemble the profile of the LD spectrum, whose intensity increases with the temperature gradient strength (Figure 11C). Under temperature gradients, the LD signals are more intense for the aggregates prepared by **method 1** in comparison to other methods. It appears clearly that as long as the CD profile is bisignate the contribution of LD to the CD spectra is negligible, but for higher temperature gradient strengths the effect of aggregate alignment becomes predominant on the supramolecular chirality. The estimation of the LD contribution to the measured CD is less than 50% for small temperature gradient strength and less than 40% under stirring, but becomes more than 50% for the stronger temperature gradient investigated (see Experimental section). The perturbation generated by the thermophoretic forces seems to favour the alignment of these very large aggregates; however, under stirring, analogous results as for the solution in **method 2** are found (Figure 11B and 11D). Also in **method 1**, the smaller CD and LD signal observed for the CW stirring could depend on the different tendency of the aggregates to adjust their supramolecular structure under opposite sense of flow.

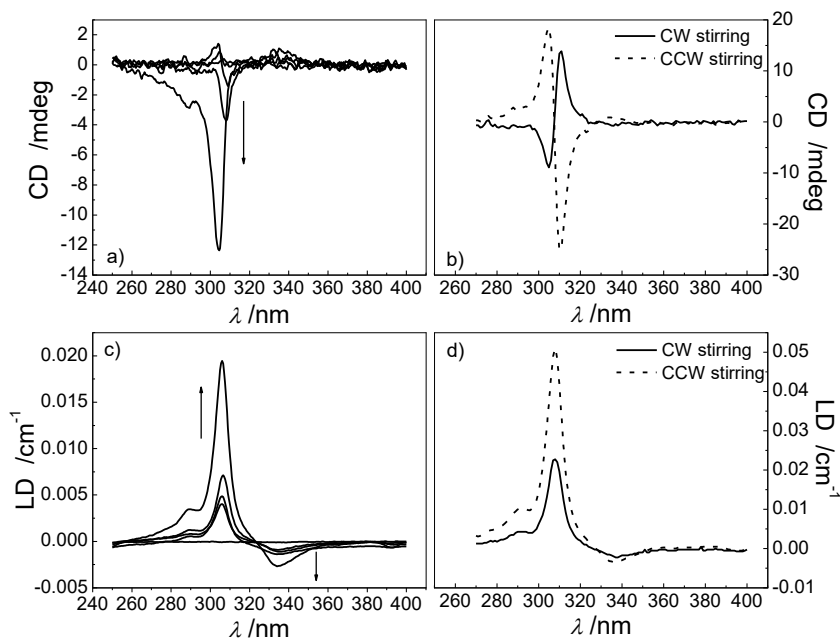


Figure 11. CD (a, b) and LD (c, d) spectra for the solution of **16Py₃** aggregates prepared using **method 1** under different temperature gradient strength (plots a and c) and under CW and CCW stirring at 0.5 Hz (plots b and d). The arrows indicate the increase of the temperature gradient. Conditions: see Experimental Section.

The comparison of the CD signal strength for the aggregates obtained with the different method becomes quantitative through the calculation of the asymmetry factor, $g = \Delta\epsilon/\epsilon$, where $\Delta\epsilon$ is the total strength of the bisignate CD band and ϵ is extinction of the J-aggregate band at 305 nm (Figure 2).

Table 1 provides the values for the g-factor for the stirred solutions of the aggregates and under small temperature gradient strength. The similarity of the g-factor values for both methods under stirring indicates that the aggregates are chiral due to the internal order of pyrene chromophores, and not due to size differences.

The sample of **16Py₃** aggregates is CD silent in the absence of thermal fluctuations or mechanical stirring. As has been already suggested by other groups, the chiral response of the 2D architectures could originate from folding of the supramolecular nanosheets,^[31] or associated with defects in a 2D supramolecular lattice,^[33] or from the twist dislocations in the lamellar GO LCs.^[32] We also

considered at least two possible scenarios for the origin of chirality in our case: 1) torque effect due to the vortex chiral flows and 2) alignment effects between individual sheets which are hierarchically organized in preferable helicity (twist grain boundary model).

Table 1. Calculated g -factors for the **16Py₃** derived aggregates induced by vortexing.

	Method 1	Method 2	Method 3
CW	0	$2.6 \cdot 10^{-3}$	$2.3 \cdot 10^{-3}$
CCW	0	$2.8 \cdot 10^{-3}$	$4.3 \cdot 10^{-3}$
Weak T-gradient ^[a]	0	$1.5 \cdot 10^{-4}$	$3 \cdot 10^{-4}$

[a] Unstirred

Based on the following, the chiral response originates from the helical twisting of the individual sheets. First, the samples of **16Py₃** are highly diluted ($c = 3 \mu\text{M}$). Therefore, the relative size of the assemblies implies that the concentration of the individual sheets (c_{agg}) in samples 2 and 3 is significantly different, i.e., $c_{\text{agg}}^{(\text{method } 2)}/c_{\text{agg}}^{(\text{method } 3)}$ is 100-1000. Such deviation of c_{agg} would impact the effect of the alignment by chiral flows. However the data demonstrate that the g -factors are almost identical, inferring that the chirality originates on a level of the single sheet. Second, a strong exciton-coupled CD signal appears only for the aggregates obtained from **methods 1 and 2**, in other words, samples that form large, continuous single layers. This observation shows that efficient π -stacking within a supramolecular sheet is a prerequisite for the potential optical activity. Moreover, exciton coupling is associated with an intense LD signal, indicating a certain spatial alignment of aggregates in solution both under gentle vortexing (**method 1 and 2**) and thermophoretic effect (only **method 1**). The LD signals retain their signs upon an inversion of the stirring sense and under temperature gradient, implying that the alignment of the dipole transition moments for the J-type (H-type) coupling keeps in

the almost horizontal (vertical) direction. Upon considering the 2D supramolecular assemblies shown in Scheme 1, it could be reasonably inferred that the **16Py₃** single nanosheets lie in the horizontal plane.

4. Conclusions

The results reported here suggest that supramolecular chirality in **16Py₃** sheets is induced by external asymmetrical perturbations, and depends on both the size of aggregates and the supramolecular order within assemblies. The high degree of structural order ensures strong cooperative effects within the aggregates, rendering them more susceptible to external stimuli.^[45] In general, the effects of the hydrodynamic vortex on the CD and LD of two-dimensional supramolecular polymers are stronger than those generated by temperature gradients. When the aggregate size is not large enough, and the degree of internal order is low (**method 3**), supramolecular chirality cannot be induced either by thermophoretic or by hydrodynamic forces. On the other hand, when the aggregates become larger in size and more spatially ordered (**method 2**), the chiral response (strong exciton coupled CD) is triggered by gentle vortexing. However, the samples from **method 2** are almost unsusceptible to the action of the thermophoretic force alone (extremely low CD and LD signals). In contrast, samples prepared by **method 1** show a stronger LD signal under a temperature gradient without stirring because the aggregates are large, with an area of tens μm^2 , and more organized. The findings imply that large numbers of chromophores are aligned. Thus, only the sample prepared by **method 1** is sensitive to thermophoretic forces. With increasing the temperature gradient, the effect of aggregate alignment contributes predominantly to the chiral response.

5. Experimental Section

Formation of 2D supramolecular polymers in aqueous solution. The **16Py₃** oligomer was stored as a 200 μM stock solution in ethanol at 2 $^{\circ}\text{C}$. Aqueous solutions of 3 μM **16Py₃** were prepared by transferring a 60 μL aliquot of the **16Py₃** ethanol stock solution to the buffer mixture (final sample volume = 4 mL). The buffer mixture contained 10 mM aqueous phosphate buffer adjusted to pH=7.2, 10 mM aqueous sodium chloride and 15% v/v ethanol. All buffers were filtered through a 0.2 μm 25-mm surfactant free cellulose acetate membrane (NalgeneTM) before use. Aqueous solutions for experiments were prepared according to one of the following methods.

Circular and Linear Dichroism. Circular dichroism (CD) spectra were recorded by means of two different JASCO instruments: J-815 and J-500A spectropolarimeters, both equipped with a 150W Xenon lamp. All measurements, corrected for the contribution from quartz cell and buffer, were performed at either different temperature gradients or under magnetic stirring. Particular attention was dedicated to the thermostating apparatus generating the temperature gradients and the consequent thermophoretic chiral forces (for more details see SI or the original paper^[39]). It has been checked that if the solution is well thermostated through a carefully controlled two-stage thermostating system (and hence in the absence of temperature gradients) the CD signal vanishes completely (see Figure S1, SI), at a thermostat temperature in the range of 15-40 $^{\circ}\text{C}$.

Static and Dynamic Light Scattering at wide angle. Dynamic Light Scattering (DLS) measurements were performed using the Photon Correlation Spectroscopy technique: the laser light of a polarized He-Ne (632.8 nm) with a power of 35 mW was scattered from the sample and collected in a self-beating mode within a scattering angle range 45 $^{\circ}$ -110 $^{\circ}$.^[46] To collect the polarized and

depolarized contribution to the light scattered from the sample, a Glan-Taylor polarizer was placed in the incident laser path and a Glan-Thomson analyser in the scattered beam. The depolarization ratio, defined as $I_{VH}/(I_{VV}+4/3I_{VH})$ (with the subscripts VV and VH referring to the polarized and depolarized intensity), provided information about the optical anisotropy of the depolarizing object. The scattered light was collected at different scattering angles and sent to a Malvern 4700 to build up the intensity autocorrelation function, $g_2(Q,t)$, $Q=(4\pi n/\lambda)\sin(\theta/2)$ being the exchanged wavevector, n the refractive index of the medium, λ the wavelength of the incident light and θ the scattering angle. For monodisperse scatterers and for scattered electric fields obeying Gaussian statistics, the intensity correlation function decays exponentially according to $g_2(Q,t)=1+a\exp(-2\Gamma t)$ (a being a constant which depends on the experimental setup). The decay rates, Γ , of the polarized and depolarized correlation functions for translation and rotation diffusion dynamics in dilute solutions are (in the absence of correlation between translational and rotational motions)^[47]:

$$\Gamma_{VV}(Q) = DQ^2 + \frac{6\Theta}{\frac{45}{4}\frac{\alpha^2}{\beta^2} + 1}$$

$$\Gamma_{VH}(Q) = DQ^2 + 6\Theta$$

where D and Θ are the translational and rotational diffusion coefficients, respectively, α is the isotropic excess polarizability of the particle with respect to the solvent, and β is the anisotropy of the particle polarizability. The translational diffusion coefficient is directly related to the hydrodynamic radius, R_H , of the particle through the Einstein-Stokes relation, $D=k_B T/(6\pi\eta R_H)$, k_B being the Boltzmann's constant, T the absolute temperature and η the solvent viscosity. For an elongated particle, modelled as a prolate ellipsoid, Θ is related to the size through the Perrin's equations (see equations S1 in the SI). For polydisperse scatterers there is a distribution of decay

rates; in this case the quantity Γ in the previous relations is the mean value of the distribution, whereas polydispersity is related to the width of the distribution.

For Static Light Scattering (SLS) experiments the scattered intensity profile was collected using the same set-up as for DLS, but without polarization analysis. Due to the low concentration of **16Py₃**, the scattered intensity profile can be considered proportional to the form factor describing the shape of the aggregates. The form factors that fit the experimental profiles are those of the homogeneous sphere and homogeneous prolate ellipsoid^[47] (equations S2 and S3). The scattered intensity profile of the aqueous buffer is not Q-independent because of the ethanol nano-domains; therefore, the profiles of all **16Py₃** samples were subtracted for the profile from the buffer alone.

Small Angle Light Scattering. The static light-scattering experiments at small angle (SALS) were performed using an apparatus with a Fourier lens to focus the scattered wave front on a linear CCD detector (a fibered 1024 element diode array). In order to collect only the scattered portion of the light, the detector was set off the transmitted beam and the scattering angle range was from 1° to 5°. A 16 bit analog-to-digital converter was employed to digitalize the signal. Such a technique was used only for investigating the solution obtained with **method 1**, in which large aggregates are formed. The intensity scattered by the solvent was subtracted from the spectra of the solution. After the geometrical corrections (due to the refraction at the flat cuvette surface), SALS data were analysed in terms of aggregate size distribution $f(R)$, according to the diffraction theory^[48,49] (equation S4).

Perrin's equations:

For an elongated particle, modelled as prolate ellipsoid, the following Perrin's equations hold:^[13]

$$D = \frac{k_B T}{6\pi\eta(L/2)} G(\rho)$$

$$\Theta = \frac{3k_B T}{16\pi\eta(L/2)^3} \frac{(2-\rho)G(\rho)-1}{(1-\rho^2)}$$
(S1)

where $L/2$ and $\rho < 1$ are the major semiaxis and the axial ratio, respectively, $(L/2)/G(\rho)$ can be regarded as the hydrodynamic radius of the equivalent sphere, with

$$G(\rho) = (1-\rho^2)^{-1/2} \ln \left\{ \frac{1+(1-\rho^2)^{1/2}}{\rho} \right\}$$

Form factors used to fit the scattered intensity profiles:

For homogeneous spherical aggregates with radius R it is:

$$P(Q) = \left[3 \frac{\sin(QR) - QR \cos(QR)}{(QR)^3} \right]^2$$
(S2)

Polydispersity is taken into account by weighting the form factor by a Gaussian size distribution.

The form factor of the homogeneous prolate ellipsoid model with minor semiaxis b and major semiaxis $b\xi$, with $\xi > 1$, is:

$$P(Q) = \int_0^1 \left[3 \frac{J_1(x)}{x} \right]^2 d\mu$$
(S3)

where $J_1(x) = [\sin(x) - x \cos(x)]/x^2$ and $x(\mu) = Qb\sqrt{\xi^2 \mu^2 + (1-\mu^2)}$ (μ being the cosine of the angle between the directions of b and Q).

Estimation of LD contribution and determination of cuvette's birefringence.

Because of the small residual static birefringence of the PE modulator and of the geometry of detection (depolarizer/photomultiplier system), the equations for the measured signals for circular dichroism can be written as:

$$CD_{meas} = G_1 [CD + 0.5(LD' LB - LDLB') + (LD' \sin 2\theta - LD \cos 2\theta) \sin \alpha]$$
(S4)

where G_1 is known from calibration.

Here LB and LD are the linear birefringence (with magnitude LB_β) and the linear dichroism (with magnitude LD_χ), respectively. LD' is the 45° linear dichroism, θ the rotation angle of the sample with respect to the polarizator/PE modulator system and α the residual static birefringence of PE modulator.

From the measurement of the birefringence of the optical system (performed with water-containing cuvette) we found that LB magnitude was about 0.01 with orientation of $\beta \cong 50^\circ$ (with respect to the horizontal orientation set as zero angle), almost independent from wavelength in the range of interest.

In order to estimate the LD contribution in the measured CD spectrum (cross-talk error), it is necessary to measure LD, given by:

$$LD_{meas} = G_2(LD' \sin 2\theta - LD \cos 2\theta) = G_2 LD_\chi \cos(2(\chi - \theta)) \quad (S5)$$

where G_2 is known from calibration and χ represent the orientation of the linear dichroism. Then,

$$CD_{meas} = G_1 \left[CD + 0.5(LD_\chi LB_\beta \sin(2(\chi - \beta))) + \frac{LD_{meas}}{G_2} \sin \alpha \right] \quad (S6)$$

CD_{meas} changes with θ only through the last term, which is negligible for small residual stress of the PE modulator and/or for small value of linear dichroism. In fact, in the present case, the value of the product between the highest measured LD_{meas} (0.025 cm^{-1}) and $\sin \alpha$ is lower than the detectability limit. Therefore, LD contributes in the measured CD only through the coupling with LB (second term in equation S4). In order to determine the amount of this cross-talk it is necessary to measure the orientation χ of the aggregates and the amplitude of LD (i.e. LD_χ and not only LD_{meas} at a single value of θ). For a liquid sample this means that the whole polarizator/PE modulator system and the detector should rotate. However, an approximate estimation of the cross-talk (see table S1) along with the empiric evaluation of the

symmetry and shape of the CD profile is still feasible. A symmetric bisignate CD spectrum centered at the absorption wavelength is a reasonable indication of the absence of distortions due to LD signals with single peak at the absorption wavelength. From the CD and LD spectra measured in this work it is possible to deduce that the CD profiles are distorted by LD only in the case of the aggregates obtained with method 3 subjected to higher temperature gradient strength.

Table S1. Maximum value of the percentage of cross-talk into the measured CD spectrum, as estimated by considering the worst condition $\sin[2(\chi-\beta)]=1$ (with LD_{meas} as LD_{χ} corresponding to an almost vertical alignment).

		CD _{meas}		LD _{meas}	Cross-talk	Cross-talk/CD _{meas}
		mdeg	cm ⁻¹	cm ⁻¹	cm ⁻¹	%
Method 2	Temp. gradient	1.5	0.45 × 10 ⁻⁴	2.5 × 10 ⁻⁴	2.5 × 10 ⁻⁶	5
	CW Stirring	25	7.6 × 10 ⁻⁴	0.025	2.5 × 10 ⁻⁴	32
	CCW Stirring	28	8.5 × 10 ⁻⁴	0.032	3.2 × 10 ⁻⁴	37
Method 3	Lower temp. gradient	3.5	1.06 × 10 ⁻⁴	0.005	0.5 × 10 ⁻⁴	47
	Higher temp. gradient	12	3.6 × 10 ⁻⁴	0.02	2 × 10 ⁻⁴	55
	CW stirring	22	6.7 × 10 ⁻⁴	0.023	2.3 × 10 ⁻⁴	34
	CCW stirring	43	13 × 10 ⁻⁴	0.05	5 × 10 ⁻⁴	38

6. References

- [1] M. Avalos, R. Babiano, P. Cintas, J. L. Jiménez, J. C. Palacios, L. D. Barron, *Chem. Rev.* **1998**, 98, 2391-2404.
- [2] D. B. Amabilino, J. Veciana, in *Supramolecular Chirality*, Eds.: M. Crego-Calama, D. N. Reinhoudt, Springer Berlin Heidelberg, 2006, pp. 253-302.
- [3] A. Tsuda, Y. Nagamine, R. Watanabe, Y. Nagatani, N. Ishii, T. Aida, *Nat. Chem.* **2010**, 2, 977-983.

- [4] B. L. Feringa, R. A. van Delden, *Angew. Chem. Int. Ed.* **1999**, *38*, 3418-3438.
- [5] H. Cao, X. Zhu, M. Liu, *Angew. Chem. Int. Ed.* **2013**, *52*, 4122-4126.
- [6] G. P. Spada, *Angew. Chem. Int. Ed.* **2008**, *47*, 636-638.
- [7] A. D'Urso, R. Randazzo, L. Lo Taro, R. Purrello, *Angew. Chem. Int. Ed.* **2010**, *49*, 108-112.
- [8] T. Buhse, D. Durand, D. Kondepudi, J. Laudadio, S. Spilker, *Phys. Rev. Lett.* **2000**, *84*, 4405-4408.
- [9] J. M. Ribo, J. Crusats, F. Sagues, J. Claret, R. Rubires, *Science* **2001**, *292*, 2063-2066.
- [10] O. Ohno, Y. Kaizu, H. Kobayashi, *J. Chem. Phys.* **1993**, *99*, 4128-4139.
- [11] A. Tsuda, M. A. Alam, T. Harada, T. Yamaguchi, N. Ishii, T. Aida, *Angew. Chem. Int. Ed.* **2007**, *46*, 8198-8202.
- [12] M. Wolffs, S. J. George, Z. Tomovic, S. C. Meskers, A. P. Schenning, E. Meijer, *Angew. Chem. Int. Ed.* **2007**, *46*, 8203-8205.
- [13] J. Crusats, Z. El-Hachemi, J. M. Ribo, *Chem. Soc. Rev.* **2010**, *39*, 569-577.
- [14] A. Tsuda, *Symmetry* **2014**, *6*, 383-395.
- [15] K. Okano, T. Yamashita, *ChemPhysChem* **2012**, *13*, 2263-2271.
- [16] M. M. Green, J. W. Park, T. Sato, A. Teramoto, S. Lifson, R. L. B. Selinger, J. V. Selinger, *Angew. Chem. Int. Ed.* **1999**, *38*, 3139-3154.
- [17] M. A. Castriciano, A. Romeo, G. De Luca, V. Villari, L. M. Scolaro, N. Micali, *J. Am. Chem. Soc.* **2011**, *133*, 765-767.
- [18] N. Micali, H. Engelkamp, P. van Rhee, P. Christianen, L. Scolaro, J. Maan, *Nat. Chem.* **2012**, *4*, 201-207.
- [19] O. Arteaga, A. Canillas, J. Crusats, Z. El-Hachemi, J. Llorens, A. Sorrenti, J. M. Ribo, *Isr. J. Chem.* **2011**, *51*, 1007-1016.

- [20] V. Babenko, M. Piejko, S. Wojcik, P. Mak, W. Dzwolak, *Langmuir* **2013**, *29*, 5271-5278.
- [21] A. Romeo, M. A. Castriciano, I. Occhiuto, R. Zagami, R. F. Pasternack, L. M. Scolaro, *J. Am. Chem. Soc.* **2014**, *136*, 40-43.
- [22] A. L. Nussbaumer, F. Samain, V. L. Malinovskii, R. Häner, *Org. Biomol. Chem.* **2012**, *10*, 4891-4898.
- [23] V. L. Malinovskii, A. L. Nussbaumer, R. Häner, *Angew. Chem. Int. Ed.* **2012**, *51*, 4905-4908.
- [24] A. L. Nussbaumer, D. Studer, V. L. Malinovskii, R. Häner, *Angew. Chem. Int. Ed.* **2011**, *50*, 5490-5494.
- [25] M. Vybornyi, A. Rudnev, R. Häner, *Chem. Mater.* **2015**, *27*, 1426-1431.
- [26] M. Vybornyi, A. V. Rudnev, S. M. Langenegger, T. Wandlowski, G. Calzaferri, R. Häner, *Angew. Chem. Int. Ed.* **2013**, *52*, 11488-11493.
- [27] R. Bholá, P. Payamyar, D. J. Murray, B. Kumar, A. J. Teator, M. U. Schmidt, S. M. Hammer, A. Saha, J. Sakamoto, A. Schlüter, B. T. King, *J. Am. Chem. Soc.* **2013**, *135*, 14134-14141.
- [28] C. Shahar, J. Baram, Y. Tidhar, H. Weissman, S. R. Cohen, I. Pinkas, B. Rybtchinski, *ACS Nano* **2013**, *7*, 3547-3556.
- [29] S. L. Cai, W. G. Zhang, R. N. Zuckermann, Z. T. Li, X. Zhao, Y. Liu, *Adv. Mater.* **2015**, DOI: 10.1002/adma.201500124.
- [30] X. Zhuang, Y. Mai, D. Wu, F. Zhang, X. Feng, *Adv. Mater.* **2015**, *27*, 403-427.
- [31] F. Li, Q. Song, X. Zhang, *Langmuir* **2014**, *30*, 6064-6070.
- [32] Z. Xu, C. Gao, *Nat. Commun* **2011**, *2*, 571.
- [33] Z. El-Hachemi, C. Escudero, F. Acosta-Reyes, M. T. Casas, V. Altoe, S. Aloni, G. Oncins, A. Sorrenti, J. Crusats, J. L. Campos, J. M. Ribo, *J. Mater. Chem. C* **2013**, *1*, 3337-3346.

- [34] J. M. Short, J. A. Berriman, C. Kuebel, Z. El-Hachemi, J. V. Naubron, T. S. Balaban, *ChemPhysChem* **2013**, *14*, 3209-3214.
- [35] P. A. Korevaar, T. F. De Greef, E. Meijer, *Chem. Mater.* **2014**, *26*, 576-586.
- [36] J. M. Ribo, Z. El-Hachemi, J. Crusats, *Rend. Fis. Acc. Lincei* **2013**, *24*, 197-211.
- [37] A. Raudino, M. Pannuzzo, *J. Chem. Phys.* **2012**, *137*, 134902.
- [38] F. Hamba, K. Niimura, Y. Kitagawa, K. Ishii, *Phys. Fluids* **2014**, *26*, 017101.
- [39] P. Mineo, V. Villari, E. Scamporrino, N. Micali, *Soft Matter* **2014**, *10*, 44-47.
- [40] P. A. May, J. S. Moore, *Chem. Soc. Rev.* **2013**, *42*, 7497-7506.
- [41] N. Micali, V. Villari, M. A. Castriciano, A. Romeo, L. M. Scolaro, *J. Phys. Chem. B* **2006**, *110*, 8289-8295.
- [42] M. Sedlak, *J. Phys. Chem. B* **2006**, *110*, 4329-4338.
- [43] G. Pescitelli, L. Di Bari, N. Berova, *Chem. Soc. Rev.* **2014**, *43*, 5211-5233.
- [44] F. D. Saeva, P. E. Sharpe, G. R. Olin, *J. Am. Chem. Soc.* **1973**, *95*, 7656-7659.
- [45] M. M. Green, N. C. Peterson, T. Sato, A. Teramoto, R. Cook, S. Lifson, *Science* **1995**, *268*, 1860-1866.
- [46] V. Villari, N. Micali, *J. Pharm. Sci* **2008**, *97*, 1703-1730.
- [47] B. J. Berne, R. Pecora, *Dynamic light scattering: with applications to chemistry, biology, and physics*, Wiley, N.Y. **1976**.
- [48] L. P. Bayvel, A. R. Jones, *Electromagnetic scattering and its applications*, 1 ed. Applied Science Publishers, London **1981**.
- [49] J. C. Knight, D. Ball, G. N. Robertson, *Applied Optics* **1991**, *30*, 4795-4799.

CHAPTER V. TUBES OR SHEETS: DIVERGENT AGGREGATION PATHWAYS OF AN AMPHIPHILIC 2,7-SUBSTITUTED PYRENE TRIMER

Published: Vybornyi, M.; Bur-Cecilio Hechevarria, Y.; Glauser, M.; Rudnev, A.; Häner, R. *Chem. Commun.*, **2015**, doi: 10.1039/C5CC05126F

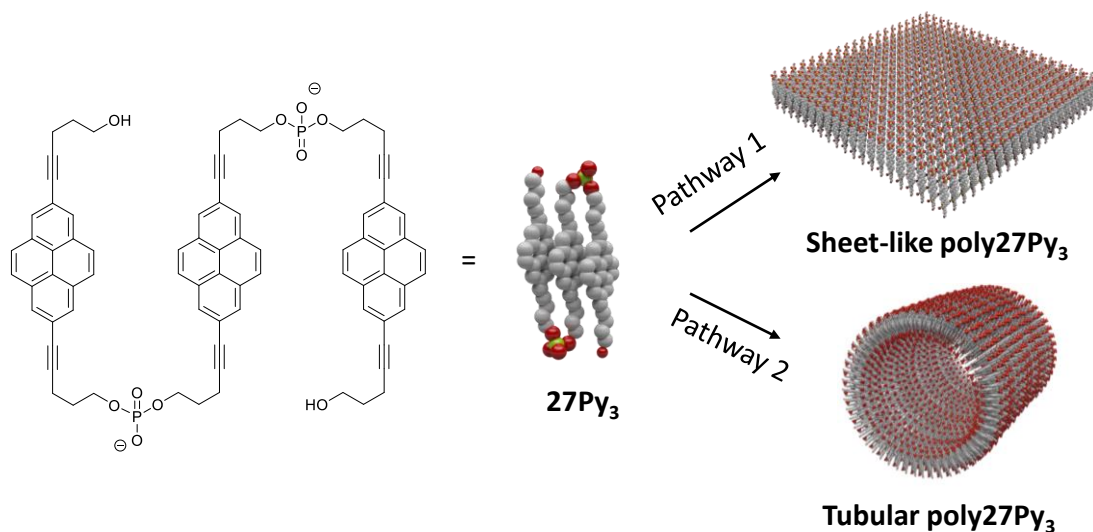
1. Abstract

Self-assembly of an amphiphilic trimer consisting of 2,7-disubstituted, phosphodiester-linked pyrenes leads to the simultaneous formation of morphologically related planar and tubular supramolecular objects in aqueous environment. The aggregation process is accompanied by major spectroscopic changes.

2. Introduction

On-demand assembly of π -conjugated molecules in morphologically-defined patterns remains a desirable task.^[1-5] Inspired by the multifaceted and versatile properties of graphene, two-dimensional (2D) organic materials have attracted great interest, yet their preparation and handling remain challenging.^[6-10] Tubular objects are morphologically related to 2D structures, such as ribbons or sheets, and can arise from the latter *via* proper connection of edges. The formation of supramolecular nanotubes *via* helical intermediates is a well-documented process.^[11,12] The description of shape-shifting pairs of covalent polymers is limited to the graphene-to-CNTs transformation.^[13] Self-assembly is a versatile tool for the preparation of morphologically adaptable platforms,^[14,15] primarily due to the non-covalent nature of the intermolecular interactions.^[16-19] We recently described the use of oligoarenotides, amphiphilic phosphodiester-linked arene oligomers,^[20] for the bottom-up assembly of functional supramolecular polymers.^[21-23] The morphological

features (nanosheets^[24,25] or fibers^[26]) of the aggregates primarily depend on the substitution pattern of the aromatic core. The importance of pyrene and its derivatives as components of functional materials largely originates in the reliable control of the electronic properties *via* the aromatic substitution pattern and environmental influences.^[27-30] In comparison to other derivatives, 2,7-substituted pyrenes have been relatively little explored but recent synthetic advances^[31-34] triggered growing interest in these compounds. Thus, 2,7-substituted pyrenes were used for the preparation of solar cells,^[35] OLEDs^[36] and conjugated polymers,^[37,38] construction of nanorings^[39,40] and covalent organic frameworks.^[41,42] Furthermore, they found application as rotaxanes^[43] and tweezers^[44] of single-walled carbon nanotubes as well as in hydrophobic host-guest nanocages.^[45] In this report, we demonstrate that a trimer of 2,7-substituted pyrenes (**27Py₃**) self-assembles into 2D (sheetlike) and 1D (tubular) supramolecular polymers (**poly27Py₃**, Scheme 1).

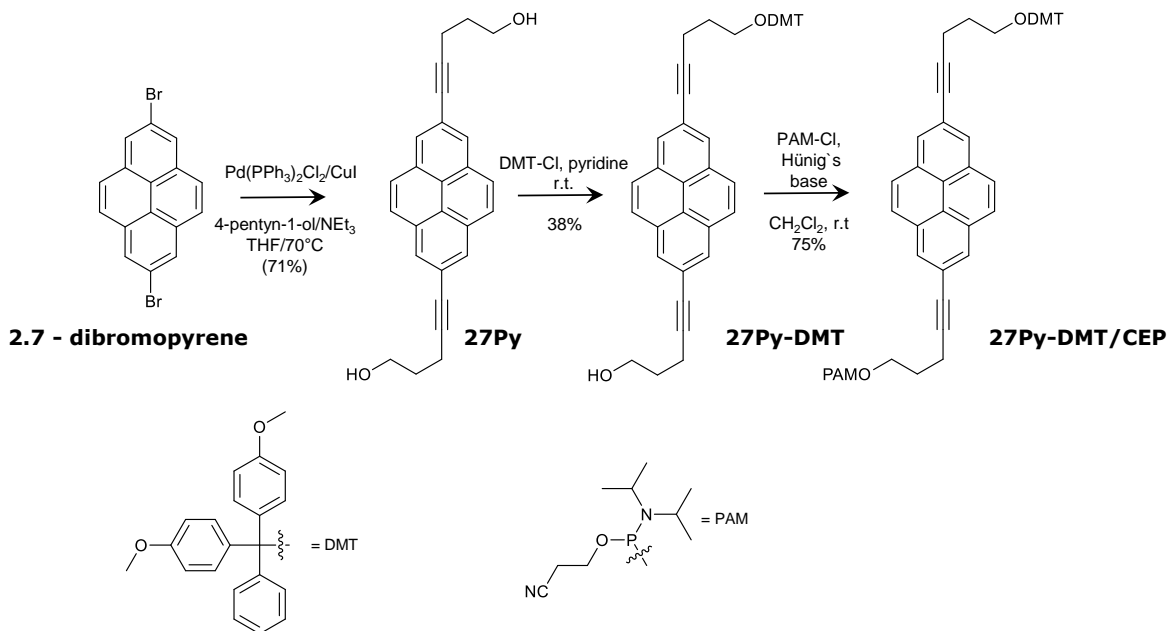


Scheme 1. Structure of **27Py₃** and illustrations of sheetlike and tubular self-assembled objects.

3. Results

3.1 Synthesis of pyrene oligomers

Oligomer **27Py₃** was prepared *via* solid-phase synthesis. The required building block was synthesized as shown in Scheme 2. Briefly, 2,7-dibromopyrene was converted to the 2,7-dialkynyl-substituted derivative **27Py** *via* a Sonogashira reaction. After DMT-protection, the obtained intermediate **27Py-DMT** was converted to phosphoramidite **27Py-DMT/CEP**. All compounds were characterized by ¹H, ¹³C NMR and HRMS. After synthesis on solid support, oligomer **27Py₃** was purified by RP-HPLC and characterized by MS (see Experimental section).



Scheme 2. Synthesis of phosphoramidite building block **27Py-DMT/CEP**.

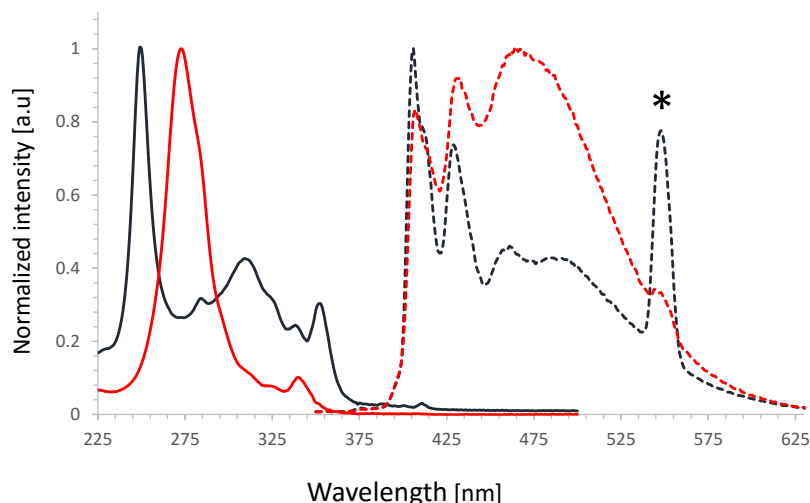


Figure 1. Normalized UV/Vis (solid) and fluorescence (dashed) spectra of at 20°C (black) and 80°C (red). Conditions: **27Py₃** = 5 μM in a mixture of aqueous buffer (10 mM sodium chloride, 10 mM phosphate buffer, pH = 7.2) and ethanol 80/20 v/v; λ_{ex} = 275 nm. *second order transmission artefacts

Absorption and emission spectra of **27Py₃** were recorded in an aqueous mixture (aqueous buffer containing 20% ethanol, see Figure 1). Temperature-dependent pyrene aggregation is accompanied by pronounced spectroscopic changes. At 80°C, the absorption spectrum consists of essentially two peaks, a very intense maximum at 273 nm and a weak maximum at 340 nm. The shape of this spectrum resembles the one recorded of **27Py₃** in ethanol (see Experimental section). Under these conditions, **27Py₃** exists as a molecularly dissolved trimer. The spectra are in-line with those reported for other 2,7-substituted pyrenes.^{29,46} Upon cooling of the aqueous solution from 80°C to 20°C, the absorption spectrum experiences significant changes in both regions as a result of trimer aggregation (**poly27Py₃**). A new, blue-shifted band arises at 250 nm (Figure 1). Furthermore, the appearance of several additional bands is observed, the most dominant ones located at 309 and 352 nm. These changes are ascribed to exciton coupling of assembled pyrenes.^{24,25,47} Fluorescence spectra for **27Py₃** in aqueous mixture consist of monomer and excimer emissions.²⁷ The former covers a range of 380-500 nm and

exhibits a well-defined vibronic structure (see e.g. spectrum of compound **2**). For **27Py₃** and its aggregates (**poly27Py₃**) the broad and structure-less excimer band appears as an additional signal in the 400-625 nm region.

The aggregation-induced spectroscopic changes in aqueous solution were further substantiated by microscopic studies. AFM imaging of **poly27Py₃** was performed on amino-modified mica plates. The images reveal two morphologically different types of supramolecular polymers, nanosheets and nanotubes (Figure 2). The nanosheets appear as large-sized 2D objects with up to 200 μm^2 area and a constant layer thickness of 2 nm. This is consistent with a model of a hydrophobic array of stacked pyrenes sandwiched between two layers of negatively charged phosphates. The nanosheets exist predominantly as mono-lamellar objects, which is explained by Coulomb repulsion between individual sheets. Alternatively, **poly27Py₃** exists in the form of nanotubes (Figure 2). This morphology has rarely been observed with pyrene-containing aggregates.⁴⁸ The tubes appear on surface as perfectly straight flat bars with an apparent thickness of 4.5 nm and a length of several micrometres. The bars exhibit a remarkably uniform width, which is in the range of 150-250 nm for individual objects. A thickness of 4.5 nm indicates a bilayer, which forms upon collapse of the nanotube during or after deposition and drying on the substrate surface. Thus, the tubes in solution are characterized by a diameter in the range of 100-200 nm and a wall thickness of ~ 2 nm, as illustrated in Figure 3. Some of the tubes exhibit sheetlike sections at their ends with a thickness of 2 nm (Figure 2B, cross-section I). It is important to note that tubes are often associated with nanosheets (Figure 2A). This may be an indication of divergent pathways leading to the parallel development of nanotubes and nanosheets at a certain stage of supramolecular polymerization.

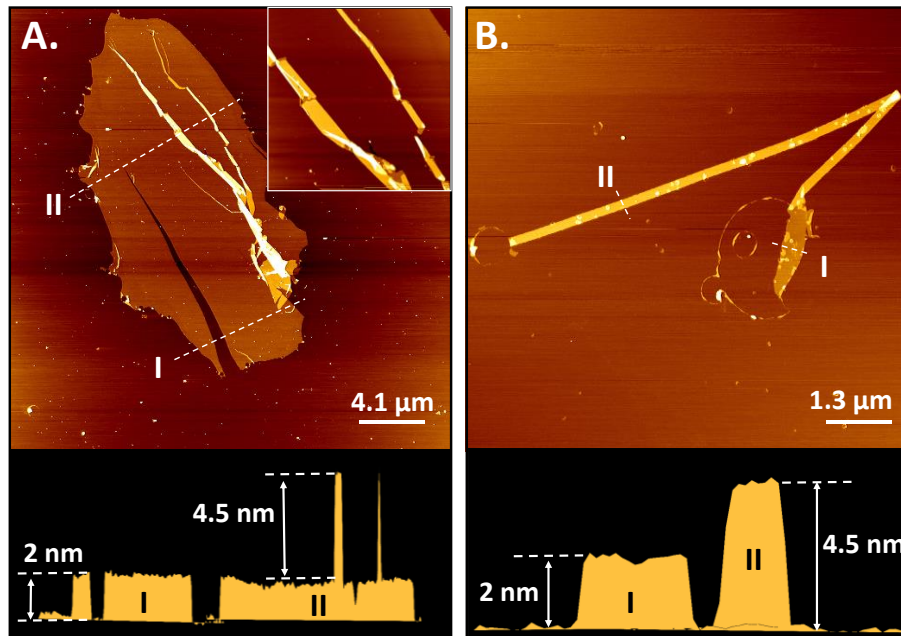


Figure 2. AFM images and cross sections along indicated lines of supramolecular polymers on an APTES-modified mica surface; A) co-existing planar and tubular objects (inset: enlarged view of cross-section area II); B) nanotube with small sheet attached. Samples were prepared via slow cooling (0.1°C/min). Conditions: see Figure 1.

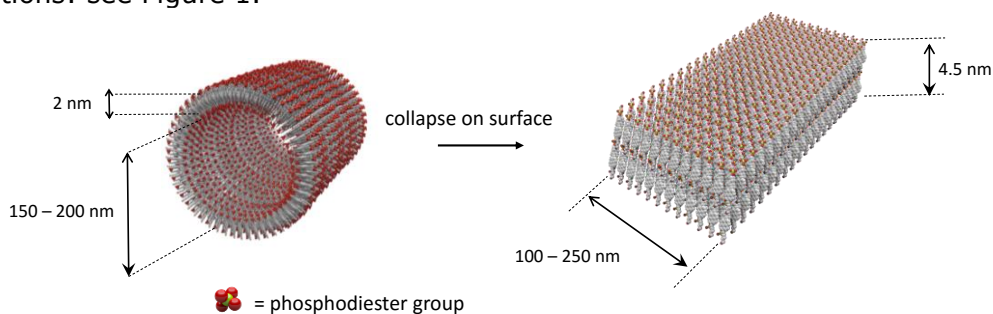


Figure 3. Illustration of a double a layer formed through collapse of a nanotube. (phosphates)

The self-assembly process has been followed by the temperature-dependent UV/Vis (Figure 4) and fluorescence experiments. Slow cooling (0.1°C/min) from 80°C to 20°C leads to a well-defined transition in both cases. Monitoring the absorption at 275 nm shows a transition starting at 65°C. The process can be also followed by excimer emission at 480 nm upon excitation at different wavelengths.

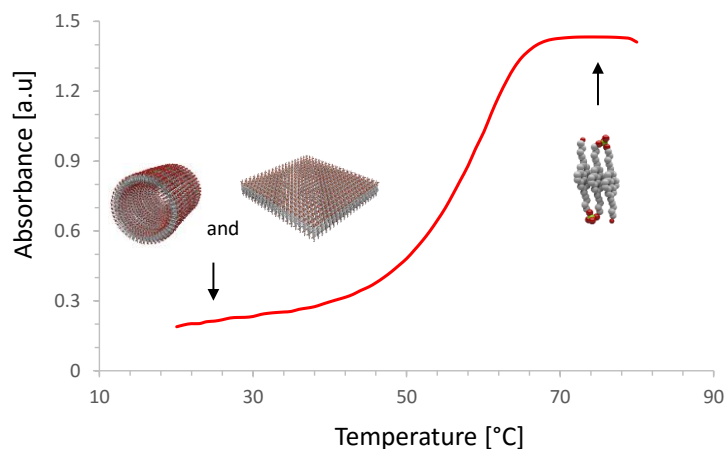


Figure 4. Supramolecular polymer formation curve (cooling rate 0.1°C/min) recorded in aqueous medium (conditions as in Figure 1) at 275 nm.

Spectroscopic and microscopic studies suggest that **27Py₃** trimers exist as molecularly dissolved chains at elevated temperatures in aqueous solution. Upon slow cooling, the oligomers tend to aggregate due to strong π -stacking and hydrophobic interactions resulting in the formation of supramolecular polymers (**poly27Py₃**). The assembly process leads to two morphologically different types of polymers, nanosheets and nanotubes. They consist of an inner pyrene layer sandwiched between densely-packed negatively-charged phosphates. The structural flexibility of the present type of supramolecular 2D-polymers^[47] may lead to the sporadic formation of meta-stable, non-planar conformations (e.g. loops, cones, or cylinder-shaped objects) from which the observed nanotube grow as a result of competing assembly pathways.

4. Conclusions

In conclusion, we have described self-assembly properties of an amphiphilic pyrene trimer **27Py₃**. Controlled via slow annealing aggregation in aqueous mixture leads to the simultaneous formation of planar and tubular objects. Also, the supramolecular polymerization is accompanied by drastic spectroscopic changes. We

assume that the morphological bias occurs at the nucleation stage. Ongoing studies aim the selective preparation of tubular objects by varying both the oligomer design and changing kinetic aspects of polymerization.

5. Experimental part

AFM experiments. AFM imaging was performed under ambient conditions in air with a Nanosurf FlexAFM (Nanosurf AG, Switzerland) instrument using either a 100×100 μm^2 or a 10×10 μm^2 scanning head. The measurements were carried out in tapping mode employing either PPP-NCHR-W cantilevers from Nanosensors (resonance frequency \sim 280 kHz, tip radius \sim 10 nm) or Tap190Al-G from BudgetSensors (resonance frequency \sim 190 kHz, force constant 48 N/m). Both types of cantilevers gave reproducible results. Sample preparation: a 15 μL aliquot of the 5 μM **poly27Py₃** was placed on an APTES-modified mica plate (20 × 20 mm^2). The mica plates were fixed on a holder and used for AFM studies. After 5 min, the plate was rinsed with Milli-Q water (0.5 ml total volume) and dried under a stream of Ar for 30 sec.

The **27Py₃** was synthesized on the Applied Biosystems 394 DNA synthesizer using preloaded USIII support. We followed a standard cyanoethyl phosphoramidite coupling protocol for the 1 μmol synthesis ("trityl-off" mode). The coupling yields per single step were \geq 95 % (monitoring by "trityl assay"). The cleavage of the **27Py₃** from the support was achieved by treatment with 0.8 ml of 2M NH_3/MeOH (Aldrich) for 16 hours at 50°C in a closed vial. The supernatant was separated from the support by centrifugation. The remained beads were treated with 0.8 ml of 2M NH_3/MeOH two times. All supernatants were collected, and 1 ml of aqueous NH_3 was added. After 30 min of a shaking at the room temperature, the sample was lyophilized. The crude product was purified by reverse-phase HPLC (LiChrospher 100 RP-C8, 5 μm , Merck, Bio-Tek Instruments); eluent A=(Et_3NH)OAc (50 mM, pH

7.0)/CH₃CN in 50/50 v/v; eluent B=CH₃CN; gradient 0–100% B over 14 min, then 100% B over 9 min. Gradient flow 1 ml/min. The pure compound was characterized by mass spectrometry: HRMS for C₇₈H₆₂O₁₀P₂²⁻: found 1220.3852 (calculated 1220.3830)

5,5'-(Pyrene-2,7-diyl)bis(pent-4-yn-1-ol) (Py27): 2,7-Dibromopyrene (1.00 g, 2.73 mmol), bis-(triphenylphosphine) palladium(II) chloride (45 mg, 0.065 mmol) and copper(I) iodide (7.0 mg, 0.036 mmol) were suspended in THF (20 mL) under argon and heated to 70 °C. After addition of triethylamine (20 mL), 4-pentyn-1-ol (1.00 mL, 11.1 mmol) was added to the mixture, which was stirred at this temperature for 36 h. After cooling to room temperature, the solvents were removed under reduced pressure. The column chromatography (dry deposition, eluent - CH₂Cl₂/ PhMe/MeOH 87:10:3) furnished yellow solid **Py27** (720 mg). Analytical data for **Py27**: R_f 0.3 (CH₂Cl₂/ methanol 97:3); ¹H NMR (300 MHz, DMSO-*d*₆) δ 8.31 (s, 4H), 8.16 (s, 4H), 4.59 (t, *J* = 5.2 Hz, 2H), 3.60 (td, *J* = 6.2, 5.1 Hz, 4H), 2.59 (t, *J* = 7.1 Hz, 4H), 1.86 – 1.72 (m, 4H). ¹³C NMR (75 MHz, DMSO-*d*₆) δ 130.67, 127.74, 127.59, 122.57, 121.30, 91.55, 80.75, 59.46, 31.58, 15.44. HRMS for C₂₆H₂₂O₂ (M+H⁺): found 367.1693 (calculated 367.1693).

5-(7-(5-(Bis(4-methoxyphenyl)(phenyl)methoxy)pent-1-yn-1-yl)pyren-2-yl)pent-4-yn-1-ol (3): To a solution of **Py27** (360 mg, 0.98 mmol) in pyridine (12 mL), a solid 4,4'-dimethoxytrityl chloride (335 mg, 0.98 mmol, 1 eq) was added dropwise. The mixture was stirred for 3 h and evaporated afterwards. The residue was dissolved in a small volume of CH₂Cl₂ and subjected to column chromatography (CH₂Cl₂/MeOH/NEt₃ 97/2/1). The fractions containing **Py27-DMT** were collected. This furnished 250 mg (38%) of yellow solid **Py27-DMT**. Analytical data for **Py27-DMT**: R_f=0.55 (CH₂Cl₂/ MeOH/ NEt₃ 97/2/1); ¹H NMR (300 MHz, DMSO-*d*₆) δ 8.31 (s, 2H), 8.22 – 8.09 (m, 6H), 7.47 – 7.16 (m, 9H), 6.93 – 6.81 (m,

4H), 4.60 (t, $J = 5.2$ Hz, 1H), 3.64 (s, 6H), 3.63 – 3.54 (m, 2H), 3.21 (t, 2H), 2.67 (t, 2H), 2.60 (t, 2H), 1.90 (m, 2H), 1.79 (m, 2H). ^{13}C NMR (75 MHz, DMSO- d_6) δ 157.93, 145.16, 135.89, 130.66, 130.59, 129.62, 127.75, 127.68, 127.64, 122.56, 121.32, 121.20, 113.09, 91.55, 91.50, 85.29, 81.14, 80.74, 61.35, 59.48, 54.87, 31.59, 28.59, 15.92, 15.42. HRMS for $\text{C}_{47}\text{H}_{40}\text{O}_4$ ($\text{M}+\text{Na}^+$): found 691.2919 (calculated 691.2817)

5-(7-(5-(Bis(4-methoxyphenyl)(phenyl)methoxy)pent-1-yn-1-yl)pyren-2-yl)pent-4-yn-1-yl (2-cyanoethyl) diisopropylphosphoramidite (4): Compound **Py27-DMT** (250 mg, 0.374 mmol) was dissolved in CH_2Cl_2 (10 mL). After addition of DIPEA (193 μL , 1.10 mmol, 3 eq) and 2-cyanoethyl- N,N -diisopropyl-chloro-phosphoramidite (113 mg, 0.487 mmol, 1.3 eq), the mixture was stirred for 5 h. The solution was evaporated and the residue was dissolved in a small volume of hexane/EtOAc/ NEt_3 50/49/1 and purified by a flash chromatography (hexane/ EtOAc/ NEt_3 50/49/1), furnished 242 mg (75%) **Py27-DMT/CEP** as a yellowish solid. Analytical data for **Py27-DMT/CEP**: $R_f = 0.60$ (hexane/ EtOAc/ NEt_3 50/49/1); ^1H NMR (300 MHz, DMSO- d_6) δ 8.31 (s, 2H), 8.21 – 8.13 (m, 6H), 7.42 – 7.27 (m, 9H), 6.92 – 6.85 (m, 4H), 3.84 – 3.75 (m, 4H), 3.64 (s, 6H), 3.61 – 3.56 (m, 2H), 3.21 (s, 2H), 2.81 – 2.61 (m, 6H), 1.95 – 1.84 (m, 4H), 1.16 (dd, $J = 6.8$, 4.7 Hz, 12H). ^{13}C NMR (75 MHz, DMSO- d_6) δ 157.93, 145.16, 135.89, 130.63, 129.63, 128.60, 127.54, 127.42, 126.52, 122.58, 121.21, 118.94, 113.10, 90.98, 85.29, 81.14, 62.47 – 60.51, 58.20, 54.87, 42.47, 30.57, 28.32, 24.36, 19.85, 15.70. ^{31}P NMR (122 MHz, DMSO) δ 146.74. HR MS for $\text{C}_{56}\text{H}_{57}\text{N}_2\text{O}_5\text{P}$: found 869.4071 (calculated 869.4078)

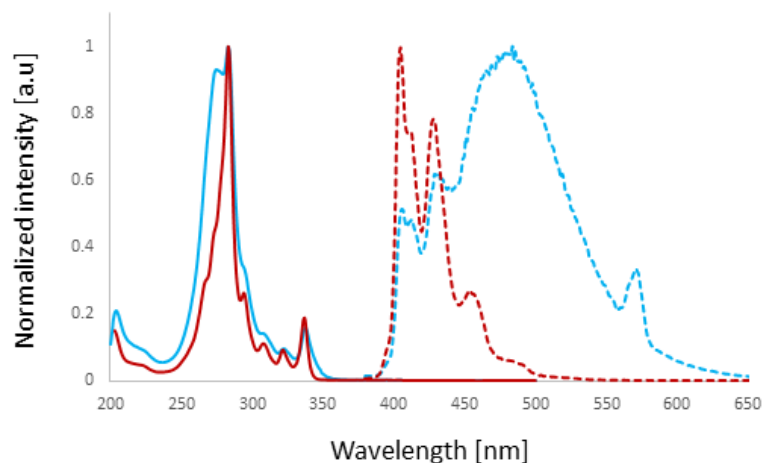


Figure 6. Normalized UV-vis (solid lines) and fluorescence (excitation at 285 nm, dashed) spectra of the 5 μM **27Py₃** (blue) and 5 μM **2** (red) in ethanol. The intense bands at 570 nm are artefacts caused by the second order transmission of the monochromator.

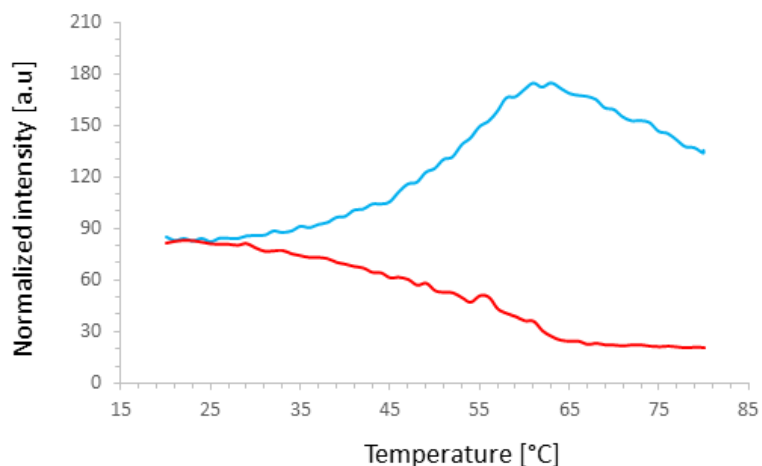


Figure 7. Supramolecular polymer formation curve (cooling rate 0.1°C/min) recorded in aqueous medium (10 mM sodium chloride, 10 mM phosphate buffer, pH = 7.2, ethanol 20% vol.) and monitored at 480 nm emission upon 275 nm (blue) and 352 nm (red) excitation wavelengths.

6. References

- [1] Y. Yan, Y. S. Zhao, *Chem. Soc. Rev.* **2014**, *43*, 4325-4340.
- [2] S. I. Stupp, L. C. Palmer, *Chem. Mater.* **2014**, *26*, 507-518.
- [3] P. A. Korevaar, T. F. De Greef, E. Meijer, *Chem. Mater.* **2014**, *26*, 576-586.
- [4] A. Wilson, G. Gasparini, S. Matile, *Chem. Soc. Rev.* **2014**, *43*, 1948-1962.

- [5] S. Sengupta, F. Würthner, *Acc. Chem. Res.* **2013**, *46*, 2498-2512.
- [6] S. L. Cai, W. G. Zhang, R. N. Zuckermann, Z. T. Li, X. Zhao, Y. Liu, *Adv. Mater.*, 2015, DOI: 10.1002/adma.201500124.
- [7] T. Govindaraju, M. B. Avinash, *Nanoscale*, **2012**, *4*, 6102-6117.
- [8] J. Sakamoto, J. van Heijst, O. Lukin, A. D. Schlüter, *Angew. Chem. Int. Ed.* **2009**, *48*, 1030-1069.
- [9] J. W. Colson, W. R. Dichtel, *Nat. Chem.* **2013**, *5*, 453-465.
- [10] M. E. Canas-Ventura, K. Ait-Mansour, P. Ruffieux, R. Rieger, K. Muellen, H. Brune, R. Fasel, *ACS Nano*, **2011**, *5*, 457-469.
- [11] T. G. Barclay, K. Constantopoulos, J. Matisons, *Chem. Rev.* **2014**, *114*, 10217-10291.
- [12] N. Kameta, H. Minamikawa, M. Masuda, *Soft Matter*, **2011**, *7*, 4539-4561.
- [13] H. E. Lim, Y. Miyata, R. Kitaura, Y. Nishimura, Y. Nishimoto, S. Irle, J. H. Warner, H. Kataura, H. Shinohara, *Nat. Commun.*, **2013**, *4*, 2548
- [14] N. Chandrasekhar, R. Chandrasekar, *Angew. Chem. Int. Ed.* **2012**, *51*, 3556-3561.
- [15] W. Li, Y. Kim, M. Lee, *Nanoscale* **2013**, *5*, 7711-7723.
- [16] L. Yang, X. Tan, Z. Wang, X. Zhang, *Chem. Rev.* **2015**, *115*, 7196-7239
- [17] M. Ramanathan, L. K. Shrestha, T. Mori, Q. Ji, J. P. Hill, K. Ariga, *PhysChemChemPhys*, **2013**, *15*, 10580-10611.
- [18] D. Wang, G. Tong, R. Dong, Y. Zhou, J. Shen, X. Zhu, *Chem. Commun.*, **2014**, *50*, 11994-12017.
- [19] A. Sorrenti, O. Illa, R. Ortuno, *Chem. Soc. Rev.* **2013**, *42*, 8200-8219.
- [20] R. Häner, F. Garo, D. Wenger, V. L. Malinovskii, *J. Am. Chem. Soc.* **2010**, *132*, 7466-7471.

- [21] V. L. Malinovskii, A. L. Nussbaumer, R. Häner, *Angew. Chem. Int. Ed.* **2012**, *51*, 4905-4908.
- [22] Y. Vyborna, M. Vybornyi, A. V. Rudnev, R. Häner, *Angew. Chem. Int. Ed.* **2015**, *54*, 7934-7938
- [23] C. B. Winiger, S. Li, G. R. Kumar, S. M. Langenegger, R. Häner, *Angew. Chem. Int. Ed.* **2014**, *53*, 13609-13613.
- [24] M. Vybornyi, A. V. Rudnev, S. M. Langenegger, T. Wandlowski, G. Calzaferri, R. Häner, *Angew. Chem. Int. Ed.* **2013**, *52*, 11488-11493.
- [25] M. Vybornyi, A. Rudnev, R. Häner, *Chem. Mater.* **2015**, *27*, 1426-1431.
- [26] A. V. Rudnev, V. L. Malinovskii, A. L. Nussbaumer, A. Mishchenko, R. Häner, T. Wandlowski, *Macromolecules* **2012**, *45*, 5986-5992.
- [27] F. M. Winnik, *Chem. Rev.* **1993**, *93*, 587-614.
- [28] T. M. Figueira-Duarte, K. Müllen, *Chem. Rev.* **2011**, *111*, 7260-7314.
- [29] A. G. Crawford, A. D. Dwyer, Z. Liu, A. Steffen, A. Beeby, L. O. Palsson, D. J. Tozer, T. B. Marder, *J. Am. Chem. Soc.* **2011**, *133*, 13349-13362.
- [30] H. Örucü, N. Acar, *Comput. Theor. Chem.* **2015**, *1056*, 11-18.
- [31] Y. Q. He, Y. W. Zhong, *Chem. Commun.* **2015**, *51*, 3411-3414.
- [32] S. I. Kawano, M. Baumgarten, D. Chercka, V. Enkelmann, K. Müllen, *Chem. Commun.* **2013**, *49*, 5058-5060.
- [33] J. M. Casas-Solvas, J. D. Howgego, A. P. Davis, *Org. Biomol. Chem.* **2014**, *12*, 212-232.
- [34] A. G. Crawford, Z. Liu, I. A. Mkhaliid, I. M. H. Thibault, N. Schwarz, G. Alcaraz, A. Steffen, J. C. Collings, A. S. Batsanov, J. A. Howard, T. B. Marder, *Chem.-Eur. J.* **2012**, *18*, 5022-5035.
- [35] S. S. Li, K. J. Jiang, C. C. Yu, J. H. Huang, L. M. Yang, Y. L. Song, *New J. Chem.*, **2014**, *38*, 4404-4408.

- [36] D. Chercka, S. J. Yoo, M. Baumgarten, J. J. Kim, K. Müllen, *J. Mater. Chem. C*, **2014**, 2, 9083-9086.
- [37] H. Chen, X. Hu, S. C. Ng, *J. Polym. Sci. Part A: Polym. Chem.*, **2010**, 48, 5562-5569.
- [38] S. I. Kawano, C. Yang, M. Ribas, S. Balushev, M. Baumgarten, K. Müllen, *Macromol.*, **2008**, 41, 7933-7937.
- [39] T. Iwamoto, E. Kayahara, N. Yasuda, T. Suzuki, S. Yamago, *Angew. Chem. Int. Ed.* **2014**, 53, 6430-6434.
- [40] A. Yagi, G. Venkataramana, Y. Segawa, K. Itami, *Chem. Commun.*, **2014**, 50, 957-959.
- [41] Y. Zhou, Z. Wang, P. Yang, X. Zu, F. Gao, *J. Mater. Chem.* **2012**, 22, 16964-16970.
- [42] S. Wan, J. Guo, J. Kim, H. Ihee, D. Jiang, *Angew. Chem. Int. Ed.* **2009**, 48, 5439-5442.
- [43] A. Lopez-Moreno, E. M. Perez, *Chem. Commun.* **2015**, 51, 5421-5424.
- [44] G. Liu, A. F. M. M. Rahman, S. Chaunчайyakul, T. Kimura, Y. Kuwahara, N. Komatsu, *Chem.- Eur. J.* **2013**, 19, 16221-16230.
- [45] T. K. Ronson, A. B. League, L. Gagliardi, C. J. Cramer, J. R. Nitschke, *J. Am. Chem. Soc.* **2014**, 136, 15615-15624.

CHAPTER VI. ASSEMBLING MULTIPORPHYRIN STACKS INSIDE THE DNA DOUBLE HELIX

Published: Vybornyi, M.; Nussbaumer, A. L.; Langenegger, S. M.; Häner, R. *Bioconjug. Chem.* **2014**, *25*, 1785 (Cover picture, highlighted in CHIMIA 2014, 68, Nr. 12)

1. Abstract

Double stranded DNA hybrids containing up to four consecutive, face-to-face stacked porphyrins are described. Non-nucleosidic, 5,15-bisphenyl-substituted porphyrin building blocks were incorporated into complementary oligonucleotide strands. Upon hybridization multiple porphyrins are well accommodated inside the DNA scaffold without disturbing the overall B-DNA structure. The formation of double strands containing up to four free base porphyrins is enabled without compromising duplex stability. UV/vis, fluorescence and CD spectroscopy demonstrate the formation of porphyrins H-aggregates inside the DNA double helix and provide evidence for the existence of strong excitonic coupling between interstrand stacked porphyrins. H-aggregation results in considerable fluorescence quenching. Most intense CD effects are observed in stacks containing four porphyrins. The findings demonstrate the value of DNA for the controlled formation of molecularly defined porphyrin aggregates.

2. Introduction

The development of supramolecular architectures for the controlled preparation of porphyrin arrays has received considerable attention over the last decades.^[1-4] The interest originates largely from the desire to mimic naturally occurring light-harvesting complexes, in which efficient energy transfer is enabled by the interaction of highly ordered, protein-bound porphyrins.^[5-9] Modern materials

science intends to elaborate suitable approaches towards artificial systems with tuneable optoelectronic properties.^[10-12] Chromophore organization can be elegantly achieved by the site-specific functionalization of DNA.^[13-21] The use of modified phosphoramidites allows placing functional molecules in a DNA network with high precision.^[22-24] Modifications of DNA are routinely achieved by chemical alteration of the nucleobases or the sugar, as well as through linkages to the phosphate backbone.^[25-28] The integration of porphyrins into DNA by the solid-phase method for structural investigations was pioneered by Richert.^[29] Since then, the number of applications of porphyrin-DNA conjugates has continuously grown.^[30-36] Balaz and Berova introduced porphyrin end-caps^[37,38] as effective optical reporters for structure-sensitive studies of DNA.^[39-41] The construction of porphyrin arrays along DNA of up to 11 molecules was reported by Stulz.^[42] Among the large number of papers on porphyrin-DNA conjugates,^[43-56] few reports describe the use of non-nucleosidic derivatives as base pair surrogates.^[29,50,57,58] Recently, Zhang investigated the interactions of porphyrins in DNA in detail^[58] and the authors clearly established face-to-face stacking of two porphyrin molecules in the double helix. Yet, questions about the structural and electronic interactions of larger arrays of porphyrins stacked inside a double-stranded DNA remained. Additional studies on multiporphyrin systems are essential for the general understanding of chromophore interactions and may help in the design and construction of discrete molecular wires.

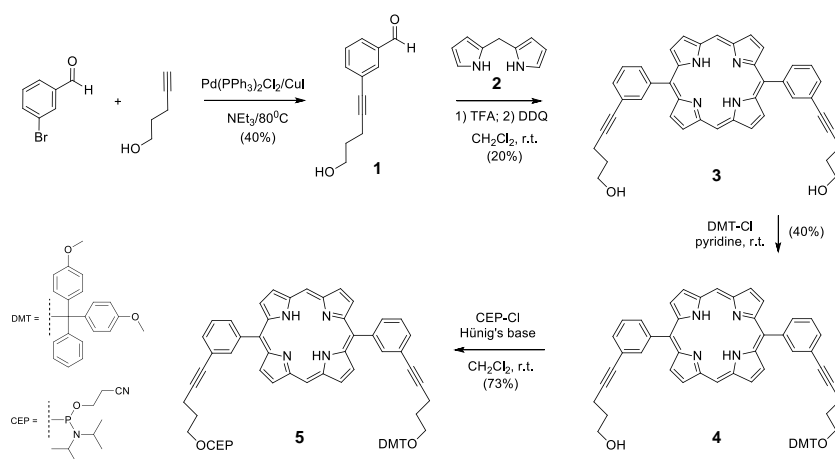
This study describes the preparation and the properties of porphyrin segments of up to four units within a DNA duplex. We demonstrate that porphyrins preferably form H-aggregates in a double helical framework. The close spatial proximity of the chromophores leads to excitonic interactions which are evident from UV/vis, fluorescence and CD data. Furthermore, the thermal denaturation

experiments display that π -stacking interactions of porphyrins contribute significantly to duplex stability.

3. Results

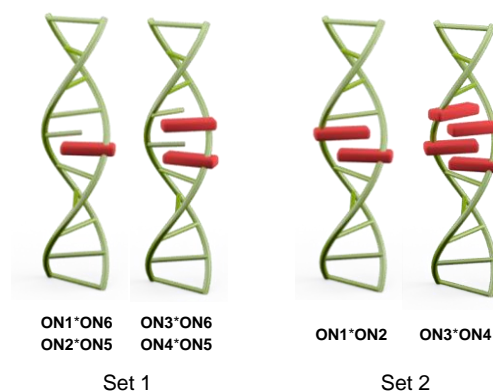
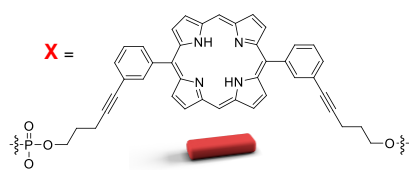
3.1 Synthesis of the porphyrin phosphoramidite and preparation of oligonucleotides

The synthetic route leading to the phosphoramidite building block and the porphyrin-modified oligodeoxynucleotides is shown in Schemes 1 and 2.



Scheme 1. Synthesis of phosphoramidite **5**.

ON1 5' - AGC TCG GTC **AXC** GAG AGT GCA
ON2 3' - TCG AGC CAG **TXG** CTC TCA CGT
ON3 5' - AGC TCG GTC **XXC** GAG AGT GCA
ON4 3' - TCG AGC CAG **XXG** CTC TCA CGT
ON5 5' - AGC TCG GTC ATC GAG AGT GCA
ON6 3' - TCG AGC CAG TAG CTC TCA CGT



Scheme 2. DNA sequences used in this study and schematic illustration of different types of hybrids investigated. Set 1 includes hybrids containing porphyrins opposite a natural nucleobase; hybrids in Set 2 have one or two porphyrin modifications in each strand positioned as shown.

Table 1. Spectroscopic and T_m data of porphyrin-modified single and double strands.

Sequence	λ_{\max}/nm	$\log \epsilon$	λ_{\max}/nm	$\Delta\lambda/$	Q - bands		T_m	$\lambda_{\text{em}}/\text{nm}$	$\lambda_{\text{em}}/\text{nm}$	Φ^h	$H^i, \%$
	20°C	20°C	90°C	nm^a	λ_{\max}/nm	$(\Delta T_m)^b$	20°C	90°C	20°C		
ON1	411	5.55	408	3	508, 542, 576, 632	n/d	634; 696 ^f	635; 697 ^f	0.96 ^f	6	
ON2	414	5.52	408	6	508, 544, 579, 633	n/d	636; 700 ^f	635; 697 ^f	1.00 ^f	9	
ON3	392	5.07	391	1	510, 547, 580, 636	n/d	641; 706 ^g	642; 705 ^g	0.20 ^g	60	
ON4	395	5.27	391	4	510, 547, 580, 636	n/d	641; 706 ^g	642; 705 ^g	0.16 ^g	14	
ON1*ON6	410	5.54	408	2	507, 541, 575, 632	61.4°C ^c (-10.6)	633; 695 ^f	636; 698 ^f	0.96 ^f	8	
ON2*ON5	408	5.54	408	0	507, 541, 573, 626	60.2°C ^c (-11.8)	631; 694 ^f	636; 698 ^f	0.90 ^f	-3	
ON3*ON6	392	5.26	391	1	511, 547, 580, 635	62.8°C ^c (-9.2)	642; 705 ^g	642; 706 ^g	0.23 ^g	3	
ON4*ON5	394	5.35	391	3	511, 546, 579, 634	56.0°C ^c (-16.0)	642; 705 ^g	642; 706 ^g	0.19 ^g	11	
ON1*ON2	391	5.32	408	-17	510, 547, 577, 633	72.2°C ^c ^d (+0.2)	638; 699 ^f	635; 697 ^f	0.73 ^f ; 0.33 ^g	76	
ON3*ON4	390	4.97	391	-1	510, 545, 580, 635	70.0°C ^c ^e (-2.0)	643; 708 ^g	642; 705 ^g	0.14 ^f ; 0.18 ^g	102	

Conditions: 1 μM of each strand, 10 mM sodium phosphate buffer pH = 7.2, 100 mM NaCl, 1 mM Na₂EDTA. ^a $\lambda_{\max}(20\text{ }^\circ\text{C}) - \lambda_{\max}(90\text{ }^\circ\text{C})$ of the Soret bands; ^b relative to the unmodified duplex **ON5*ON6** ($T_m = 72.0\text{ }^\circ\text{C}$), estimated error $\pm 1\text{ }^\circ\text{C}$; ^c value determined at 260 nm; ^d value determined at 408 nm; ^e value determined at 391 nm; ^f λ_{ex} : 408 nm; ^g λ_{ex} : 391 nm; ^h quantum yield relative to the oligomer **ON2**, which was defined as 1.0 (for details see SI); ⁱ hyperchromicity, the value was calculated from the Soret band maxima at 20 $^\circ\text{C}$ and 90 $^\circ\text{C}$.

The required phosphoramidite building block suitable for solid-phase DNA synthesis was prepared as shown in Scheme 1. Condensation of aldehyde **1**, prepared from 3-bromobenzaldehyde and 4-pentyn-1-ol, with 2,2'-dipyrrromethane (**2**)⁵⁹ in the presence of trifluoroacetic acid gave the bis-hydroxy derived porphyrin **3**. Compound

3 shows the typical spectroscopic features of porphyrins. The UV-spectrum of **3** in organic solvents, such as THF, exhibits an intense Soret band at 412 nm and four low-intensity Q-bands (Figure 1). Subsequent protection of **3** with 4,4'-dimethoxytrityl chloride provided derivative **4**, which was converted into phosphoramidite **5**. The average stepwise coupling yields obtained for incorporation of **5** during automated oligonucleotide synthesis were in the range of 80% using a coupling time of 600 seconds. Four oligonucleotides (**ON1-ON4**, Scheme 2) containing one or two porphyrin-units were synthesized and purified by RP HPLC and their molecular weights were confirmed by MS. **ON5** and **ON6** serve as reference oligonucleotides.

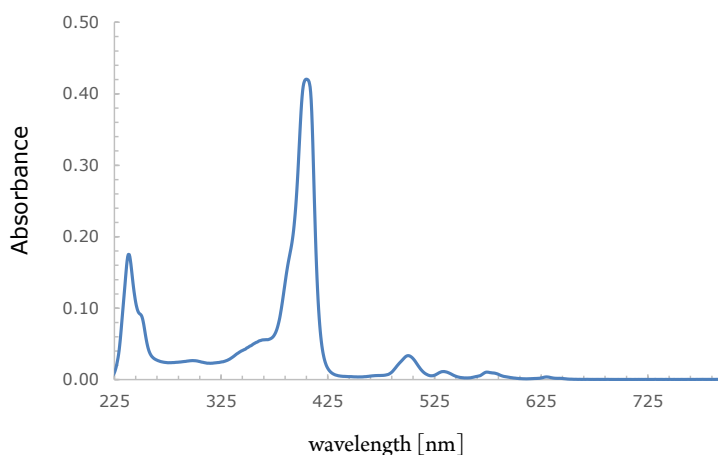


Figure 1. UV/vis of **3** in THF ($c=10^{-6}$ M)

3.2 Hybrid stability

Thermal denaturation experiments were carried out to establish the influence of the porphyrin modification on duplex stability. Melting curves were measured in the nucleobase region (260 nm) and at the Soret band (Figures 2-4). The melting temperatures (T_m) are summarized in Table 1. Hybrid **ON5*ON6**, which is used as the unmodified reference duplex, has a T_m of 72 °C. All hybrids carrying porphyrin molecules opposite a natural base (Set 1, see Scheme 2) show a relatively large decrease in the T_m ($\Delta T_m \sim 10-16$ °C). This observation is in agreement with previous

findings that incorporation of one^{29,50,57} or several⁴² porphyrins in the absence of interstrand porphyrin-porphyrin interactions leads to a considerable reduction of duplex stability. Obviously, stacking and hydrophobic interactions between porphyrin and the DNA cannot counterbalance the energetic cost associated with the loss of an AT base pair. On the other hand, hybrids of Set 2 containing one or two modifications in opposite positions possess approximately the same thermal stabilities as the unmodified duplex. Thus, porphyrin-porphyrin interstrand interactions compensate for the loss of binding energy of a canonical base pair.

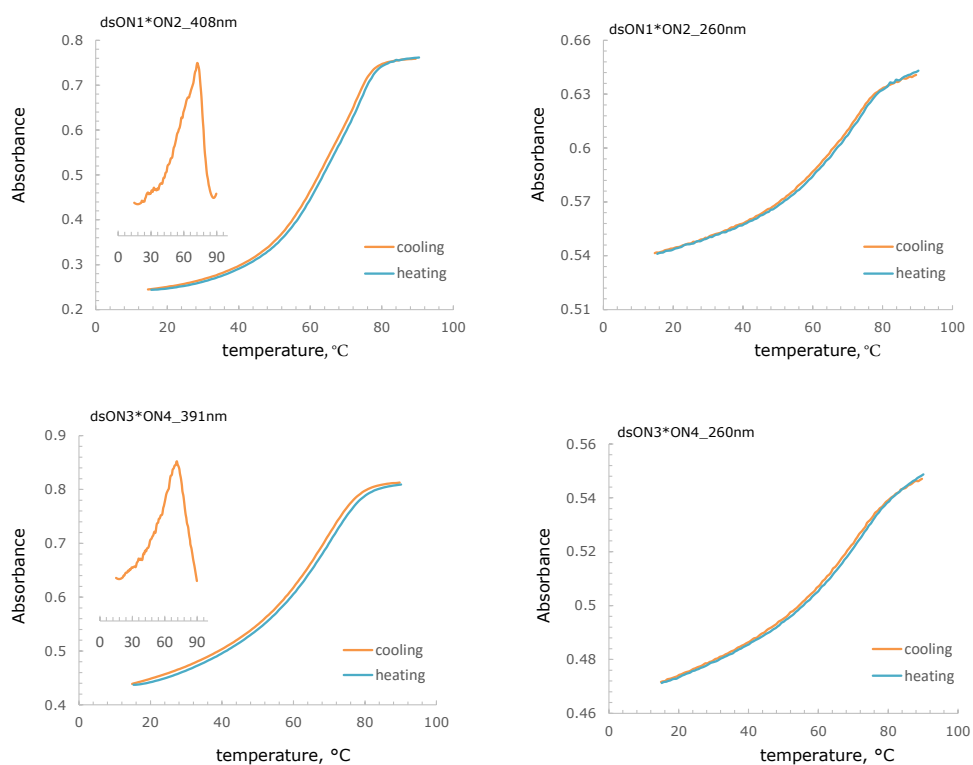


Figure 2. T_m curves of the double strands (set 2). Inset: the first derivatives. Conditions: see Table 1.

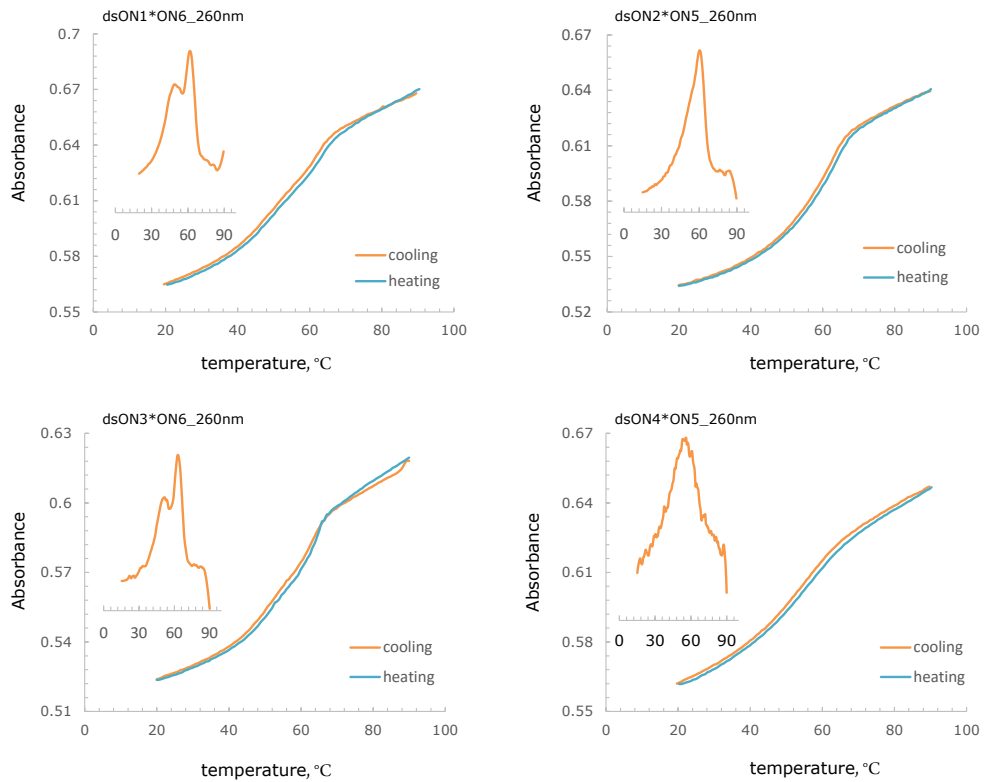


Figure 3. T_m of the double strands (set 1). Inset: the first derivatives. Conditions: see Table 1.

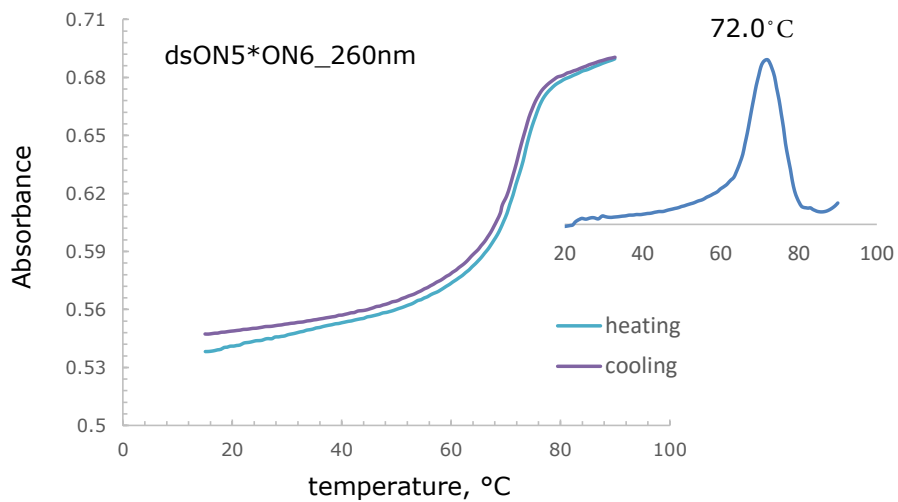


Figure 4. T_m of the reference duplex **ON5*ON6**. Inset: the first derivative. Conditions: see Table 1.

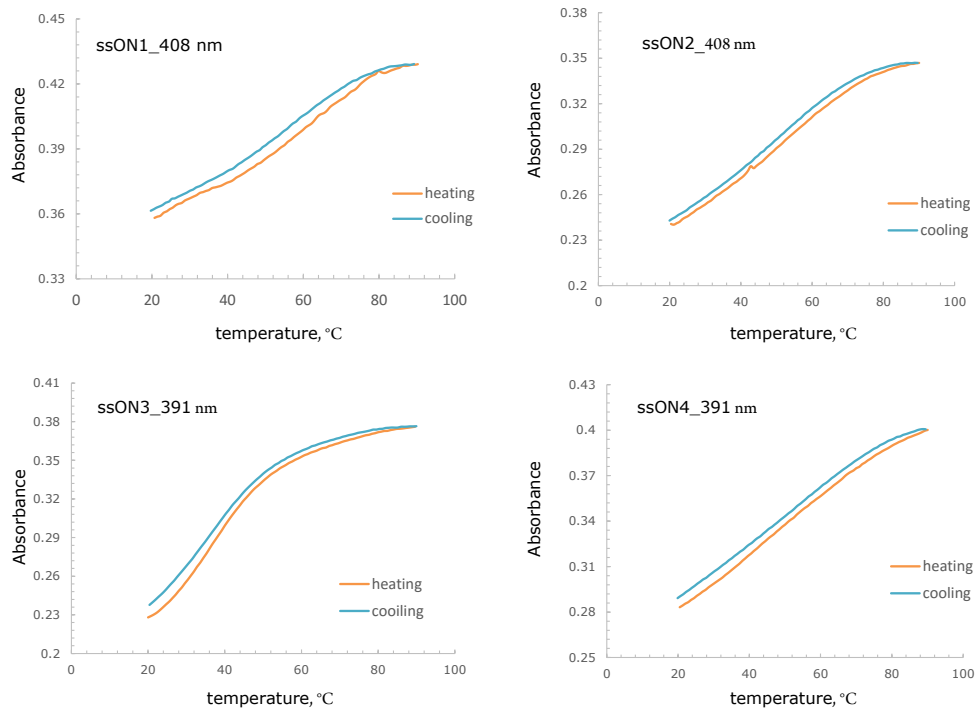


Figure 5. T_m of the single strands. Conditions: see Table 1.

3.3 UV/vis spectroscopy

Porphyrin interactions are conveniently monitored by UV/vis spectroscopy. The most prominent changes occur in the Soret region. Absorption spectra of single strands **ON1-ON4** are shown in Figure 6. All oligomers exhibit the signals expected for porphyrin–DNA conjugates: the Soret band around 400 nm and four Q-bands, (~500–640 nm); the region below 300 nm is dominated by the absorption of the nucleobases. All numerical data are summarized in Table 1. The hydrophobic aromatic part of DNA supports stacking interactions also in single strands. In the present case, interactions between nucleobases and porphyrins as well as between two adjacent porphyrins (possible in **ON3** and **ON4**) are confirmed by changes in the position of the Soret band.⁶⁰ A blue-shift of 19 nm is observed between the oligomers containing a single (**ON1**, **ON2**) and those containing two adjacent porphyrin modification (**ON3**, **ON4**, Table 1, $\lambda_{\text{max}}@20^{\circ}\text{C}$). A blue-shift of this

magnitude suggests the presence of face-to-face interactions of the neighboring porphyrins. In single strands with one modification, the interaction between porphyrin and nucleobases can be followed in temperature-dependent experiments. Thus, a red-shift is observed in **ON1** (3 nm) and **ON2** (6 nm) when the temperature is decreased from 90°C to 20°C (Table 1, column $\Delta\lambda$). Hypochromicities measured at the Soret band are small (<10%) in oligomers containing a single porphyrin unit (**ON1** and **ON2**) and larger in those with two consecutive moieties (**ON3** and **ON4**; 60% and 14%).

Absorption spectra of the different double stranded hybrids are given in Figure 7. Set 1 comprises the strand combinations in which only *intrastrand* porphyrin interactions are possible. The UV/vis spectra of these oligomers in dissociated (90 °C) and hybridized form (20 °C) are depicted in Figure 7. Duplex formation is accompanied by minor changes in the porphyrin absorbance region. For example, the Soret band is not (**ON2*ON5**) or only slightly red-shifted upon cooling, i.e. hybrid formation (see Table 1, $\Delta\lambda$). Also, the hyperchromicity for the maximum of the porphyrin absorbance is rather small for these samples ($\leq 11\%$).

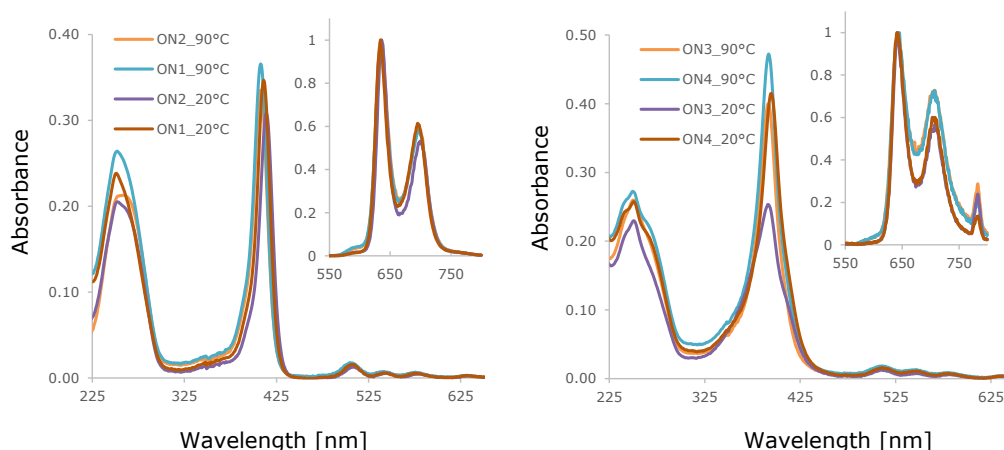


Figure 6. Absorption and normalized emission (inset) spectra of single strands containing one (top) or two (bottom) porphyrin units. Conditions: see Table 1; λ_{ex} 408 nm (**ON1**, **ON2**) and 391 nm (**ON3**, **ON4**).

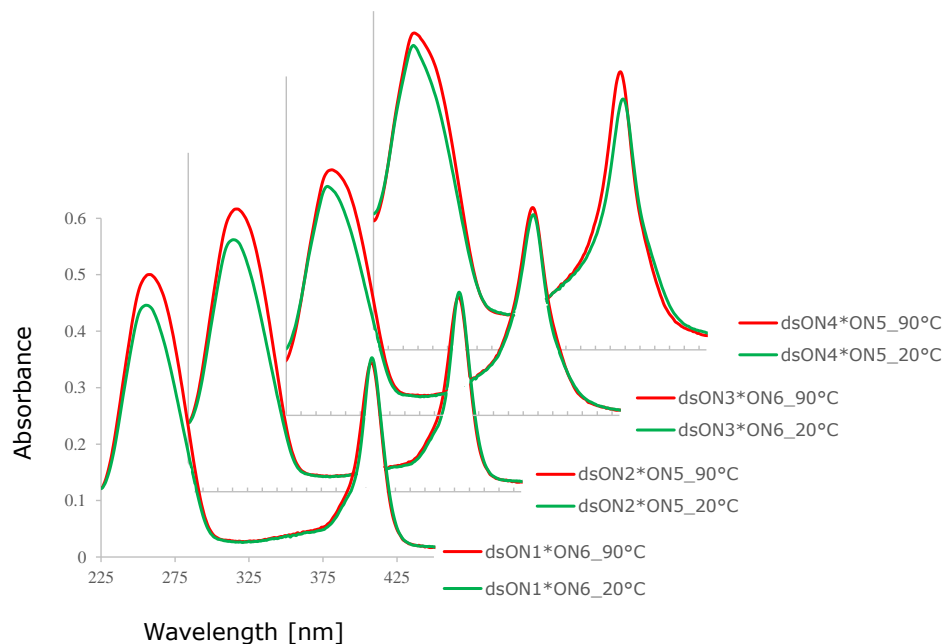


Figure 7. Temperature effect (90 vs. 20 °C) in UV/vis spectra observed for oligomer combinations of Set 1. Conditions: see Table 1.

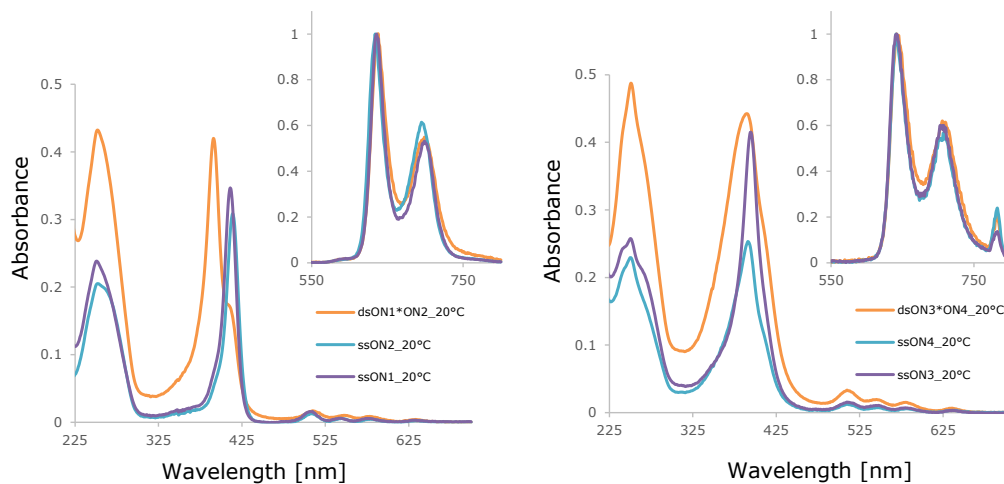


Figure 8. Absorption and normalized emission (inset) spectra of hybrids and single strands of Set 2 at 20 °C. Conditions: see Table 1; $\lambda_{\text{ex}} = 408 \text{ nm}$ (**ON1**, **ON2**) and 391 nm (**ON3**, **ON4**).

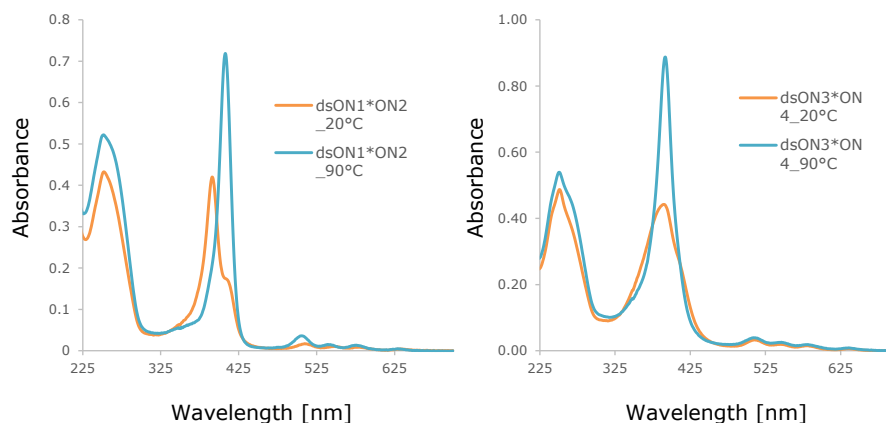


Figure 9. Temperature effect (90 vs. 20 °C) in UV/vis spectra observed for oligomer combinations of Set 2. Conditions: see Table 1.

Spectroscopic effects are much more significant in Set 2. This set contains the strands which, upon duplex formation, bring together porphyrins from the two single strands thus assembling porphyrin stacks inside the DNA double helix. Formation of interstrand stacks results in strong excitonic interactions between porphyrins. Hybridization of **ON1** and **ON2**, which bring together two porphyrins (Figure 8), results in a considerable blue shift of the Soret band (391 nm in the hybrid vs. 411 and 414 nm in the single strands). A second, weaker signal (shoulder) appears at 408 nm. Thermal denaturation at 90 °C leads to the complete disappearance of the 391 nm band and concurrent growth of the 408 nm band (see Figure 9). At the same time, a strong hyperchromicity (76%., Table 1) is observed. These changes provide strong support for the presence of H-type interaction.⁶¹⁻⁶³ Along with the blue shift of the Soret band, formation of porphyrin H-aggregates has been reported to result in a red shift of the Q-bands.⁶⁴ Such a red shift, albeit to a slight extent, is also observed in the present system (see e.g. Table 1). The formation of the hybrid **ON3*ON4**, which results in a stack of four porphyrins, is accompanied by a more complex behavior. A substantial broadening of the Soret band (maximum at 390 nm) occurs, suggesting the presence of multiple electronic interactions between the

individual porphyrin molecules (Figure 8). Additionally, a strong hyperchromicity of $\sim 100\%$ results from thermal dissociation. In summary, UV/vis data support a model in which the hydrophobic porphyrins are assembled in between the DNA base stack, thus maximizing π -stacking interactions and minimizing exposure to the aqueous environment.

3.4 Fluorescence spectroscopy

The emission spectra of porphyrin-modified single strands exhibit the characteristic pattern of free-base porphyrin fluorescence. Upon excitation at the Soret band, two separate emission bands are observed for all samples in the area of 600-750 nm (Figure 6, insets). The normalized emission spectra of **ON1** and **ON2** or **ON3** and **ON4** are essentially superimposable. Emission maxima of **ON3** and **ON4** are red-shifted (5-10 nm) compared to **ON1** and **ON2** (Table 1, column λ_{em}). When two porphyrins are adjacent, their stacking leads to a quenching of the fluorescence. Thus, single strands **ON1** and **ON2** have higher quantum yields (Φ_f , Table 1) relative to **ON3** and **ON4**, which is in agreement with the general observation that fluorescence of porphyrin H-aggregates is quenched. Emission spectra of the double strands of Set 1 are similar to those of the single strands. This includes a small red shift of the emission bands of hybrids **ON3*ON6** and **ON4*ON5** compared to the duplexes containing a single porphyrin incorporation. Furthermore, the relative quantum yields are hardly changed upon duplex assembly.

In Set 2, duplex formation does not result in substantial changes in the shape of the fluorescence spectra with respect to the single strands (Figure 9, insets). However, the relative quantum yield (Φ_f , Table 1) strongly depends on the excitation wavelength in hybrid **ON1*ON2**. It equals 0.73 when excited at 408 nm compared to 0.33 after excitation at 391 nm. This difference can again be rationalized by

fluorescence quenching due to H-aggregation (391 nm). In hybrid **ON3*ON4**, however, the excitation wavelength exhibits a modest influence on Φ_f , which is 0.18 (408 nm) and 0.14 (391nm). Interestingly, combining four porphyrin units by annealing **ON3** and **ON4** within a DNA scaffold doubles the size of the stack without a substantial loss in the quantum yield.

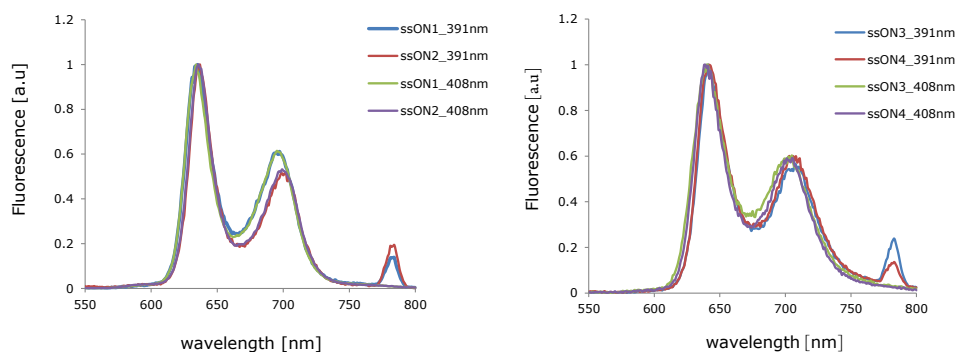


Figure 10. Fluorescence spectra (excitation wavelengths are shown in a graph legend). (The bands at 782 nm are artifacts caused by the second order transmission of the monochromator (782 nm = 2x391nm)).

3.5 Excitation spectra

For the single strands **ON1** and **ON2** containing a single porphyrin unit, absorption and excitation spectra in the region of the Soret band coincide entirely (Figure 11). For doubly modified single strands (**ON3** and **ON4**) a modest broadening is observed due to electronic interaction of the neighboring porphyrin rings. Hybrids of Set 1 show very similar behavior as the single strands (Figure 11). The picture changes with hybrids of Set 2, in particular for **ON1*ON2** (Figure 13). Absorption and excitation spectra for this hybrid differ significantly in the 370-420 nm region. As described above, interstrand stacking of the porphyrins leads to the splitting of the Soret band in the absorption spectrum into a high-intensity blue-shifted and a low-intensity red-shifted component. In the excitation spectrum, however, the signal intensity is reversed with the 408 nm band being dominant.

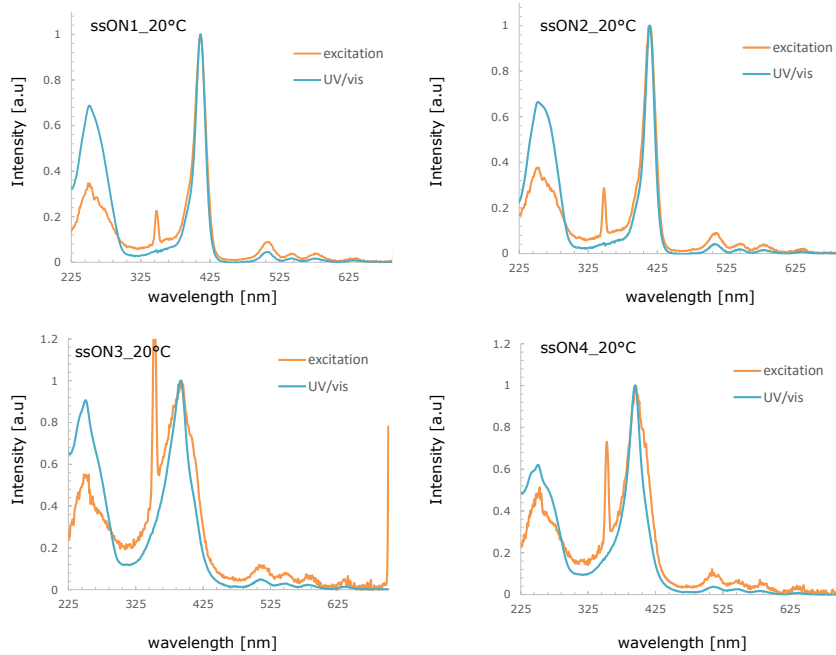


Figure 11. Normalized fluorescence excitation spectra for the single strands (recorded for the 696 nm emission band of the **ON1** and **ON2** strands, and 706 nm of the **ON3** and **ON4**) and UV/vis.

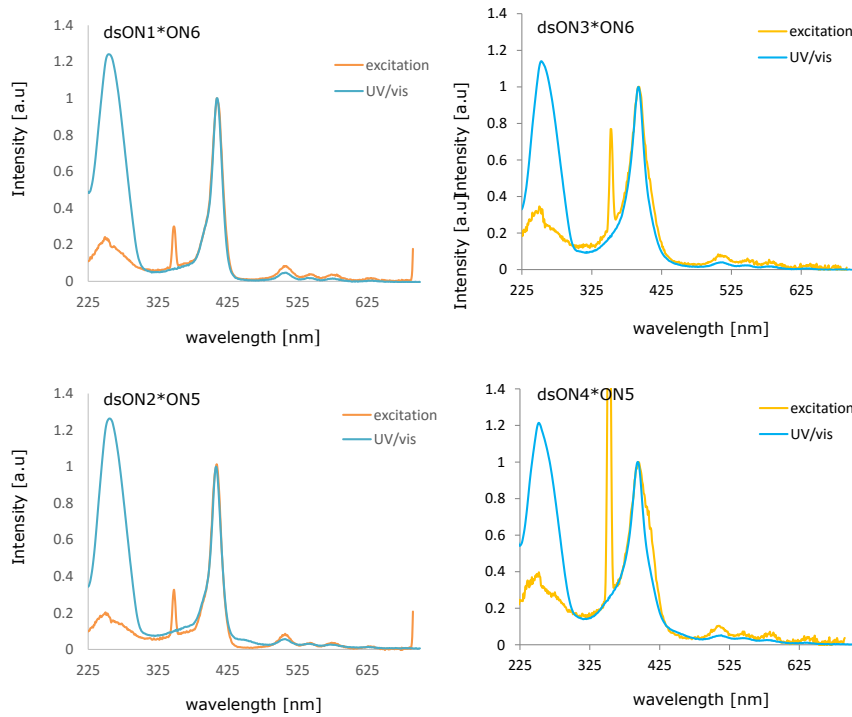


Figure 12. Normalized fluorescence excitation spectra for the double strands from the set 1 (recorded for the 696 nm emission band of the **ON1*ON6** and **ON2*ON5** hybrids, and 706 nm of the **ON3*ON6** and **ON4*ON5**) and UV/vis.

This is in alignment with the general observation that the formation of H-aggregates (blue-shifted band) results in a reduction of emission intensity.⁶⁵ These features are less well recognizable in hybrid **ON3*ON4** (Figure 13) since signals are considerably broadened due to aggregation of four porphyrins.

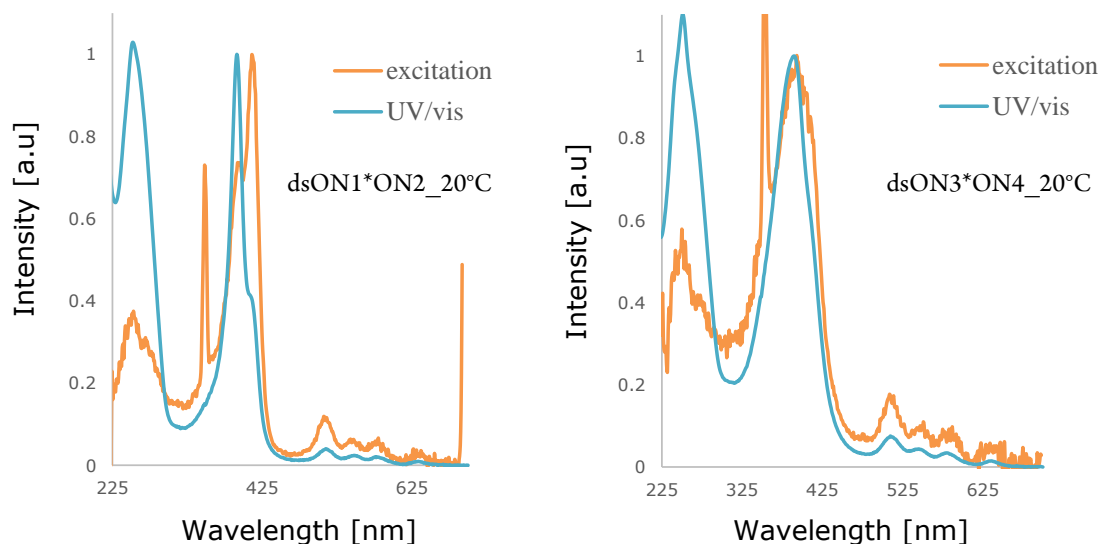


Figure 13. Normalized UV/vis absorption and excitation spectra at 20 °C. Conditions: see Table 1; λ_{ex} 696 nm (**ON1*ON2**) and 706 nm (**ON3*ON4**).

3.6 CD spectroscopy

Porphyrins are well-documented reporters for structural studies on the basis of excitonic coupling.^[66,67] Single strands **ON1** and **ON2** exhibit weak or no CD effects in the region of the Soret band (see Figure 14). A weak induced CD signal at 408 nm is observed ($\Delta\epsilon = 20 \text{ M}^{-1}\text{cm}^{-1}$) for **ON1**. Similar findings were reported for different type of single-stranded porphyrin-DNA conjugates.⁶⁸ No significant signals are present for **ON2** in the 400 nm region. For **ON3**, which has two adjacent porphyrins, a strong, complex signal (430 nm, $\Delta\epsilon = +15 \text{ M}^{-1}\text{cm}^{-1}$ and 387 nm, $\Delta\epsilon = -54 \text{ M}^{-1}\text{cm}^{-1}$) is observed. **ON4** exhibits only a very weak positive signal 391 nm. All aforementioned features disappear after unfolding of the strands at 90 °C (Figure 14).

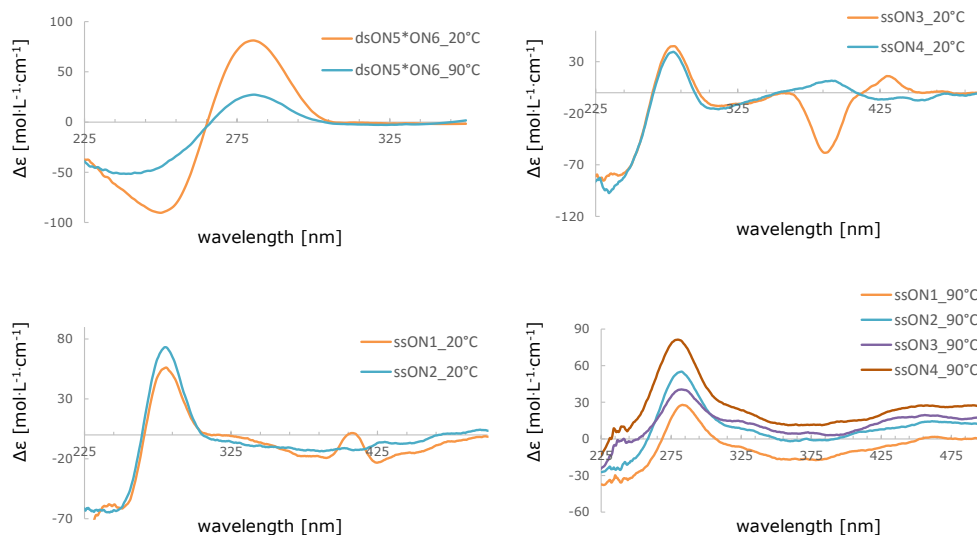


Figure 14. CD data. Conditions: see Table 1.

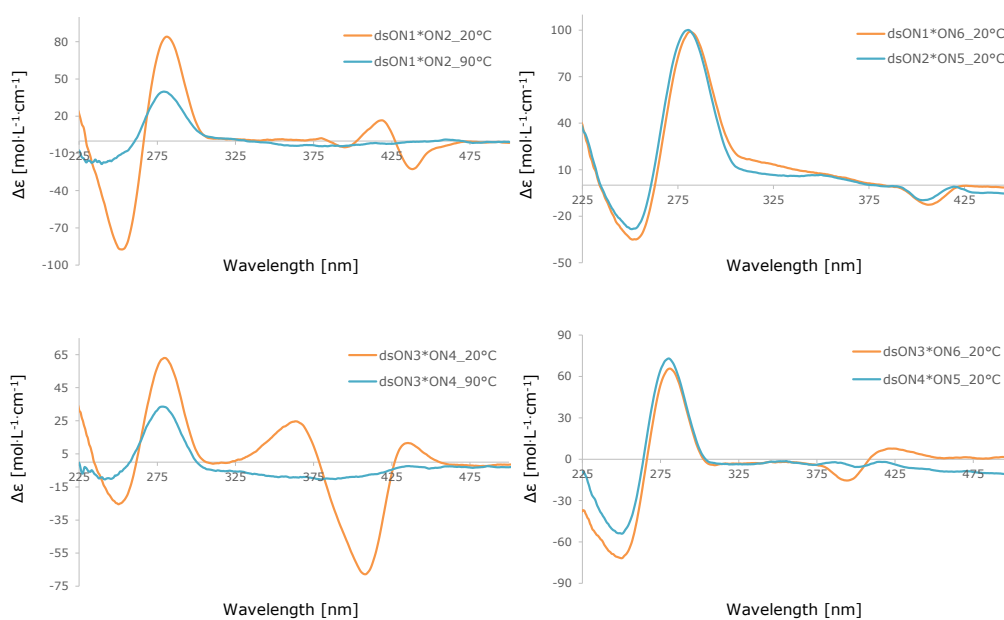


Figure 15. CD spectra of double strands (left: Set 1; right: Set 2 at different temperature). Conditions: see Table 1.

CD spectra of duplexes are displayed in Figure 15. All hybrids exhibit the typical DNA B-form signal in the nucleobase absorbance region. Thus, porphyrins are well accommodated in the double helix perturbing the B-DNA structure to a significant extent. For example, both **ON1*ON6** and **ON2*ON5** have a weak

induced CD ($\Delta\epsilon = -13 M^{-1}cm^{-1}$ and $-10 M^{-1}cm^{-1}$, respectively) with a maximum almost coinciding with the Soret band (see also Figure 16). This type of CD signal is strongly reminiscent of DNA-intercalated cationic porphyrins.⁶⁹⁻⁷¹ CD spectra of **ON3*ON6** show a bisignate profile (424 nm, $\Delta\epsilon = +8 M^{-1}cm^{-1}$ and 394 nm, $\Delta\epsilon = -15 M^{-1}cm^{-1}$), whereas hybrid **ON4*ON5** is basically CD silent in this region. The most significant effects are observed in Set 2. Interstrand porphyrin interactions in duplex **ON1*ON2** lead to a bisignate Cotton effect due to exciton coupling (438 nm, $\Delta\epsilon = -23 M^{-1}cm^{-1}$ and 418 nm, $\Delta\epsilon = +17 M^{-1}cm^{-1}$). Interestingly, the center of the couplet lies in the region of the red-shifted absorption shoulder (Figure 16). Negligible CD activity is present, however, at the dominant absorption signal (391 nm) ascribed to H-type (face-to-face) aggregation. Finally, aggregation of four porphyrins in duplex **ON3*ON4** gives rise to very intense signals. At the same time, these signals are also rather complex (435 nm, $\Delta\epsilon = +12 M^{-1}cm^{-1}$, 408 nm, $\Delta\epsilon = -68 M^{-1}cm^{-1}$ and 364 nm, $\Delta\epsilon = +25 M^{-1}cm^{-1}$), which can be ascribed to the presence of multiple porphyrin interactions.^[72] Again, all features disappear upon heating to 90°C, showing that structural organization of the porphyrins is governed by the DNA supramolecular framework.

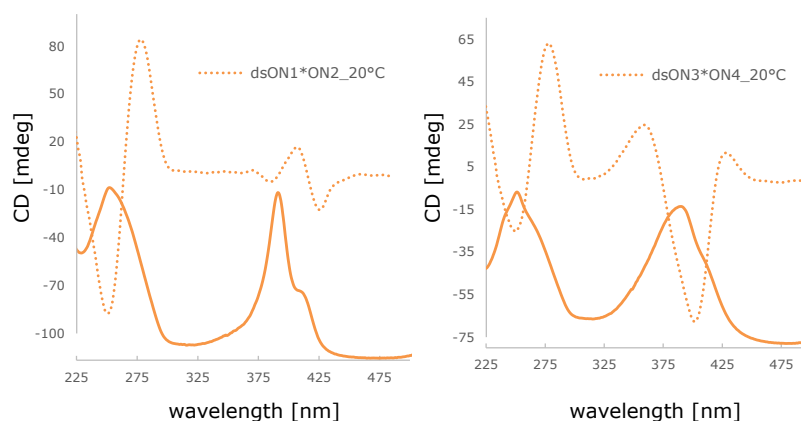


Figure 16. CD-UV/vis correlation for the **ON1*ON2** and **ON3*ON4** (dotted lines correspond to CD spectra and solid lines to UV/vis).

4. Conclusions

In summary, we have presented the synthesis and spectroscopic characterization of porphyrin-DNA conjugates. Modified oligonucleotides are prepared by incorporation of one or two non-nucleosidic, 5,15-bisphenyl-substituted porphyrin building block *via* phosphoramidite chemistry. Hybridization of complementary strands enables the formation of duplexes containing up to four consecutive free base porphyrins. Pairwise placement of porphyrins in opposite positions maintains duplex stability, whereas a considerable reduction in the T_m is observed when porphyrins are positioned opposite to natural nucleobases (ΔT_m up to -12 °C per modification). UV/vis spectroscopy supports a model of H-aggregated porphyrins assembled inside the DNA double helix. H-aggregation results in considerable fluorescence quenching. Furthermore, CD spectroscopy provides additional evidence for substantial excitonic coupling of interstrand stacked porphyrins; in particular, strong CD effects are observed in the duplex with four stacked porphyrins. Notably, stacks of multiple porphyrins are well accommodated inside the DNA scaffold without disturbing the overall B-DNA structure and duplex stability. The present findings demonstrate the value of DNA for the controlled formation of molecularly defined porphyrin aggregates.

5. Experimental part

Organic synthesis and characterization of the compounds. All chemical reagents and solvents required for the synthesis have been purchased from commercial suppliers (Aldrich, Alfa Aesar or TCI) and used without further purification. Water for spectroscopic measurements was obtained from MilliQ system. Analytical thin layer chromatography (TLC) was carried out using aluminium sheets, pre-coated with silica gel 60 and fluorescent indicator. The silica gel for the column

chromatography had 60Å pore size, 230-400 mesh. AIOx (507-C-1, neutral) for a flash chromatography was purchased from CAMAG (Switzerland). Air-sensitive reactions and manipulations have been carried out under Ar atmosphere. Glassware was dried in an oven at 100 °C before usage. All synthesized materials were kept in a fridge at 2°C under Ar. NMR spectra were obtained on a Bruker AV 300 (300 MHz) spectrometer at 298 K. High resolution mass-spectrometric data for building blocks were obtained on Thermo Fisher LTQ Orbitrap XL using Nano Electrospray Ionization. Mass spectrometry of oligonucleotides was performed on a Sciex QSTAR pulsar (hybrid quadrupole time-of-flight mass spectrometer, Applied Biosystems). The method used: ESI-MS in negative mode, CH₃CN/H₂O/TEA.

Spectroscopic measurements. UV/VIS spectra were collected in the cuvettes with an optical path of 1 cm over the range of 200-700 nm on a Varian Cary-100 Bio-UV/VIS spectrophotometer equipped with a Varian Cary-block temperature controller. Heating-cooling cycles were recorded with temperature changing 0.5°C/min. Fluorescence data were collected on the Varian Cary Eclipse fluorescence spectrofluorimeter equipped with the Varian Cary-block temperature controller. Unless otherwise noted the following settings of the instrument were used: the slit width 5 nm for fluorescence and excitation spectra, medium sensitivity of the detector. If not stated otherwise, all samples for the UV/vis and fluorescence were measured for the following mixture composition: 1µM of each strand, 10mM phosphate buffer pH=7.2, 100mM NaCl, 1mM Na₂EDTA. Melting temperature (T_m) values were determined as the maximum of the first derivative of the melting curve.

Measurements of the relative fluorescence quantum yields. The absorbance A_s of the porphyrin in the Soret region was adjusted at a selected wavelength (0.04-0.05). The fluorescence was recorded, and the emission profile for each sample was integrated (F_s). The maximal ratio of the A_s/F_s was taken as 1. Since

refractive indexes of all solutions are equal, it is possible to calculate a relative quantum yield by calculating a ratio between A_i/F_i (where i is a sample number) and a maximum value for A_s/F_s .

CD spectroscopy. CD spectra were recorded on a JASCO J-715 spectropolarimeter using quartz cuvettes with an optical path of 1 cm (50 nm/min measurement speed, 1 nm data pitch). The data were collected in Θ (mdeg) and recalculated to $\Delta\epsilon$ ($M^{-1}\cdot cm^{-1}$).

Synthesis and characterization of compounds

3-(5-Hydroxypent-1-ynyl)benzaldehyde (1). 4-Bromobenzaldehyde (3 ml, 26 mmol), $Pd(PPh_3)_2Cl_2$ (105 mg, 0.15 mmol), and CuI (55 mg, 1.5 mmol) were placed in a reaction flask. After heating to 80°C, triethylamine (50 mL) and 4-pentyn-1-ol (3 ml, 31 mmol) were added. The reaction mixture was stirred at 80°C overnight. After cooling to room temperature, 20 mL of EtOAc were added and a grey precipitate was removed by filtration, and the filtrate was concentrated. The product was purified by column chromatography (SiO_2 , EtOAc/hexane, 1:2), which furnished 1.9 g (yield 40 %) of **1**. Analytical data for **1**: $R_f=0.36$ (SiO_2 , EtOAc/hexane, 1:2). 1H NMR (300 MHz, DMSO), δ : 9.99 (s, 1H), 7.92–7.81 (m, 2H), 7.70 (d, $J=7.7$ Hz, 1H), 7.58 (t, $J = 7.6$ Hz, 1H), 4.56 (t, $J = 5.1$ Hz, 1H), 3.54 (dd, $J = 11.5, 6.0$ Hz, 2H), 2.50 (t, $J = 7.1$ Hz, 2H), 1.71 (t, $J=6.6$ Hz, 2H). ^{13}C NMR (75 MHz, DMSO), δ :192.6, 136.7, 136.4, 132.4, 129.5, 128.2, 124.2, 92.2, 79.2, 59.4, 31.4, 15.3. HRMS for $C_{12}H_{12}O_2$: found (calculated 188.0821).

5,15-bis-3-(5-hydroxypent-1-ynyl)phenylporphyrin (3). Compounds **1** (500 mg, 3.42 mmol) and **2**⁵⁹ (640 mg, 3.42 mmol) were dissolved in dry CH_2Cl_2 (300 ml). TFA (0.45 mL) was added dropwise. The reaction mixture was stirred at room temperature for 2 hours, after which time DDQ (770 mg, 3.42 mmol) was added. The dark brown solution was stirred overnight. Afterwards, the reaction

mixture was filtered through AlOx. After washing with CH₂Cl₂/MeOH 96/4, the filtrate was concentrated and purified by flash chromatography on AlOx (eluent: CH₂Cl₂/MeOH 96/4). The solvents were evaporated and the precipitate was collected. This furnished 228 mg (yield 20%) of the title compound **3**. Analytical data for **3**: R_f=0.3 (AlOx, CH₂Cl₂/MeOH 96/4). ¹H NMR (300 MHz, DMSO), δ: 10.66 (s, 2H), 9.68 (d, J = 4.7 Hz, 4H), 9.02 (d, J=4.6 Hz, 4H), 8.24 (d, J=2.2 Hz, 4H), 8.03–7.72 (m, 4H), 3.54 (t, J=6.2 Hz, 4H), 2.58–2.50 (t, 4H), 1.73 (t, J=6.6 Hz, 4H), -3.33 (s, 2H). The ¹³C NMR was difficult to measure due to a low solubility of **3**. HRMS (M+H⁺) for C₄₂H₃₅N₄O₂⁺: found 627.2740 (calculated 627.2755).

15-3-[(5-hydroxypent-1-ynyl)-phenyl]-5-3-[[bis(4-methoxyphenyl)phenylmethoxy]-(pent-1-ynyl)phenyl]-porphyrin (4). 4,4'-Dimethoxytrityl chloride (115 mg, 0.34 mmol) was added to solution of **3** (228 mg, 0.34 mmol) in dry pyridine (10 mL). The mixture was stirred overnight and concentrated. The residue was dissolved in a small volume of CH₂Cl₂ and subjected to column chromatography (AlOx, CH₂Cl₂/MeOH/NEt₃ 97.5/2/0.5). This furnished 125 mg (yield 38%) of purple crystals. Analytical data for **4**: R_f=0.45 (AlOx, CH₂Cl₂/MeOH/ NEt₃ 97.5/2/0.5); ¹H NMR (300 MHz, DMSO), δ: 10.66 (s, 2H), 9.67 (s, 4H), 9.01 (dd, J=8.8, 4.6 Hz, 4H), 8.25 (s, 3H), 8.10 (s, 1H), 7.9–7.71 (m, 4H), 7.45–7.04 (m, 8H), 6.88–6.78 (t, J=25.4 Hz, 5H), 4.53 (s, 1H), 3.54 (d, J=5.5 Hz, 2H), 3.43 (s, 6H), 3.14 (s, 2H), 2.59 (d, J = 26.9 Hz, 4H), 1.76 (dd, J = 23.7, 17.0 Hz, 4H), -3.31 (s, 2H). ¹³C NMR (75 MHz, DMSO), δ: 157.8, 146.2, 144.9, 140.7, 136.8, 135.9, 133.9, 132.7, 130.7, 129.5, 127.6, 126.8, 126.3, 122.2, 117.6, 112.9, 105.8, 90.9, 85.2, 80.6, 61.3, 59.4, 54.6, 31.5, 28.4, 15.6. HRMS for C₆₃H₅₂N₄O₂: found 928.3981 (calculated 928.2983)

15-3-[(5-hydroxypent-1-ynyl)phenyl]-5-3-[[bis(4-methoxyphenyl)phenylmethoxy]-(pent-1-ynyl)phenyl]-porphyrin cyanoethyl

(diisopropylamino)phosphoramidite (5). Compound **4** (125 mg, 0.128 mmol) was dissolved in CH₂Cl₂ (10 mL). After addition of *N,N*-diisopropyl-ethylamine (150 μL), a solution of 2-cyanoethyl-*N,N*-diisopropylchloro-phosphoramidite (40 mg, 0.166 mmol, 1.3 eq) was added. The mixture was stirred for 3 h. The solvent was evaporated, and the residue was dissolved in EtOAc/NEt₃ 99.5/0.5 and purified by column chromatography (AlOx; EtOAc/NEt₃ 99.5/0.5), furnished 110 mg (yield 73%) of **5** as a dark brown foam. Analytical data for **5**: R_f=0.9 (AlOx, EtOAc/NEt₃ 99.5/0.5); ¹H NMR (300 MHz, DMSO), δ: 10.65 (s, 2H), 9.65 (dd, J=4.6, 1.9 Hz, 4H), 9.00 (dd, J=7.0, 4.7 Hz, 4H), 8.24 (s, 3H), 8.10 (d, J=4.1 Hz, 1H), 7.94–7.70 (m, 4H), 7.48–7.00 (m, 8H), 6.90–6.71 (dd, J=51.7, 7.1 Hz, 5H), 3.81–3.63 (m, 2H), 3.57–3.47 (m, 1H), 3.42 (s, 4H), 3.14 (t, J=6.0 Hz, 1H), 2.77–2.55 (m, 3H), 1.85 (s, 2H), 1.10–0.98 (m, 6H), -3.31 (s, 1H). ¹³C NMR (75 MHz, DMSO), δ: 157.8, 146.2, 144.9, 140.7, 140.7, 136.8, 136.8, 135.9, 134.0, 132.7, 130.7, 130.6, 129.5, 127.6, 126.3, 122.2, 118.8, 117.6, 112.9, 105.9, 90.6, 85.2, 80.8, 61.5, 58.1, 54.6, 42.34, 29.1, 24.3, 19.8, 15.6. ³¹P NMR (122 MHz, DMSO), δ: 146.64. HRMS (M+H⁺) for C₇₂H₇₀N₆O₅P⁺: found 1129.5136 (calculated 1129.5140).

Table 2. Molecular weights of the oligonucleotides

Code	Oligonucleotide sequence	Mass found	Mass calculated
ON1	5'-AGC TCG GTC AXC GAG AGT GCA-3'	6852.25	6855.03
ON2	5'-TGC ACT CTC GXT GAC CGA GCT-3'	6754.27	6756.95
ON3	5'-AGC TCG GTC XXC GAG AGT GCA-3'	7227.49	7229.80
ON4	5'-TGC ACT CTC GXX GAC CGA GCT-3'	7139.42	7140.74
ON5	5'-AGC TCG GTC ATC GAG AGT GCA-3'	6468.11	6471.24
ON6	5'-TGC ACT CTC GAT GAC CGA GCT-3'	6379.11	6382.18

Oligonucleotide synthesis and purification. Oligonucleotides were prepared via automated DNA synthesis by a standard synthetic procedure ('trityl-off' mode) on a 394-DNA/RNA synthesizer (Applied Biosystems Instruments). The coupling time for phosphoramidite **5** (0.1M solution in THF) was elongated to 600 seconds. Cleavage from the solid support and final deprotection were performed without delay after completion of the oligonucleotide synthesis by treatment with 27% aqueous ammonia solution (Aldrich, Trace Select®) at 55 °C for 16 hours. All oligonucleotides were purified by reverse-phase HPLC (LiChrospher 100 RP-8, 5 µm, Merck, Bio-Tek Instruments); eluent A=(Et₃NH)OAc (0.01 M, pH 7.0)/CH₃CN in 80/20 v/v; eluent B = CH₃CN; gradient 0–40% B over 22 min, then 40–100% B over 5 min. Mass spectrometry of oligonucleotides was carried out with a Sciex QSTAR pulsar (hybrid quadrupole time-of-flight mass spectrometer, Applied Biosystems).

6. References

- [1] M. K. Panda, K. Ladomenou, A.G. Coutsolelos, *Coord. Chem. Rev.* **2012** 256, 2601-2627.
- [2] A. Satake, Y. Kobuke, *Org. Biomol. Chem.* **2007**, 5, 1679-1691.
- [3] C. M. Drain, *Proc. Natl. Acad. Sci.* **2002** 99, 5178-5182.
- [4] S. S. Babu, D. Bonifazi, *ChemPlusChem* 2014, 79, 895–906.
- [5] Y. S. Nam, T. Shin, H. Park, A.P. Magyar, K. Choi, G. Fantner, K.A. Nelson, A. M. Belcher, *J. Am. Chem. Soc.* **2010**, 132, 1462-1463.
- [6] S. Bahatyrova, R.N. Frese, C. A. Siebert, J. D. Olsen, K.O. Van Der Werf, R. Van Grondelle, R. Niederman, P. A. Bullough, C. Otto, C., C. N. Hunter, *Nature* **2004** 430, 1058-1062.
- [7] M. S. Choi, T. Yamazaki, I. Yamazaki, T. Aida, *Angew. Chem. Int. Ed.* **2004**, 43, 150-158.

- [8] H. Imahori, Y. Mori, Y. Matano, *J. Photochem. Photobiol. C: Photochem. Rev.* **2003**, *4*, 51-83.
- [9] *Light-Harvesting Antennas in Photosynthesis*, Green, B. R. and Parson, W. W., **2003** Kluwer Acad. Publ., Dordrecht.
- [10] V. L. Malinovskii, D. Wenger, R. Häner *Chem. Soc. Rev.* **2010**, *39*, 410-422.
- [11] B. Albinsson, J.K. Hannestad, K. Börjesson, *Coord. Chem. Rev.* **2012**, *256*, 2399-2413.
- [12] E. Stulz, *Chem. -Eur. J.* **2012**, *18*, 4456-4469.
- [13] M. Endo, H. Sugiyama, *ChemBioChem* **2009**, *10*, 2420-2443.
- [14] K. Pan, E. Boulais, L. Yang, M. Bathe, *Nucleic Acids Res.* **2014**, *42*, 2159-2170.
- [15] R. Varghese, H. A. Wagenknecht, *Chem. Commun.* **2009**, 2615-2624.
- [16] S.H. Weisbrod, A. Marx, **2008** *Chem. Commun.* 5675-5685.
- [17] Y. N. Teo, E. T. Kool, *Chem. Rev.* **2012**, *112*, 4221-4245.
- [18] V. V. Filichev, E. B. Pedersen in *Wiley Encycl.Chem.Biol.* [Begley, T. P., Ed.) **2009** pp 493-524, Wiley, Hoboken.
- [19] M. E. Ostergaard, P. J. Hrdlicka, *Chem. Soc. Rev.* **2011**, *40*, 5771-5788.
- [20] I. K. Astakhova, J. Wengel, *Acc. Chem. Res.* **2014**, *47*, 1768-1777.
- [21] M. Nakamura, Y. Shimomura, Y. Ohtoshi, K. Sasa, H. Hayashi, H. Nakano, K. Yamana, *Org. Biomol. Chem.* **2007**, *5*, 1945-1951.
- [22] D. Y. Yang, M. J. Campolongo, T. N. N. Tran, R. C. H. Ruiz, J. S. Kahn, D. Luo, *WIREs Nanomed. Nanobiotech.* 20102, 648-669.
- [23] F. A. Aldaye, A. L. Palmer, H. F. Sleiman, *Science* **2008**, *321*, 1795-1799.
- [24] U. Feldkamp, C. M. Niemeyer, *Angew. Chem. Int. Ed.* **2006**, *45*, 1856-1876.
- [25] J. Goodchild, *Bioconjug. Chem.* **1990**, *1*, 165-187.
- [26] S. L. Beaucage, R. Iyer, *Tetrahedron* **1993**, *49*, 1925-1963.

- [27] A. H. El-Sagheer, T. Brown, *Chem. Soc. Rev.* **2010**, *39*, 1388-1405.
- [28] A. J. A. Cobb, *Org. Biomol. Chem.* **2007**, *5*, 3260-3275.
- [29] K. Berlin, R. K. Jain, M. D. Simon, C. Richert, *J. Org. Chem.* **1998**, *63*, 1527-1535.
- [30] I. Grabowska, D.G. Singleton, A. Stachyra, A. Gora-Sochacka, A. Sirko, W. Zagorski-Ostoja, H. Radecka, E. Stulz, J. Radecki, *Chem. Commun.* **2014**, *50*, 4196-4199.
- [31] J. K. Choi, G. Sargsyan, A. M. Olive, M. Balaz, *Chem.-Eur. J.* **2013**, *19*, 2515-2522.
- [32] J. R. Burns, K. Göpfrich, J. W. Wood, V. V. Thacker, E. Stulz, U. F. Keyser, S. Howorka, *Angew. Chem., Int. Ed.* **2013**, *52*, 12069-12072.
- [33] J. G. Woller, J. K. Hannestad, B. Albinsson, *J. Am. Chem. Soc.* **2013**, *135*, 2759-2768.
- [34] K. Borjesson, J. Wiberg, A. H. El-Sagheer, *ACS Nano* **2010**, *4*, 5037-5046.
- [35] T. Nguyen, A. Brewer, E. Stulz, *Angew. Chem. Int. Ed.* **2009**, *48*, 1974-1977.
- [36] M. Endo, N. C. Seeman, T. Majima, T. *Angew. Chem. Int. Ed.* **2005**, *44*, 6074-6077.
- [37] G. Sargsyan, M. Balaz, *Org. Biomol. Chem.* **2012**, *10*, 5533.
- [38] M. Balaz, A. E. Holmes, M. Benedetti, P. C. Rodriguez, N. Berova, K. Nakanishi, G. Proni, *J. Am. Chem. Soc.* **2005**, *127*, 4172-4173.
- [39] A. Mammana, G. Pescitelli, T. Asakawa, S. Jockusch, A. G. Petrovic, R. R. Monaco, R. Purrello, N. J. Turro, K. Nakanishi, G. A. Ellestad, M. Balaz, N. Berova, *Chem.-Eur. J.* **2009**, *15*, 11853-11866.
- [40] M. Balaz, K. Bitsch-Jensen, A. Mammana, G. A. Ellestad, K. Nakanishi, N. Berova, *Pure Appl. Chem.* **2007**, *79*, 801-809.

- [41] M. Balaz, B. C. Li, S. Jockusch, G. A. Ellestad, N. Berova, *Angew. Chem. Int. Ed.* **2006**, *45*, 3530-3533.
- [42] L. A. Fendt, I. Bouamaied, S. Thoeni, N. Amiot, E. Stulz, *J. Am. Chem. Soc.* **2007**, *129*, 15319-15329.
- [43] C. Casas, C. J. Lacey, B. Meunier, *Bioconjug. Chem.* **1993**, *4*, 366-371.
- [44] T. Le Doan, D. Praseuth, L. Perrouault, M. Chassignol, N. T. Thuong, C. Helene, *Bioconjug. Chem.* **1990**, *1*, 108-113.
- [45] O. S. Fedorova, A. P. Savitskii, K. G. Shoikhet, G. V. Ponomarev, *FEBS Lett.* **1990**, *259*, 335-337.
- [46] L. Mastruzzo, A. Woisard, D. D. F. Ma, E. Rizzarelli, A. Favre, T. Le Doan, *Photochem. Photobiol.* **1994**, *60*, 316-322.
- [47] B. Mestre, A. Jakobs, G. Pratviel, B. Meunier, *Biochemistry* **1996**, *2960*, 9140-9149.
- [48] H. Morales-Rojas, E. T. Kool, *Org. Lett.* **2002**, *4*, 4377-4380.
- [49] M. Endo, T. Shiroyama, M. Fujitsuka, T. Majima, *J. Org. Chem.* **2005**, *70*, 7468-7472.
- [50] T. Murashima, K. Hayata, Y. Saiki, J. Matsui, D. Miyoshi, T. Yamada, T. Miyazawa, N. Sugimoto, *Tetrahedron Lett.* **2007**, *48*, 8514-8517.
- [51] I. Bouamaied, T. Nguyen, T. Ruhl, E. Stulz, *Org. Biomol. Chem.* **2008**, *6*, 3888-3891.
- [52] S. Sitaula, S. M. Reed, *Bioorg. Med. Chem. Lett.* **2008**, *18*, 850-855.
- [53] A. Mammana, T. Asakawa, K. Bitsch-Jensen, A. Wolfe, S. Chaturantabut, Y. Otani, X. Li, Z. Li, K. Nakanishi, M. Balaz, G. A. Ellestad, N. Berova, *Bioorg. Med. Chem.* **2008**, *16*, 6544-6551.
- [54] A. W. I. Stephenson, A. C. Partridge, V. V. Filichev, *Chem.-Eur. J.* **2011**, *17*, 6227-6238.

- [55] G. Clavé, G. Chatelain, A. Filoramo, D. Gasparutto, C. Saint-Pierre, E. Le Cam, O. Piétrement, V. Guérineau, S. Campidelli, *Org. Biomol. Chem.* **2014**, *12*, 2778-2783.
- [56] C. Wellner, H. A. Wagenknecht, *Org. Lett.* **2014**, *16*, 1692-1695.
- [57] Y. Ohya, N. Hashimoto, S. Jo, T. Nohori, T. Yoshikuni, T. Ouchi, H. Tamiaki, *Supramol. Chem.* **2009**, *21*, 301-309.
- [58] H. Zhou, A. T. Johnson, O. Wiest, L. L. Zhang, *Org. Biomol. Chem.* **2011**, *9*, 2840-2849.
- [59] J. K. Laha, S. Dhanalekshmi, M. Taniguchi, A. Ambroise, J. S. Lindsey, N. Carolina, S. Uni, *Org. Proc. Res. Dev.* **2003**, *7*, 799-812.
- [60] H. Asanuma, T. Fujii, T. Kato, H. Kashida, *J. Photochem. Photobiol. C-Photochem. Rev.* **2012**, *13*, 124-135.
- [61] C. A. Hunter, J. K. M. Sanders, A. J. Stone, *Chem. Phys.* **1989**, *133*, 395-404.
- [62] A. W. I. Stephenson, N. Bomholt, A. C. Partridge, V. V. Filichev, *Chembiochem* **2010**, *11*, 1833-1839.
- [63] M. Endo, M. Fujitsuka, T. Majima, *J. Org. Chem.* **2008**, *73*, 1106-1112.
- [64] N. C. Maiti, M. Ravikanth, S. Mazumdar, N. Periasamy, *J. Phys. Chem.* **1995**, *99*, 17192-17197.
- [65] U. See e.g. Rösch, S. Yao, R. Wortmann, F. Würthner, *Angew. Chem., Int. Ed.* **2006**, *45*, 7026-7030
- [66] X. Huang, K. Nakanishi, N. Berova, *Chirality* **2000**, *255*, 237-255.
- [67] S. Matile, N. Berova, K. Nakanishi, *J. Am. Chem. Soc.* **1995**, *117*, 7021-7022.
- [68] M. Balaz, J. D. Steinkruger, G. A. Ellestad, N. Berova, *Org. Lett.* **2005**, *7*, 5613-5616.
- [69] R. F. Pasternack, E. J. Gibbs, J. J. Villafranca, *Biochemistry* **1983**, *22*, 2406-2414.

[70] V. L. Malinovskij, A. L. Nussbaumer, R. Häner, *Angew. Chem. Int. Ed.* **2012**, *51*, 4905-4908.

[71] E. J. Gibbs, , I. Tinoco, , M. F. Maestre, , P. A. Ellinas, , R. F. Pasternack, *Biochem. Biophys. Res. Comm.* **1988**, *157*, 350-358.

CHAPTER VII. GENERAL CONCLUSIONS AND OUTLOOK

The synthesis and properties of phosphodiester-linked oligomers of different chromophores were described in this work. The synthesis was performed using phosphoramidite chemistry on a solid support. The oligomers composed of dialkynyl-substituted pyrenes self-assemble in an aqueous environment, resulting in the formation of morphologically well-defined shapes. The aggregation process is reliably followed by substantial changes in absorption and fluorescence spectra. The morphology of the aggregates formed is confirmed by AFM and TEM experiments. For the oligomers of pyrenes, the self-assembly is dependent on a substitution pattern. Two-dimensional (2D) nanosheets are formed in case of 1,6- and 2,7-substitution whereas 1D tubular structures could be built from 2,7-substituted isomers. The preparation protocols are very important for the assembly of the ordered chromophore arrays in solution; slow cooling is crucial to prepare extra-large sheets with an aspect ratio (area/thickness) of 10^7 nm. The sheets are mostly free-standing due to the repulsion between their negatively charged surfaces. Interestingly, these nanosheets are efficiently rendered chiral by applying asymmetric physical perturbations.

The model dialkynyl-substituted pyrene oligomers offer general structural guidelines to direct the assembly in stable 1D or 2D architectures for another π -conjugated molecules, enabling a rational design of sequences. Currently, many oligomers consisting of various dialkynyl-substituted chromophores (phenanthrenes, anthracenes, chrysenes, and perylenes) are studied in the Häner group. Moreover, pyrene oligomers conjugated to DNA or other biomolecules can be used as a reliable supramolecular platform. Based on the findings described in this thesis, the self-assembly of DNA hybrids was used for the noncovalent synthesis of DNA-grafted supramolecular polymers. The oligomers are composed of an oligopyrenotide strand

attached to the 5'-end of an oligodeoxynucleotide. The supramolecular polymerization of these oligomers in an aqueous medium leads to the formation of one-dimensional (1D) helical ribbon structures.

Finally, the chromophore-containing oligomers described can find their applications in various fields of material science as supramolecular synthons. Self-assembly of these oligomers enables the preparation of 2D or 1D materials in a controllable and programmable manner via a proper design of their sequences.

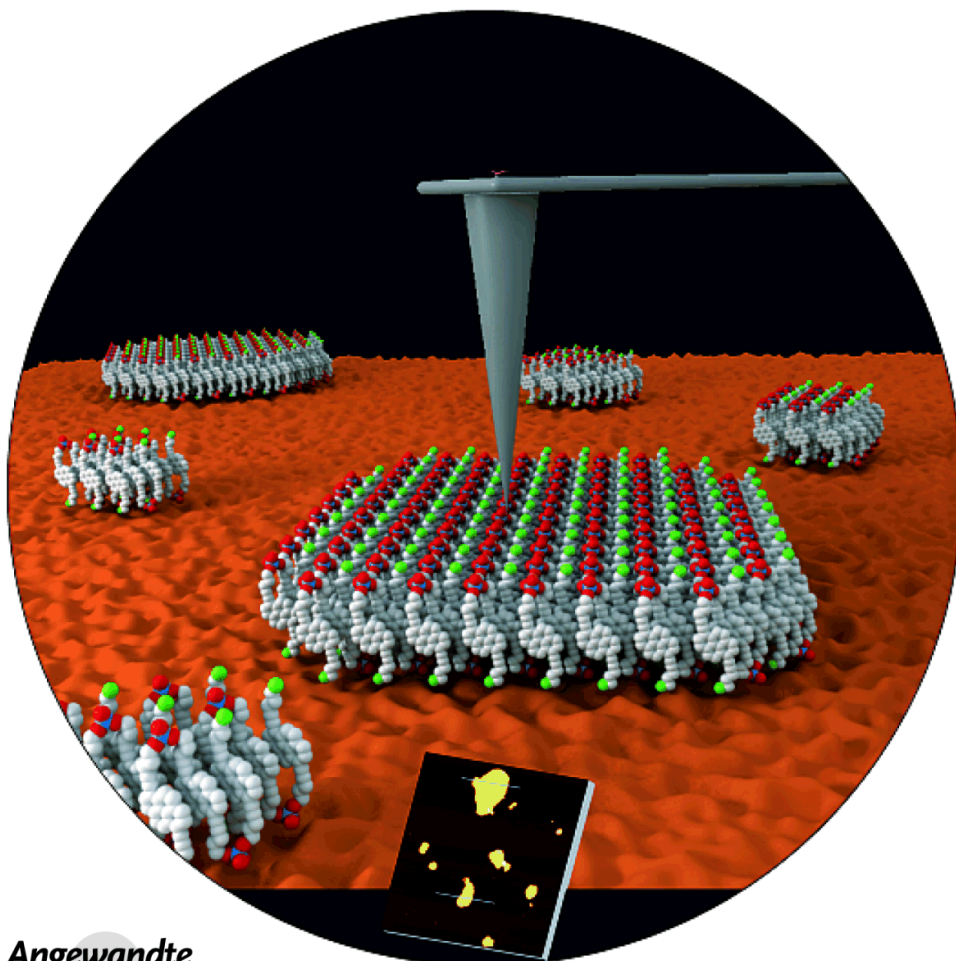
Angewandte
Communications

2D Supramolecular Polymers

DOI: 10.1002/anie.201307029

Formation of Two-Dimensional Supramolecular Polymers by Amphiphilic Pyrene Oligomers**

Mykhailo Vybornyi, Alexander V. Rudnev, Simon M. Langenegger,
Thomas Wandlowski, Gion Calzaferri, and Robert Häner*



Angewandte
International Edition
Chemie

11488 Wiley Online Library

© 2013 Wiley-VCH Verlag GmbH & Co. KGaA, Weinheim

Angew. Chem. Int. Ed. 2013, 52, 11488–11493

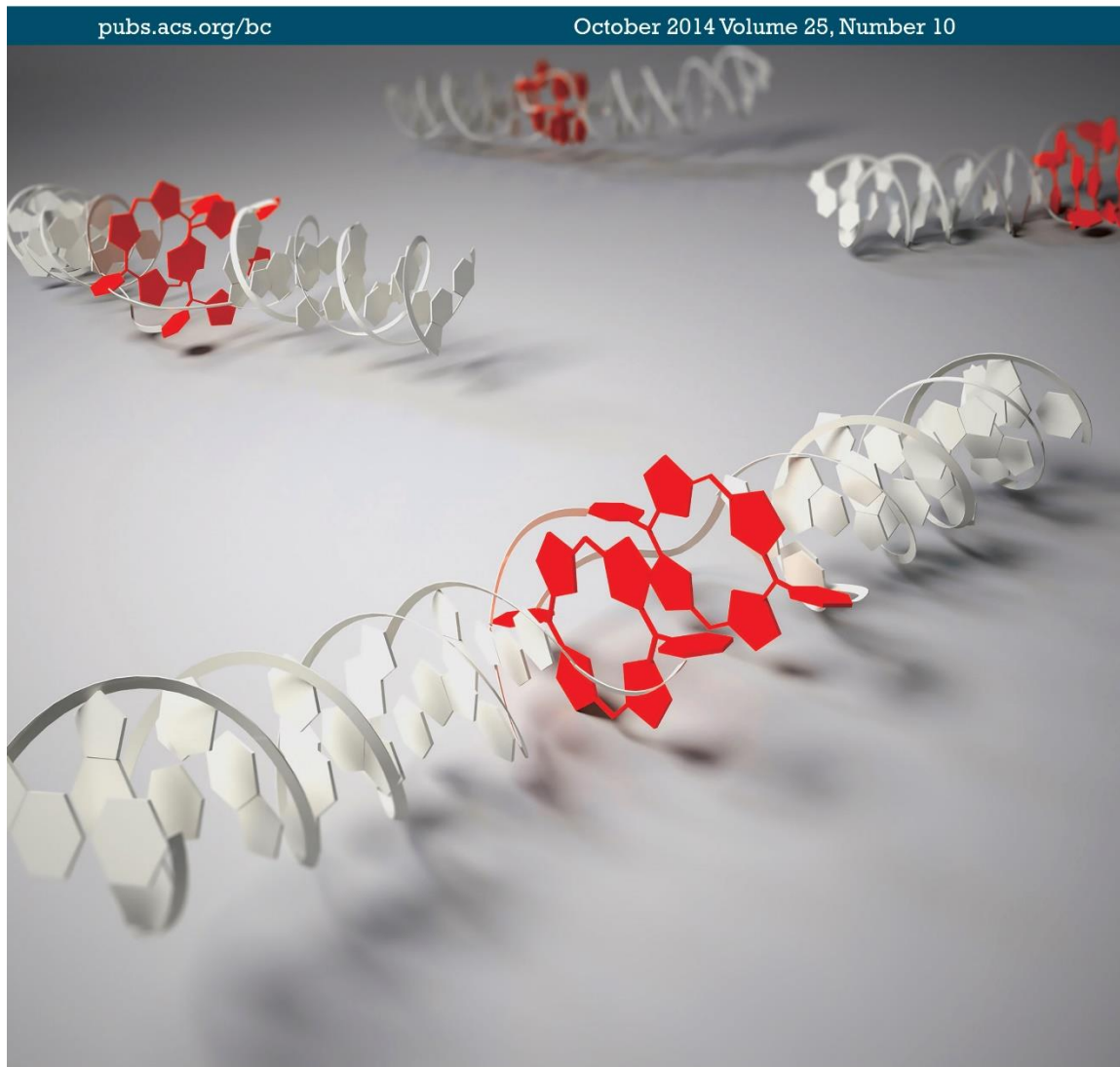
APPENDIX B. COVER IMAGE IN BIOCONJUG. CHEM. 2014, 25, 1785

25th Anniversary

BC Bioconjugate Chemistry

pubs.acs.org/bc

October 2014 Volume 25, Number 10

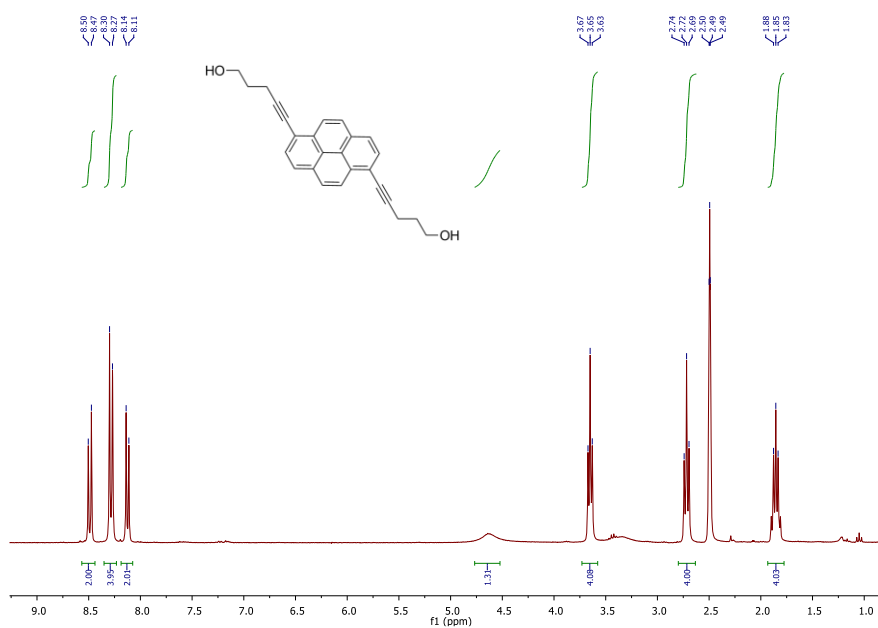


 ACS Publications
Most Trusted. Most Cited. Most Read.

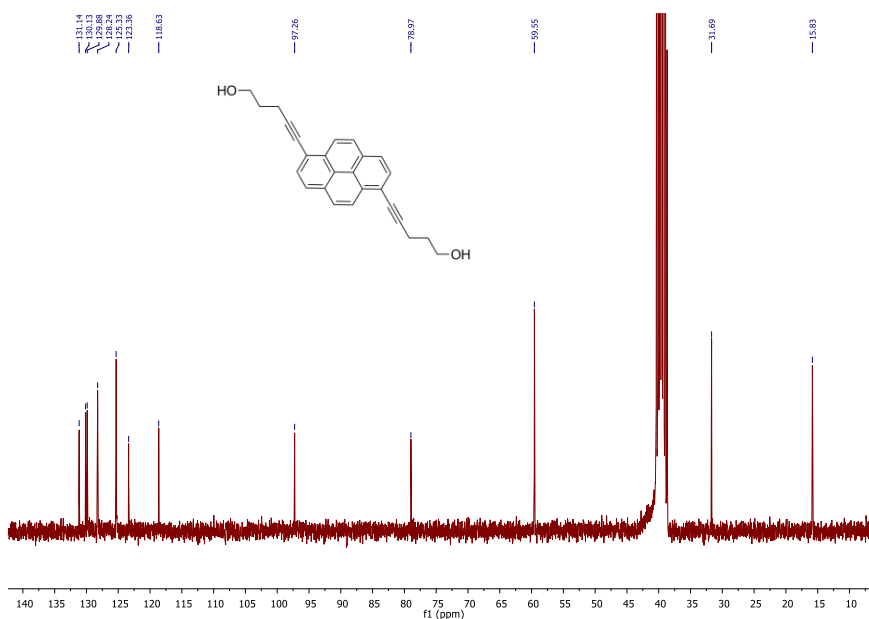
www.acs.org

APPENDIX C. NMR SPECTRA OF 1,6-SUBSTITUTED DERIVATIVES OF PYRENE

^1H NMR (300 MHz, DMSO) of **16Py**:

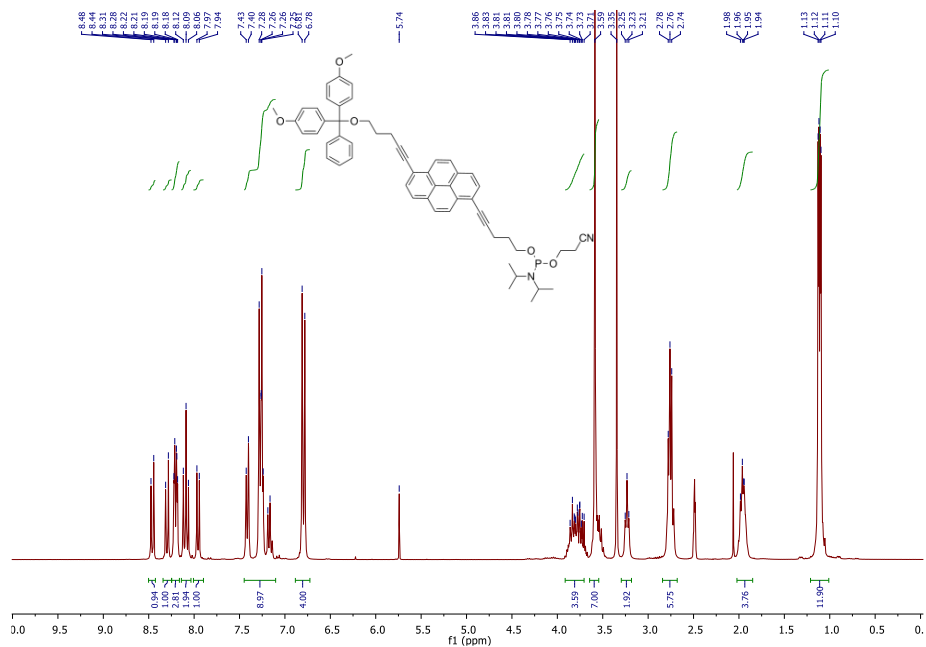


^{13}C NMR (75 MHz, DMSO) of **16Py**:

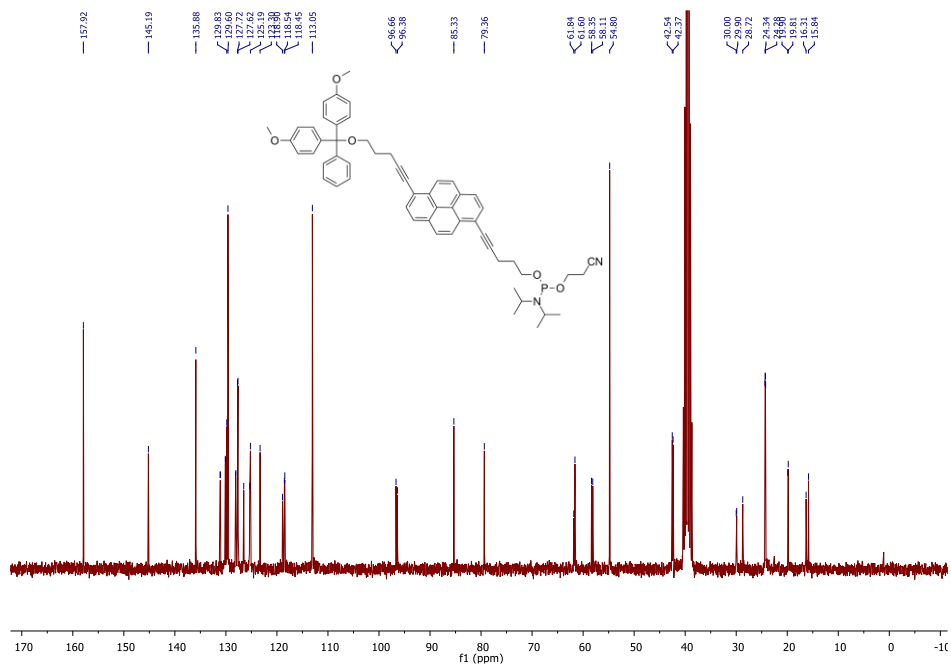


^1H NMR (300 MHz, CDCl_3) of **16PY-DMT**:

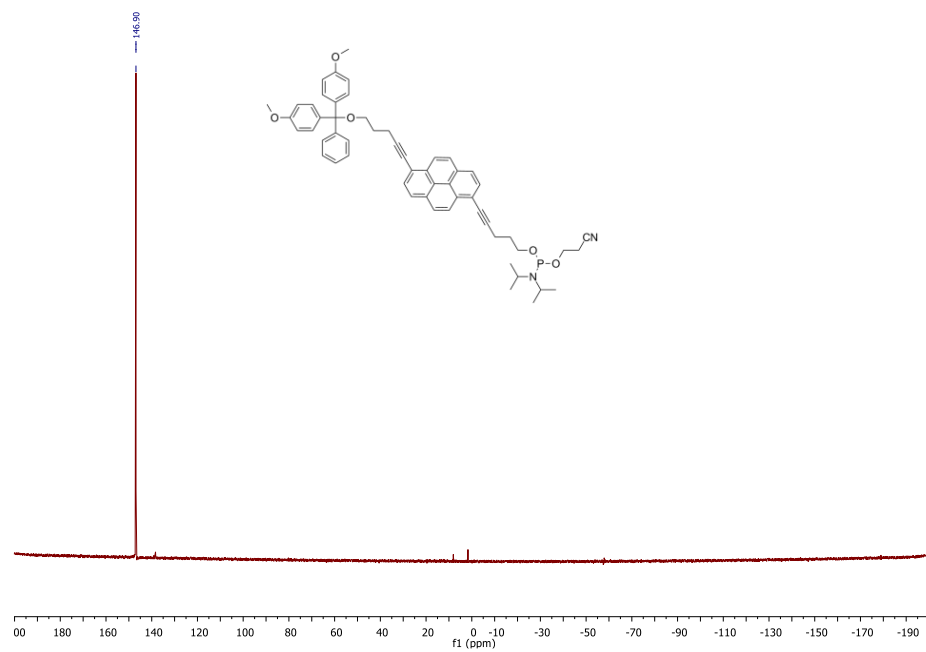
¹H NMR (300 MHz, DMSO) of **16PY-DMT/CEP**:



¹³C NMR (75 MHz, DMSO) of **16PY-DMT/CEP**:



^{31}P NMR (122 MHz, DMSO) of **16PY-DMT/CEP**:



APPENDIX D. HPLC PURIFICATION AND CHARACTERIZATION OF 16PY₃

The purification method used (eluent A=(Et₃NH)OAc (50 mM, pH 7.0)/CH₃CN in 50/50 v/v; eluent B=CH₃CN):

Time, min	Solvent A, %	Solvent B, %
0 - 2	100	0
2 - 16	0	100
16 - 22	0	100
22 - 24	100	0
24 - 30	100	0

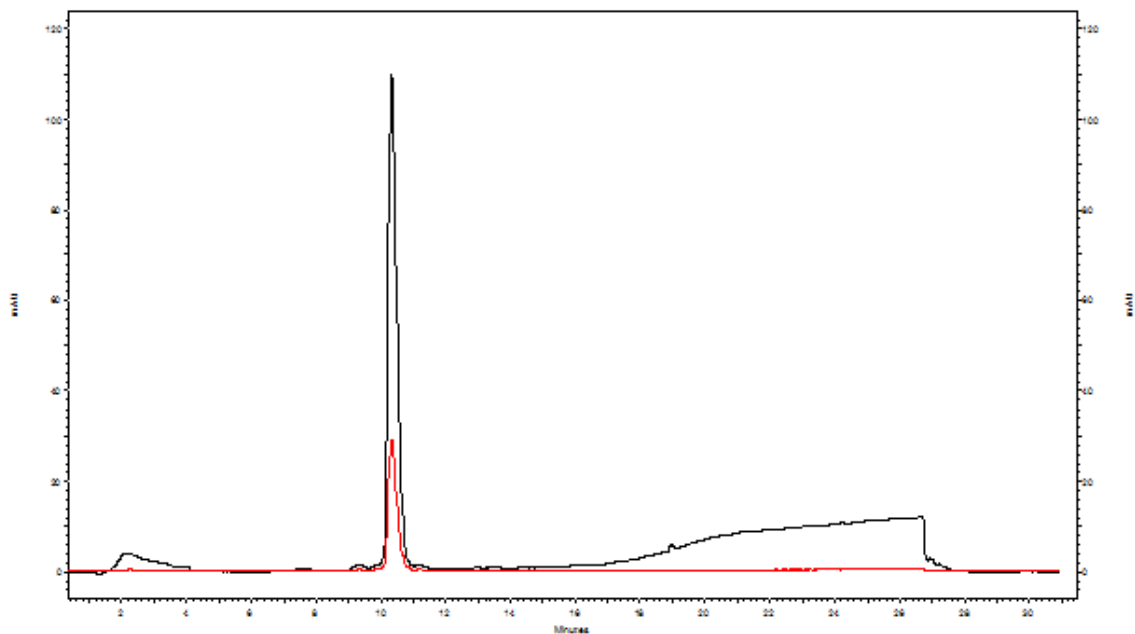
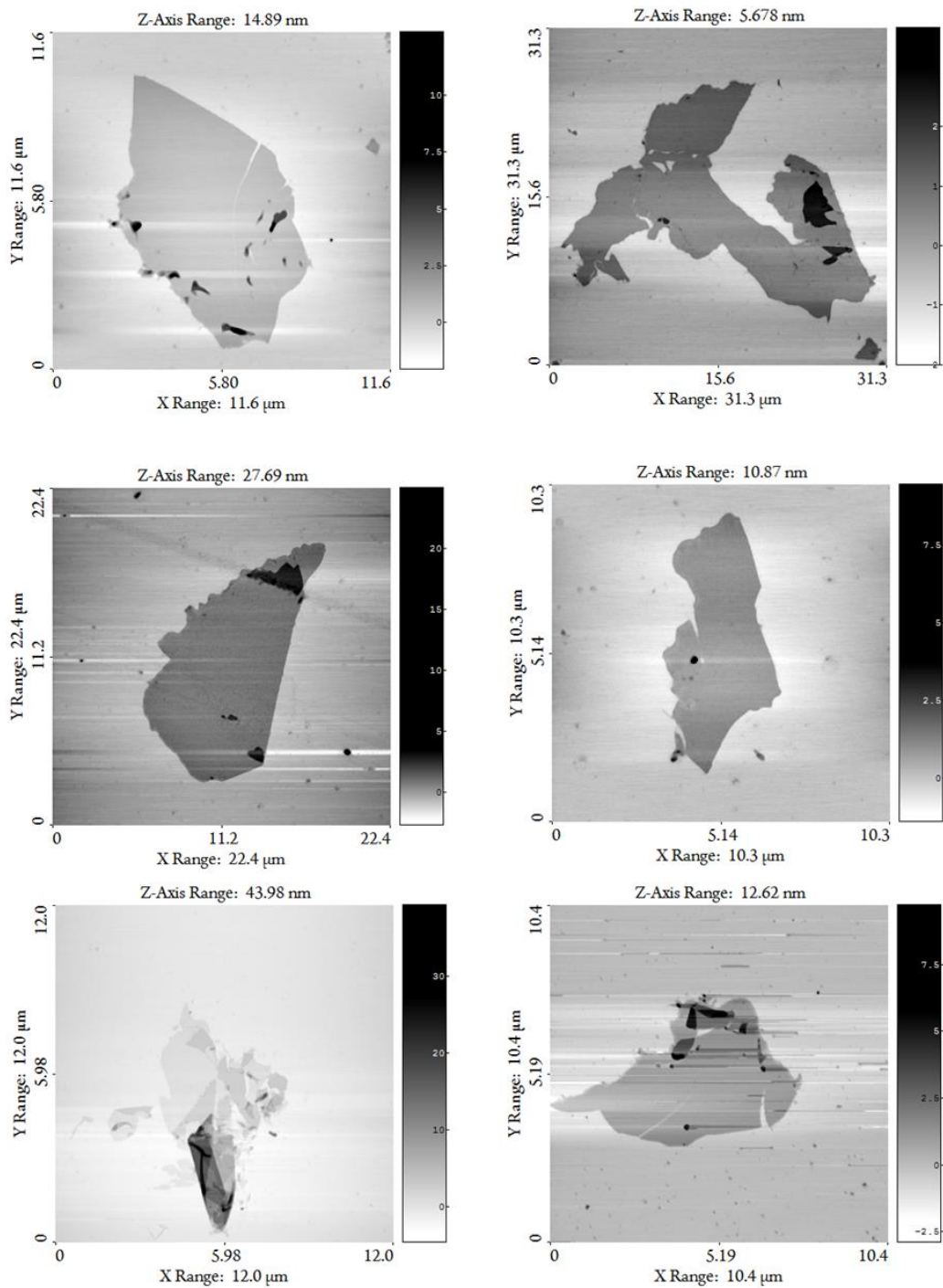
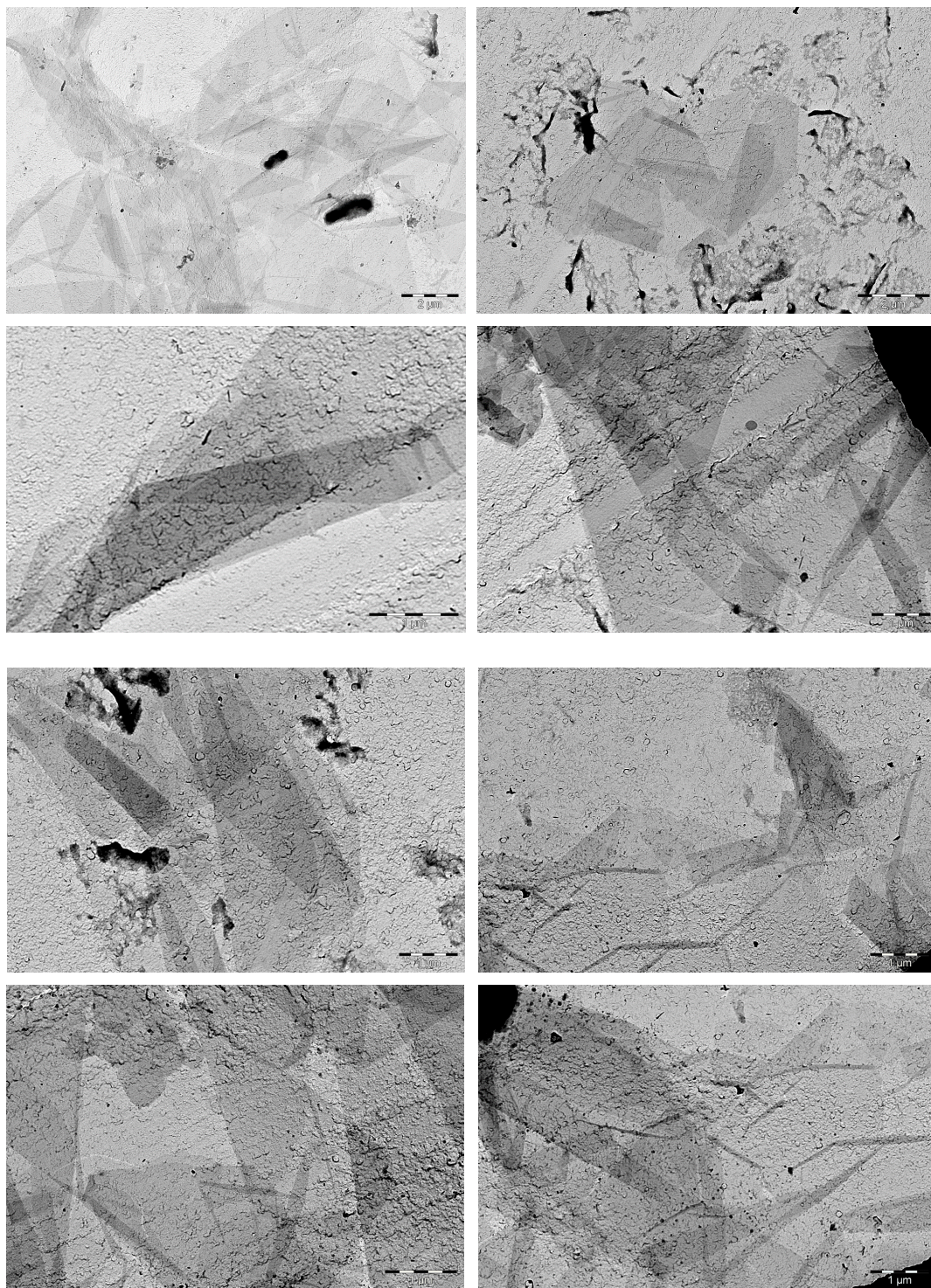


Figure 1. HPLC trace of 16Py₃.

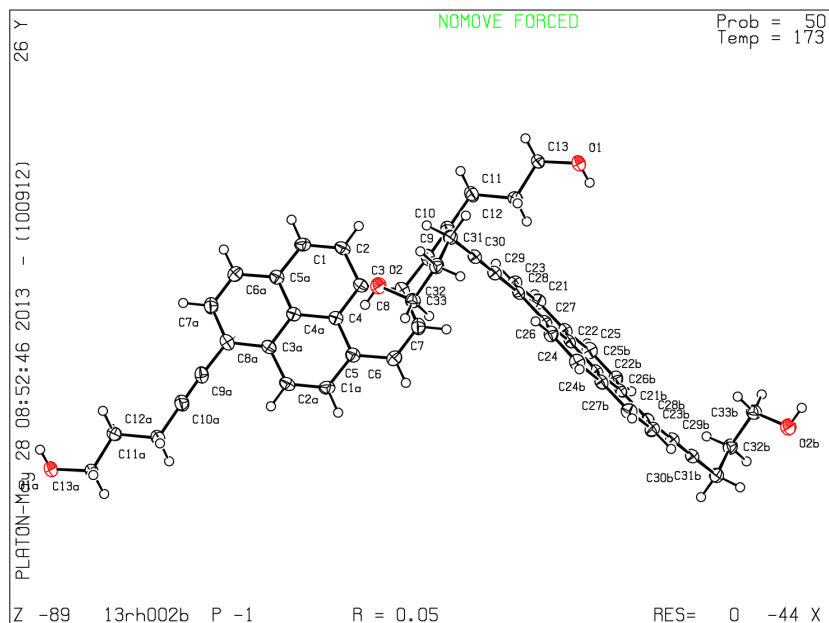
APPENDIX E. ADDITIONAL AFM IMAGES OF POLY16PY₃ PREPARED BY SLOW COOLING



APPENDIX F. ADDITIONAL TEM IMAGES OF POLY16PY₃ PREPARED BY SLOW COOLING



APPENDIX G. X-RAY DATA OF 16PY



Crystal-Structure Determination. – A purple transparent crystal of $C_{26}H_{22}O_2$ was mounted in air and used for X-ray structure determination at ambient conditions. All measurements were made on a *Oxford Diffraction SuperNova* area-detector diffractometer¹ using mirror optics monochromated Mo $K\alpha$ radiation ($\lambda = 0.71073 \text{ \AA}$) and Al filtered.² The unit cell constants and an orientation matrix for data collection were obtained from a least-squares refinement of the setting angles of reflections in the range $1.8^\circ < \theta < 27.2^\circ$. A total of 708 frames were collected using ω scans, with 20+20 seconds exposure time, a rotation angle of 1.0° per frame, a crystal-detector distance of 65.1 mm, at $T = 173(2) \text{ K}$. Data reduction was performed using the *CrysAlisPro*¹ program. The intensities were corrected for Lorentz and polarization effects, and an absorption correction based on the multi-scan method using SCALE3 ABSPACK in *CrysAlisPro*¹ was applied. Data collection and refinement parameters are given in *Table 1*. The structure was solved by direct methods using *SHELXS-97*³, which revealed the positions of all non-hydrogen atoms

of the title compound. The non-hydrogen atoms were refined anisotropically. All H-atoms were placed in geometrically calculated positions and refined using a riding model where each H-atom was assigned a fixed isotropic displacement parameter with a value equal to 1.2Ueq of its parent atom. Refinement of the structure was carried out on F^2 using full-matrix least-squares procedures, which minimized the function $\sum w(F_o^2 - F_c^2)^2$. The weighting scheme was based on counting statistics and included a factor to downweight the intense reflections. All calculations were performed using the *SHELXL-97*² program. Two independent molecules occupy the asymmetric unit. Both are sitting on an inversion center, but they differ for the conformation of the side chains: all-trans (about C11-C12 and C12-C13 bonds) in one molecule, all gauche (about C31-C32 and C32-C33) in the other. The crystal structure has been deposited at the Cambridge Crystallographic Data Centre (deposition number CCDC 948491). Support for a staircase-like folding is also provided by the crystal structure of monomer **16Py**. Crystals of this compound were obtained from dichloromethane. Two types of pyrene arrangement are present inside the crystal lattice. In one arrangement, pyrene monomers are organized in a staircase-type fashion with partial overlap of the pyrene π -systems. A 3.42 Å stacking distance and a 2.1 Å transverse shift of two adjacent pyrenes are observed.

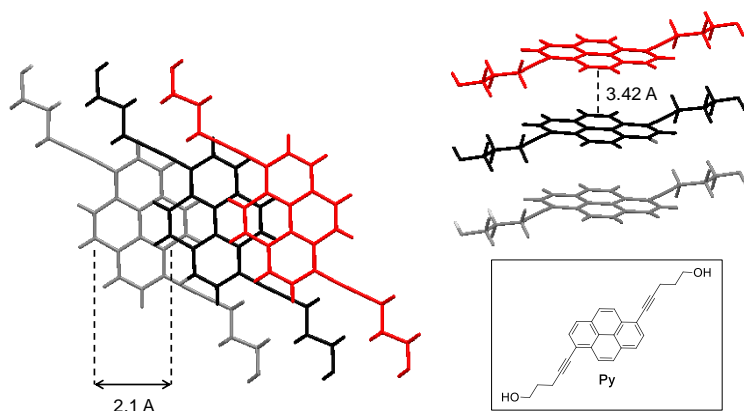
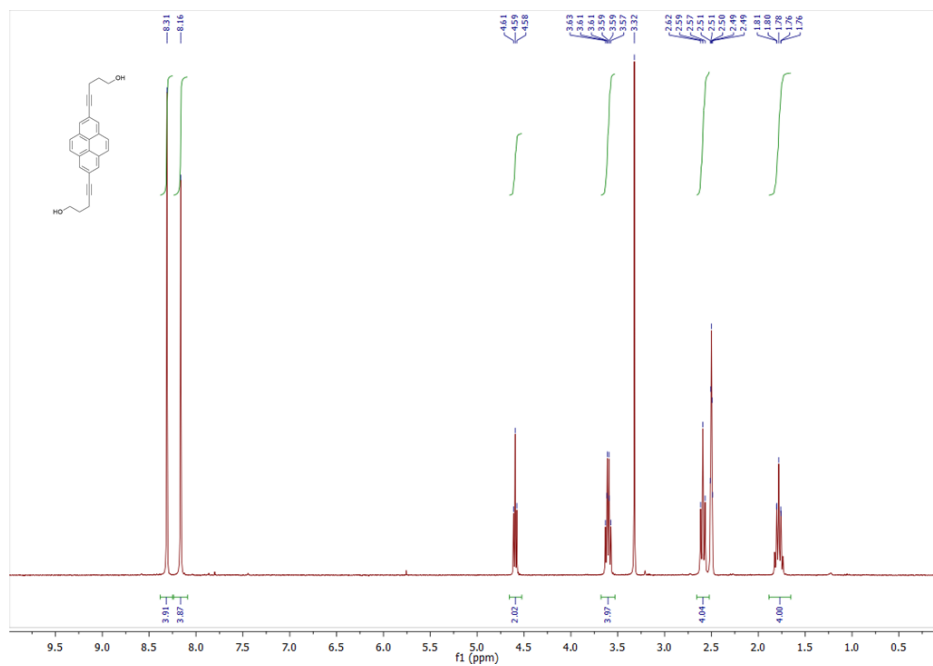


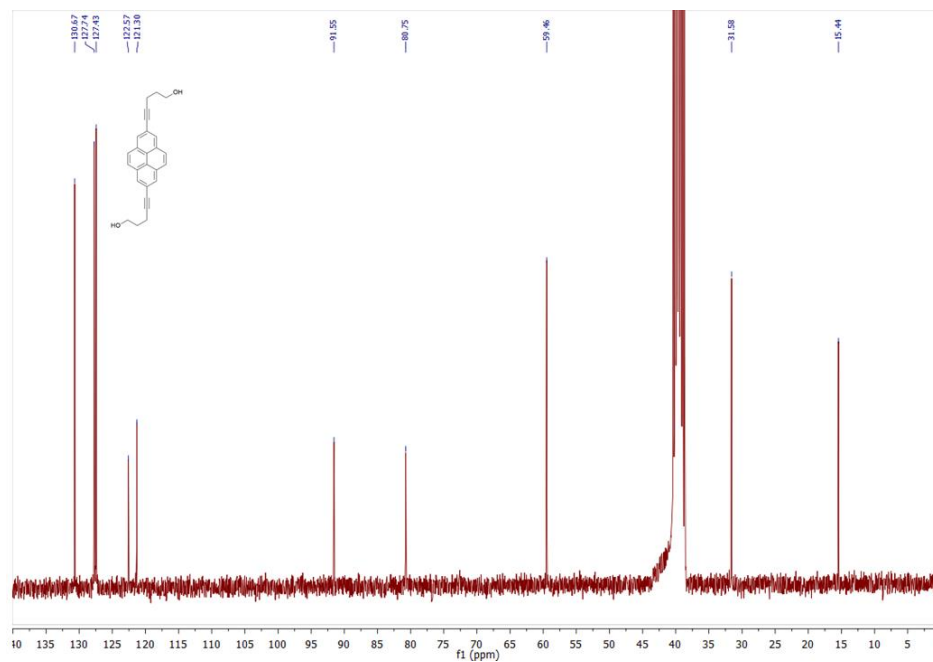
Figure 1. Illustrations of the pyrenes arrangement within crystals of **16Py**

APPENDIX K. NMR SPECTRA OF 2,7-SUBSTITUTED DERIVATIVES OF PYRENE

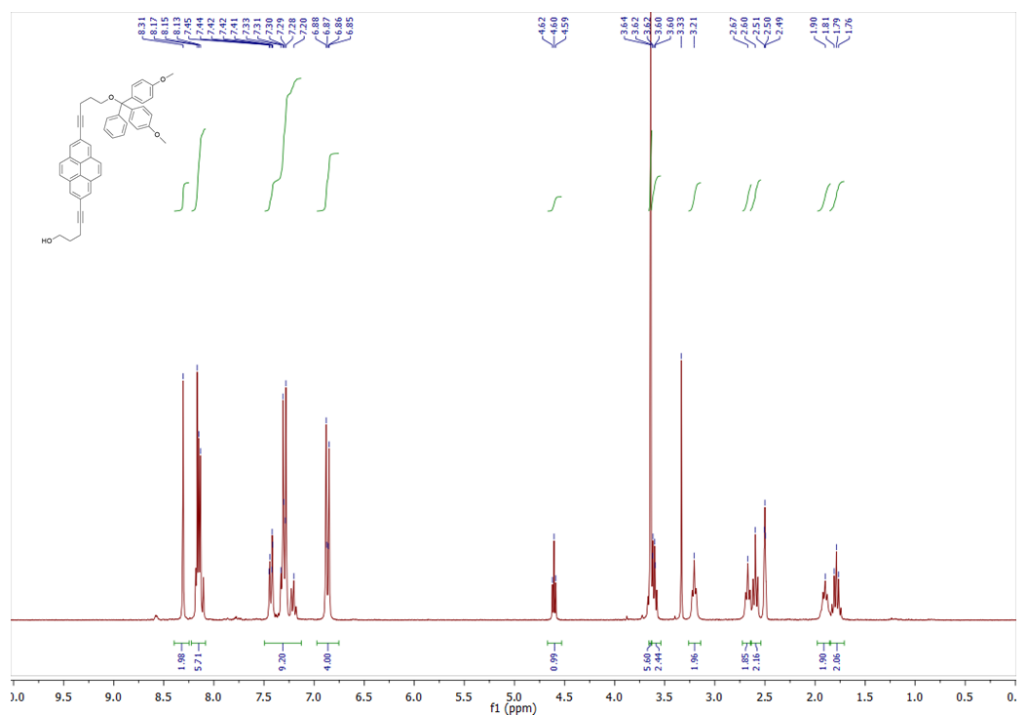
^1H NMR (300 MHz, DMSO) of **27PY**:



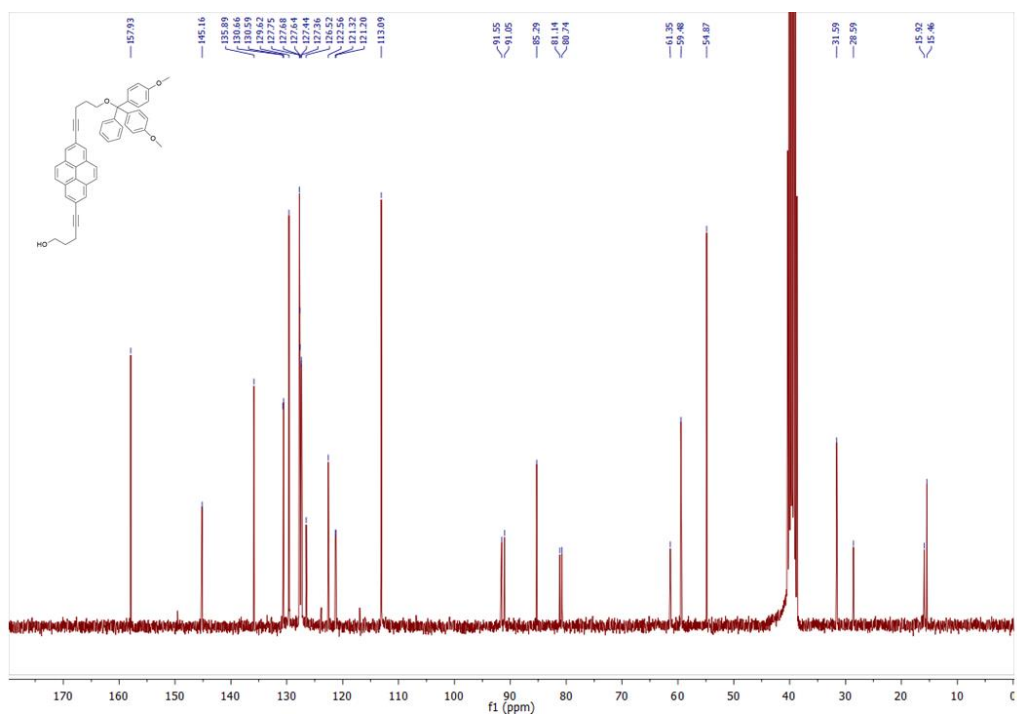
^{13}C NMR (75 MHz, DMSO) of **27PY**:



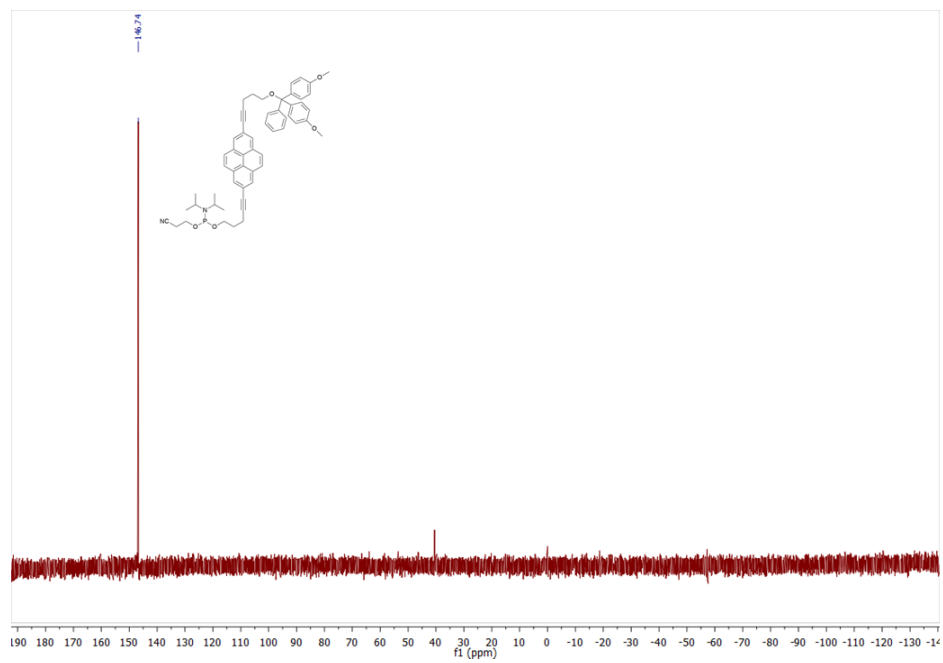
^1H NMR (300 MHz, CDCl_3) of **27PY-DMT**:



^{13}C NMR (75 MHz, DMSO) of **27PY-DMT**:



^{31}P NMR (122 MHz, DMSO) of **27PY-DMT/CEP**:



APPENDIX L. HPLC PURIFICATION AND CHARACTERIZATION OF 27PY₃

The purification method used (eluent A=(Et₃NH)OAc (50 mM, pH 7.0)/CH₃CN in 50/50 v/v; eluent B=CH₃CN):

Time, min	Eluent A, %	Eluent B, %
0 – 2	100	0
2 – 16	0	100
16 – 22	0	100
22 – 24	100	0
24 – 30	100	0

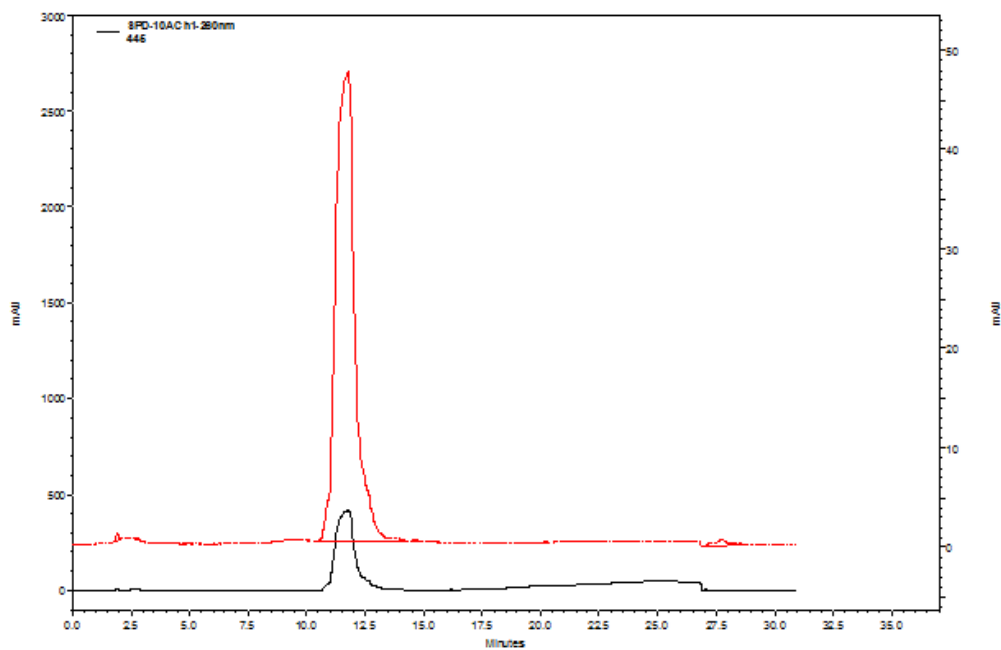
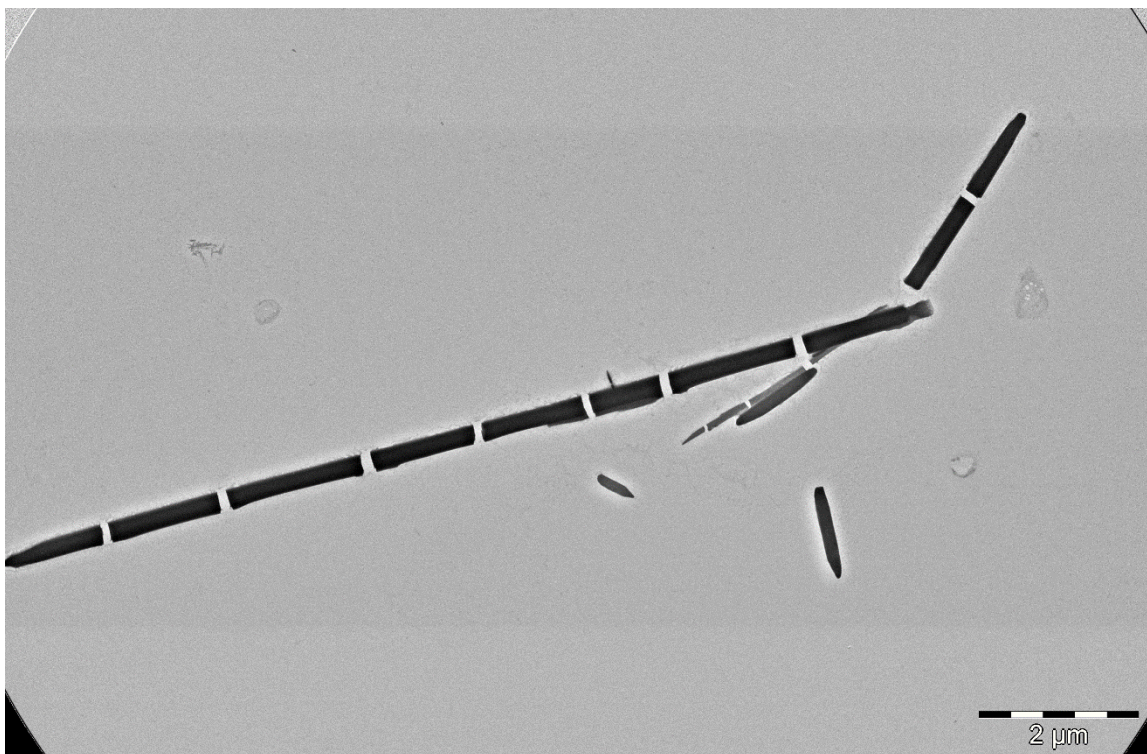
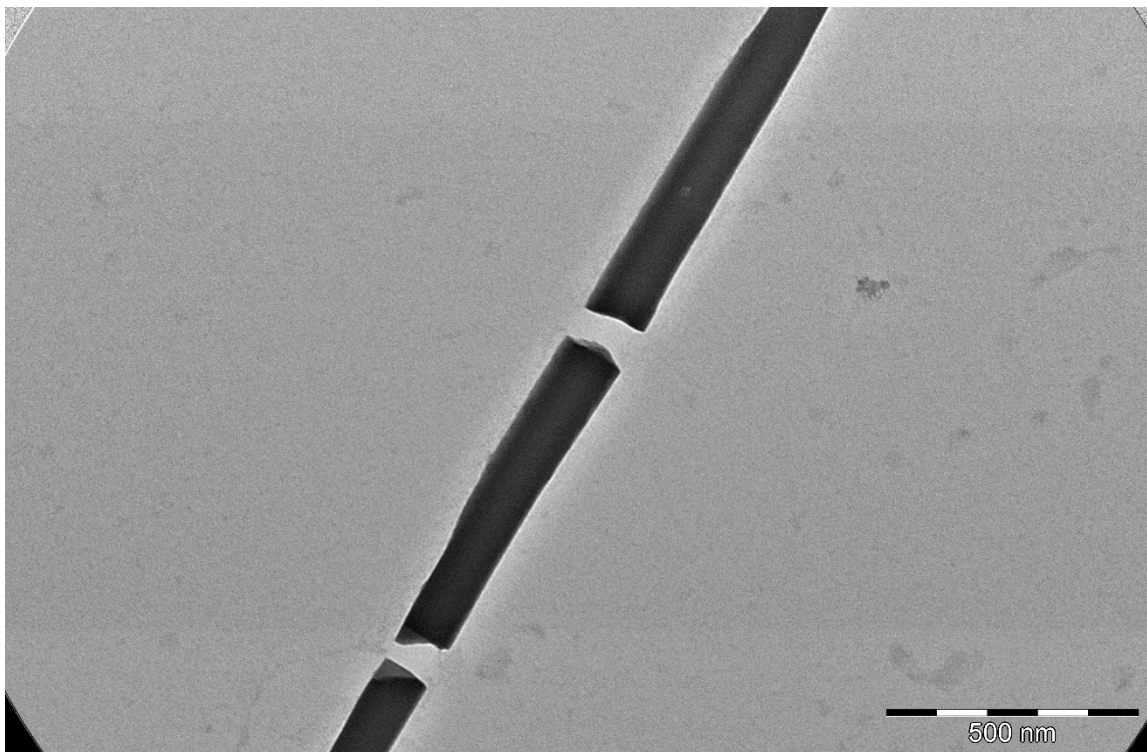


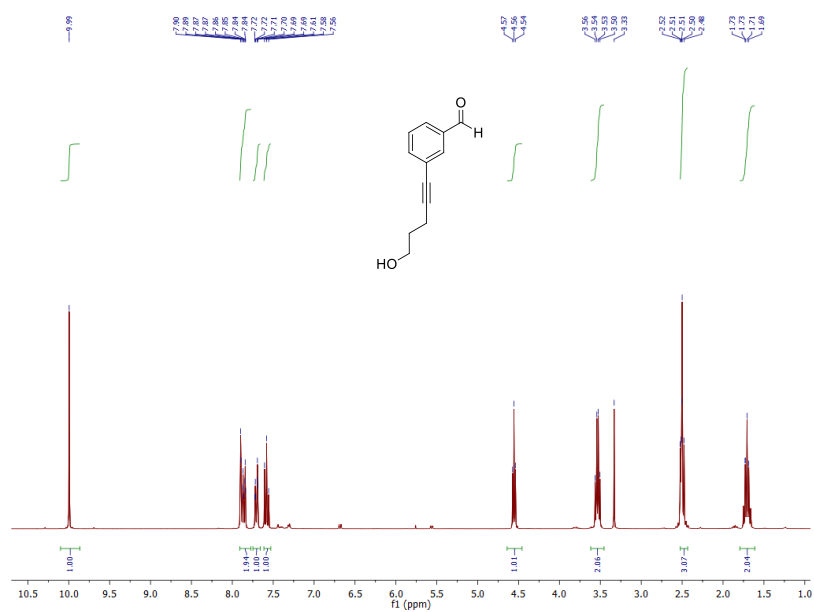
Figure 1. HPLC trace of **27Py₃** monitored at 260 nm (red) and 350 nm (black)

APPENDIX M. ADDITIONAL AFM IMAGES OF POLY27PY₃

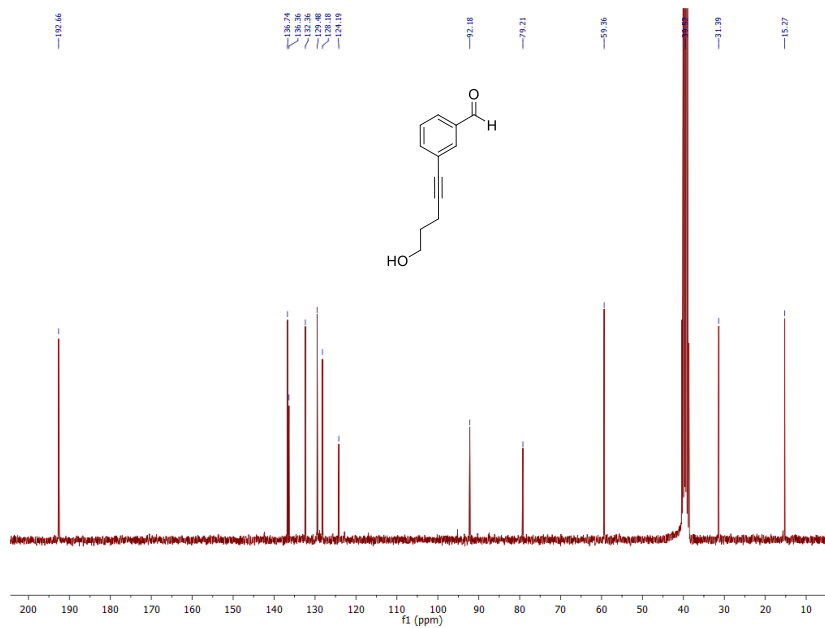


APPENDIX N. NMR SPECTRA OF COMPOUNDS FROM CHAPTER VI

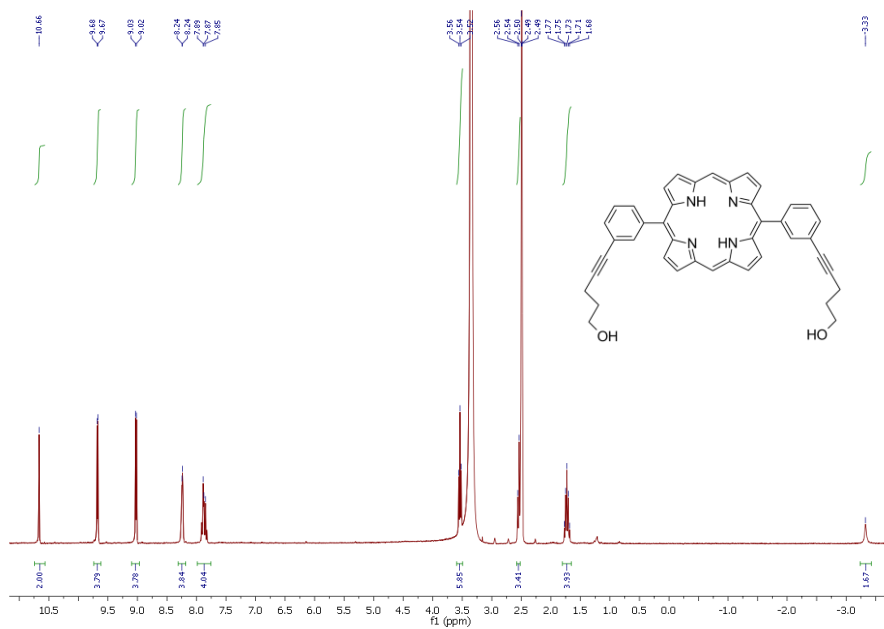
^1H NMR (300 MHz, DMSO) of **1**



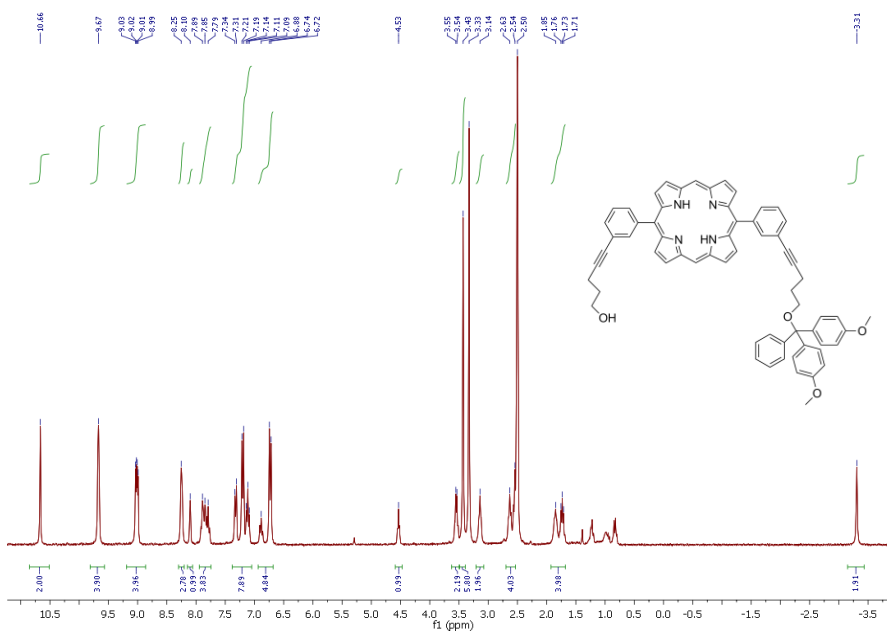
^{13}C NMR (75 MHz, DMSO) of **1**



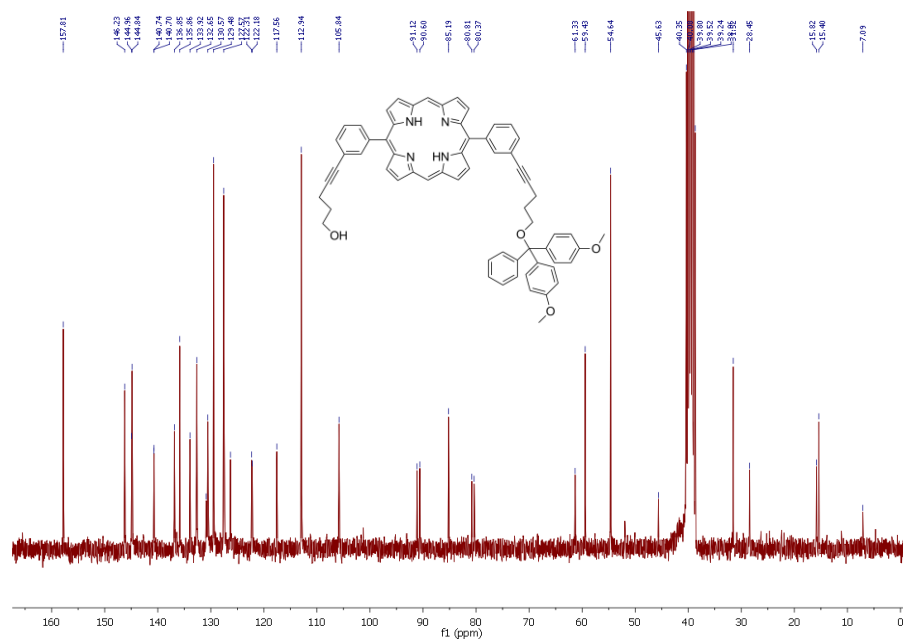
^1H NMR (300 MHz, DMSO) of **3**



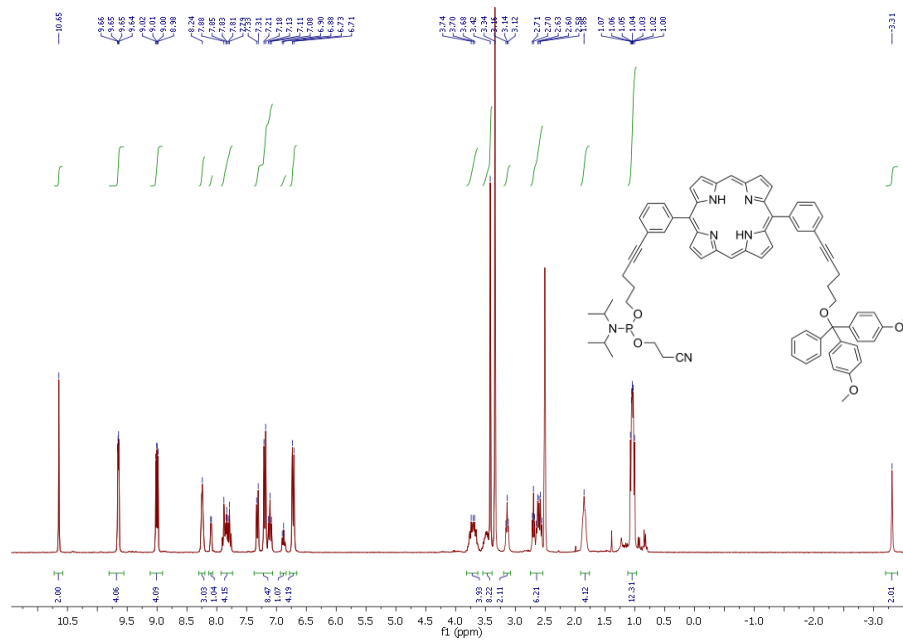
^1H NMR (300 MHz, DMSO) of **4**



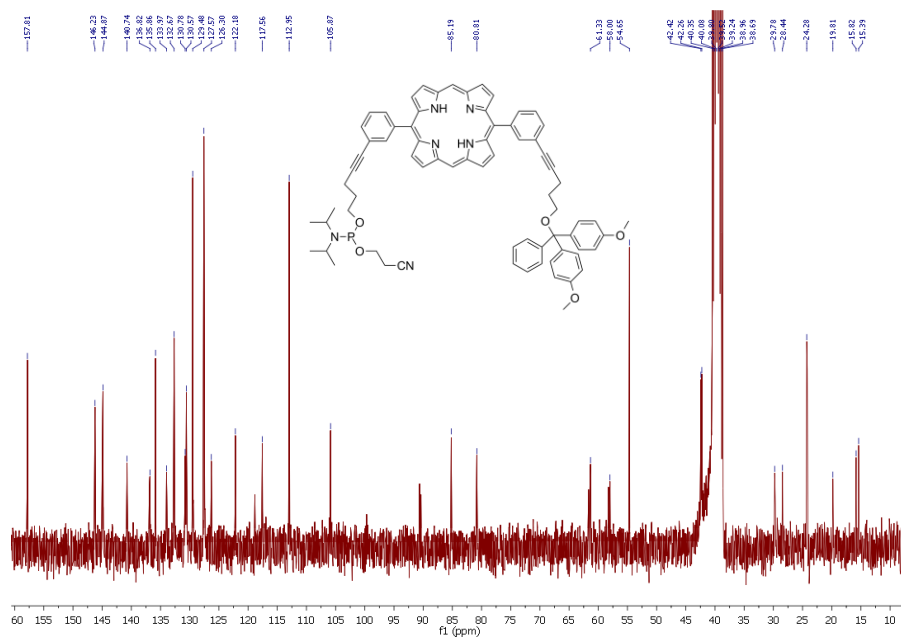
^{13}C NMR (75 MHz, DMSO) of **4**



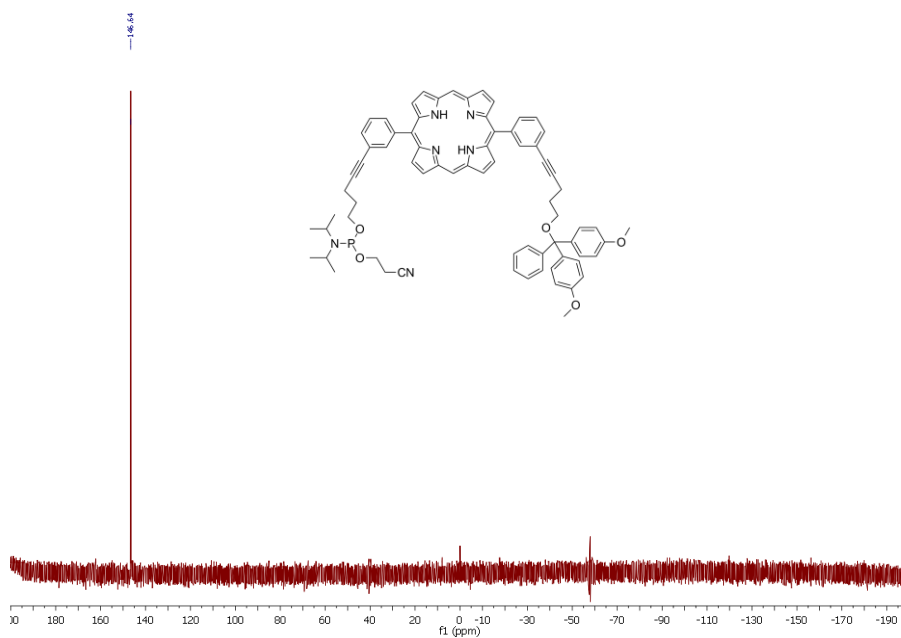
^1H NMR (300 MHz, DMSO) of **5**



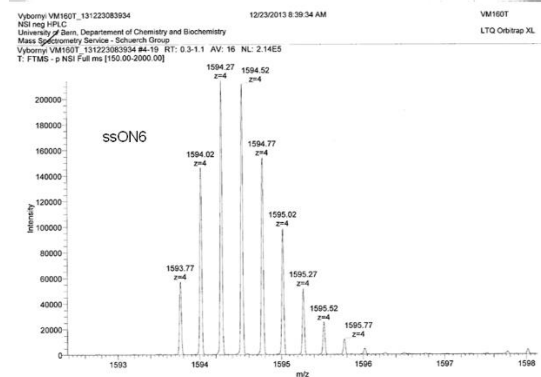
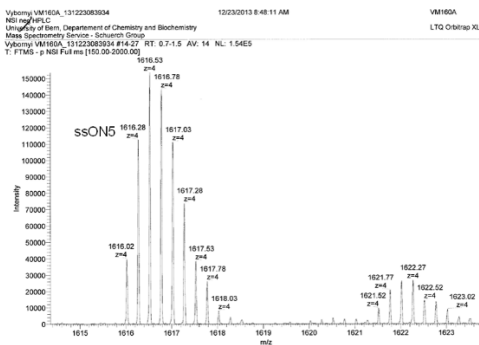
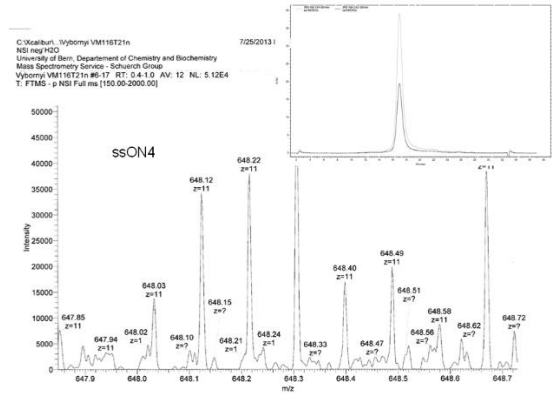
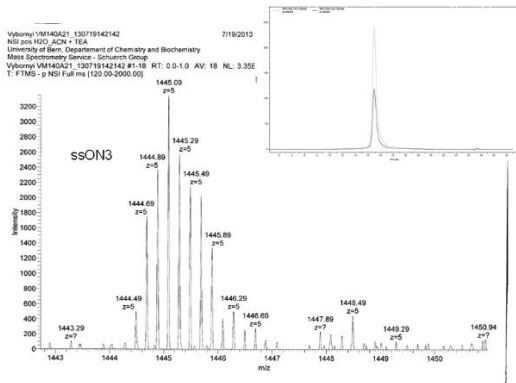
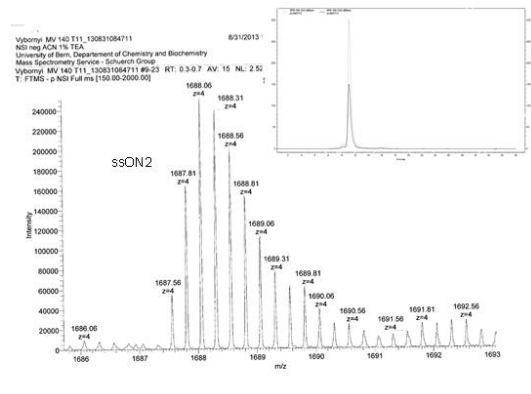
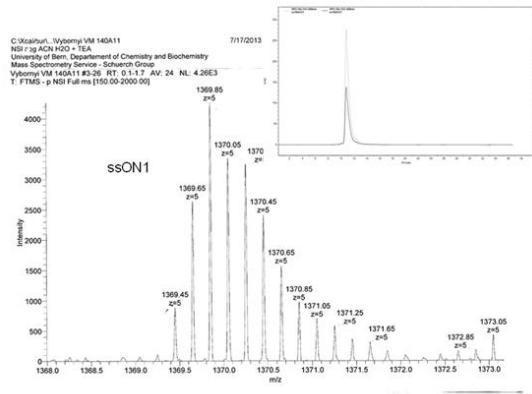
^{13}C NMR (75 MHz, DMSO) of **5**



^{31}P NMR (122 MHz, DMSO) of **5**



APPENDIX N. MS SPECTRA AND HPLC TRACES OF OLIGONUCLEOTIDES FROM CHAPTER VI



Erklärung

gemäss Art. 28 Abs. 2RSL 05

Name/Vorname: Vybornyi Mykhailo

Matrikelnummer: 11-117-884

Studiengang: Chemistry and Molecular Sciences

Bachelor Master Dissertation

Titel der Arbeit

Leiter der Arbeit

Prof. Robert Häner

Ich erkläre hiermit, dass ich diese Arbeit selbständig verfasst und keine anderen als die angegebenen Quellen benutzt habe. Alle Stellen, die wörtlich oder sinngemäss aus Quellen entnommen wurden, habe ich als solche gekennzeichnet. Mir ist bekannt, dass andernfalls der Senat gemäss Artikel 36 Absatz 1 Buchstabe r des Gesetzes vom 5. September 1996 über die Universität zum Entzug des auf Grund dieser Arbeit verliehenen Titels berechtigt ist. Ich gewähre hiermit Einsicht in diese Arbeit.

Ort/ Datum

Unterschrift

CV

Personal information

Name, First name Vybornyi Mykhailo
Date of birth 24 August 1987
Hometown Mykolajiw, Ukraine

Education

2011-present Ph.D., the Robert Häner group, University of Bern, Switzerland (defense in December)
2010-2011 M.Sc., the SOMaF team, Nanoscience and Materials Chemistry, University of Angers, France
2005-2010 B.Sc., Organic Chemistry, Kyiv National University, Ukraine

Peer-reviewed papers

- (1) Vybornyi, M., Bur-Cecilio Hechevarria, Y., Glauser, M., Rudnev, A., Häner, R. **(2015)** Tubes or Sheets: Divergent Aggregation Pathways of an Amphiphilic 2,7-Substituted Pyrene Trimer. *Chem. Commun.* doi: 10.1039/C5CC05126F
- (2) Vyborna, Y., Vybornyi, M., Rudnev, A. V., and Häner, R. **(2015)** DNA-Grafted Supramolecular Polymers: Helical Ribbon Structures Formed by Self-Assembly of Pyrene-DNA Chimeric Oligomers. *Angew. Chem. Int. Ed.* 54, 7934–7938. **(Cover picture)**
- (3) Micali, N., Vybornyi, M., Mineo, P., Khorev, O., Häner, R., and Villari, V. **(2015)** Hydrodynamic and Thermophoretic Effects on the Supramolecular Chirality of Pyrene-Derived Nanosheets. *Chem. - A Eur. J.* 21, 9505–9513.
- (4) Vybornyi, M., Rudnev, A., and Häner, R. **(2015)** Assembly of Extra-Large Nanosheets by Supramolecular Polymerization of Amphiphilic Pyrene Oligomers in Aqueous Solution. *Chem. Mater.* 27, 1426–1431.
- (5) Vybornyi, M., Nussbaumer, A. L., Langenegger, S. M., and Häner, R. **(2014)** Assembling Multiporphyrin Stacks Inside the DNA Double Helix. *Bioconjug. Chem.* 25, 1785–1793. **(Cover picture)**
- (6) Vybornyi, M., Rudnev, A. V., Langenegger, S. M., Wandlowski, T., Calzaferri, G., and Häner, R. **(2013)** Formation of Two-dimensional Supramolecular Polymers by Amphiphilic Pyrene Oligomers. *Angew. Chem. Int. Ed.* 52, 11488–114893. **(Frontispiece)**
- (7) Faye, D., Vybornyi, M., Boeda, F., and Legoupy, S. **(2013)** Solvent Free Hydrostannation and Stille Reactions Using Ionic Liquid Supported Organotin Reagents. *Tetrahedron* 69, 5421–5425.

